The University Of Sheffield.

Currents in Carbon and Heterocyclic Networks

By:

Christopher Michael Gibson

A thesis submitted in partial fulfilment of the requirements for the degree of Doctor of Philosophy

The University of Sheffield

Faculty of Science

Department of Chemistry

30th September 2015

Abstract

Current-density maps are calculated within the ipsocentric approach for a variety of systems, to determine the nature of their aromatic magnetic response, and to probe the underlying principles governing ring-current aromaticity. The first chapter briefly discusses the history of the term aromaticity, from the discovery of benzene, to ring-current theory, the modern quantum mechanical ipsocentric approach, and the simple but powerful selection rules that are derived from it. Examples of systems displaying aromatic, antiaromatic and localised, non-aromatic responses are provided in Chapter 2 to demonstrate the utility of the method, and the in-depth analysis of aromaticity that it permits. Chapter 3 explores the possibility of designing tailored ring current responses on finite nanographene flakes via functionalisation by examining a variety of nanographene/nanographane hybrids derived from coronene and ovalene. This idea is extended in Chapter 4, by consideration of substitution of C_6 cycles for borazine-like B_3N_3 cycles, creating benzenoid/borazinoid hybrids. Chapter 5 investigates how BN-heteroannulenes can be successfully aromatised by alteration of electronic charge. The approaches for altering current response introduced in Chapters 3 to 5 are unified in Chapter 6 in a case study of pyrene and structures derived from it by variation of charge, substitution, and functionalisation. Chapter 7 further examines how changing the electronic environment by substitution of carbon centres for heteroatoms alters ring-current patterns, using linear polyacenes as the example systems. Chapter 8 moves away from the methods of controlling ring current by chemical manipulation and considers the effects of *geometric* change on aromaticity of the homotropenylium cation and the extended family of *N*-homoannulenes. A brief discussion of the possibilities of designing aromatic systems using extended non-standard ring architectures concludes the thesis.

Some of the chapters in this thesis are expanded accounts of published work on which the author of this thesis is a co-author. The main overlaps are listed below.

Chapter 2. Gibson, C. M.; Fowler, P. W. *Tetrahedron Lett.* **2014**, *55*, 2078–2081.

Chapter 3. Fowler, P. W.; Gibson, C. M.; Bean, D. E. *Proc. R. Soc. A* **2014**, *470*, 20130617:1–18.

Chapter 4. Fowler, P. W.; Gibson, C. M.; Nightingale, E. L. *Polycycl. Aromat. Compd.* **2013**, *33*, 72–81.

Chapter 8. Gibson, C. M.; Havenith, R. W. A.; Fowler, P. W.; Jenneskens, L. W. *J. Org. Chem.* **2015**, *80*, 1395–1401.

Chapter 9. Oziminski, W. P.; Palusiak, M.; Dominikowska, J.; Krygowski, T. M.; Havenith, R. W. 1A.; Gibson, C. M.; Fowler, P. W. *Phys. Chem. Chem. Phys.* **2013**, *15*, 3286–3293.

Acknowledgements

I would like to thank the following people for their help and support throughout my Ph.D.:

My supervisor, Prof. Patrick W. Fowler, FRS, for giving me such an enjoyable project, and for the considerable amount of time and effort he gave me throughout. My collaborators on all the projects I have worked on throughout the last four years, including, but not limited to, Dr Remco W. A. Havenith, Prof. Leonardus W. Jenneskens, Prof. Amnon Stanger, Dr David E. Bean, Dr Wei Huang, Ms Cate S. Anstöter and Mr Joseph Clarke. Dr Anthony J. H. M. Meijer for lots of advice and technical support throughout the project.

My friends at the University of Sheffield, especially Dr Alexander Johnson and David Hopkins, and my friends outside of the University for making my time here so enjoyable.

My family, Mum, Dad and sister Reb for their constant support.

The University of Sheffield for financial support.

And finally, my wife Sylvie for absolutely everything.

Contents

Chapter 1: Introduction

What is Aromaticity?

Benzene and the concept of aromaticity have been inexorably linked since the term was coined by August Hofmann in 1855.[1] The archetypal aromatic system and its derivatives were first described as 'aromatic compounds' because of their characteristic odour, and the name has survived to take a central place in modern chemical thought thanks to the unique properties that these systems displayed. First isolated from a source of illuminating gas derived from whale oil by Michael Faraday in 1825,[2] benzene soon provoked the interest of the wider academic community thanks to its high carbon to hydrogen ratio and unusual properties when compared to aliphatic compounds with a similar number of carbon atoms. These differences were manifold; 'aromatic character', the label given to benzene and the related compounds, was applied to those systems observed to, for example, possess high thermal stability, react to form substitution rather than addition products, and to be resistant to oxidation.

In the mid 1860s, Kekulé proposed the familiar cyclic structure for benzene,[3,4] reasoning that this novel combination of properties could be rationalised by a ring system, later improving this picture to include alternating single and double bonds to account for the carbon valency of four (see Figure 1.1),[5] and although many other possibilities were considered in the literature at the time, his idea quickly became the preferred structure. In a later review of the subject,[6] Kekulé asserted the pre-eminence of his cyclohexatriene arrangement by noting that this form accounted for benzene's formation from acetylene as successfully as any of the alternatives, it better connected benzene with the larger systems naphthalene and anthracene than the other isomers, and it accounted for the fact that disubstituted products of addition reactions corresponded to three isomers.

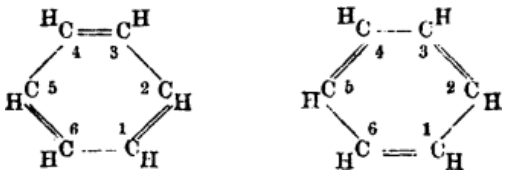

Figure 1.1. Illustration of the two possible arrangements of benzenes single and double bonds, as defined by Kekulé. Taken from reference [5].

The modern meaning of the term aromaticity is less easy to define. On occasion, it can seem that each chemist has their own personal definition. As with many other central terms in the chemical lexicon, there is no single, universally agreed definition. As aromaticity is not a measurable quality, this is perhaps not a surprise.

Aside from the continuous fine-tuning of the definition in the literature, two recent reviews from 1996, recent being a relative term in the long historical perspective necessary when discussing this phenomenon, have attempted to reconcile the individual, intuitive, approach to the problem with the utility offered by a fixed definition. The two reviews take a different view of the history associated with the area and the problems that surround it. The discrepancies in the conclusions they reach highlight the difficulty of achieving consensus within the subject. The first review,[7] by Lloyd, considers the historical contradictions and uncertainties in how the term is applied, and ultimately does not settle on any fixed criterion or criteria for aromaticity, preferring instead the ambiguity and flexibility of interpretation that are fostered in the absence of a rigid definition.

The second review,[8] by Schleyer and Jiao, is methodical in its approach to analysis of the subject. After summarising the history of the discussion of the term, the authors identify four key criteria for aromaticity. The first, reactivity, is that aromatic systems favour electrophilic substitution over addition-type reactions. The second concerns energetic effects, whereby it is expected that aromatic molecules are unusually stable when compared to consideration of their σ frameworks alone. The third criterion, based on geometric properties, states that equal, or near-equal, bond lengths should be present around the cycles. The final criterion, the magnetic criterion, concerns the inference of ring current from a variety of magnetic effects. The limitations of the four criteria were examined case-by-case, with examples of systems that

are intuitively aromatic, but do not adhere to all four criteria are discussed at some length. Some of these systems are shown in Figure 1.2, below.

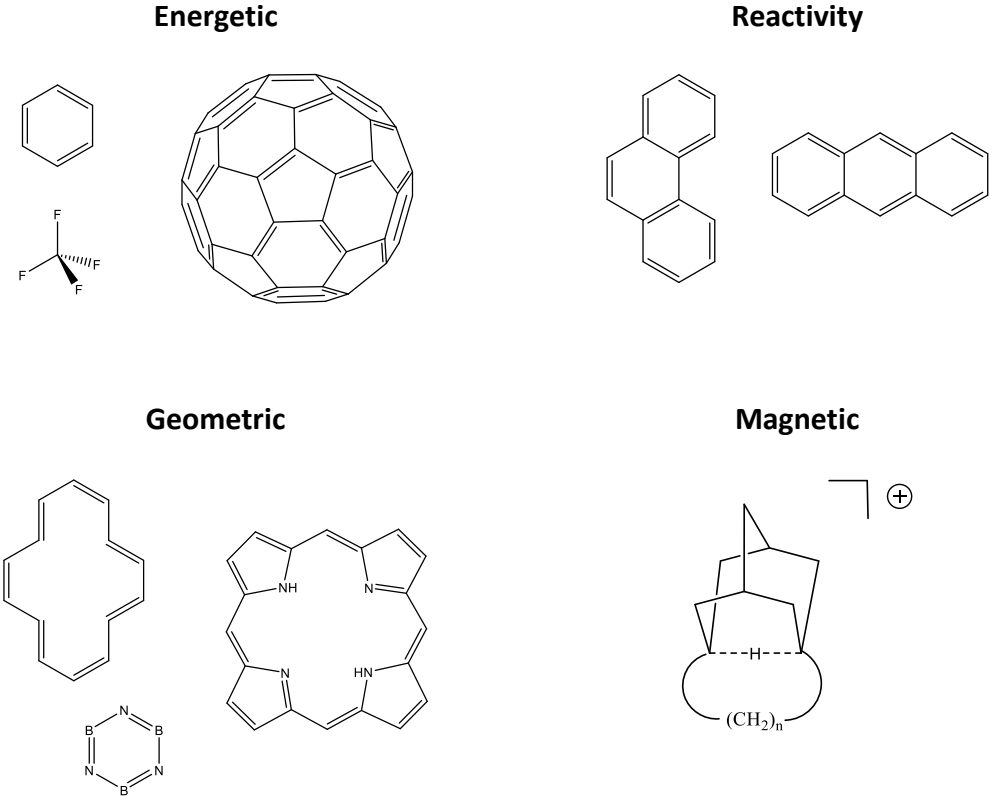

Figure 1.2. The four criteria of aromaticity and some of their exceptions. Taken from reference [8].

Criticisms of the energetic criterion stem from the difficulty of determining the degree of aromatic stabilisation present in a system. Even taking benzene as an example, the aromatic stabilisation energy has been calculated to be in the range 90 – 270 kJ mol^{-1}.[8] This range is large and demonstrates the difficulty in separating aromatic stabilisation from other effects, such as the anomeric effect,[9] where, for example, in tetrafluoromethane, the system is stabilised by overlapping of fluorine lone pairs with the σ* orbitals of the neighbouring CF bonds. This stabilisation has been calculated as approximately 160 kJ mol^{-1}. A further effect of these difficulties is found in the balance of strain and aromatisation energies in fullerenes, which again is difficult to determine.

Similar problems occur when considering the reactivity criterion. The two systems shown above, anthracene and phenanthrene, are both intuitively aromatic, but unlike benzene, preferentially undergo addition rather than substitution reactions.[8]

The use of the geometric criterion is again fraught with danger. Borazine, like benzene, has equal bond lengths around the ring, but, as will be discussed at length in Chapter 2, is not aromatic. In contrast to this, the two aromatic systems shown above, [14]annulene and porphyrin, display strong single-double bond alternation around their perimeters, whilst being undeniably aromatic in character.

Problems also arise with the magnetic criterion, although in this case they may be more subtle. Three separate experimentally-measurable properties were considered as a means of determining aromaticity: ^{1}H-NMR chemical shifts, Li^{+}-NMR chemical shifts, and magnetic susceptibility anisotropy. All three techniques had previously been advocated as diagnostics for determining aromaticity. ^{1}H chemical shifts are very successful at determining aromaticity in many systems,[8] with Pople postulating that the relative 2 ppm proton deshielding of the ^{1}H centres in benzene compared to ethylene was evidence of ring current.[10] The method, however, is unsuitable for systems that do not have appropriately situated protons. A high degree of proton deshielding has also been observed in hydrogen-bridged carbon cations (e.g., the bridged cation shown in Figure 1.2), where the acidic proton possesses an abnormal shift, a result that shows the technique is not suitable as a single 'yes/no' indicator of aromaticity. Use of calculated Li^{+} chemical shifts can, in hindsight, be thought of as the precursor to the nucleus-independent chemical shift (NICS) method,[11] which employs a bq centre as a theoretical probe for the chemical shift at a given point. Large negative NICS values are taken to indicate diatropicity in possible aromatic systems. NICS will be discussed in more detail later in the thesis. Li^{+} centres can be used as probes for ring current, as they are able to form complexes with π systems, with the shift in resonance used to infer the aromatic character of the system. A clear disadvantage of this approach is that it requires direct interaction of the probe and the system under scrutiny, which is likely to change the nature of the effect under investigation in the process. The final effect considered was the presence of large diamagnetic anisotropies. This property also has a history as an aromaticity criterion, and was the inspiration for Pauling's ring-current theory,[12] which is discussed below.

Schleyer and Jiao finally proposed the following definition of aromaticity:[8] '*Compounds which exhibit significantly exalted diamagnetic susceptibility are aromatic. Cyclic electron delocalization also may result in bond length equalization, abnormal chemical shifts and magnetic anisotropies, as well as chemical and physical properties which reflect energetic stabilization. Those compounds which exalted paramagnetic susceptibility may be antiaromatic.'* Hence, they concluded that whilst all the criteria and techniques discussed above are useful in the characterisation of aromaticity, only magnetic susceptibility exaltation is uniquely associated with the phenomenon.

To date, no one, universally approved definition of aromaticity has been found. One succinct description of aromaticity compatible with that seen so far, and the most popular definition amongst theoretical and physical chemists,[13] is simply that an aromatic system is able to sustain a ring current when subjected to an external magnetic field. This is the working definition used in this thesis.

Diamagnetic Susceptibility Exaltation and Anisotropies

Magnetic susceptibility is a proportionality constant that is used to indicate the degree of magnetisation, that is, the vector field that expresses the density of permanent or induced magnetic dipole moments per unit volume (measured in A m^{-1}), of a material in response to an applied magnetic field. To account for the orientation of the system in three-dimensions, the tensor magnetic susceptibility is used. The relationship between the volume magnetic susceptibility χ and the magnetisation, $\mathbf{M}$, of a system is:[14]

$$\mathbf{M}_{\alpha} = \chi_{\alpha\beta}\mathbf{B}_{\beta} \tag{1.1}$$

where $\mathbf{B}$ is the magnetic field strength (with units of A m^{-1}) and α and β are the respective directions of the applied field and magnetisation. The molar susceptibility, χ^{M} (with SI units of $m^3\,mol^{-1}$, often quotes at $cm^3\,mol^{-1}$) is calculated by multiplying χ by the molar mass of the system divided by the density of the system. A positive χ^{M} indicates a paramagnetic

substance, whereby the direction of the induced field is the same as the applied field, and a negative χ^M indicates a diamagnetic substance, whereby the induced field is in the opposite direction to the applied field. In disordered systems such as liquids, solutions, and gasses, the mean molar susceptibility, $\bar{\chi}^{\boldsymbol{M}}$, is used. $\bar{\chi}^{\boldsymbol{M}}$ is defined as the average molar susceptibility over the x, y and z axes:

$$\bar{\chi}^{\boldsymbol{M}} = \frac{1}{3}\left(\chi_{xx}^{\boldsymbol{M}} + \chi_{yy}^{\boldsymbol{M}} + \chi_{zz}^{\boldsymbol{M}}\right) \tag{1.2}$$

Magnetic susceptibilities may be measured experimentally by using a Gouy balance,[15] where a sample is suspended between two magnetic poles and subjected to a magnetic field. The apparent change in mass of the sample, positive in the case of paramagnetic compounds and negative in the case of diamagnetic compounds, is related to the volume susceptibility of the sample by $(\Delta \mathrm{m})\mathrm{g} = \frac{1}{2}(\chi_{medium} - \chi_{sample})\mathrm{A}\mathbf{M}^2$, where $\Delta \mathrm{m}$ is the measured mass difference, g is acceleration due to gravity, χ_{medium} is the (usually negligible) volume susceptibility of the medium, χ_{sample} is the volume susceptibility of the sample, A is the cross sectional area of the sample and $\mathbf{M}$ is the strength of the applied magnetic field.

In planar aromatic molecules, large diamagnetic susceptibility anisotropies ($\Delta\chi$, see Equation 1.3) are also informative. If the system lies in the xy plane, the χ_{zz} component of magnetic susceptibility in aromatics will be much greater than the contributions of the in-plane components, i.e., $\Delta\chi \gg 0$.

$$\Delta\chi = \chi_{zz} - \frac{1}{2}\left(\chi_{xx} + \chi_{yy}\right) \tag{1.3}$$

It is possible to calculate a molar susceptibility value, $\chi_{calc}^{\boldsymbol{M}}$, as a prediction of the experimental χ^M of the system. As reported by Musher,[16] Pascal, in his 1910 publication,[17] claimed that the diamagnetism of a molecule could be determined by summation of individual reference values of the diamagnetic susceptibility of each atom (χ_{at}) and bond (λ) in a given system (see Equation 1.4).

$$\chi_{calc}^{\boldsymbol{M}} = \sum \chi_{at} + \sum \lambda \tag{1.4}$$

These atomic and bond diamagnetic susceptibilities are now known as Pascal's constants, and are available in tabular form sources such as [18]. The difference between the experimental magnetic susceptibilities and those calculated from the Pascal increments is known as the diamagnetic susceptibility exaltation, Λ:[19,20]

$$\Lambda = \chi^{\boldsymbol{M}} - \chi^{\boldsymbol{M}}_{calc} \tag{1.5}$$

Aromatic systems have a large diamagnetic susceptibility exaltation. For example, in benzene $\chi^{\boldsymbol{M}} =$ -54.8 × 10^{6} cm^{3} mol^{-1} and $\chi^{\boldsymbol{M}}_{calc} =$ -41.1 × 10^{-6} cm^{3} mol^{-1}, and the resulting Λ is therefore -13.7 × 10^{-6} cm^{3} mol^{-1}. Pauling, in 1936,[12] was the first to suggest ring current, i.e., a diatropic flow of π electrons in a ring system under an external magnetic, as the cause of the large values of diamagnetic susceptibility anisotropies and the exaltations seen in aromatic molecules. Ring currents and the method of their calculation will now be introduced.

Ring Currents and the Calculation of Ring Currents

As discussed above, diamagnetic susceptibility anisotropies and exaltations were historically used to determine the aromatic status of a molecule. Anomalously strong values for benzene and other planar aromatic systems led Pauling to suggest in his 1936 paper[12] that π electrons could be flowing in delocalised ring currents around these cyclic π-systems. Pauling's model of ring current states that in aromatic systems, a magnetic field $\mathbf{B}$ perpendicular to the plane of the molecule induces a current $\mathbf{J}$, which circulates in accordance with Lenz's law, a qualitative law that states current induced by a change in a magnetic field at in a direction opposing that of the change in flux. The current gives rise to the induced magnetic moment $\mathbf{M}$, which has a direction opposite to the external field. This information is summarised in Figure 1.3.

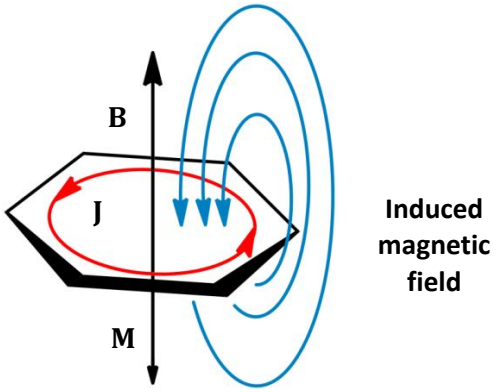

Figure 1.3. Schematic showing the origin of ring currents, **J**, induced in benzene. **B** shows the direction of the applied magnetic field, **M** the opposing diamagnetism arising from the induced ring current. Figure adapted from reference[21].

Unlike electric fields, which can always be expressed as the gradient of a scalar potential, magnetic fields, $\mathbf{B}$, have no general scalar potential.[22] Instead, to calculate the magnetic response of an electron in the presence of an external magnetic field, a modified Hamiltonian operator containing the vector potential, $\mathbf{A}$, is used. From Maxwell's equations $\nabla \cdot \mathbf{B} = 0$,[22] and as the vector identity div curl $\equiv 0$, $\mathbf{A}$ can be related to the field, $\mathbf{B}$, by the operator curl ($\nabla \times$), which in vector calculus is an operator that describes the infinitesimal rotation of a 3-dimensional vector field:

$$\mathbf{B} = \nabla \times \mathbf{A} \tag{1.6}$$

When using a complete basis, the results upon solving the modified Schrödinger equation that accounts for the external field are invariant to gauge origin (the origin of vector potential). In finite-basis treatments this is no longer the case,[23] as a change in the origin of $\mathbf{A}$ alters the Hamiltonian. This has the result that the solutions to the Schrödinger equation have varying paramagnetic and diamagnetic parts as the origin is moved, albeit with unchanging total energy. This observation highlights the necessity of choosing unique, gauge-invariant, wavefunctions when calculating ring-current response. An early attempt to formulate a quantum-mechanical method for calculating ring-current response was made by London in 1937.[24] Building upon the semi-classical formulation of Pauling in 1936,[12] London assumed that molecular orbitals, ψ_n , could be written as linear combinations of gauge-invariant atomic

orbitals, ϕ (see equation 1.7) This was achieved by ignoring the variation of $\mathbf{A}$ over distances of more than one bond length (i.e., applying the Hückel approximation).[24]

$$\psi_n = \sum_i c_i^n \phi_i \tag{1.7}$$

where

$$\phi_i = \phi_i^{(0)} exp\left(-\frac{ie}{\hbar c}\mathbf{A}_i.\mathbf{r}\right) \tag{1.8}$$

and $\phi_i^{(0)}$ is the p_π orbital on atom i and $\mathbf{A}_i$ is the vector potential at nuclear position $\mathbf{r}$.

With these approximations, only the resonance integrals, β, differ from the formulation of simple Hückel theory. As with simple Hückel theory, where a fully conjugated π-system is treated using a simplified Hamiltonian matrix H_{ij}, which is parameterised by $H_{ii} = \alpha$ for carbon atoms, $H_{ij} = \beta$ when atoms neighbour each other, and $H_{ij} = 0$ in all other cases, the resonance integral is nonzero only when centres i and j are formally connected by a bond. For a system under an applied magnetic field, the resonance integral between atoms i and j is:

$$\beta_{ij} = \beta_{ij}^{(0)} \exp\left\{\frac{ie}{2\hbar c}\left(\mathbf{A}_i - \mathbf{A}_j\right).\left(\mathbf{R}_i - \mathbf{R}_j\right)\right\} \tag{1.9}$$

The form of the resonance integral may be simplified by defining the signed area of a triangle formed by the bond i-j and the origin $\mathbf{A} = 0$ as S_{ij} (see Figure 1.4 and Equation 1.10).

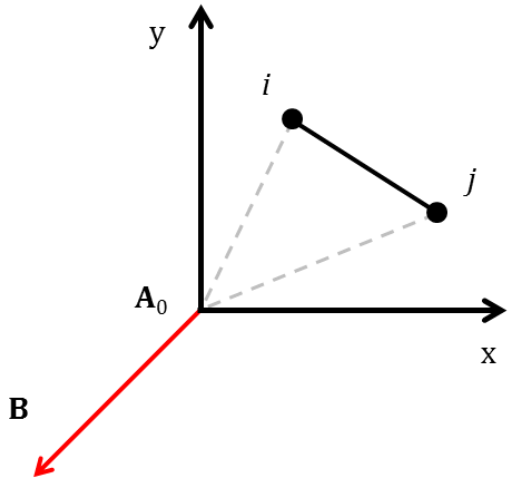

Figure 1.4. The triangle formed by the bond i-j and the origin $\mathbf{A} = 0$, i.e., S_{ij}. Adapted from Ref. [14]

$$\beta_{ij} = \beta_{ij}^{(0)} \exp\left(\frac{ie}{2\hbar c} \mathrm{S}_{ij}\mathbf{B}\right) \tag{1.10}$$

The above modifications to Hückel theory form what is today known as Hückel-London (HL) theory. The HL Hamiltonian for a molecule in a uniform magnetic field is a modified adjacency matrix for the underlying molecular structure with the new resonance integrals, above, substituted in. The resultant Hamiltonian matrix is Hermitian, and the total energy of the system is obtained by the sum of the $n/2$ lowest real eigenvalues.[25] In the same way as simple Hückel theory, the HL method can be further adapted to incorporate heteroatoms by further modification of the coulomb and resonance integrals. This approach will be used in later chapters.

The current density flowing along an individual bond J_{ij} in the direction $i \rightarrow j$, can be obtained from HL theory by differentiation of the total energy with respect to magnetic flux (the surface integral of the normal component of magnetic field passing through the surface), as shown in Equation 1.11.[26] J_{ij} is therefore related to eigenvector entries c_i^n and triangle areas S_{ij} through the sum over occupied orbitals,[25] and the total current in the bond i-j is calculated from $J_{ij} + J_{ji}$.

$$J_{ij} = \left[\sum_{n}(c_i^n)^*\left(c_j^n\right)\right]\exp\left\{\frac{ie}{2\hbar c}S_{ij}\mathbf{B}\right\}j_{ij} \tag{1.11}$$

where j_{ij} is a vector along bond i-j. The calculated current is a real quantity that satisfies Kirchhoff's law of current conservation.

Despite the age of the model, it is still used for the efficient estimation of current in large systems, and as a useful comparison for conjugated-circuit calculations.[25] Coupled to the real utility and advantages offered by the model, drawbacks also, unfortunately, abound. As the model is based on simple Hückel theory, issues regarding orbital topology, energy, and ordering have their effect on the calculated current. Aside from this, the method calculates all current as occurring along π bonds only, and as such cannot contain the full through-space detail of the magnetic response of the full system. For a more in-depth description of ring current, modern *ab initio* methods may be employed. The next section provides a brief account of the calculation of magnetic response properties using coupled Hartree-Fock perturbation theory (CHF).

Ab Initio Calculation of Ring Currents

This section is a summarised form of the detailed account of the topic given in reference [27].

For an *N*-electron system in state Ψ, the charge density $\rho(\mathbf{r})$ and current density $\mathbf{j}(\mathbf{r})$ are given by:[27,28]

$$\rho(\mathbf{r}) = -eN\int \Psi^*\Psi \mathrm{d}\tau' \tag{1.12}$$

and

$$\mathbf{j}(\mathbf{r}) = \frac{e}{m_e}\mathbf{A}\rho(\mathbf{r}) - \frac{e\hbar N}{2im_e}\int(\Psi^*\nabla\Psi - \Psi\nabla\Psi^*)\mathrm{d}\tau' \tag{1.13}$$

where $\int\cdots d\tau'$ represents summation over all electron spins and integration over all space for all electrons excluding the electron with coordinates $\mathbf{r}$. The vector potential $\mathbf{A}$ is related by $\mathbf{B} = \nabla \times \mathbf{A}$ to the magnetic field. In a constant uniform field the simplest form of $\mathbf{A}$ is:[27]

$$\mathbf{A} = \frac{1}{2}\mathbf{B} \times (\mathbf{r} - \mathbf{d}) \tag{1.14}$$

Note that $\mathbf{d}$, the origin of vector potential, is explicitly included.

The Hamiltonian in the absence of the magnetic field is:

$$\hat{H}_0 = -\frac{\hbar^2}{2m_e}\sum_{e^i=1}^{N}\nabla_i^2 + V \tag{1.15}$$

where *V* is the potential energy function. The Hamiltonian for the first-order response of $\mathbf{B}$ is:

$$\hat{H} = \hat{H}_0 + \frac{e}{2m_e}\hat{\mathbf{L}} \cdot \mathbf{B} \tag{1.16}$$

where $\hat{\mathbf{L}}$ is the angular momentum operator for rotation about $\mathbf{d}$. $\hat{\mathbf{L}}$ is the sum of one-electron terms such as $\hat{\mathbf{l}} = (\mathbf{r} - \mathbf{d}) \times \hat{\mathbf{p}}$, where $\hat{\mathbf{p}} = -i\hbar\nabla$ (the linear momentum operator for one electron).

Considering here only closed-shell systems in their ground state, perturbation theory gives the first-order correction to Ψ_0 as:

$$\Psi_0{}^{(1)} = -\frac{e}{2m_e}\sum_{I>0}\Psi_I\frac{\langle\Psi_I|\hat{\mathbf{L}} \cdot \mathbf{B}|\Psi_0\rangle}{E_I - E_0} \tag{1.17}$$

with the first order correction to the current density as:

$$\begin{aligned}\mathbf{j}^{(1)}(\mathbf{r}) &= \frac{e}{2m_e}\mathbf{B} \times (\mathbf{r} - \mathbf{d})\rho_0(\mathbf{r}) + \frac{ie\hbar N}{m_e}\int\left[\Psi_0\nabla\Psi_0{}^{(1)} - \Psi_0{}^{(1)}\nabla\Psi_0\right]d\tau' \\ &= \mathbf{j}^{(\mathrm{d})}(\mathbf{r}) + \mathbf{j}^{(\mathrm{p})}(\mathbf{r})\end{aligned} \tag{1.18}$$

$\mathbf{j}^{(\mathrm{d})}$ is the classical response of a charge distribution to an applied magnetic field (Figure 1.3), the conventional diamagnetic current density. For a single atom with its nucleus as gauge origin ($\mathbf{d}$), this is the sole contribution to the current density.[27] In the general case, the flow

lines of $\mathbf{j}^{(\mathrm{d})}$ are circles with magnitude $|\mathbf{j}^{(\mathrm{d})}|$ (proportional to radius and local charge density) in planes normal to the applied field. $\mathbf{j}^{(\mathrm{p})}$, the paramagnetic-current density, is a sum-over-states quality whose value depends on the accessibility of excited states via rotational transitions; this term effectively represents the interfering effect of the noncylindrical molecular field on the free flow of $\mathbf{j}^{(\mathrm{d})}$.[27]

Although the exact total current density $\mathbf{j}^{(1)}$ is independent of gauge origin, the partitioning between $\mathbf{j}^{(\mathrm{d})}$ and $\mathbf{j}^{(\mathrm{p})}$ is not. The distinction between the diamagnetic and paramagnetic terms has no physical meaning (excluding the above case when $\mathbf{j}^{(\mathrm{p})}$ is zero), leading to the problem of where to place the origin in calculations of the magnetic properties of molecules. A further, related, problem is that second-order magnetic effects, such as nuclear shielding, magnetisability, and polarisability, calculated by integration of the first order current density, also suffer from the problem of gauge dependence.[29]

An early approach to this problem was to use a simple gauge origin placed at the centre of mass,[29] which unfortunately introduces large diamagnetic and paramagnetic artefacts into the calculated current when finite basis sets are used. Multiple-origin techniques such as IGLO (Individual Gauges for Localised Orbitals)[30,31] were put forward as a solution to the problems that arose from a single-origin approach, and did indeed damp the violations of origin-dependence, but it was not until the Ansatz made by Keith and Bader that the corner was turned in addressing this problem.

The Ipsocentric Method

In 1993,[28] Keith and Bader proposed using a continuous set of gauge transformations (CSGT) rather than the discrete distribution-of-origin approach used in other methods. CSGT worked by taking a different origin in real space for each point $\mathbf{r}$ at which $\mathbf{j}(\mathbf{r})$ is calculated, using a continuous shift function $\mathbf{d}(\mathbf{r})$. This numerical approach was immediately shown to be an improvement on previous efforts, with reliable approximations of current density being calculated with smaller basis sets than ever before.[28] This method was renamed and

reformulated into a fully analytical solution at the coupled Hartree-Fock level by Lazzeretti and the Modena group to form the CTOCD-DZ (Continuous Transformation of Origin of Current Density – Diamagnetic Zero) method,[32] the DZ referring to the choice of origin of vector potential via the shift function $\mathbf{d}(\mathbf{r}) = \mathbf{r}$, whereby the current at each point is calculated using that point as origin, and the first-order wavefunction is calculated as an analytic derivative. Steiner and Fowler later renamed CTOCD-DZ as *ipsocentric* to highlight that each calculated point serves as its own origin.[27] The shift-function modification removes the $\mathbf{j}^{(\mathrm{d})}$ term in Equation 1.18. As the total current $\mathbf{j}^{(1)}$ is independent of the partitioning between $\mathbf{j}^{(\mathrm{d})}$ and $\mathbf{j}^{(\mathrm{p})}$, this choice of gauge allows the response of the system to a magnetic field to be described by a single term in which both diamagnetic and paramagnetic effects are interpretable in terms of the accessibility of excited states:[27,33,34]

$$\mathbf{j}^{(1)}(\mathbf{r}) = \frac{ie\hbar N}{m_e}\int\left[(\Psi_0\nabla{\Psi_0}^{(1)} - {\Psi_0}^{(1)}\nabla\Psi_0)\mathrm{d}\tau'\right]_{\mathrm{d=r}} \tag{1.19}$$

Further work undertaken by Steiner and Fowler allowed consideration of orbital contributions to the current density. The angular momentum operator about a point $\mathbf{d}$ can be written as $\hat{\mathbf{L}}(\mathbf{d}) = \hat{\mathbf{L}}(0) + \mathbf{d}\times\hat{\mathbf{p}}$. Here $\hat{\mathbf{L}}(\mathbf{d})$ denotes the origin of the coordinates and $\hat{\mathbf{p}}$ the *N*-electron linear momentum operator (which has the symmetry of a translation). A rotation around the origin and a displacement term replace the rotation about the origin of vector potential. The first-order wavefunction for any choice of $\mathbf{d}$ is therefore:

$$\begin{aligned}{\psi_0}^{(1)} &= \frac{e}{2m_e}\left[\sum_{I>0}\Psi_I\frac{\langle\Psi_I|\hat{\mathbf{L}}(0)|\Psi_0\rangle}{E_I - E_0}\right]\cdot\mathbf{B} + \frac{e}{2m_e}\left[\mathbf{d}\times\sum_{I>0}\Psi_I\frac{\langle\Psi_I|\hat{\mathbf{p}}|\Psi_0\rangle}{E_I - E_0}\right]\cdot\mathbf{B}\\ &= {\psi_0}^{(\mathrm{p})} + {\psi_0}^{(\mathrm{d})}\end{aligned} \tag{1.20}$$

where the sum-over-states terms ${\psi_0}^{(\mathrm{p})}$ and ${\psi_0}^{(\mathrm{d})}$ are the conventional paratropic and diatropic contributions to $\mathbf{j}^{(\mathrm{p})}$ and $\mathbf{j}^{(\mathrm{d})}$ (determined by the accessibility of *rotational* or *translational* excited states), respectively. $\hat{\mathbf{L}}$ and $\hat{\mathbf{p}}$ are sums of one-electron operators. This allows ${\psi_0}^{(1)}$ to be written as a sum over states in which ψ_I are singly-excited electron configurations, ψ_n^p, the result of (in a closed shell *N*-electron system) the excitation of an electron from an occupied ($\psi_n, n \leq N/2$) to a virtual ($\psi_p, p > N/2$) orbital. The first-order current-density is therefore a sum of orbital contributions:[27,35]

$$\mathbf{j}^{(1)}(\mathbf{r}) = 2\sum_{n=1}^{N/2} \mathbf{j}_n^{(1)}(\mathbf{r}) \tag{1.21}$$

with orbital densities:

$$\mathbf{j}_n^{(1)}(\mathbf{r}) = -\frac{e^2}{2m_e}\mathbf{B}\times(\mathbf{r}-\mathbf{d})\psi_n^2 + \frac{ie\hbar}{m_e}\left[\psi_n\nabla\psi_n^{(1)} - \psi_n^{(1)}\nabla\psi_n\right] \tag{1.22}$$

$$= \mathbf{j}_{\boldsymbol{n}}^{(\mathrm{d})} + \mathbf{j}_{\boldsymbol{n}}^{(\mathrm{p})}$$

Assuming (ignoring for simplicity the self-consistency corrections) that ψ_n are eigenfunctions of a one-electron Hamiltonian with eigenvalues ε_n, the first-order correction to ψ_n is then

$$\psi_n{}^{(1)}(\mathbf{r}) = -\frac{e}{2m_e}\left[\sum_{p>N/2}\psi_p(\mathbf{r})\frac{\langle\psi_p|\hat{\mathbf{l}}(0)|\psi_n\rangle}{\varepsilon_p-\varepsilon_n}\right]\cdot\mathbf{B} + \frac{e}{2m_e}\left[\mathbf{d}\times\sum_{p>N/2}\psi_p(\mathbf{r})\frac{\langle\psi_p|\hat{\mathbf{p}}|\psi_n\rangle}{\varepsilon_p-\varepsilon_n}\right]\cdot\mathbf{B} \tag{1.23}$$

$$= \psi_n^{(\mathrm{para})}(\mathbf{r}) + \psi_n^{(\mathrm{dia})}(\mathbf{r})$$

Hence the orbital current density $\mathbf{j}_n^{(1)}$ is determined in its entirety by the accessibility of orbital transitions between occupied, ψ_n, and unoccupied, ψ_p, orbitals. This information is summarised in the next section to enable the arguments to be applied in the discussion of aromaticity in real systems.

For completeness, a brief discussion of other approaches developed via a similar rationale is necessary. Whilst the ipsocentric CTOCD-DZ approach offers results that converge rapidly with basis size to the Hartree-Fock limit[36] and permits partitioning of reduced current into non-redundant orbital contributions,[27,35] it does not give accurate computation of magnetisability and shieldings as a well as some other methods. The first, CTOCD-PZ,[37] where PZ stands for Paramagnetic Zero, labelled the *allocentric* approach by Lazzeretti,[29] offers advantages over the ipsocentric approach in these areas. Under this method, the perpendicular components of paratropic current are set to zero. In this approach, the origin of vector potential is moved to a point other than that being calculated. Only in the limit of an exact wavefunction is an analytical expression for the allocentric shift function $\mathbf{d}(\mathbf{r})$

obtainable, where is it found to depend on the inverse of electron density.[37] This implies that $\mathbf{d}(\mathbf{r})$ will have discontinuities where the electron density is zero, although with appropriate numerical safeguards, total current density and the integrated magnetic properties, magnetisability and shieldings may be safely calculated.[37] However, despite this, only the latter two properties are improved by application of this method, as no partitioning of induced current into physically non-redundant orbital contributions is possible.[38]

Two further variants of the above two CTOCD methods were later defined: CTOCD-DZ2[37] and CTOCD-PZ2.[37] In these methods, the origin $\mathbf{d}(\mathbf{r})$ is shifted to the nearest nucleus by an exponential pushing function.[37] The computed numerical values of the integrated properties are significantly improved with both methods, with CTOCD-PZ2 offering accurate results that converge more quickly with basis set.

As it stands, therefore, there are four related methods for computing magnetic response. The question arises as to which is most suitable for the purpose of calculating induced current density. Current-density maps calculated by Soncini and Fowler[38] were used to address this question. Considering five representative systems, namely benzene, cyclooctatetraene, borazine, tris(cyclobutano)benzene and tris(cyclobutadieno)benzene, maps of total π current-density were calculated for each system. The maps of all five systems were found to be qualitatively identical in each of the DZ, PZ, DZ2 and PZ2 approaches, with values of current-density across the molecule varying at most by approximately 1%.[38] The advantages of non-redundant orbital deconstruction of current offered by the CTOCD-DZ ipsocentric method are, therefore, clear, making the method the obvious choice for use here.

Selection Rules

The resultant key features of the ipsocentric approach can be distilled into simple selection rules that govern the presence (or absence) of both diatropic and paratropic ring currents.[27] These rules, detailed below, are based upon three factors: symmetry, spatial distribution, and energy. In the rules, $R_{\parallel}$ and $T_{\perp}$ represent rotation about the field direction and translation at

right angles to the field. $\Gamma(\psi)$, $\Gamma(R_{\parallel})$, $\Gamma(T_{\perp})$ and Γ_0 (the totally symmetric component) are the representations of an orbital (or a set of degenerate orbitals), rotations about the field direction, translations at right angles to the field and the totally symmetric representation, G, respectively. Assuming that the relevant orbitals occupy the same region of space, five selection rules may be derived from the above concerning the transition from ψ_n to ψ_p.

The rules state that:

1. the transition has a diamagnetic (*diatropic*) contribution to $\mathbf{j}_n^{(1)}$ if the direct product of representations $\Gamma(\psi_n) \times \Gamma(\psi_p) \times \Gamma(T_{\perp})$ contains Γ_0, i.e., the transition is translationally allowed and aromatic.
2. the transition has a paramagnetic (*paratropic*) contribution to $\mathbf{j}_n^{(1)}$ if the direct product of representations $\Gamma(\psi_n) \times \Gamma(\psi_p) \times \Gamma(R_{\parallel})$ contains Γ_0, i.e., the transition is rotationally allowed and antiaromatic.
3. the transition has a diamagnetic *and* a paramagnetic contribution to $\mathbf{j}_n^{(1)}$ if both of the direct products of representations $\Gamma(\psi_n) \times \Gamma(\psi_p) \times \Gamma(T_{\perp})$ or $\Gamma(\psi_n) \times \Gamma(\psi_p) \times \Gamma(R_{\parallel})$ contain Γ_0.
4. the transition has no contribution to $\mathbf{j}_n^{(1)}$ if neither of the direct products of representations $\Gamma(\psi_n) \times \Gamma(\psi_p) \times \Gamma(T_{\perp})$ or $\Gamma(\psi_n) \times \Gamma(\psi_p) \times \Gamma(R_{\parallel})$ contain Γ_0.
5. the transition has an inverse proportionality relationship between the difference in energy of ψ_n and ψ_p and the size of the contribution (from the $\frac{1}{\varepsilon_p - \varepsilon_n}$ terms in Equation 1.23), suggesting a major role for π-HOMO to π-LUMO 'frontier' transitions.

The power of these selection rules, in terms of prediction and interpretation of ring currents, is exploited repeatedly throughout this thesis. The essence of the approach is that it gives interpretable visualisations of magnetic response. Results from ipsocentric current-density calculations are rarely displayed as numerical values, but instead plotted as vectors on a grid as current-density maps. Chapter 2 provides examples of these maps for aromatic, antiaromatic, and nonaromatic systems, and explores in depth the utility of the non-redundant orbital contributions provided by the ipsocentric method, and the use of the above selection rules in investigations into ring current aromaticity.

Chapter 2: Ipsocentric Ring Currents*

This chapter introduces ipsocentric current-density maps, the primary source of information used in all subsequent chapters to determine the nature of π ring-current response of a system to magnetic perturbation. Details of the standard plotting conventions are presented alongside a discussion of the features in the maps used to diagnose aromaticity. Examples of closed shell aromatic, antiaromatic and nonaromatic systems are provided, and their currents analysed in terms of canonical and localised molecular orbitals (CMOs and LMOs), the principal bases for describing the origin of ring currents. The power of these techniques is then illustrated using a case study of a family of molecules where the aromaticity was until recently in dispute: the sydnones.

Current-Density Maps

The standard approach to produce current-density maps is to perform an ipsocentric[27,33] coupled Hartree-Fock calculation on an optimised geometry of the system of interest. The ipsocentric calculation is carried out using the SYSMO[39] suite of programs, which is comprised of routines for evaluating 1- and 2-electron integrals, performing an iterative restricted Hartree-Fock calculation of the unperturbed system, evaluating the matrices of the perturbation operators in the chosen atomic basis, and calculating using coupled Hartree-Fock theory the result of linear- and angular-momentum perturbations. The direction of the applied magnetic perturbation is then chosen, and current-density maps are plotted in the desired orbital basis – usually the Pople type 6-31G** set. The optimised geometry, by convention, is

* Some of the material in this chapter has been published in: Gibson, C. M.; Fowler, P. W. *Tetrahedron Lett.* **2014**, *55*, 2078–2081. Prof. Joseph P. A. Harrity is gratefully thanked for his assistance in writing the section on sydnone aromaticity.

normally calculated in the same 6-31G** basis set but at the DFT/B3LYP level of theory to avoid the symmetry breaking that can occur in HF optimisations. As mentioned in Chapter 1, this modest level of theory is appropriate for general use as it provides well converged results for atoms belonging to the first row of the periodic table.[36]

The maps themselves show first-order π current-density in the plotting plane, which will usually be defined as being 1 a_0 above the median plane of the nuclei, chosen to be approximately aligned with the point of maximum density of a carbon-carbon π-orbital. Nuclear positions are represented by symbols based on Dalton's symbols for the elements, as shown in Figure 2.1. The induced magnetic field, unless specified to the contrary, is positioned perpendicular to the plotting plane. Contours and shading indicate the modulus of the induced current density per unit external magnetic field, and arrows indicate the vector current density resolved into the plotting plane. Maps report diatropic ring currents as anticlockwise circulations and paratropic currents as clockwise circulations. A quantitative measure of the strength of an induced current is given by its j_{max} value, defined as the maximum current density per unit inducing field taken over the plotting plane. These values are generally quoted with reference to those of related molecules or the benzene standard (0.078 a.u. at the CHF/6-31G** level or 0.079 a.u. at the B3LYP/6-31G** level).

Figure 2.1. Symbols used to denote nuclear positions in current-density maps.

Methods

All structures in this chapter were optimised at the B3LYP/6-31G** level using Gaussian 09.[40] Frequency calculations showed D_{4h} cyclooctatetraene, **2**, to have a single imaginary frequency (152*i* cm^{-1}) corresponding to the conjugation breaking puckering motion to form the 'tub-shaped' D_{2d} minimum energy structure. All other systems were found to be geometric minima on the potential energy surface at the symmetries reported. Current-density maps were calculated using the ipsocentric method at the CHF/6-31G** as implemented in the SYSMO package.[39] In cases where ring structures have small deviations from planarity, σ and π symmetries are not rigorously mathematically defined. 'π-like' canonical or localised molecular orbitals are instead identified by inspection, and total π currents produced as sums of these contributions.

Aromatic Ring Currents: Benzene

The natural choice of system to introduce current-density maps and the explanations provided by the ipsocentric approach is the archetypal aromatic molecule, D_{6h} benzene, **1**. Figure 2.2 shows the total current induced in benzene, alongside its breakdown into individual σ and π orbital contributions, where σ is defined as any orbital with a positive character for its irreducible representation under the $\sigma_h(xy)$ transformation, and π as any orbital with negative character for the same transformation.

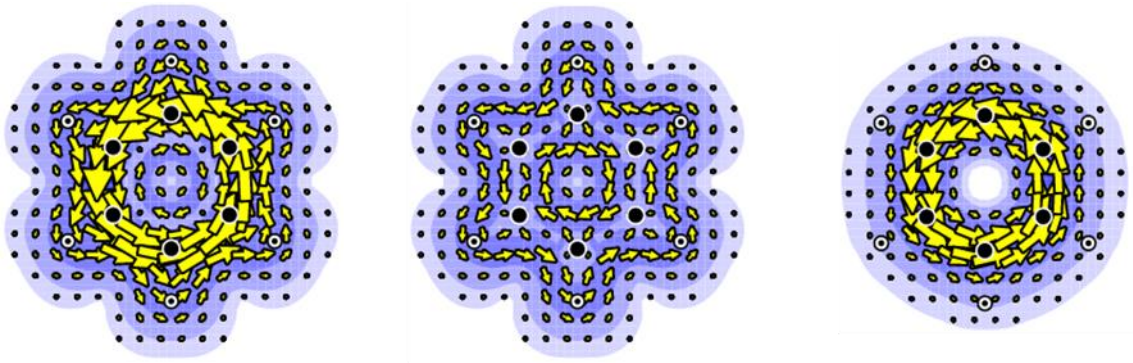

Figure 2.2. Current-density maps calculated at the CHF/6-31G** level on B3LYP/6-31G** optimised D_{6h} benzene showing (a) the total induced current, (b) the response of the 18 orbital σ system, and (c) the 3 orbital π system. Plotting conventions are described in the text.

Initial inspection of these maps shows that the total current (Figure 2.2 (a)) is dominated by a strong, anticlockwise, diatropic circulation. Breaking down this picture into its constituent σ- (Figure 2.2 (b)) and π-parts (Figure 2.2 (c)), it becomes clear that the aromatic ring current in benzene arises solely from π-orbital contributions. The most interesting aspect of the current derived from the σ-framework is a weak, in plane, paratropic circulation visible in the total map as a diminished internal current within the C_6 ring. This response will be discussed in more detail when LMO contributions to current are introduced.

Examination of the contributions to current from individual π orbitals offers an explanation for the dominant aromatic signature displayed in the maps. As discussed in Chapter 1, the ipsocentric model allows currents to be rationalised as occurring via virtual transitions between occupied and unoccupied frontier π orbitals. These excitations result in diatropic circulations if translationally allowed, and paratropic circulations if rotationally allowed. The resultant currents are moderated by the size of the energy gap between the orbitals involved. In benzene the three occupied π orbitals are of e_{1g} and a_{2u} symmetry, with the three lowest energy π* orbitals consisting of a degenerate e_{2u} pair and a single b_{2g}. Figure 2.3 shows the individual CMO contributions to π current in benzene.

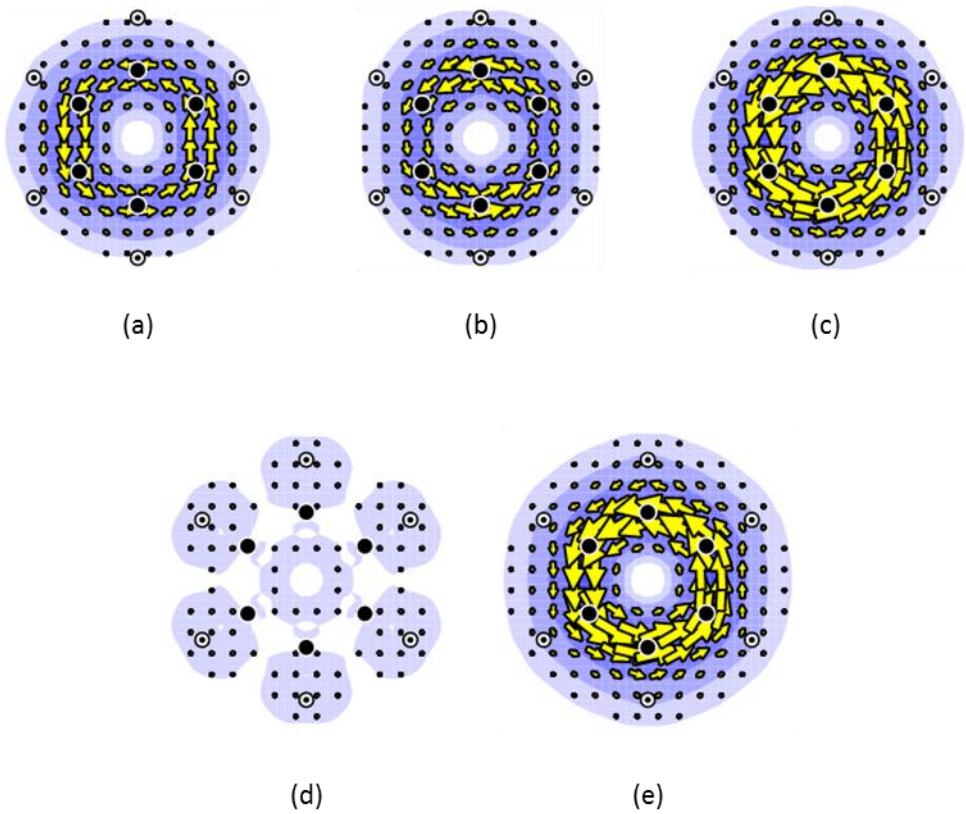

Figure 2.3. CMO contributions to π current density in D_{6h} benzene from: (a and b) the two individual orbitals of the e_{1g} degenerate HOMO pair, (c) the combined sum of the e_{1g} HOMO pair, (d) the a_{2u} HOMO-1, and (e) the total π current, *i.e.*, the summed contributions of (c) and (d). Plotting conventions are described in the text.

The immediate conclusion that can be drawn from the maps in Figure 2.3 is that the majority of the π current in benzene originates from just two orbitals, the degenerate e_{1g} HOMO pair (see Figure 2.3(a to c)). This observation is easily rationalised using ipsocentric symmetry-based arguments. In the D_{6h} point group the translations T_x and T_y are of e_{1u} symmetry, the virtual excitations between the $\Lambda = 1$ e_{1g} HOMO and the $\Lambda = 2$ e_{2u} LUMO are therefore allowed and result in a diatropic current, as indicated in the energy-level diagram Figure 2.4. This 4-electron HOMO current dominates the response of the π system as the a_{1u} HOMO-1 is translationally related only to orbitals of e_{1g} symmetry, which are fully occupied in the frontier space, yielding the almost negligible contribution to current seen in Figure 2.3(d). The completeness of this 4-electron description of the origins of the induced diatropic current can be quantified with reference to their j_{max} values: for the total π current (Figure 2.3(e))

j_{max} = 0.078 a.u., c.f. the map from the HOMO pair, j_{max} = 0.078 a.u., which therefore accounts for the complete total π response. There is no paratropic contribution to current as the rotation R_z is of a_{2g} symmetry and the only π product of the representations of the occupied set and the rotation is of a_{1u} symmetry, which is not present in the frontier space.

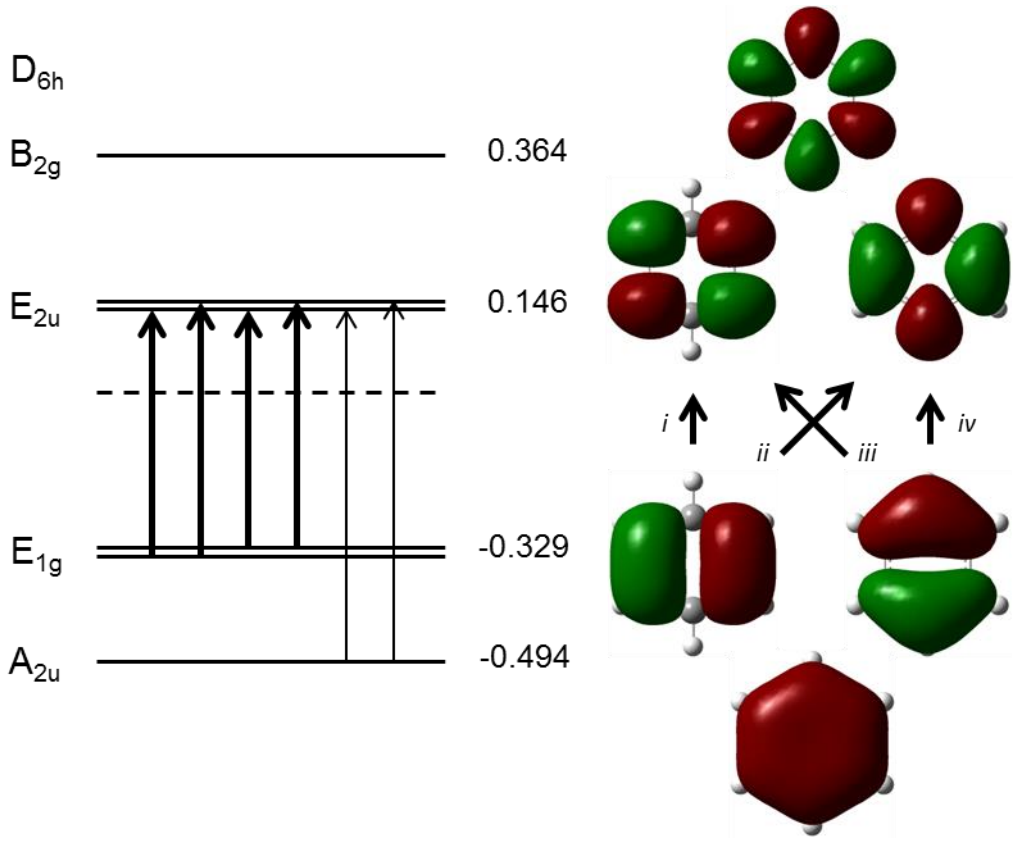

Figure 2.4. Orbital energy-level diagram showing the first six frontier π-π* excitations from the occupied CMOs of D_{6h} benzene. Canonical molecular orbital topologies are shown, with orbital energies in E_h. The conventions used to denote excitations are as follows: dominant excitations are shown in bold, translationally allowed excitations are shown as narrow, solid arrows, whilst rotationally allowed excitations (not present in this figure) represented as wide, hollow arrows. Roman numerals refer to the individual occupied-to-virtual orbital excitations shown in Figure 2.5.

Looking at the orbital topologies in Figure 2.4 highlights the fact that the HOMO/LUMO excitation in benzene can be considered as the sum of four separate transitions, one from each of the occupied e_{1g} pair to each of the virtual e_{2u} pair. It is possible, under the ipsocentric model, to further decompose the orbital contributions to ring current into these individual spectral transitions,[41] thereby identifying the exact nature of the excitations responsible for current. Figure 2.5(a) shows the current density maps corresponding to the four separate excitations between the degenerate HOMO and LUMO pairs. The Roman numerals *i* – *iv* from Figure 2.4 are used to connect each map to its parent virtual transition.

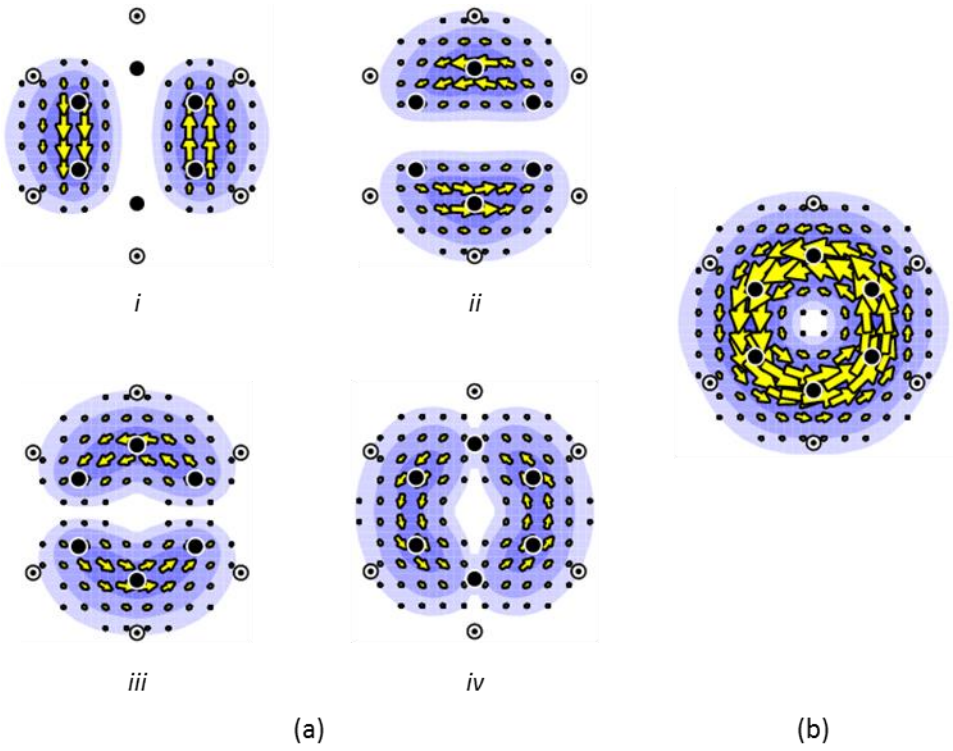

Figure 2.5. Spectral decomposition of the dominant CMO contributions to π current in D_{6h} benzene. (a) shows the four currents arising from excitations between the e_{1g} HOMO and e_{2u} LUMO pairs, Roman numerals identify the individual orbital-to-orbital transitions as in Figure 2.4. (b) is the summed product of the four maps and is qualitatively identical to the total benzene π current map In Figure 2.2(c). Plotting conventions are described in the text.

The four maps that are the result of spectral decomposition, whilst all incomplete, all display a different current response owing to their different orbital origins *i* – *iv*. Summation of the four contributions, as shown in Figure 2.5(b), produces a map that effectively accounts for the entire benzene ring current, again quantitatively confirmed by a j_{max} value: 0.077 a.u., 99 % of the benzene total π value.

It should be noted at this point that simple Hückel theory is able to reproduce the essential features of the energy-level diagram (Figure 2.4). In the Hückel approximation for a ring of *n* atoms with equal coulomb parameters (α), connected by bonds with equal resonance parameters (β), the π MOs and their energies can be described by a Frost-Musulin diagram.[42] The diagram is constructed from a regular *n*-gon, drawn point facing down, imposed onto a circle of radius 2β centred on the origin. Energies correspond to the position of the vertices on the β scale, and the orbitals are formed from sine and cosine combinations related to the angular momentum quantum number, Λ. See Figure 2.6 for the Frost-Musulin diagram of benzene.

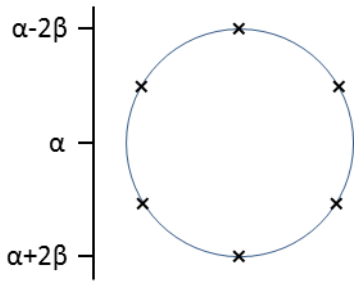

Figure 2.6. The Frost-Musulin diagram of D_{6h} benzene.

The above picture shows the three occupied, bonding orbitals of the π-system precisely mirroring the unoccupied, antibonding set, with a degenerate HOMO and LUMO pair on the frontier. This arrangement is to be found in all closed-shell neutral configurations of [*n*]annulenes with *n*/2 occupied orbitals. Similar arguments also apply in all other cases with closed shell, 'aromatic' 4N + 2 π electrons counts. In all these cases, ipsocentric arguments show that these systems cannot produce paratropic currents. As in-plane rotations mix only orbitals with the same Λ, only diatropic, node-increasing transitions will contribute to current.

So far the origin of ring current in benzene has been analysed solely in terms of the CMO basis, which has been shown to provide an economical two-orbital account of the induced current. To complement this picture, it is often instructive to break down current in terms of localised orbital contributions, providing as they do a different view point from which to discuss and rationalise observed magnetic response. The three π LMOs are generated using the Pipek-Mezey localisation procedure,[43] offering as it does the advantage of maintaining the distinction between σ- and π-symmetry.

Although the choice of orbital representation is ultimately arbitrary, as any unitary transformation amongst occupied orbitals will result in the same total electron density, and under the ipsocentric approach, the same current density, the LMO basis offers distinct advantages to investigations of aromaticity. The LMO contributions to current are able to reveal whether what appears to be a ring current is indeed intrinsically delocalised, or merely an illusion formed by a combination of localised features. Figure 2.7 shows the current associated with the three degenerate π LMOs of benzene.

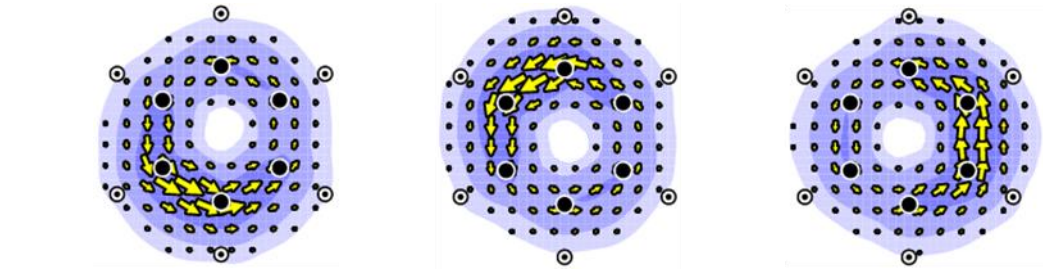

Figure 2.7. LMO contributions to π current density in D_{6h} benzene showing the three equivalent open-ended currents produced via Pipek-Mezey localisation. Plotting conventions are described in the text.

Even though the CMO description of π ring current is more economical, requiring only two molecular orbitals to account for the aromaticity of benzene, the three equivalent LMO current density maps confirm with their open ended flowlines the genuine delocalised current around the ring. Summation of the maps would result in a precisely identical picture of total π current of benzene as the three localised orbitals describe the entire π system exactly. The remaining 18 LMOs form the σ framework, and are split into three sets of six, one

corresponding to the carbon-carbon σ bonds, one to the carbon-hydrogen bonds and one to the carbon $1s^2$ cores. The maps of these features display closed loops of current, identifying them as purely localised features (see Figure 2.8). The localised behaviour of the σ system offers an explanation for the internal vortex of current seen inside the C_6 ring in the map of total σ current (see Figure 2.2). As neighbouring maps of localised carbon-carbon single bond circulations (Figure 2.8 (a)) are summed, the current at their interface cancels out, resulting in counter flowing inner and outer circulations that appear delocalised.

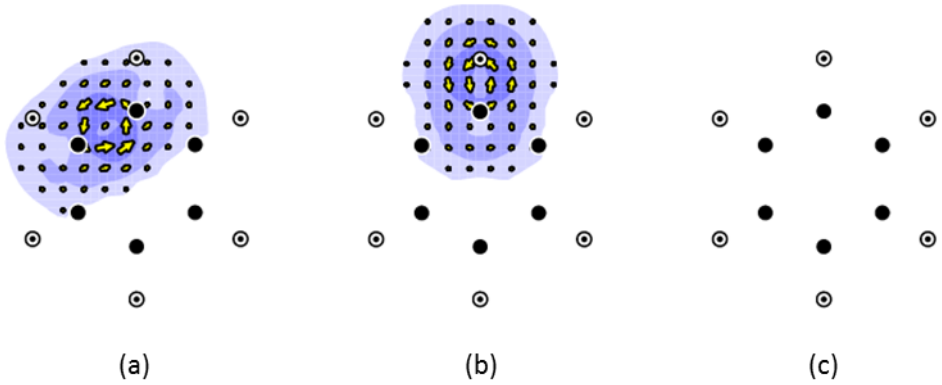

Figure 2.8. Example LMO contributions to σ current-density in D_{6h} benzene. (a) One of six equivalent localised carbon-carbon single bonds. (b) One of six equivalent localised carbon-hydrogen single bonds. (c) A $1s^2$ orbital. Plotting conventions are described in the text.

Antiaromatic Ring Currents: Planar Cyclooctatetraene (COT)

The logical choice of a system to illustrate antiaromatic ring currents is perhaps less clear. Use of the Hückel arguments tells us that no regular *n*-gon, i.e., a neutral, closed-shell maximally symmetric [*n*]annulene, can possess rotationally allowed excitations from HOMO to LUMO, and hence cannot be antiaromatic. Monocycles with $4N\,\pi$ electrons, which are open shell doublets in their maximum symmetry D_{nh} states, can, via reduction in symmetry by Jahn-Teller distortion, form closed-shell singlet systems with a rotationally allowed $\Delta\Lambda = 0$ transition between HOMO and LUMO across the frontier.

Planar D_{4h} cyclooctatetraene (COT), **2**, although energetically a transition state on the reaction coordinate corresponding to the inversion motion of the D_{2d} 'tub' geometry,[44] is the classic example of such a system. This ring system, with its alternating single and double carbon-carbon bonds, is not just hypothetical. Synthetic chemists have succeeded in producing the uncommon antiaromatic structure by use of an appropriate σ-framework, for example by use of 'clamping' functional groups.[45–47] Figure 2.9 shows the total current induced in D_{4h} COT, alongside the breakdown into individual σ- and π-orbital contributions, where π is again defined as orbitals with a negative character for their irreducible representation under the $\sigma_h(xy)$ transformation.

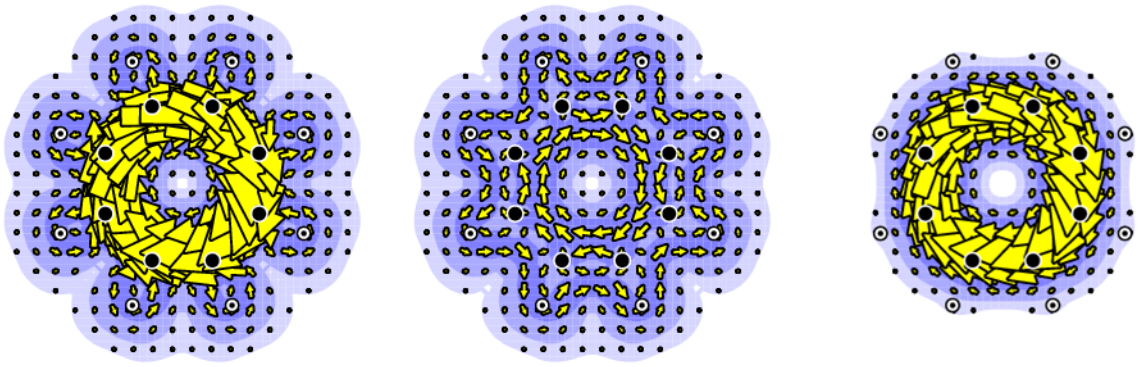

Figure 2.9. Current-density maps calculated at the CHF/6-31G** level on B3LYP/6-31G** optima of planarised D_{4h} cyclooctatetraene, showing (a) the total induced current, (b) the response of the 24 orbital σ system, and (c) the 4 orbital π system. Plotting conventions are described in the text.

The primary view of the induced current-density maps shows that the total current (Figure 2.9 (a)) in this case is dominated by a strong, clockwise, paratropic antiaromatic current. Breaking down this picture into its constituent σ- (Figure 2.9 (b)) and π-parts (Figure 2.9 (c)) again confirms that the ring current arises solely from π-orbital contributions.

Further decomposition of the total π-current density (j_{max} 0.157 a.u.) reveals the origin of the antiaromaticity of COT. Separating the π-component of current into individual CMO contributions to current (see Figure 2.10) shows that, as expected by ipsocentric frontier

orbital arguments, the majority of the current arises from excitations from the b_{2u} HOMO. The sum of all the transitions from this orbital (Figure 2.10 (a), j_{max} 0.182 a.u.) are actually 1.16 times stronger than the total π current. Examination of the energy-level diagram of COT (Figure 2.11) provides an explanation of this discrepancy. Excitations from the degenerate e_g Λ = 1 HOMO-1 pair to the b_{1u} Λ = 2 LUMO are translationally allowed, and hence diatropic. This weaker, aromatic source of current (see Figure 2.10 (b)) cancels out some of the dominant HOMO contribution, thereby diminishing the overall strength of the total π current accordingly.

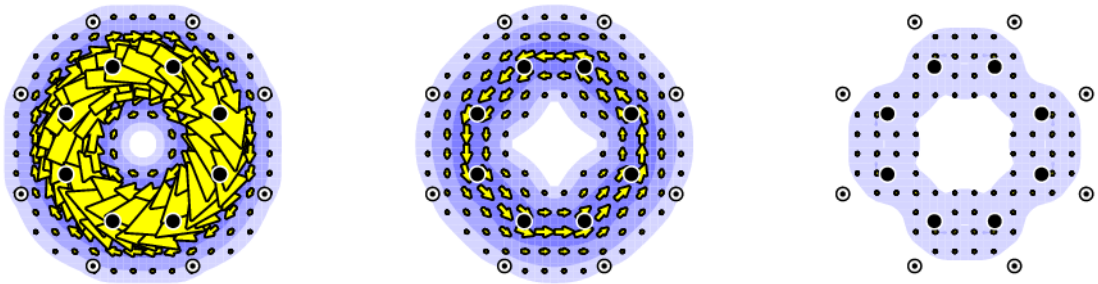

Figure 2.10. CMO contributions to π current density in D_{4h} COT from: (a) the dominant paratropic current arising from the b_{2u} HOMO, (b) the weaker, diatropic, cancelling contribution from the degenerate e_g HOMO-1 pair, and (c) the negligible circulation due to the a_{2u} HOMO-2. Plotting conventions are described in the text.

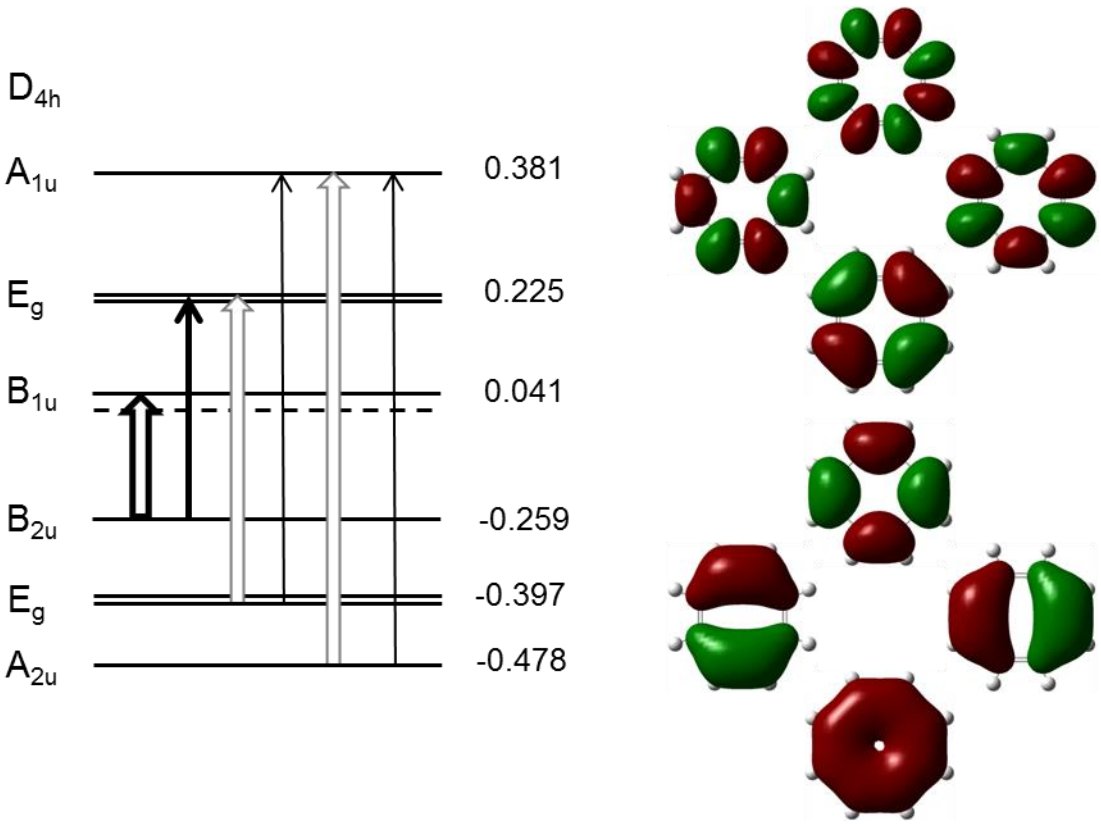

Figure 2.11. Orbital energy-level diagram showing the first six frontier π-π* excitations from the occupied CMOs of D_{4h} COT. Canonical molecular orbital topologies are shown, with orbital energies in E_h. Narrow, solid arrows and wide, hollow arrows represent allowed excitations of translational and rotational symmetry, respectively. The dominant contributions to current are shown in bold.

The HOMO contribution to current can be still further broken down by spectral decomposition; Figure 2.12 shows the result of this analysis of current into the major frontier orbital contributions. The b_{1u} $\Lambda = 2$ LUMO and the degenerate e_g $\Lambda = 3$ LUMO+1 pair are both energetically and symmetrically accessible from the b_{2u} $\Lambda = 2$ HOMO. The excellent rotational match and small energy gap between the HOMO and LUMO results in a very strong (Figure 2.12 (a), $j_{max} = 0.233$ a.u.) paratropic current, whilst the HOMO to LUMO+1 translationally allowed transition acts to weaken the HOMO current by diluting it with another cancelling diatropic flow (Figure 2.12 (b), $j_{max} = 0.070$ a.u.).

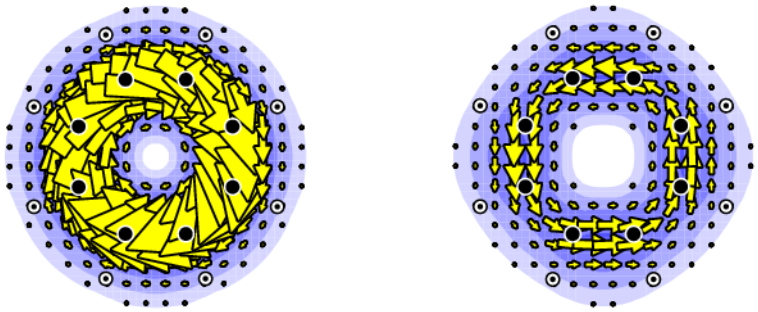

(a) (b)

Figure 2.12. (a) The strong paratropic π current arising from the single b_{2u} HOMO to b_{1u} LUMO virtual transition in D_{4h} COT. (b) The opposing weaker diatropic π current arising from the excitation between the b_{2u} HOMO and the degenerate e_g LUMO+1 pair. Plotting conventions are described in the text.

Localised Magnetic Response: Borazine

D_{3h} borazine, **3**, is often described as 'inorganic benzene';[48–60] this appellative, whilst attractive owing to borazine being isoelectronic with and geometrically similar to benzene, is undeserved. Ipsocentric current-density calculations show that the current arising from the 3 π orbitals of borazine result in distinct islands of 'lone-pair' circulations above the three electronegative nitrogen centres,[61] as shown in Figure 2.13 (j_{max} = 0.041 a.u.). A canonical breakdown of the π current into its constituent e" and $a"_2$ components shows that all three CMOs contribute significantly to current. This is in contrast to the four- and two-electron accounts of aromaticity encountered so far.

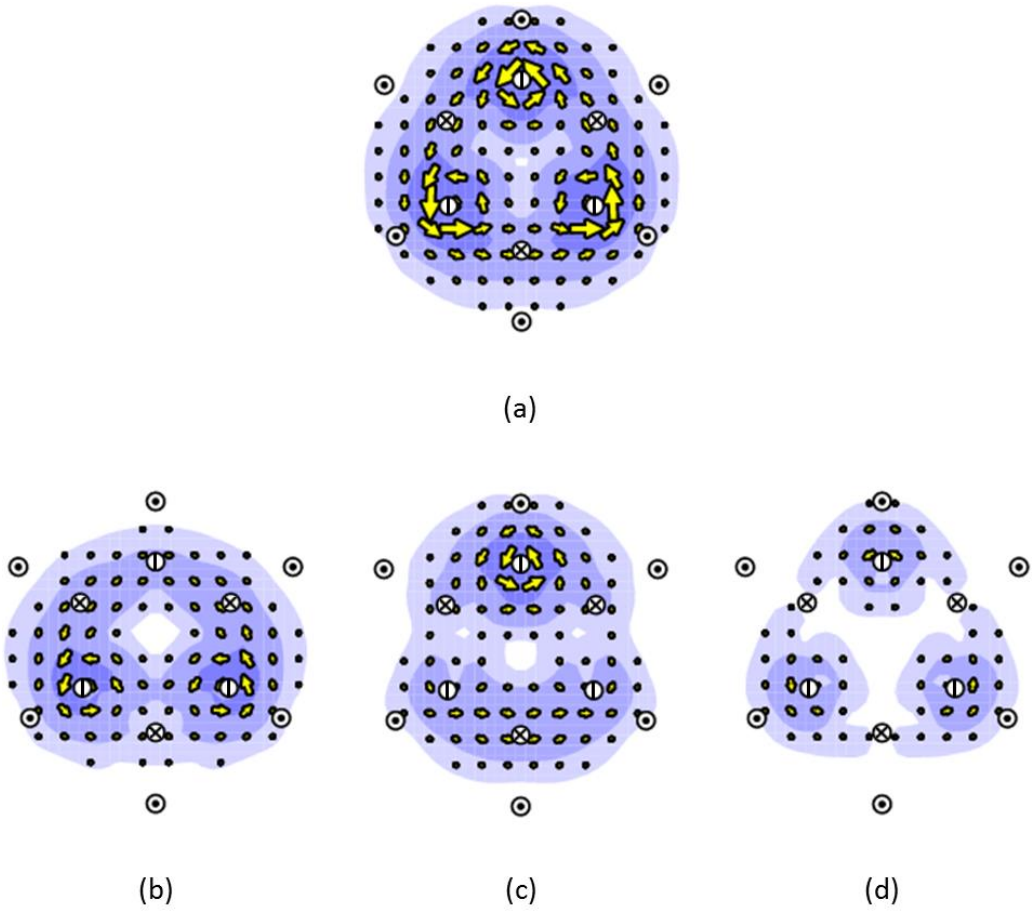

Figure 2.13. Total π CMO breakdown of π current density in D_{3h} borazine from: (a) The total π current, (b) the current arising from one of the two e" HOMO pair, (c) the current arising from the second of the two e" HOMO pair, and (d) the current arising from the $a"_2$ HOMO-1. Plotting conventions are described in the text.

Further evidence for the behaviour underlying the aromatic response in borazine deviating from that of systems that display ring current appear upon spectral decomposition of the total π current; in benzene, **1**, and COT, **2**, the primary contribution to current occurs at the frontier, arising from the four possible transitions between the HOMO and LUMO pairs in the case of benzene (see Figure 2.4 and 2.5), and from the single HOMO to LUMO transition in COT (see Figure 2.11 and 2.12). Although the orbital topologies of benzene and borazine bear more than a passing resemblance to each other, differences in orbital density mean that the contribution to current is not fully accounted for by even summation of the first eight possible occupied to virtual excitations (see Figure 2.14).

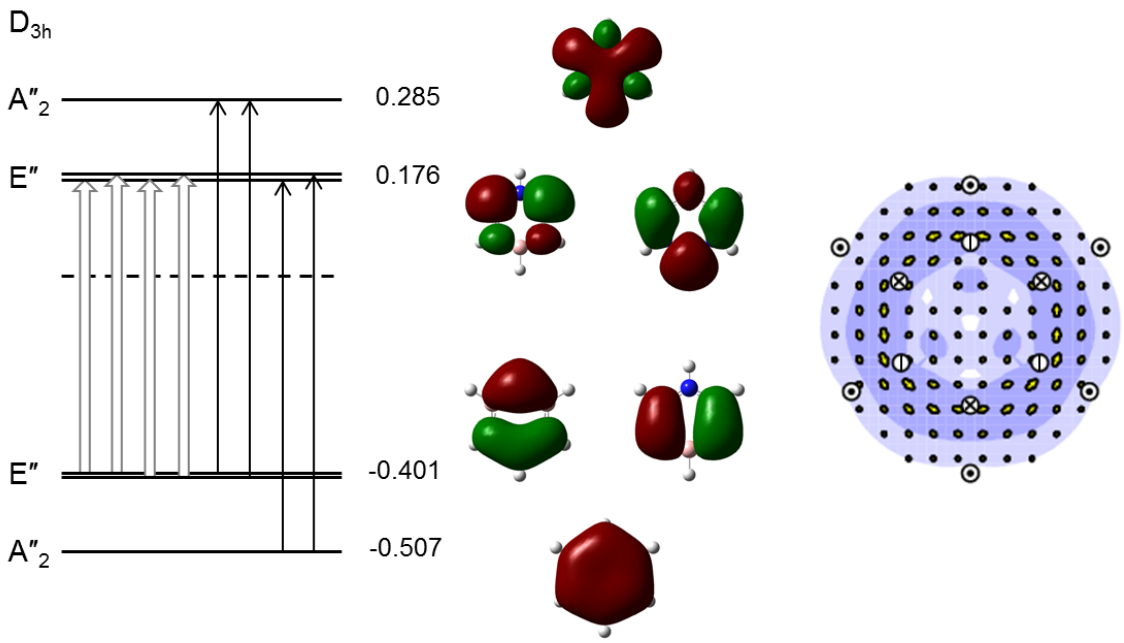

Figure 2.14. (Left) Orbital energy-level diagram showing the first eight frontier π-π* excitations from the occupied CMOs of D_{3h} borazine. Canonical molecular orbital topologies are shown, with orbital energies in E_h. Narrow, solid arrows and wide, hollow arrows represent allowed excitations of translational and rotational symmetry, respectively. (Right) The summed product of current arising from the first eight allowed frontier π-π* excitations. Plotting conventions are described in the text.

As can be expected from the presence of the three individually defined 'lone-pair' circulations visible in the total π map in Figure 2.13(a), the π-current breakdown derived from the Pipek-Mezey localised variants of the molecular orbitals produce results more economical and easily interpretable than those from CMOs. Figure 2.15 shows the three LMOs, each with j_{max} = 0.038 a.u., that when summed result in the total π current of borazine, j_{max} = 0.041 a.u.. Although the choice of orbital representation is ultimately arbitrary, in the sense that any unitary transformation amongst occupied orbitals will result in the same total electron density, it is clear from contrasting the breakdown of current in borazine and benzene, that each offers clear advantages in terms of intelligibility when systems are intrinsically localised or delocalised, as the case may be.

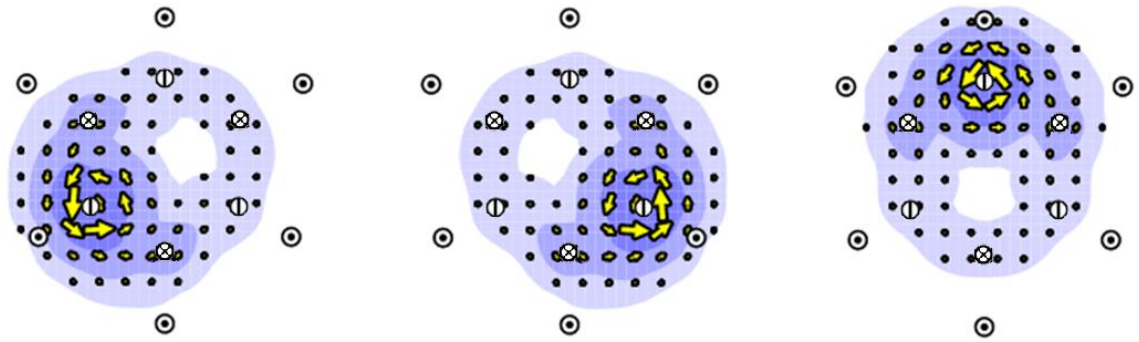

Figure 2.15. LMO contributions to π current density in D_{3h} borazine, showing the three equivalent, separate closed currents produced via Pipek-Mezey localisation. Plotting conventions are described in the text.

DFT Ipsocentric Ring Currents

Recently, the ipsocentric approach has been implemented in density functional theory in the GAMESS-UK software package.[62] DFT and Kohn-Sham magnetic response calculations are used in the ipsocentric approach, with the first-order perturbed Kohn-Sham orbitals employed in the standard SYSMO routines for calculating current density. Current-density maps produced at both the mixed HF//DFT and DFT consistent levels of theory tend to be extremely similar,[63] both methods resulting in calculated HF and Kohn-Sham frontier orbitals with qualitatively identical topologies.[64]

Figure 2.16 shows induced π currents of benzene, COT and borazine calculated at the ipsocentric B3LYP/6-31G**, alongside their standard CHF/6-31G** counterparts. Qualitatively, the current maps from both levels of theory display the same response, as should be expected from the results of earlier work[63] which found that the level of theory of optimisation had a greater effect on ring current than at which implementation of the ipsocentric approach was used. A small increase in current strength is however seen in the B3LYP/6-31G** map of COT (Figure 2.16 (b)), due to a small underestimation of the HOMO/LUMO gap. This difference does not, however, significantly change the conclusions that may be drawn from the calculation.

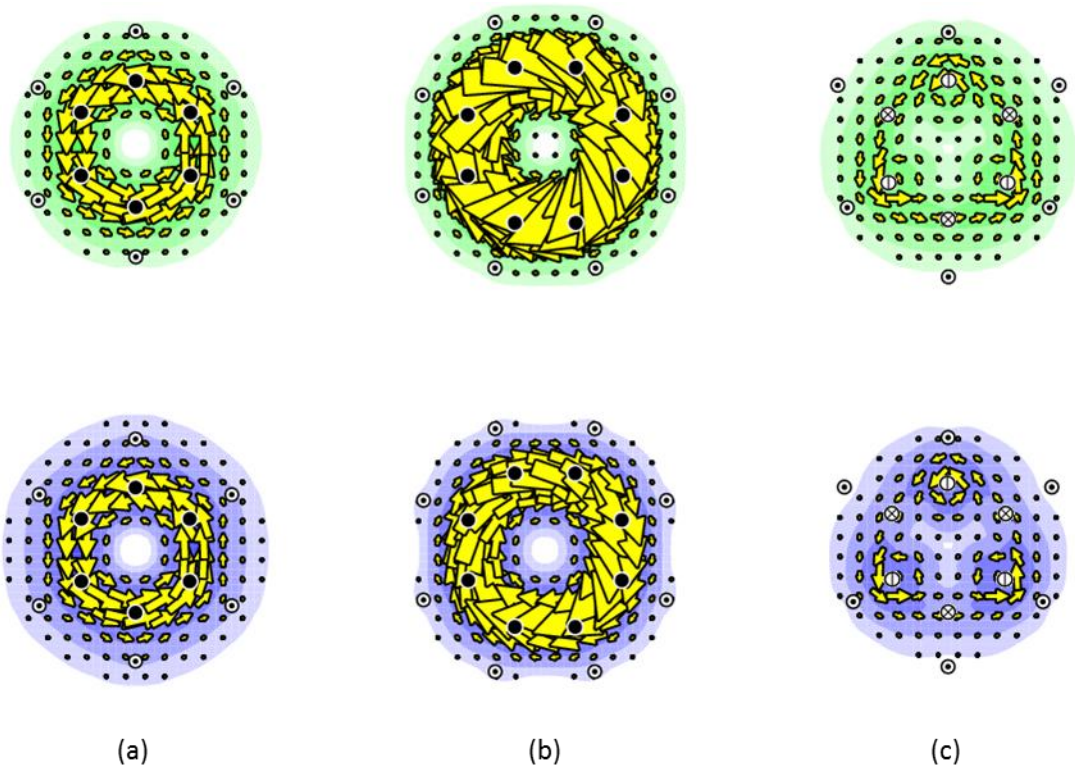

Figure 2.16. Total π current density maps of (a) D_{6h} benzene, **1**, (b) D_{4h} COT, **2**, and, (c) D_{3h} borazine, **3**. Maps are calculated on B3LYP/6-31G** optimised structures at the B3LYP/6-31G** (top) and the CHF/6-31G** (bottom) levels of theory. Green contours are used for the maps calculated at the B3LYP/6-31G** level to differentiate between the two methods. Plotting conventions are described in the text.

Pseudo-π Currents

On occasion it may be desirable to calculate the ring-current response of a system of interest without incurring the expense, in terms of both computational time and storage, of running a full ipsocentric calculation. At these times, simulations of *ab initio* currents may be obtained by the pseudo-π method.[65] Under this simplified model, the true current-density map is approximated by a reduced computation which includes only one electron and one hydrogen STO-3G 1s-orbital per carbon centre. The geometries used for these calculations are usually in

practice chosen to be either idealised 1.4 Å bond lengths, or that of the carbon framework of the standard B3LYP/6-31G** optimised structure. Currents are then obtained by the standard CHF ipsocentric approach, with maps plotted in the molecular plane.

The justification for this simplified model is similar to that of Hückel theory: treating the N p_π orbitals of a conjugated C_N network as N σ orbitals of a H_N network of hydrogen centres results in identical adjacency matrices, $\mathbf{A}$, for both systems. $\mathbf{A}$ can be diagonalised to give the eigenvalues, λ, and coefficients, $\mathbf{c}$, for each centre, i. The molecular orbitals, ψ, of a π system in Hückel theory are described by

$$\psi_i = \sum_i^N c_i \chi_i$$

where χ is a p_π basis function. Orbital energies, ε, are given by

$$\varepsilon_i = \alpha + \lambda_i \beta$$

For a given system, there is a strong correspondence in the C_N π orbitals in the Hückel calculation and the H_N σ orbitals in the pseudo-π calculation (exact in cases with high symmetry), with both yielding orbitals with the same nodal pattern and similar order in terms of energy. Ipsocentric arguments result in selection rules that allow total current, which in pseudo-π reflects the total π current of the complete *ab initio* calculation of the full system, to be rationalised and broken down in the familiar CMO and LMO bases.

In planar systems, a given π CMO of the full system in the *xy* plane is related to a σ CMO of its pseudo-π analogue by $\Gamma(\sigma) = \Gamma(\pi) \times \Gamma_z$. For example, the occupied π orbitals of D_{6h} benzene span $e_{1g} + a_{2u}$, and Γ_z has character a_{2u}. The products of these orbitals, and hence the identities of the occupied orbitals of the pseudo-π system, are $e_{1u} + a_{1g}$. Figure 2.17 shows the CMO breakdown of current in D_{6h} pseudo-π benzene.

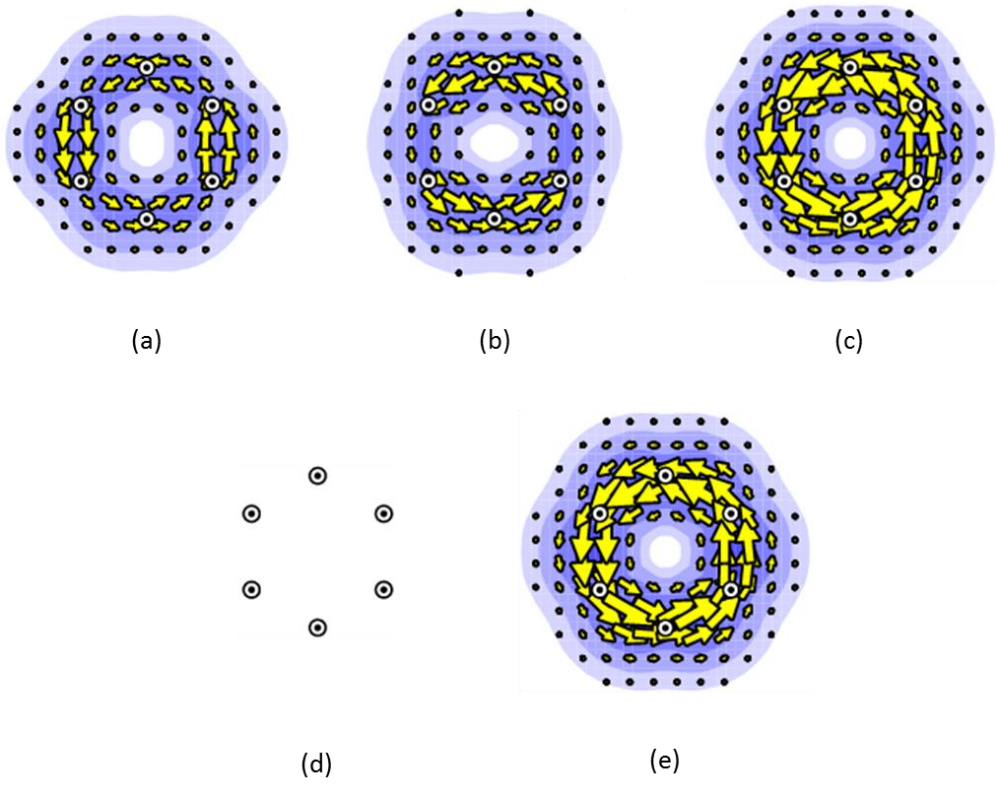

Figure 2.17. CMO contributions to current density in D_{6h} pseudo-π benzene from: (a and b) the two individual orbitals of the e_{1u} degenerate HOMO pair, (c) the combined sum of the e_{1u} HOMO pair, (d) the a_{1g} HOMO-1, and (e) the total current.

The striking resemblance between the pseudo-π current density maps in Figure 2.17 and their *ab initio* counterparts shown in Figure 2.3, immediately validate the approximations made in the simplified model. As in the full calculation, the maps show that the dominant contribution to current in benzene arises from the degenerate HOMO pair (see Figure 2.17(c), c.f. Figure 2.3(c)); as discussed above, this observation is easily rationalised using ipsocentric symmetry-based arguments with, in this case, the e_{1u} symmetry translations T_x and T_y relating the $\Lambda = 1$ e_{1u} HOMO to the $\Lambda = 2$ e_{2g} LUMO. Less predictably, this agreement also extends to current strength, with the j_{max} = 0.079 a.u. of the total pseudo-π map comparing well with the j_{max} = 0.078 a.u. of the total π current of the full calculation.

Pseudo-π calculations are commonly utilised in cases that are either too large to be subjected to full *ab initio* calculation, such as fullerenes and other large carbon networks, or when a comparison is required for conjugated circuit or Hückel-London current maps. The method will, on occasion, be used in later chapters.

To provide examples of how some of the above methods are used to both analyse and determine the presence of aromatic response in chemically relevant contexts, a pair of case studies are presented. The first focuses on an important family of bio-active molecules and illustrates how both CMO and LMO breakdowns offer different insights into aromaticity, whilst the second revives the historical debate over the nature of aromaticity in the sydnones, and serves to highlight the unique strengths of the ipsocentric approach in uncovering ring current response.

Applications of the Methods: Aromaticity of Caffeine, Xanthine and the Dimethyl Xanthines

The methylated derivatives of xanthine (**4**) (i.e., caffeine (**5**), paraxanthine (**6**), theobromine (**7**) and theophylline (**8**)) are all mild stimulants with many and varied bio-active properties. All five are widely consumed in sources such as tea, coffee and chocolate. Caffeine was first isolated in 1819 by Ferdinand Runge from Arabian mocha coffee beans given to him by Johann Wolfgang von Goethe.[66,67] It has recently been linked to Parkinson's disease as both a preventative measure and a palliative treatment.[68–72] The claimed neuroprotective effect has been attributed to binding to adenosine A_{2A} receptors.[68,72–74]

Paraxanthine, theobromine and theophylline are the primary metabolites of caffeine.[75] All three, to a greater or lesser extent, share the propensity of their parent molecule to act as an inhibitor of A_{2A} receptors,[73,76–78] show therapeutic uses as stimulants of the central nervous system,[76,77] and exhibit diuretic properties.[78] The general schematic structure of all five systems is given in Figure 2.18.

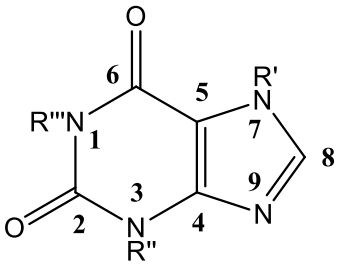

Figure 2.18. Schematic structures of the aromatic molecules treated in this study, as described in Table 2.1: xanthine (**4**), caffeine (**5**), paraxanthine (**6**), theobromine (**7**) and theophylline (**8**). Also considered are imidazole (**9**), which corresponds to heavy atoms 4, 5, 7, 8 and 9, R' = H on atom 7, and methylimidazole (**10**), with R' = Me.

Compound	R'	R''	R'''
4 Xanthine	H	H	H
5 Caffeine	Me	Me	Me
6 Paraxanthine	Me	H	Me
7 Theobromine	Me	Me	H
8 Theophylline	H	Me	Me

Table 2.1. Functional groups present on the three R groups of **5** to **8**, as depicted in Figure 2.18.

The potential aromaticity of these 14π structures has been discussed extensively,[79,80] and it should be noted that the planarity of the heavy-atom framework and the participation of these molecules in π-stacking interactions may be interpreted as evidence of aromaticity in these structures. Ring current models have been invoked in discussions of intermolecular interactions of caffeine,[81] and ^{1}H NMR data for the molecules **4** – **8** are consistent with the existence of a ring current in, at least, the imidazole portions of these molecules.[80–82] In spite of this corroborative support, no direct theoretical evidence of the aromaticity of these systems has yet been provided. If indeed the xanthines are aromatic, it should be possible to

calculate and to visualise the ring currents to confirm their aromaticity on the magnetic criterion.

Structures **4** – **8** and, for comparison, imidazole itself (**9**) and methylimidazole (**10**), were first optimised in C_s symmetry and confirmed as energetic minima at the B3LYP/6-31G** level before magnetic response was calculated at the ipsocentric[27] CHF/6-31G** level. The calculated geometries agree well with previous experimental and theoretical studies.[83–87] Calculations of the induced currents at the B3LYP/6-31G** level were also performed, but as there was no significant variation from the maps of induced current density calculated using HF-based methods (see Table 2.2), the resultant maps are not shown.

In these planar systems, the CMOs are of a' and a" symmetries. All σ orbitals are a', and all π orbitals are a", but some (one per Me group) a" orbitals correspond simply to out-of-phase combinations of CH bonds and so are not part of the unsaturated π system. These orbitals are easily identified and discounted in the discussion of π ring current. The systems **4** to **8** thus all have 7 CMOs in the π space. In the localised treatment, 7 π LMOs are obtained immediately on removal of cores and σ bonds. Figure 2.19 shows the total π current-density maps for systems **4** to **10**.

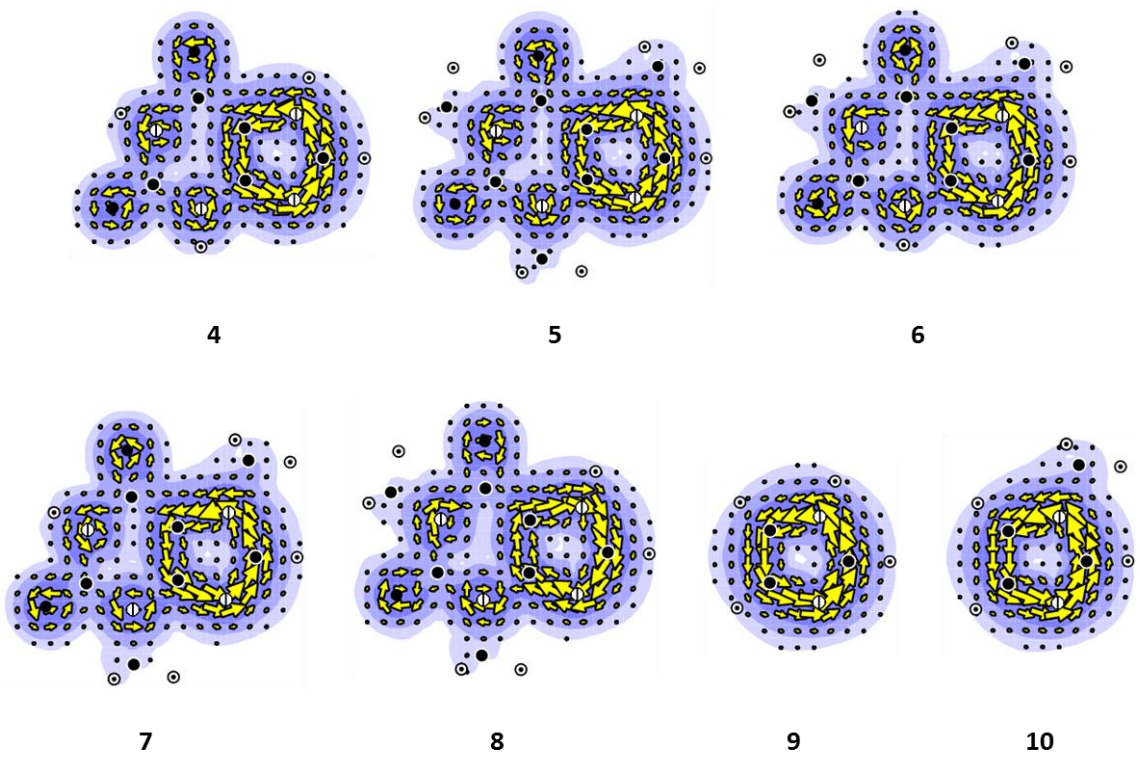

Figure 2.19. Total π current-density maps for systems **4** to **10**. Maps are constructed by summation of the contributions of 4 LMOs corresponding to the contributions of nitrogen lone pair and carbonyl circulations (**4 – 8**), plus those of 3 LMOs corresponding to the π system of the imidazole moiety (**4 – 10**). Plotting conventions are described in the text.

To a first approximation, all five xanthine-derived systems display the same ring-current pattern: strong, coherent diatropic circulation around the imidazole unit consistent with that in imidazole itself (**9**), with weaker, localised circulations positioned on the nitrogen and oxygen centres in the rest of the system. The imidazole-based circulations in **4 – 10** can be shown by LMO analysis to be genuinely delocalised features (see Figure 2.20); they can each be constructed in their entirety by superposition of contributions from 3 π LMOs, none of which individually are closed circulations.[35,88] These imidazole-like currents are delocalised, but over a confined region of the molecular skeleton. Table 2.2 reports j_{max} for the π-system in each molecule calculated at the CHF and DFT levels of theory. The agreement between two is, as expected,[33] excellent.

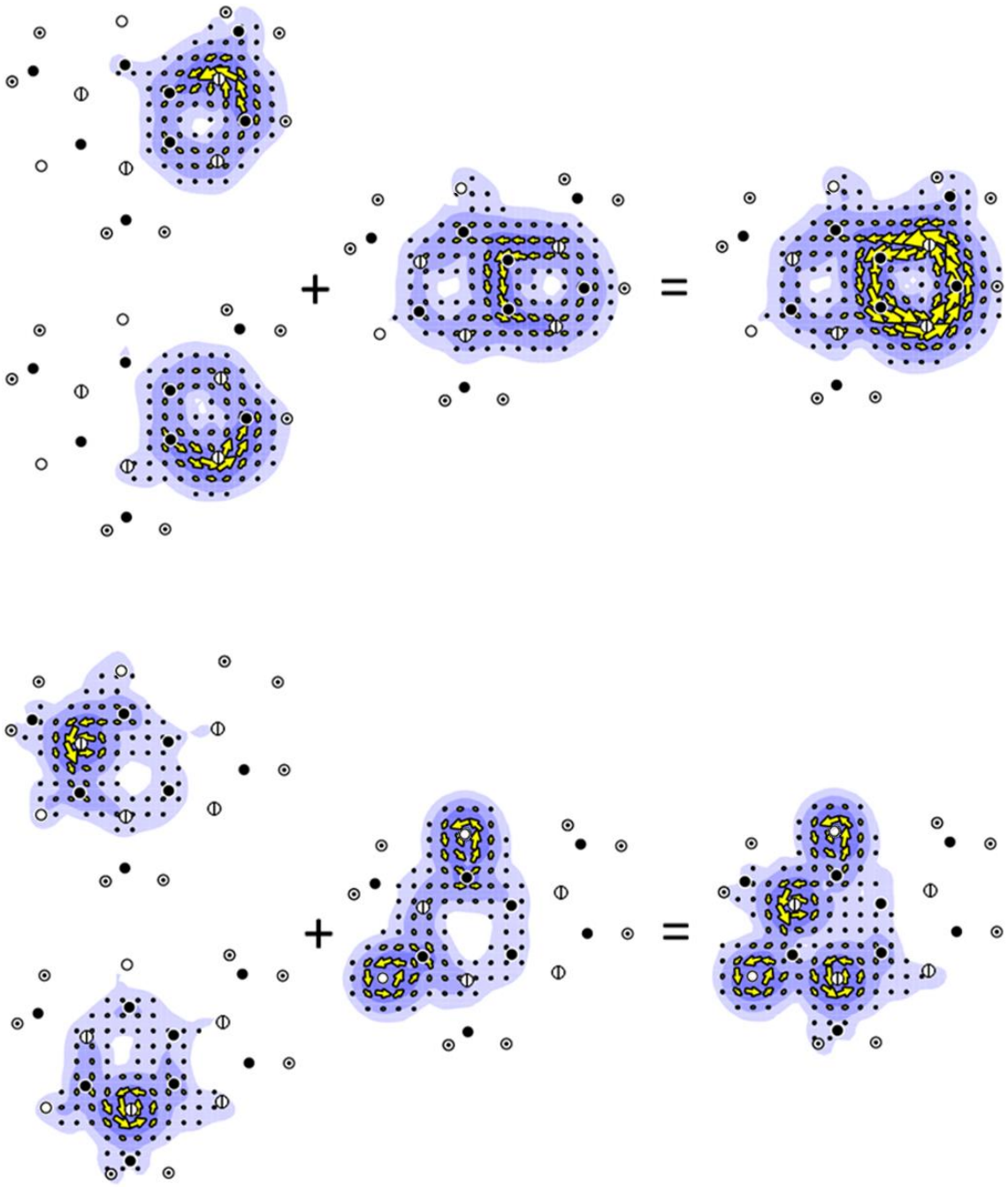

Figure 2.20. LMO analysis of the π-current in caffeine (**5**), showing (top) the three LMO contributions to the imidazole ring only, (bottom) the two nitrogen lone pairs and the carbonyl oxygen π-circulations that form the remainder of the π system. Plotting conventions are described in the text.

	Total π current (CHF)	Total π current (DFT)
4 Xanthine	0.071	0.070
5 Caffeine	0.080	0.079
6 Paraxanthine	0.080	0.079
7 Theobromine	0.079	0.079
8 Theophylline	0.070	0.070
9 Imidazole	0.077	0.077
10 Methylimidazole	0.087	0.088

Table 2.2. Total π current-density j_{max} values (a.u.) for structures **4** – **10**.

Examination of Table 2.2 brings to light some second order differences in the strengths of the induced current that were not immediately evident from inspection of the maps. In particular, the currents in the delocalised rings of caffeine, paraxanthine and theobromine (j_{max} = 0.079 to 0.080 a.u.) are noticeably stronger than those in xanthine and theophylline (j_{max} = 0.070 to 0.071 a.u.).

The primary structural differences between these systems arise from the presence of methyl groups on the imidazole units of **5**, **6** and **7**. This suggests that the differences in magnetic response may be attributable to the σ-inductive effect of the methyl groups. Comparison of the induced π-currents of imidazole, **9** (j_{max} = 0.077 a.u.), and methyl imidazole, **10** (functionalised in the same position, j_{max} = 0.087 a.u.), leads to the same conclusion; the presence of a methyl group at this site noticeably increases the strength of the π current circulation.

The same trend is found for imidazole itself, where methylation at the site corresponding to N7 leads to an increase of approximately 0.010 a.u.. A crude point-charge model suggests that the direction of this change is attributable to the σ-inductive effect of the methyl group: if nuclear charge is formally transferred from H to N in units of 0.1 *e*, the calculated j_{max} increases, although by only approximately 0.001 a.u. for each step.

Sydnones: a Case Study

The strengths of the analytical methods expounded upon above are now employed to answer the contentious question of aromaticity in a structurally unusual group of compounds: the mesoionic sydnones.

Mesoionic compounds have been defined as 5-membered heterocycles possessing a sextet of π-electrons that cannot be satisfactorily represented by a single covalent or dipolar structure;[89] sydnones are Type A[90] mesoionic (see Figure 2.21) heterocyclic betaines, and reviews of their chemistry can be found in references[91–93]. First discovered in 1935,[94] they have recently been the subject of significant interest owing to their biological activity[95] and their participation in cycloaddition reactions with alkynes to generate pyrazoles.[96–99] Owing to their curious ring structure there has been much debate with regard to their most appropriate representation. Two extreme depictions are provided in Figure 1. **I** shows sydnones as being aromatic heterocycles with an anionic exocyclic oxygen atom. This structure is consistent with past valence bond calculations that ascribe a large negative charge to the exocyclic O-atom.[100,101] In contrast, **II** describes sydnones as azomethine imines, a structure that is supported by early molecular-orbital calculations[102] and by the strong measured infrared absorbance at approximately 1730 cm^{-1} that is indicative of a carbonyl group.

Whilst, historically, the definition of a mesoionic compound *required* a degree of aromaticity,[91] and representations such as **I** imply aromatic character based on a conjugated ring of 6 π electrons, the extent of conjugation has been repeatedly disputed, leaving the question of their aromaticity in doubt.[103,104] Indeed, some commentators have been more emphatic, in their recent study on the use of deprotonated sydnones as abnormal *N*-heterocyclic ligands for Pd-catalysed cross-coupling reactions, Schmidt and co-workers concluded explicitly that N-phenyl sydnone (**I** or **II** where R = Ph) and other sydnones were not, in fact, aromatic.[105]

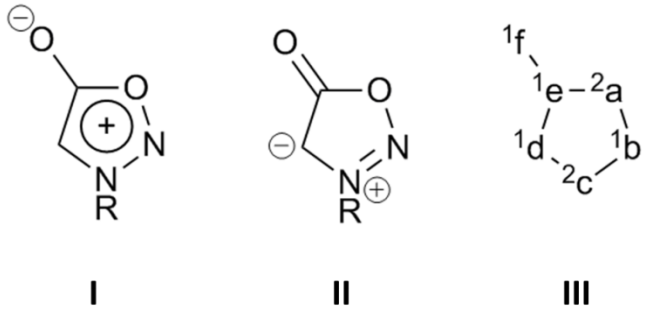

I II III

Figure 2.21. **I** and **II** are schematic representations of two extreme resonance forms of a general sydnone. **III** is the general form of a type A mesoionic system,[90] where superscripts refer to the numbers of π electrons donated by each atom.

This debate, which extends to the aromaticity of the whole family of mesoionic compounds in general, is ongoing. In a review, Simas *et al.*[104] drew evidence from synthetic and kinetic studies which indicated areas of localised positive and negative charge around the mesoionic rings, and crystallographic data showing long carbon-heteroatom bonds, which was taken to imply a lack of π-conjugation within the ring concluded that the systems should not be considered aromatic. Support for this claim is offered by systems that react as both electrophiles and nucleophiles.[106] On the other side of the debate, recent work on sydnones and other mesoionics employing aromaticity indices such as NICS,[107] HOMA (or the harmonic oscillator model of aromaticity, a geometry-derived value of aromaticity calculated as the normalised sum of squared deviations of bond lengths from uniformity) and the bond-order index I_5-Bird[108] (which considers the deviation from uniformity of bond-order around a five membered ring) found behaviour typically associated with aromaticity.

As has been extensively discussed in the literature, a key advantage of the ipsocentric approach that allows the magnetic response of these systems to be understood is that it uniquely allows the calculated current density to be partitioned into non-redundant canonical and localised molecular orbital contributions. Both choices are necessary to fully understand the ring current response of the sydnones, and will be used, for the first time, to provide direct theoretical evidence of their aromaticity. As they possess heteroatoms with different formal π electron counts, the best description of their aromaticity could be expected to lie between the extreme CMO and LMO representations of the origin of current. Here, current-density maps

and orbital analysis of the hypothetical simplest conceivable sydnone, **11**, and the experimentally accessible systems *N*-phenyl sydnone **12**, are presented to finally answer the open question of their aromaticity.

11 **12**

Figure 2.22. Schematic representation of a single resonance form of **11** and **12**.

The optima of both structures displayed the same qualitative distribution of long and short bonds around the heterocycles as found by crystallographic studies,[109] and the vibrational modes corresponding to the exocyclic CO stretch consistent with that of a classical carbonyl vibration: $\tilde{\nu}_{CO}$ (**11**) = 1829 cm^{-1} and $\tilde{\nu}_{CO}$ (**12**) = 1821 cm^{-1}, when calculated at the B3LYP/6-31G** level and scaled by a factor of 0.96 as in reference.[110] Current-density maps computed at the CHF/6-31G**, and B3LYP/6-31G** for these systems are practically identical, as expected.[63,111] Owing to this, only the CHF maps are displayed here. Structure **12** has C_1 symmetry caused by small deviations from ring planarity (≤ 0.01 Å), σ and π symmetries are therefore not rigorously mathematically defined in this molecule. Because of this, LMO analysis is used in this case to provide a summed four-orbital 'π-like' total current by inspection.

The maps of **11** and **12** are plotted to show the first-order current density in a plane 1 a_0 above the median plane defined by the five atoms of the sydnone cycle. All other plotting conventions are as above. Figure 2.23 shows the π current-density maps of **11** and **12**.

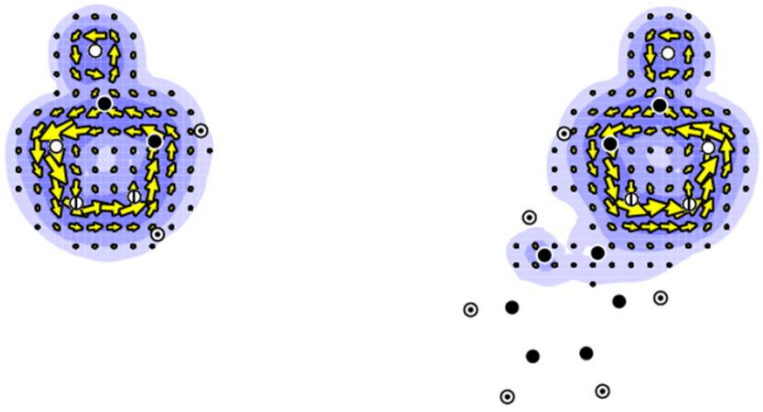

11 **12**

Figure 2.23. Total π current-density maps of the heterocyclic moiety in **11** and **12**. Contribution to π current in these systems is defined by superposition of four π or 'π-like' LMOs. Plotting conventions are described in the text.

To a first approximation, both systems have the same ring-current response: an unambiguous, delocalised diatropic current flowing around the heterocyclic ring, accompanied by an exocyclic localised circulation associated with the external oxygen centre. Breakdown into LMO contributions shows these two features to have distinct origins; the current on the ring is a sum of contributions from three π LMOs, and the exocyclic oxygen circulation is described by a single π LMO. Current density-maps of this breakdown are shown in Figure 2.24.

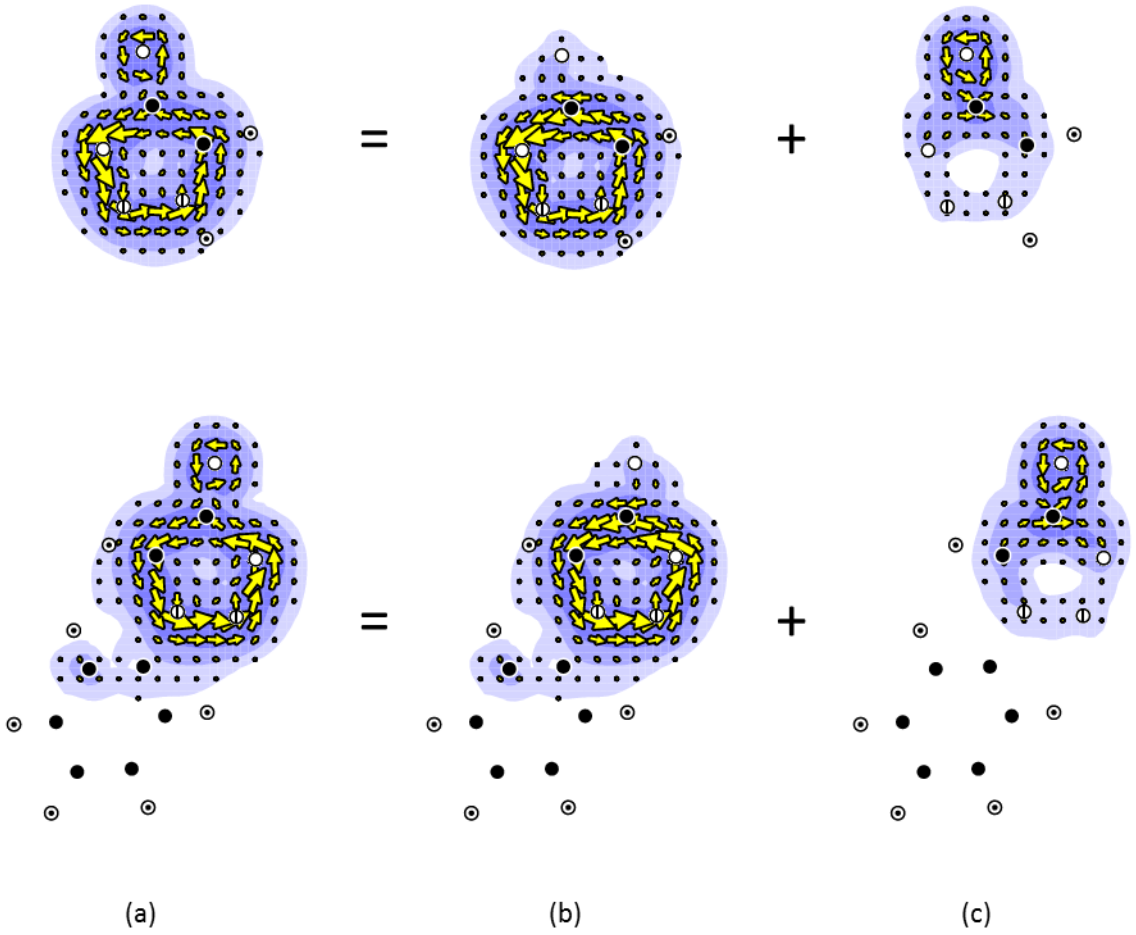

Figure 2.24. LMO analysis of the π current in sydnones **11** (top) and **12** (bottom). (a)The total four-LMO contribution, (b) the three-LMO ring-localised contribution, and (c) contribution of the exocyclic oxygen LMO. Plotting conventions are described in the text.

Examination of the strengths of the 6π ring-localised currents further reinforces this diagnosis; the values of j_{max} for the summed three ring-localised LMOs are 0.072 a.u. for both **11** and **12**, (92 % of the π ring-current of benzene). These estimates are only weakly dependent on the number of LMOs included in the sum, the total 8π currents have j_{max} values of 0.066 (**11**) and 0.067 a.u. (**12**), results consistent with the near-independence of 6π and 2π circulations deduced from the maps. The small discrepancies between strengths of the 6π and 8π maps are due to cancellation effects that occur at the interface between the two flows.

A repeatedly exploited strength of the ipsocentric approach is that it provides an explanation for the presence and direction of ring-current in a delocalised π-system using only simple node-counting arguments. This reasoning, derived from a Hückel-theory interpretation, suggests that contributions to current are typically dominated by a small number of excitations amongst the frontier orbitals. The energy-level diagrams of **11** and **12** are given in Figure 2.25.

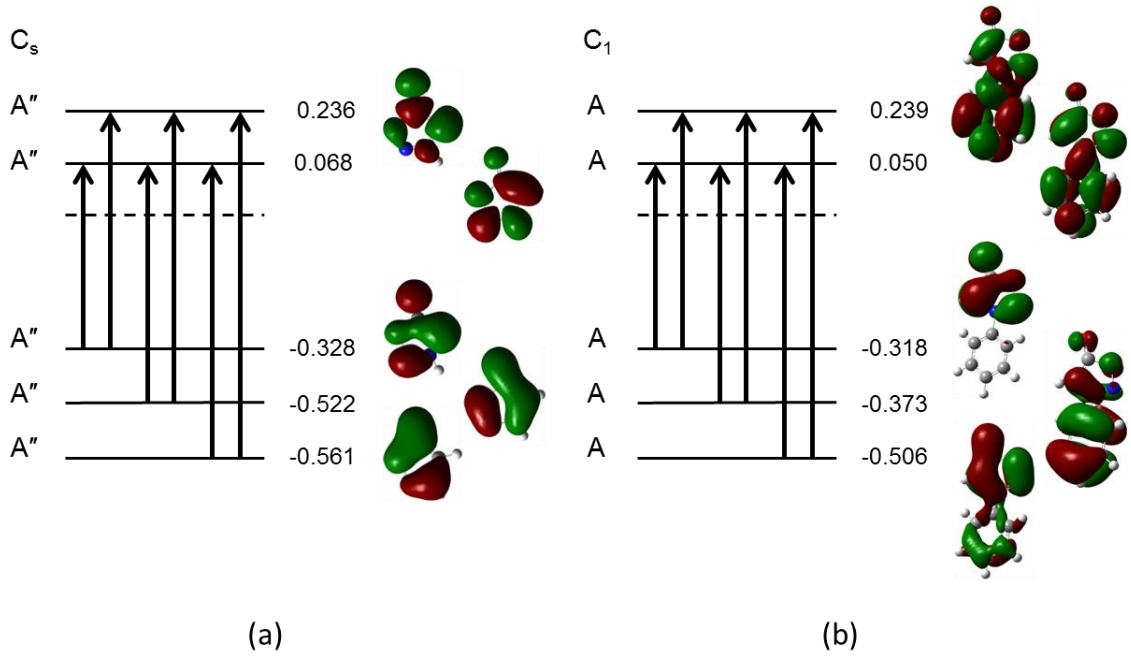

Figure 2.25. Schematic orbital energy-level diagrams calculated at the HF/6-31G** level of theory on B3LYP/6-31G** optimised structures showing selected allowed occupied–virtual π orbital excitations for (a) C_s **11** and (b) C_1 **12**. Arrows indicate translationally allowed excitations between π canonical molecular orbitals; orbital energies are given in E_h.

Figure 2.25(a) shows a schematic of the virtual π-π* CMO transitions that give the frontier-orbital contributions to total π current in planar prototype sydnone, **11**. The main contributions arise from three π-like canonical molecular orbitals, all of a" symmetry in C_s, and all π-π* excitations in the frontier region lead to an increase in the number of ring nodes. This implies constructive interference of three diatropic contributions to the current in the ring, as found. In this account of electronic structure, the ring current in sydnone **11** has essentially the

same origin as the classic π-currents of benzene (see Figure 2.4) and the cyclopentadienide anion.[33]

Figure 2.25(b) shows the highest and lowest lying π*-like orbitals of **12**. This system has a more extended π system than **11** and the canonical orbitals show mixing between the heterocyclic and phenyl rings. By focusing only on the sydnone unit, it is possible to identify the same pattern of increase of angular node count between π and π* orbitals, proving that the induced current in the more complex system has the same orbital origin as in **11**.

The presence of diatropic π-ring currents in **11** and **12** shows unequivocally that these sydnones are aromatic under the magnetic criterion. The sense of ring current can also sometimes be obtained by probing the distribution at a well-chosen single point: e.g., the popular NICS(1) value is the negative of the chemical shift at 1 Å above the geometric ring centre; for simple monocycles, where the magnitude of NICS(1) is large, the sign correlates well with the sense of current: negative NICS(1) usually implies a diatropic current. Concurrence between current density and the indirect probes offered by NICS for polycyclic systems without strong competing local effects has also been documented.[112] Although Schmidt *et al.* asserted that the sydnones are *not* aromatic,[105] their GIAO LACVP*/B3LYP calculated NICS(1) value of -6.8 ppm for **12**, (c.f. -11.2 ppm for benzene calculated at the same level of theory) correlates with our ipsocentric current-density maps, and indeed would normally be read in isolation as indications of the presence of diatropic ring current.

To summarise, views on the aromaticity of sydnones have fluctuated in the eight decades since their first synthesis. The heterocyclic ring of the neutral sydnone fulfils the Hückel 4*N*+2 rule with 6π electrons, albeit with charge separation in all contributing resonance structures. This mesoionic character[1,33,3] has been used to cast doubt on sydnone aromaticity, as it seems to militate against delocalisation of the 6π system. Early calculations[100,102,115,116] supported non-uniformity of charge around the ring; bond lengths within the ring and vibrational frequencies of the exocyclic CO bond were also adduced as evidence for non-aromaticity. In spite of these arguments, the present study shows that electronic structure calculations, while compatible with experimental geometry and frequency data, give evidence of aromatic π-electron delocalisation through the prediction of ring currents in sydnones and derivatives. In spite of geometric and presumed charge inhomogeneity around the ring, the frontier orbital structure of the sydnone is fully consistent with the existence of a diatropic ring current, with

the same physical origins as in benzene, depending as it does essentially on HOMO and LUMO nodal topology, and so being robust against changes in bond length,[117] planarity[118] and formal atom charge.[119]

The tools and approaches used to explore and understand ring current introduced in this chapter will be essential in the investigations to be covered in the rest of the thesis. Chapter 3 will use many of the ideas encountered so far to rationalise the aromaticity of a range of graphene/graphane hybrid systems.

Chapter 3: Aromaticity in Nanographanes*

Introduction

Although much of the avalanche of recent research on graphene and related carbon nanostructures has been concentrated on physical properties,[120–122] strategies for chemical functionalisation of these materials are receiving increasing attention.[123–131] Controlled regio-functionalisation would offer the intriguing prospect of 'writing' circuit diagrams onto the conducting carbon sheet[123] by, for example, selective hydrogenation. Graphane, the fully hydrogenated derivative of graphene, was proposed as a theoretical possibility by Sofo *et al*.,[132] who found a low-energy structure resulting from hydrogenation of both faces of a sheet of carbons that are rings in the chair conformation (Figure 3.1). In this structure every CH bond is in a favourable antiperiplanar relation to its nearest neighbours, but other combinations of ring conformations in the carbon sheet are also predicted to be competitive in energy for graphane, and some of these may be present in experimental samples.[133] Experimental evidence for graphane comes from the work of Elias *et al.,*[134] who reacted atomic hydrogen with free-standing graphene films. Partial hydrogenation can also be achieved, as in the work of Balog et al.,[135] which demonstrated the formation of graphane-like islands on a graphene sheet grown on an Ir(111) substrate. Fluorinated analogues are also accessible. Cheng et al.[136] have synthesized multilayer graphene fluoride and found evidence for a perfluoro-graphane-like structure.

* Some of the material in this chapter has been published in: Fowler, P. W.; Gibson, C. M.; Bean, D. E. *Proc. R. Soc. A* **2014**, *470*, 20130617:1–18. This chapter contains additional systems, figures, current-density maps, and discussion.

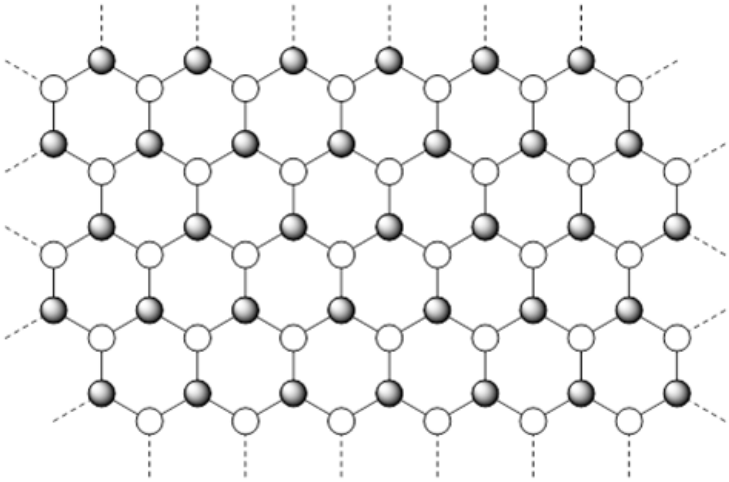

Figure 3.1. A schematic representation of the graphane sheet. Shaded spheres correspond to hydrogen centres in axial CH bonds pointing out from the median plane towards the viewer, and white spheres to those in CH bonds that point away.

Finite analogues of graphene have in fact been known for a long time in chemistry, in the guise of large benzenoids of the polycyclic aromatic hydrocarbon (PAH) family. This analogy is acknowledged in the increasing use of 'nanographene'[137] and 'graphene flake'[138] as synonyms for older terms such as 'giant PAH'.[139] In this picture, benzenoid PAH molecules are regarded as fragments of graphene that have been passivated by termination of dangling bonds with hydrogen atoms.[140] This chapter suggests an extension of this analogy to structures that would correspond to 'nanographanes'. Specifically, model systems constructed by full or partial saturation of the two 'faces' of a benzenoid (Figure 3.2) are considered. A C_xH_y system constructed in this way is not necessarily the lowest-energy form of that hydrocarbon, but, as will be seen, it typically occupies a local minimum on the potential energy surface for the finite system and, by extension, remains locally stable when embedded in an infinite analogue. Selective hydrogenation of the nanographene, or dehydrogenation of the nanographane, gives a model for the printing/etching of conduction channels on the graphene/graphane sheet.

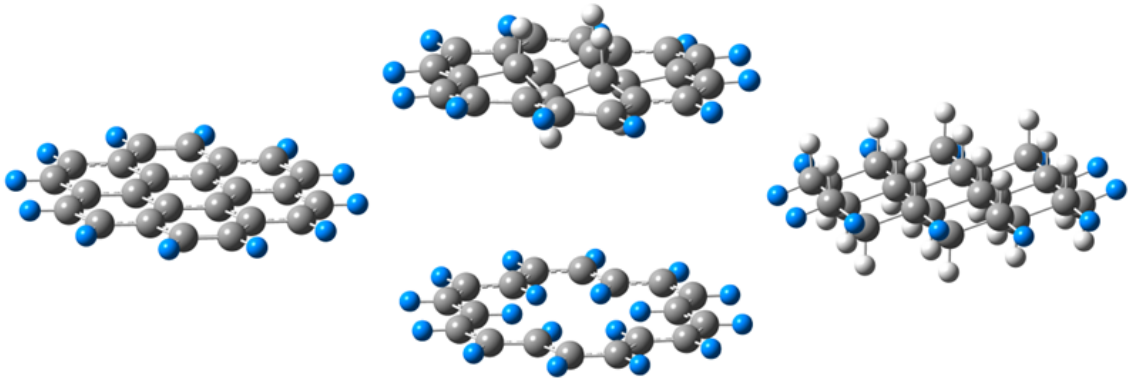

Figure 3.2. The nanographene/nanographane analogy. Coronene, $C_{24}H_{12}$ (left); the fully hydrogenated 'coronane', $C_{24}H_{36}$ (right); an inner-hydrogenated coronene, $C_{24}H_{18}$ (top) and corresponding model [18]annulene, $C_{18}H_{18}$ (bottom). Equatorial hydrogens are labelled blue and axial hydrogens white.

For device applications, delocalisation of the π-electron distribution and the ability of a system to support flow of π-current are key properties. For example, in finite systems, the ring currents induced by external magnetic fields can act as proxies for these properties: ring-current maps have been shown to correlate well with cyclic delocalisation indices for polycyclic aromatic hydrocarbons,[141] and the paths taken by ring currents and by electrons driven by a potential difference through an aromatic system[142] show clear similarities. A primary question for applicability of the design ideas mentioned above to materials and devices is the extent to which the properties of an unsaturated motif can be predicted from those of the sp^2 hydrocarbon with the same set of bare carbon centres. Does this model calculation suffice or must we use calculations that also include the (potentially extensive) saturated environment? In this chapter comparative analysis of current-density maps for nanographanes and the corresponding sp^2 hydrocarbons are applied to address this question.

To aid discussion of these nanographene/nanographane hybrid systems, the notation used to name these systems is first outlined. The ipsocentric method is then applied to a variety of selected nanographanes, giving a general rationale for the similarity of the predicted ring currents to those in the corresponding sp^2 hydrocarbon. Alternative functionalisation where hydrogen is replaced by fluorine is also considered, as is an alternative architecture of the carbon sheet, where the requirement for all-chair rings and fully anti-periplanar hydrogenation is relaxed.

Notation

Extra notation is necessary to simply distinguish between the different systems encountered in this chapter. The nanographene (or benzenoid) and its hydrogenated derivative share a common molecular graph G representing the carbon framework: G has n vertices (carbon centres) and m edges (carbon-carbon σ bonds), with $n = n_2 + n_3$ and $m = n_2 + \frac{3}{2}n_3$, where n_i is the number of carbon centres with exactly i carbon neighbours. The molecular formula of the nanographene is then:

$$\mathrm{C}_n\mathrm{H}_{n_2} \equiv \mathrm{C}_n\mathrm{H}_{3n-2m} \tag{1}$$

and the formula of the fully saturated nanographane is:

$$\mathrm{C}_n\mathrm{H}_{2n_2+n_3} \equiv \mathrm{C}_n\mathrm{H}_{4n-2m} \tag{2}$$

A partially hydrogenated intermediate system can be seen as arising by formal deletion of one hydrogen from each of p carbon centres of the fully saturated system (2), or addition of one hydrogen to each of $n - p$ carbon centres of the nanographene (1), to give formula:

$$\mathrm{C}_n\mathrm{H}_{2n_2+n_3-p} \equiv \mathrm{C}_n\mathrm{H}_{4n-2m} \tag{3}$$

Typically, the resulting set of p sp^2 carbon centres will itself correspond to the skeleton G' of a chemically interesting annulene, benzenoid, or disjoint union of such molecules. Our comparison is then between the properties of the whole system (3) with sp^3 carbons forming subgraph $G - G'$, and sp^2 carbons forming subgraph G', and those of the isolated molecule(s) with sp^2 graph G'. The intermediate system (3) can then be thought of as formally equivalent to the sp^3 nanographane (2) with the molecular sp^2 system 'carved out', i.e.,

$$\mathrm{C}_n\mathrm{H}_{2n_2+n_3-p} \equiv \mathrm{C}_n\mathrm{H}_{2n_2+n_3}/\mathrm{C}_{p'}\mathrm{H}_{q'}\ \ \mathrm{C}_{p''}\mathrm{H}_{q''}, \ldots$$

with $p' + p'' + \cdots = p_2 + p_3 = p$ and $q' + q'' + \cdots = q + p_2$, where q is the number of edges in G between $G - G'$ and G', i.e., the number of hydrogens needed to replace dangling σ bonds

in the molecules when they are cut out of the nanographane, and p_i is the number of vertices in G' that had degree i in G. For example, coronene with hydrogenation of the central hexagonal ring would be:

$$C_{24}H_{24} \equiv C_{24}H_{42} / C_{18}H_{18},$$

whereas coronene with hydrogenation of all except one hexagonal ring would be (one of two isomers of):

$$C_{24}H_{36} \equiv C_{24}H_{42} / C_6H_6,$$

indicating that the appropriate comparisons of current patterns would be with [18]annulene and benzene, respectively.

Methods

All structures, with the exceptions of the model systems [18]- (**4**) and [22]annulene (**13**) and [6]radialene (**6**), were optimised and confirmed as local minima on the potential energy surface at the B3LYP/6-31G** level using the Gaussian09 package.[40] The model D_{6h} [18]annulene and D_{2h} [22]annulene were constructed from the geometries of D_{6h} optimised coronene and D_{2h} optimised ovalene with the interior sp^2 cycles deleted and replaced with hydrogens positioned 1.08 Å along the CC vectors formerly connecting them to the perimeter. The model [6]radialene in its energetic minimum possesses a heavily distorted tub-shaped structure. To give a useful comparison to the related nanographane, in which the etched sp^2 region is restricted by the sp^3 fragments to only small deviations from planarity, the free radialene model was optimised with fixed D_{6h} symmetry, which resulted in a planar structure with threee imaginary vibrational frequencies (belonging to a single mode at 152*i* cm^{-1} and a pair at 123*i* cm^{-1}), also at the B3LYP/6-31G** level of theory. Current-density maps were calculated using the ipsocentric method at the CHF/6-31G** as implemented in the SYSMO package[39] when shown with a blue shading for contours of modulus of current density, and at the B3LYP/6-31G** as implemented in the GAMESS-UK[62] package when shown with green

shading. All nanographane sp^2 ring structures have small deviations from planarity, and so σ and π symmetries are not rigorously mathematically defined. 'π-like' canonical or Pipek-Mezey localised molecular orbitals[43] are identified by inspection, with total π currents produced as sums of these contributions. All current maps are plotted in a plane 1 a_o above the median plane of the sp^2 carbon cycle.

Nanographanes Derived From Coronene

As a first example, consider the nanographane modification of a small and highly symmetrical benzenoid, coronene. There are three symmetrical possibilities (Figure 3): we can hydrogenate the central benzene ring or fully or partially hydrogenate the perimeter to give D_{3d} species **1** ($C_{24}H_{42}/C_{18}H_{18}$), **2** ($C_{24}H_{42}/C_6H_6$) and **3** ($C_{24}H_{42}/C_{12}H_{12}$), mimicking [18]annulene, benzene and [6]radialene patches carved into the graphane environment, respectively.

The lowering of symmetry from D_{6h} to D_{3d} leaves sp^2 frameworks that are effectively planar in the cases of **1** and **2**. At the B3LYP/6-31G** level used here, the maximum vertical deviation from the mean plane of the sp^2 region of the molecule is ±0.06 Å for the annulene of **1**, and ±0.01 Å for the benzene ring of **2**. Retention of delocalisation is also indicated by the uniform sp^2-sp^2 bond lengths (12 × 1.401 Å and 6 × 1.406 Å in **1**; 6 × 1.411 Å in **2**). The radialene patch of **3** has a near-planar C_6 ring (vertical deviation ±0.03 Å, bond lengths 1.480 Å) with exo CC bonds (1.358 Å) bent out of plane (deviation ±0.21Å). The geometries already indicate retention of delocalisation in the sp^2 frameworks of **1** and **2** but localisation towards exo double bonds in **3**, as in [6]radialene **6**. The π-current density maps constructed using localised molecular orbitals as described above are shown in Figure 3.3, where they are compared with free-molecule models.

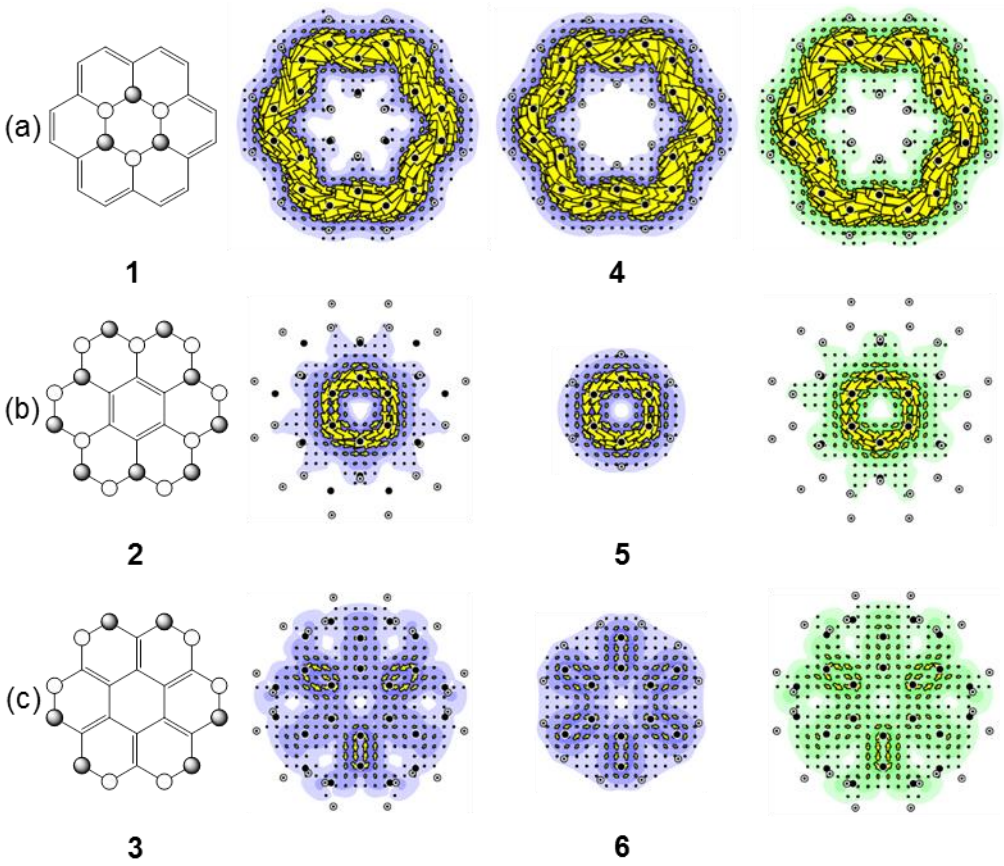

Figure 3.3. Three nanographanes formally derived from coronene by hydrogenation of the central ring, or full or partial hydrogenation of the perimeter: (a) **1** ($C_{24}H_{42}/C_{18}H_{18}$); (b) **2** ($C_{24}H_{42}/C_6H_6$); (c) **3** ($C_{24}H_{42}/C_{12}H_{12}$). The first column shows the schematic molecular structures. The second column shows the π ring current maps, defined by superposition of localised molecular orbital (LMO) contributions, chosen as described in the text. The third column shows the corresponding total π currents in analogous annulene ([18]annulene, **4**, and benzene, **5**) and radialene ([6]radialene, **6**) model systems. The final column shows total π currents calculated as for column 2 but replacing CHF perturbed densities by B3LYP. Plotting conventions are described in the text.

As is clear from the maps, **1** and **2** support delocalised (diatropic) currents flowing around the circuits of sp^2 centres, comparable in strength to the ring currents in the free-molecule model systems, which are themselves similar to the currents in the fully relaxed systems (values of j_{max} at 1 a_0 above the median plane of the sp^2 centres are 0.187 a.u. for **1** and 0.078 a.u. for **2** c.f. 0.178 a.u. and 0.078 a.u. for the annulene model, **4**, and for benzene, **5**, respectively). Nanographane **2** therefore supports a full benzene ring current and the larger circuit of

nanographane **1** has a current that is more than twice as strong. The radialene-like system, **3**, however shows only weak, localised currents in the bonds exo to the central ring. Three of the bonds point away from the median plane and hence the plotting plane above it, and so only the three upper bond circulations are visible in Figure 3.3 but three exactly identical features are of course found in a plotting plane of -1 a_0, and all six features are visible in a single plotting plane for the D_{6h}-constrained [6]radialene, **6** which is known to have localised magnetic response rather than a ring current.[143]

The final column of Figure 3 shows the effect of replacing the CHF ipsocentric calculation by a fully consistent B3LYP DFT calculation of current density.[144] As a comparison of the second and fourth columns of Figure 2.3 confirms, the maps are robust to this change in level of theory. This is to be expected as the qualitative pattern of current and its similarity to the currents in the annulene and radialene models are essentially determined by orbital nodal topologies.

The similarity in overall patterns of current between nanographanes and models of free molecules is striking, and perhaps expected on structural grounds, but it can be given a deeper explanation. It can be traced to the retention in the nanographane of nodal patterns and approximate symmetries of the orbitals of the π system of the isolated molecule. When a π system is delocalised, as it is here, an analysis in terms of canonical molecular orbitals (CMOs) is revealing.[61] Figures 3.4 and 3.5 compare the CMOs and their contributions to current for [18]annulene in a model geometry derived from coronene, **4**, with those for the nanographane **1**.

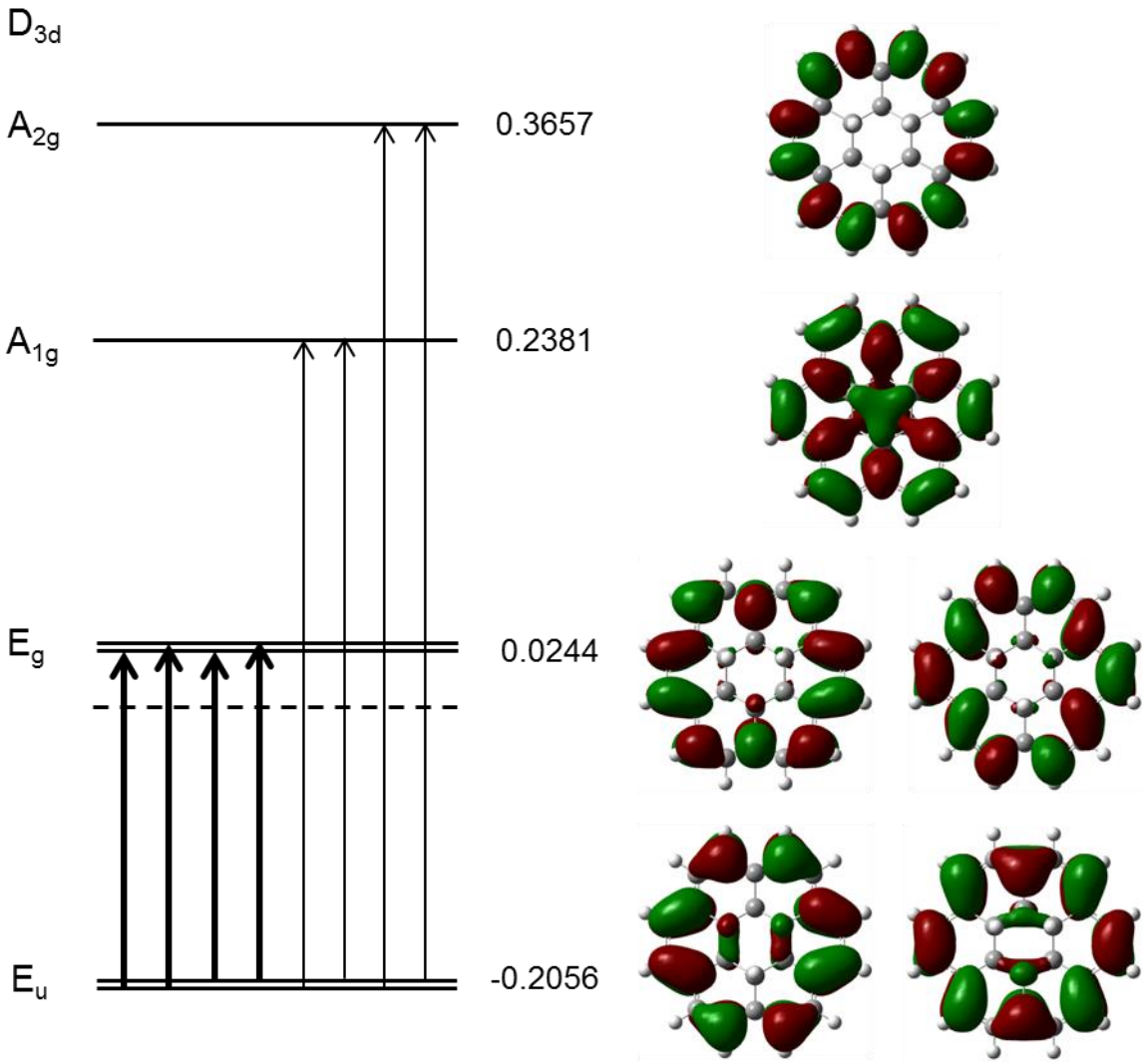

Figure 3.4. Orbital energy level diagram showing the first three π-π* excitations from the degenerate HOMO pairs of $C_{24}H_{42}/C_{18}H_{18}$, **1**. Canonical molecular orbitals are shown, with orbital energies in E_h; general conventions for excitations are: dominant excitations are shown in bold, translationally allowed excitations are shown as narrow, solid arrows.

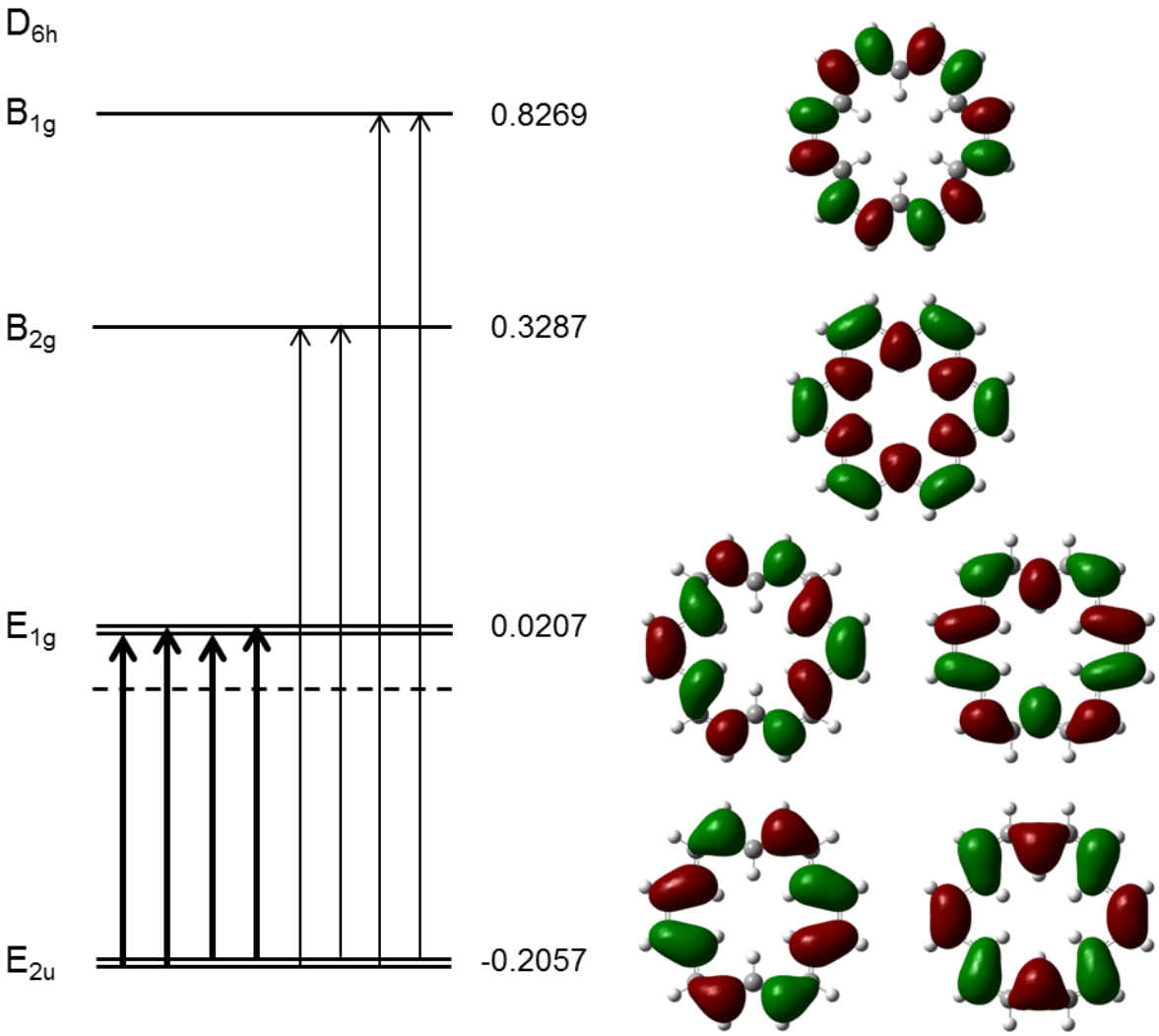

Figure 3.5. Orbital energy level diagram showing the first three π-π* excitations from the model [18]annulene, **4** (right). Canonical molecular orbitals are shown, with orbital energies in E_h; general conventions for excitations are: dominant excitations are shown in bold, translationally allowed excitations are shown as narrow, solid arrows.

As comparison of Figures 3.4 and 3.5 shows, there is a one-to-one correspondence between the canonical molecular orbitals (CMOs) of $C_{24}H_{42}/C_{18}H_{18}$, **1**, and those of the [18]annulene, **4**. Although the frontier orbitals of **1** show some small central features associated with symmetry-allowed admixture of local CH bonds, they retain a clear angular-momentum assignment: a HOMO pair with an effective angular-momentum quantum number Λ = 4 (eight sign changes in the perimeter) lies below a LUMO pair with Λ = 5 and a split pair of higher π*

orbitals with Λ = 6, as in the annulene. In full cylindrical symmetry, the only allowed orbital contribution to π ring current would arise from the HOMO-LUMO virtual excitation, and would be diatropic. In the finite point groups of **1** and its annulene model, further (weaker) excitations become allowed, again contributing diatropic current as they are translational in nature. The HOMO orbital contributions in **1** and in the annulene dominate the total π current and arise from essentially pure HOMO-LUMO excitations. The retention of a few-electron, annulene-like current in **1** is therefore fully compatible with the deduction from the ipsocentric approach, given the preservation of the nodal structure of the frontier π orbitals. This qualitative interpretation is confirmed by the near-quantitative match in j_{max} values between the maps of total π current (0.187 a.u.) and of the HOMO pair contribution (0.178 a.u.), in spite of the fact that the first is calculated with localised, and the second with canonical, orbitals.

A similar analysis can be applied to **2**, where the central ring current arises predominantly from the HOMO-LUMO Λ = 1 to Λ = 2 virtual excitation responsible for the current in benzene.[27,33]

In contrast, the six localised π current loops of **3** are individually ascribable to local π to π* excitations and can only be recovered in the CMO picture by superposition of the full set of occupied orbitals. This is as expected from the magnetically localised nature of **3** and is again compatible with the published analysis of currents in the model [6]radialene.[143]

Diatropic and paratropic currents in nanographanes

This discussion of nanographanes based on coronene has revealed some design principles which can be applied to construct current patterns of arbitrary complexity. The smallest building blocks of diatropic and paratropic currents enclosing graphane islands are evidently those derived from pyrene and phenalene perimeters respectively, as these are the smallest non-trival (4*N*+2) and (4*N*) circuits in graphene. Figure 3.6 shows schematic structures and patterns of π current for the two nanographanes **7** ($C_{16}H_{26}/C_{14}H_{14}$) and **8** ($C_{13}H_{22}/C_{12}H_{12}$), which as noted above are not necessarily the global optima for $C_{16}H_{12}$ and $C_{13}H_{10}$, respectively; in the experimental isomer of phenalene, $C_{13}H_{10}$, one of the perimeter carbons carries hydrogen atoms and the central carbon none, for example.

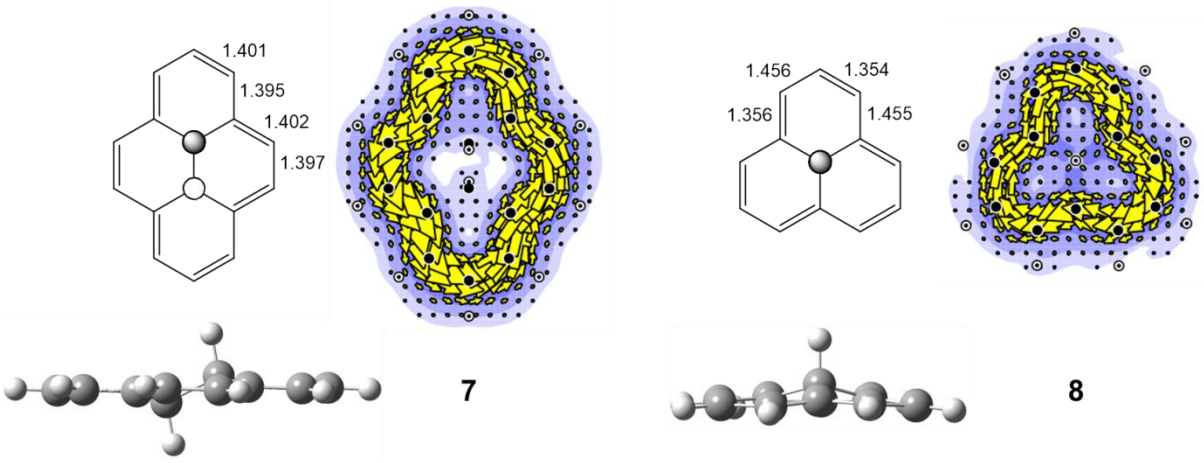

Figure 3.6. The smallest loops of diatropic and paratropic current enclosing graphane islands: the (4*N*+2) pyrene-like **7** (left), and (4*N*) phenalene-like **8** (right), perimeters. The right hand side of each panel shows a map of total π current obtained by the LMO superposition procedure. Bondlengths (in Å) calculated at the B3LYP/6-31G** level are reported on the schematic on the left and a side-on view of the structure is shown at the bottom of each panel. Plotting conventions are described in the text.

Central hydrogenation of pyrene to give **7** leads to a structure of C_{2h} symmetry with near-uniform perimeter bondlengths (maximum deviation 0.01 Å) and a near planar geometry of the sp^2 carbon framework (deviation ± 0.06 Å). The diatropic current of the dihydropyrene (**7**) is readily rationalised in terms of the analogy with a delocalised C_{2h}-constrained [14]annulene, and again arises essentially from node-increasing excitations between $\Lambda = 3$ HOMO and $\Lambda = 4$ LUMO pairs, each of which is split into two components under C_{2h} symmetry.

Construction of a closed-shell $C_{13}H_{10}$ nanographane system by formal hydrogenation at the central atom of the phenalenyl radical leads to a structure with reduced C_3 point-group symmetry. The perimeter bonds show pronounced single/double alteration (± 0.10 Å) as expected for an antiaromatic 12 π system undergoing Jahn-Teller distortion from ideal C_{3v} symmetry, but the unsaturated carbon framework remains essentially planar (heights within an interval of 0.14 Å).

Paratropic currents have a more subtle explanation than diatropic currents in the ipsocentric approach. The dominant contribution is paratropic in character and arises from the rotational HOMO-LUMO excitation across a split angular momentum pair ($\Delta\Lambda = 0$); this is inevitably accompanied by a weaker translational diatropic contribution from HOMO-1 to LUMO

(ΔΛ = +1). In the present case, Figure 3.7 shows the frontier orbital energy-level diagram for **8** in which the non-degenerate HOMO and LUMO, both corresponding to Λ = 3 in idealised full cylindrical symmetry, where they would be interconverted by a rotation of π/6 about the principal axis. In the C_3 group they are each of a symmetry and remain approximately rotationally equivalent, although split in energy. The HOMO-1 pair corresponds to Λ = 2 and is of e symmetry in the C_3 group. Therefore in **8**, the dominant rotationally allowed ΔΛ = 0 HOMO-LUMO transition (a to a) gives the paratropic contribution and the translationally allowed (HOMO-1)-LUMO ΔΛ = +1 transition (e to a) across a larger energy gap gives a much weaker diatropic perimeter current (Figure 6).

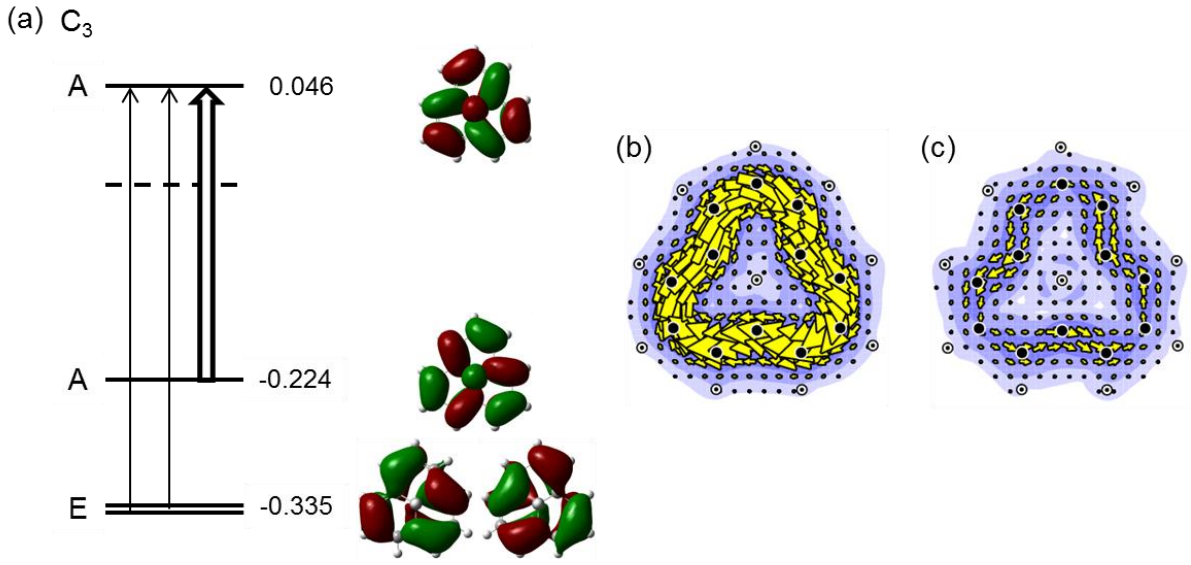

Figure 3.7. Energy level diagram and contributions of canonical molecular orbitals (CMO) to π current in **8**: (a) frontier CMOs and the associated π-π* excitations, showing the dominance of the rotationally allowed HOMO-LUMO transition; (b) paratropic π-current contribution of the HOMO; (c) diatropic π current contribution of the degenerate HOMO-1 pair. Orbital energies are given in E_h. Dominant excitations are shown in bold, translationally allowed excitations are shown as narrow, solid arrows, and rotationally allowed excitations as wide, hollow arrows. Plotting conventions are described in the text.

This pattern of strong paratropic current with partial cancellation from a weak diatropic contribution is characteristic of planar geometries of antiaromatic [4n]annulenes, where the separation of HOMO and LUMO arises from a Jahn-Teller splitting.[33] The total π current in **8** (Figure 3.6), is therefore most simply interpreted as a strong paratropic π HOMO contribution (Figure 3.7 (b)) partly damped by weaker diatropic contributions (Figure 3.7 (c)). This interpretation is supported by the j_{max} values of 0.110, 0.145 and 0.042 a.u. obtained from the total π, HOMO, and HOMO-1 maps, respectively.

Ring Current Patterns by Design

Given the success of the analogy between cycles of sp^2 hybridised carbon in 'etched' graphanes and free annulenes, one can hope to apply the same design principles more widely to additional conjugated patches and model systems, and to more complex patterns of conjugation. Figure 3.8 shows further examples illustrating the etching of an annulene-like current pattern in a nanographane. The examples illustrate benzene-like (**9**) and naphthalene-like (**10**) circuits in unsymmetrical positions, and a centrally positioned anthracene circuit (**11**), all derived formally from coronene, and symmetrical naphthalene (**12**), and [22]annulene (**13**) circuits derived from ovalene. Each of these nanographane systems shows near-planarity of the sp^3 region and a narrow distribution of bondlengths consistent with substantial electron delocalisation.

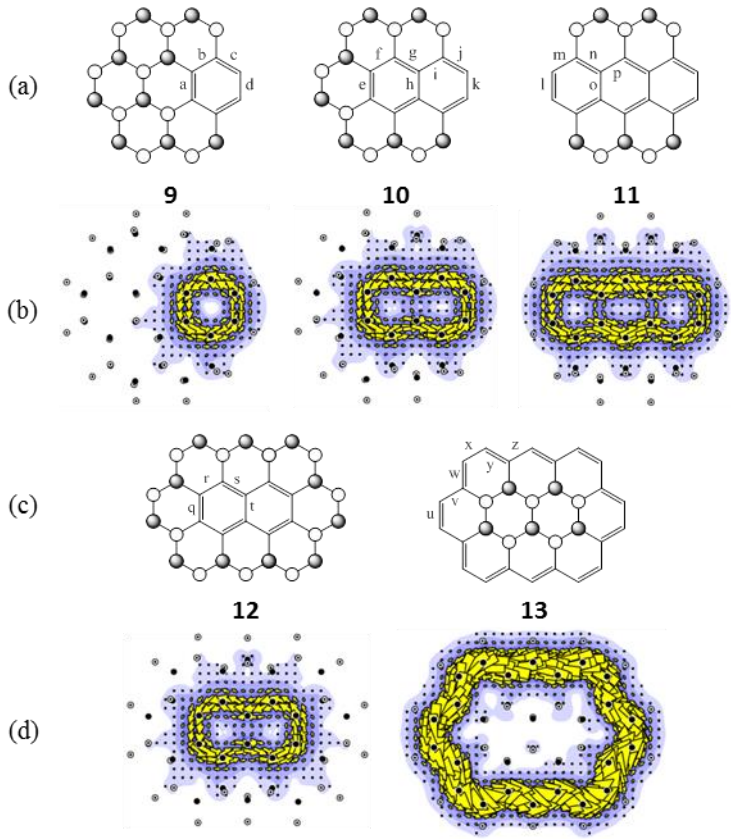

Figure 3.8. A further three nanographanes formally derived from coronene and ovalene by partial hydrogenation: C_2 symmetric **9** ($C_{24}H_{42}/C_6H_6$); C_2 symmetric **10** ($C_{24}H_{42}/C_{10}H_8$); C_{2h} symmetric **11** ($C_{24}H_{42}/C_{14}H_{10}$); C_{2h} symmetric **12** ($C_{32}H_{56}/C_{10}H_8$); C_{2h} symmetric **13** ($C_{32}H_{56}/C_{22}H_{22}$). Rows (a) and (c) show the schematic structures of the five systems, rows (b) and (d) their π ring currents obtained by the LMO superposition procedure. Unique bondlengths (in Å) of interest are: a, 1.415; b,1.407; c, 1.399; d, 1.387; e, 1.437; f, 1.389; g, 1.434; h, 1.435; i, 1.432; j, 1.379; k, 1.406; l, 1.416; m, 1.372; n, 1.442; o, 1.448, p, 1.412; q, 1.434; r, 1.369; s, 1.439; t, 1.408; u, 1.407; v, 1.401; w, 1.402; x, 1.406; y, 1.404; z, 1.406. Plotting conventions are described in the text.

Total π currents calculated by the procedure of identifying suitable localised molecular orbitals are shown for all cases, and in every case display the hoped-for similarity to the related annulenes and polyacenes. (See, for example, Figure 3.9.) The analogy extends to the analysis of orbital contributions and need not be given in detail here. For anthracene, the map shares the same feature of larger current in the central part of the perimeter found for the free molecule, which has been called the 'anthracene problem', and has been shown to be a feature of molecular orbital and conjugated circuit treatments alike.[25]

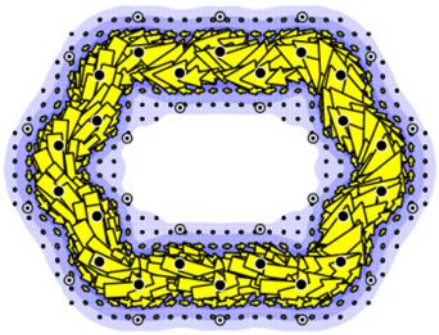

Figure 3.9. Map of π current density for the [22]annulene model of **14**. As the molecule is rigorously planar, CMOs and LMOs give identical maps. Plotting conventions are described in the text.

The same design principles can be applied to produce patterns with multiple closed circulations. Three examples are shown in Figure 3.10, two showing paired diatropic circulations and one a pair of paratropic currents.

In **15**, two phenanthrene-like regions are constructed by partitioning ovalene with a central strip of sp^3-carbon centres. Each of the two independent currents follows a phenanthrene pathway and is of similar strength to that of the isolated molecule (j_{max} = 0.101 a.u. for **15** and 0.092 a.u. for phenanthrene itself).

In **16**, the isolation of a perylene-like sp^2 region produces a pair of diatropic circulations. Here, the separation of the two currents is a consequence of the internal electronic structure of the sp^2 region: perylene itself shows two almost independent naphthalene-like currents, a fact that is easy to understand on a conjugated-circuit model, as all nine Kekulé structures of perylene have formal single bonds on the two perimeter edges of the central ring.[27,141,145] The separation into two circulations is advanced in **16** by geometric factors: the two naphthalene fragments are twisted by ~10° (local median plane to local median plane), which again indicates reduced double bond character in the linking edges, and accounts for the apparent left-right asymmetry in the map shown in Figure 3.9, where the plotting plane is parallel to the sp^2-median plane.

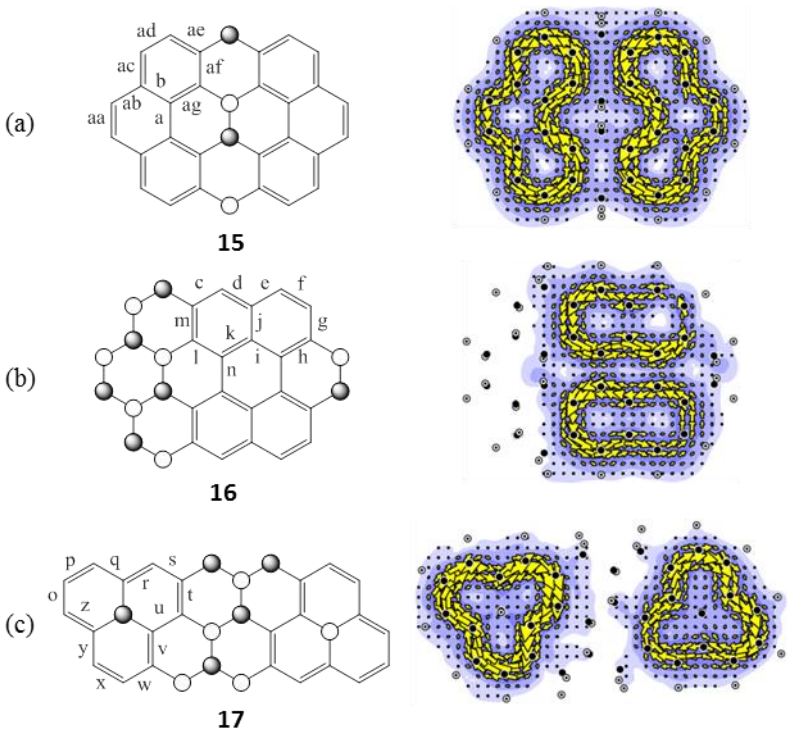

Figure 3.10. Examples of nanographanes that exhibit multiple closed circulations: (a) C_{2h} symmetric **15** ($C_{32}H_{56}/C_{14}H_{10},C_{14}H_{10}$); (b) C_2 symmetric **16** ($C_{32}H_{56}/C_{10}H_8,C_{10}H_8$); (c) C_i symmetric **17** ($C_{34}H_{50}/C_{12}H_{12},C_{12}H_{12}$). Schematic structures are shown in the left hand column, π ring current maps produced by the localisation procedure in the right. Unique bondlengths (in Å) of interest are: aa, 1.343; ab, 1.348; ac, 1.410; ad, 1.361; ae, 1.411; af, 1.368; ag, 1.417; a, 1.448; b, 1.398; c, 1.382; d, 1.415; e, 1.419; f, 1.377; g, 1.412; h, 1.396; i, 1.427; j, 1.428; k, 1.428; l, 1.398; m, 1.422; n, 1.470; o, 1.455; p, 1.354; q, 1.455; r, 1.353; s, 1.462; t, 1.363; u, 1.460; v, 1.362; w, 1.461; x, 1.354; y, 1.453; z, 1.356. Plotting conventions are described in the text.

Finally, the map for nanographane **17** shows that disjoint *paratropic* circulations can exist in closed-shell systems. Two phenalene subunits are produced using a separating strip of hydrogen atoms in conjunction with internal hydrogenation. They each support a ring current mimicking the free system **8**. The full nanographane system **17** as a whole has C_i point-group symmetry, but the map appears less symmetric owing to the twisting of the two 12π circuits with respect to each other and to the plotting plane (1 a_0 from the median plane of the sp^2 centres).

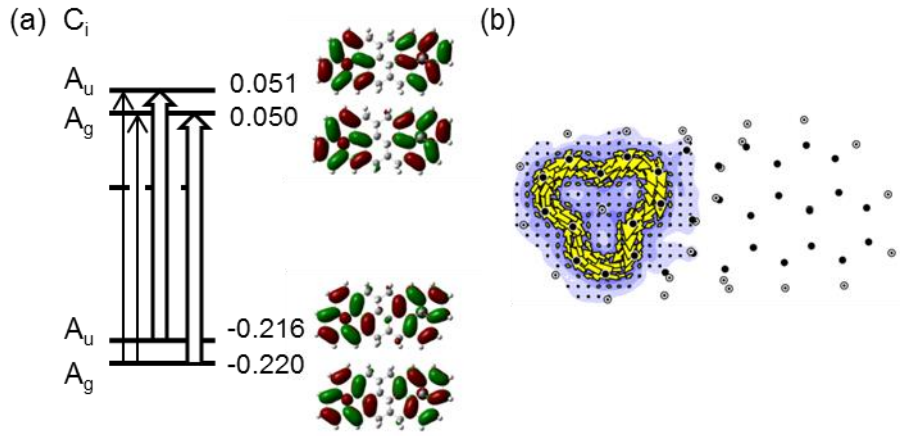

Figure 3.11. Energy level diagram and contributions to π current in **17**: (a) frontier *canonical* molecular orbital and the associated π-π* excitations, showing the dominance of rotationally allowed HOMO-LUMO and (HOMO-1)-(LUMO+1) transitions; (b) paratropic π current contribution of the 6 *localised* molecular orbitals that correspond to the left hand phenalene fragment. Orbital energies are given in E_h. Dominant excitations are shown in bold, translationally allowed excitations are shown as narrow, solid arrows, and rotationally allowed excitations as wide, hollow arrows. Plotting conventions are described in the text.

The map in Figure 3.10 (c) shows the total π current of **17**. This can be partitioned in different ways. For a delocalised π system, it can be expected that the total current can be accounted for by a small number of contributions from canonical molecular orbitals. As Figure 3.11 (a) shows, the occupied and unoccupied frontier orbitals of **17** derive from in- and out-of-plane combinations of the respective frontier orbitals of the two phenalenyl fragments. Four HOMO-LUMO virtual excitations are allowed in C_i symmetry: the 'diagonal' a_g-a_g and a_u-a_u excitations have rotational character and the 'off-diagonal' a_g-a_u and a_u-a_g excitations have translational character. The diagonal contributions involve simultaneous rotational excitation on each fragment (as highlighted in Figure 3.12), and hence dominate the contribution from the HOMO pair leading to the observed strongly paratropic overall current. The net contributions from the HOMO-2 to HOMO-5 CMOs are a pair of weak diatropic currents on the fragments consistent with local translational excitations. The current therefore is economically represented by 6 CMOs spread over the whole molecule. An alternative representation can be formed from the 6 LMOs associated with one phenalene fragment (Figure 3.11 (b)). The map separates neatly into two circulations, supporting our claim that **17** is an example of a locally

delocalised π system: two delocalised sp^2 circuits (directly related to that of **8**, as in Figure 3.7) separated by an insulating sp^3 region, each the product of the local environment on each free oligocyclic unsaturated path, as envisaged in the printing/etching analogy. Figure 3.12 shows the local orbital topology of one of the identical, dominant, orbital contributions to current in **17**, illustrating the origin of this 'locally delocalised' phenomenon and highlighting the centring of orbital lobes on different bonds in the HOMO and LUMO pairs.

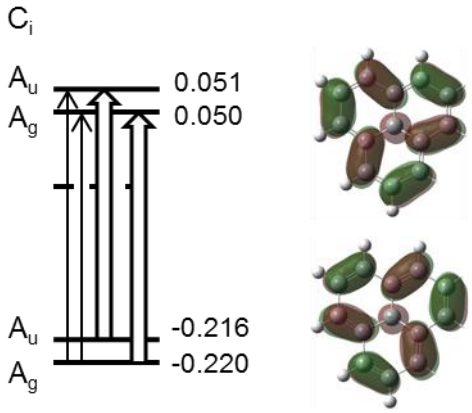

Figure 3.12. Energy level diagram and local orbital topology of one of the possible rotationally allowed transition in **17**. Plotting conventions are as in Figure 3.11.

Alternative Modifications of Nanographanes

All examples shown so far have been constructed by hydrogenation of the graphene sheet in a manner that is consistent with the all-chair form of graphane. Both fluorinated analogues of graphane, and configurational isomers of graphene, have featured in literature reports, and it is of interest to check whether the printing/etching analogy survives chemical and structural variations of this kind.

(i) Perfluoro-Nanographanes

To test sensitivity to chemical substitution, calculations in which all hydrogen atoms of the nanographane were replaced by fluorine atoms were carried out for **1** and **2**, the two symmetrical 'aromatic' nanographane derivatives of coronene, to produce **18** and **19**, respectively.

Replacement of hydrogen with fluorine leads to small changes in geometry of the sp^2 regions in **1**. Vertical deviation of the 18 carbon perimeter increases from ±0.06 Å (**1**) to ±0.10 Å (**18**), and dispersion in perimeter bond lengths increases slightly, with the long bonds extending from 1.406 Å (**1**) to 1.408 Å (**18**), and the short bonds shortening from 1.401 Å (**1**) to 1.393 Å (**18**). D_{3d} symmetry is retained. Changes in the ring-current are also small: the currents for **1** and **18** in Figure 3.3 and Figure 3.13 are essentially visually indistinguishable.

A similar picture is found on comparison of **2** and **19**, where the perfluoro analogue has a reduced symmetry (S_6) corresponding to distortion along a low-energy a_{2g} mode of an idealised D_{3d} structure. The C_6 ring has negligible vertical deviation in **19** (~0.001 Å) and a uniform bond length of 1.408 Å (c.f. 1.401 Å in **2**). Again, the ring current in **19**, like that in **2**, is satisfyingly similar to that of benzene itself.

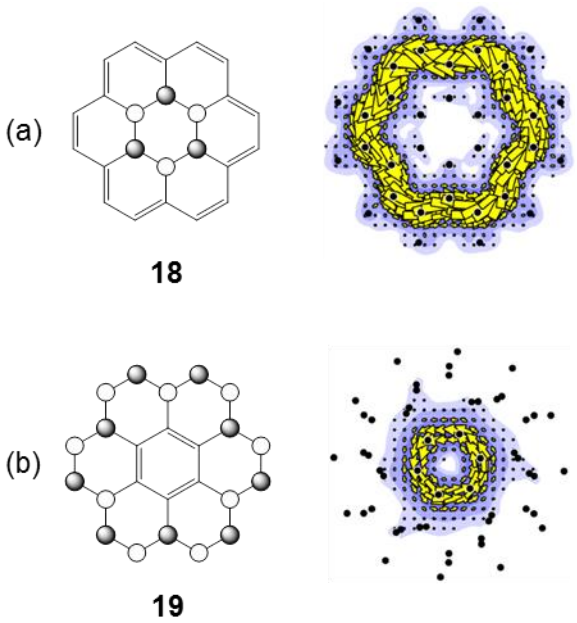

Figure 3.13. Two perfluoro nanographanes formally derived from coronene: (a) **18** ($C_{24}F_{42}/C_{18}F_{18}$); (b) **19** ($C_{24}F_{42}/C_6F_6$). The first column shows the schematic molecular structures, the second column shows the π ring current maps defined by superposition of LMO contributions. Plotting conventions are described in the text.

(ii) Alternative Configurational Isomers

As an initial exploration of sensitivity to the conformation of the underlying carbon framework, two forms of the nanographane produced by full hydrogenation of coronene were constructed (see Figure 3.14). Consistent antiperiplanar hydrogenation leads to the all chair-form; hydrogenation where each CH bond is involved in one eclipsing interaction leads to the all-boat form. Removal of one hydrogen atom at each peripheral site leads either to D_{3d} **1** or to C_{2v} **20**, where the central hexagonal ring has a boat conformation. The 18 carbon sp^2 cycle in **20** has uniform bond lengths (all 1.400 ± 0.001 Å) and a larger vertical range of 0.26 Å (c.f. 0.01 Å in **1**), but still supports an [18]annulene-like ring current (see Figure 3.15).

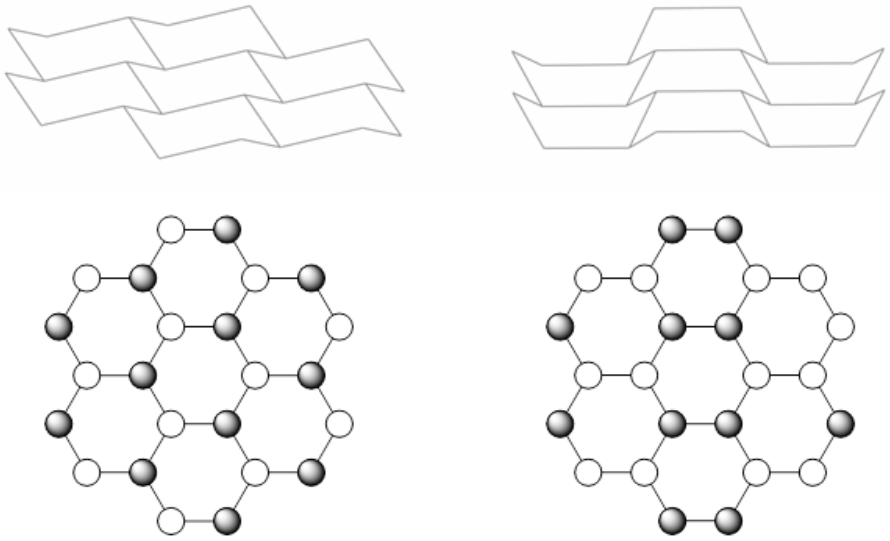

Figure 3.14. Alternative all-chair (left) and all-boat (right) conformations of the carbon framework in a nanographane as imposed by suitable choices of hydrogenation pattern.

Likewise, dehydrogenation of the central ring leads either to D_{3d} **2** or C_{2v} **21**. The central sp^2 region has near uniform bondlengths (1 × 1.405 and 2 × 1.407 Å). In spite of the rumpling produced by unfavourable CH bond interactions around the perimeter, **21** still has an essentially planar central ring (height range 0.03 Å), with a typical benzenoid ring current (Figure 3.15).

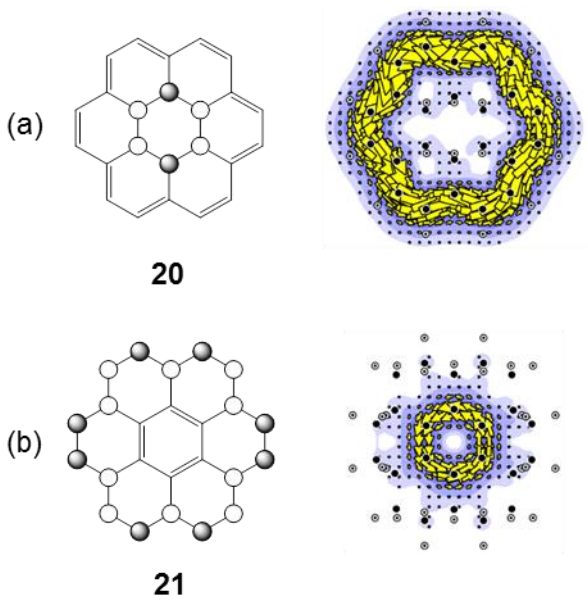

Figure 3.15. Two nanographanes formally derived by selective dehydrogenation of a *coronane* fragment of the all-boat graphane sheet (see Figure 12). The first column shows the schematic molecular structures. **20** and **21** share formulas $C_{24}H_{42}/C_{18}H_{18}$ and $C_{24}H_{42}/C_6H_6$ with **1** and **2**, respectively. The π ring current maps are formed by the LMO superposition procedure. Plotting conventions are described in the text.

These preliminary calculations reinforce the expectation that the printing/etching analogy survives chemical and conformational changes as a useful design principle for π electron delocalisation pathways in graphene/graphane hybrids. Overall, the induced 'ring' currents in these hybrid systems have essentially the same sense, strength and orbital origin as in the free hydrocarbon. Subject to the important experimental proviso of the need for atomic-scale control of hydrogenation, this finding predicts the possibility of writing single, multiple and concentric diatropic and/or paratropic ring currents on the graphene/graphane sheet. The implication is that pathways for free flow of ballistic current can be modelled in the same way.

The ideas encountered in this chapter will be used to design and interpret investigations throughout the rest of this thesis, starting with mixed carbon and boron nitride ring systems in Chapter 4, and aromatised $B_nN_nH_{2n}$ heterocycles in Chapter 5.

Chapter 4: Aromaticity of Benzenoid-Borazinoid Hybrids*

Introduction

Polycyclic aromatic hydrocarbons (PAHs) are central species in the study of a variety of subjects including synthetic organic chemistry, photochemistry, environmental and interstellar chemistry, and in design of materials for applications in electronics.[139,140,146,147] They have come to new prominence, as discussed in Chapter 3, as prototypes of finite graphene flakes.[148–150] They have long played a central rôle in the theory of aromaticity. Given the structural analogy between hexagonal boron nitride and graphite [151,152] and the (albeit equivocal[50–60]) description of borazine as 'the inorganic benzene', there is increasing experimental interest in the properties and synthesis of boron-nitride/carbon hybrids.[46,153–161] The possibility of partial replacement of C_6 rings in coronene has also been explored theoretically as a route to the design of new aromatic systems.[162,163]

A comparative study by Türker[163] considered 'central' *vs*. 'outer' substitutions of a C_6 cycle in coronene, and their effects on energetics, geometry, charge distributions and some magnetic properties. The interesting conclusion of this work is that 'outer' substitution leads to the more stable form, even if some measures of aromaticity would appear to suggest that this isomer is 'less aromatic' than the alternative produced by 'central' substitution.

* Some of the material in this chapter has been published in: Fowler, P. W.; Gibson, C. M.; Nightingale, E. L. *Polycycl. Aromat. Compd.* **2013**, *33*, 72–81. The chapter contains additional systems, figures, current-density maps, and discussion.

In the present chapter, the ipsocentric[27,33] method is employed first to present an account of the aromaticity of these systems in terms of their ring-current response. As has been seen, the ipsocentric method offers simple and intuitive interpretation of currents as contributions from either localised or delocalised orbitals; current-density maps can be understood simply in terms of 'ring currents' flowing around the perimeters of all-carbon fragments, and nitrogen-localised 'lone-pair' currents. In the limit, complete replacement of all C_6 cycles with B_3N_3 rings, preserving alternation, leads to a fully localised π-current map. It can be concluded that π-currents may be 'written' on graphene/boron-nitride analogues by selective replacement of benzene rings, achievable insofar as progress in synthetic methods allows.

Methods

Structures **1**, **2**, and **3** (see Figure 4.1) were optimised at the B3LYP/6-31G** (and to be consistent with reference [163], B3LYP/6-311G**) levels of theory using the Gaussian09 package,[40] and confirmed as local minima on the potential energy hypersurface by diagonalisation of the Hessian. Calculations of current-density maps were performed using the ipsocentric coupled-Hartree-Fock approach embodied in the SYSMO package.[39] As in previous chapters, DFT optimisation is preferred here, as previous calculations on macrocycles, including **1**, have shown spurious symmetry-breaking effects in Hartree-Fock calculations, which can be avoided in DFT thanks to its treatment of electron correlation.[63,162] For example, in the present calculations, DFT optimisation of **1** converges to a structure of D_{3h} symmetry, whereas Hartree-Fock calculations give the broken C_{3h} symmetry. Optimisations[163] carried out with lower symmetries (C_s for **1** and C_1 for **2**) show some dispersion in symmetry-related bond lengths, but this can be removed by use of stricter convergence criteria. For **2** and **3**, the maximum combinational symmetries are C_s and D_{3h}, and both are realised in the DFT optimisations.

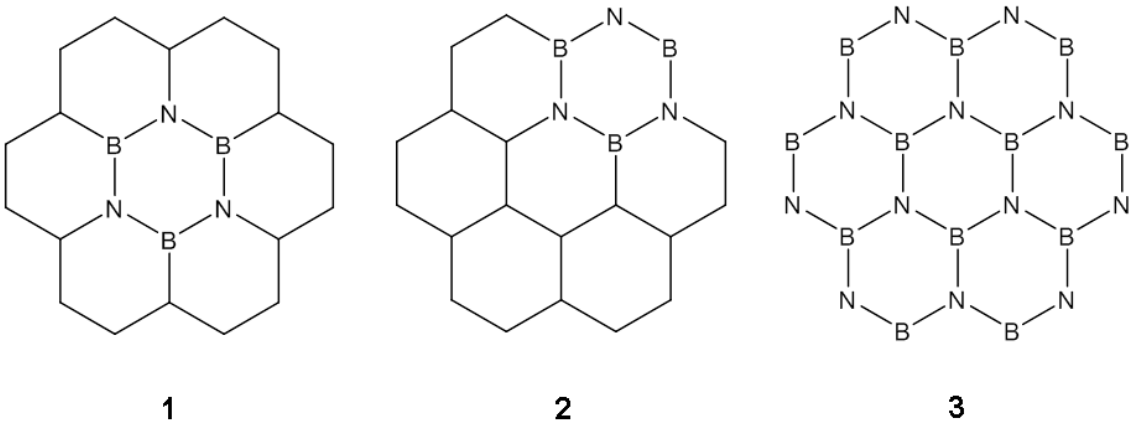

Figure 4.1. Three derivatives of coronene considered in the present paper: **1** and **2**, $C_{18}B_3N_3H_{12}$ (two isomers), and **3**, $B_{12}N_{12}H_{12}$.

Structure **1** has energy -932.2762 E_h at the B3LYP/6-31G** level, with a zero-point energy correction of +0.2749 E_h. For structure **2**, the corresponding energies are -932.3083 E_h and +0.2748 E_h. The net stabilisation of **2** over **1** is therefore 0.0322 E_h, or 84.5 kJ/mol^{-1}, which is consistent with the range of values of 77 to 85 kJ/mol^{-1} for this stabilisation reported in Reference ([163]). The vibrational modes of lowest frequency have wavenumbers 88 and 81 cm^{-1}, respectively. The fully borazinoid isomer **3** has energy -963.7627 E_h and zero-point correction +0.2580 E_h, with lowest vibrational mode at 62 cm^{-1}.

Current-density maps were calculated for the total π-distribution, in each molecule for various partitions based on canonical molecular orbitals, and also for localised π orbitals obtained by the Pipek-Mezey method.[43] The maps show first-order current density in the plotting plane at 1 a_0 above the plane of the nuclei, with nuclear positions (see Figure 2.1) projected into the plotting plane. Contours and shading indicate the modulus of the induced current-density per unit external magnetic field, and arrows indicate the vector current density resolved into the plotting plane. A measure of current strength is given by j_{max}, the maximum current density per unit inducing field taken over the plotting plane, and is often compared to the benzene standard of 0.078 a.u. at this level of theory. Current-density maps computed in the 6-31G** and 6-311G** basis sets are practically identical, and therefore only the maps for the 6-31G** basis set are shown here.

Results and Discussion

The total π current-density maps for the three molecules are shown in Figure 4.2. Both **1** and **2** show coherent diatropic global ring currents. In the case of **1**, the current shows a single consistent flow around the perimeter (j_{max} = 0.133 a.u., or 1.66 times the benzene standard), i.e., following the C_{18} carbon cycle. Smaller features within the central region are associated with the nitrogen centres of the B_3N_3 cycle. In contrast, the map for **2** shows a coherent circulation localised on the three-hexagon phenylene fragment (j_{max} = 0.113 a.u.), although with some indications of a weaker perimeter circulation, and again only nitrogen-centred circulations in the B_3N_3 region. Finally, the fully carbon-replaced structure **3** shows a set of 12 nitrogen-localised 'lone-pair' circulations (j_{max} = 0.076 a.u.).

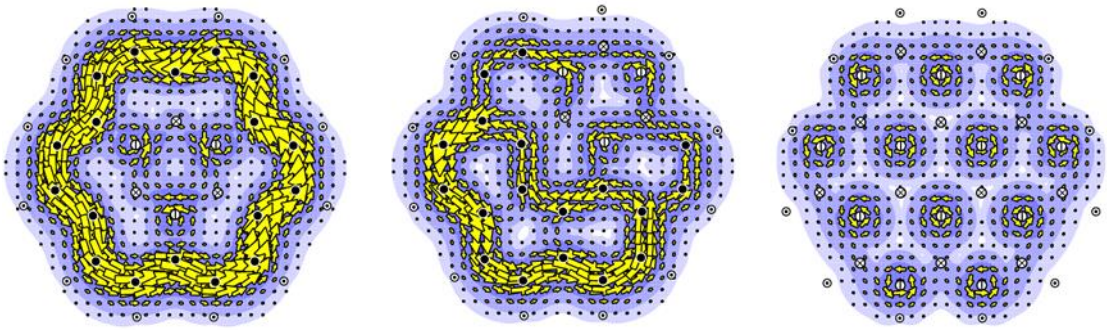

Figure 4.2. Maps of total π current-density induced by a perpendicular external magnetic field in molecules **1**, **2** and **3**. Plotting conventions are described in the text.

All three maps offer informative contrasts with the map of π-current for the parent coronene molecule, as shown in Figure 4.3(a).[27,164] Coronene supports a pair of counter-rotating ring currents, strong and diatropic on the rim of the molecule, but weak and paratropic on the central C_6 hub.[164] This current can be interpreted in terms of opposing contributions from virtual excitations amongst frontier orbitals, with the diatropic perimeter current arising from the dominant translational excitations between the e_{2u} HOMO e_{1g} LUMO pairs (Figure 4.3(b)), and the central paratropic contribution from the rotational excitation between the e_{2u} HOMO and LUMO+1 pairs (Figure 4.3(c)). In **1**, the perimeter circulation of the parent is retained, but in **2** it is diverted through the molecular interior, and in **3** it is lost altogether.

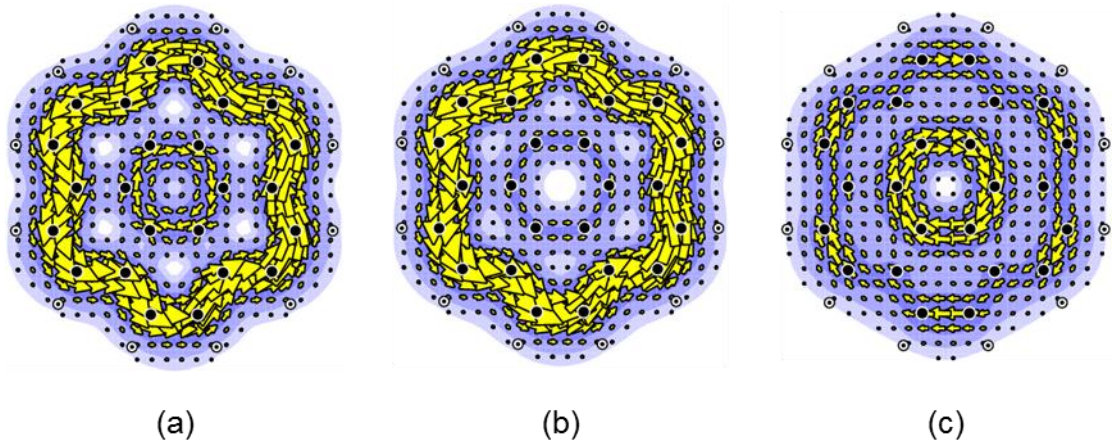

Figure 4.3. Current-density maps of D_{6h} coronene ($C_{24}H_{12}$). Showing: (a) The total 12π current. (b) The dominant, diatropic contribution to current arising from the sum of the four possible excitations between the e_{2u} HOMO e_{1g} LUMO pairs. (c) The paratropic contribution to current arising from the sum of the four possible excitations between the e_{2u} HOMO e_{2u} LUMO pairs+1. Plotting conventions are described in the text.

The maps given here can also be analysed further to reveal the orbital structure of the currents. Previous work has shown how contributions from a small number of 'frontier' canonical molecular orbitals can characterise the currents in fully delocalised systems,[27,33] and how this gives a ready rationalisation in terms of nodal character of starting occupied and target virtual orbitals. To reiterate, diatropic currents correspond to node-increasing virtual excitations from occupied to unoccupied orbitals.[27]

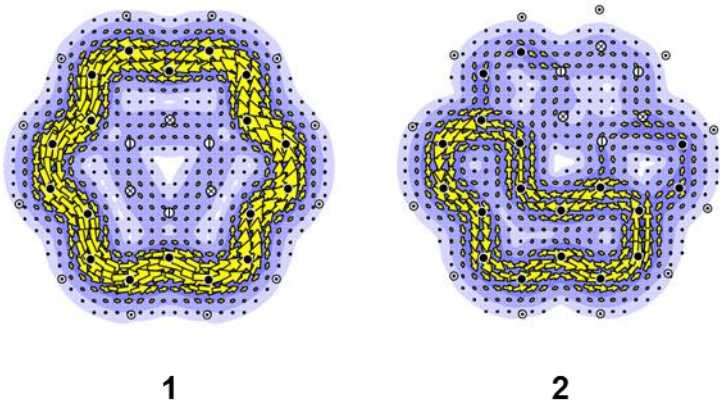

Figure 4.4. π current-density maps for canonical-orbital breakdown of species **1** and **2** showing the total contribution of the HOMO pair in each case. Plotting conventions are described in the text.

Here, we may expect a mixture of localised and delocalised response. As in the parent molecule coronene, the dominant circulations in **1** and **2** originate essentially from the HOMO electrons (occupying an e" pair in **1** and a near-degenerate 2a" pair in **2**, corresponding to the e_{2u} HOMO pair in coronene), as shown in Figure 4.4. Their diatropic nature arises from the increase in the number of angular nodes between π-HOMO and π-LUMO, as illustrated in Figure 4.5.

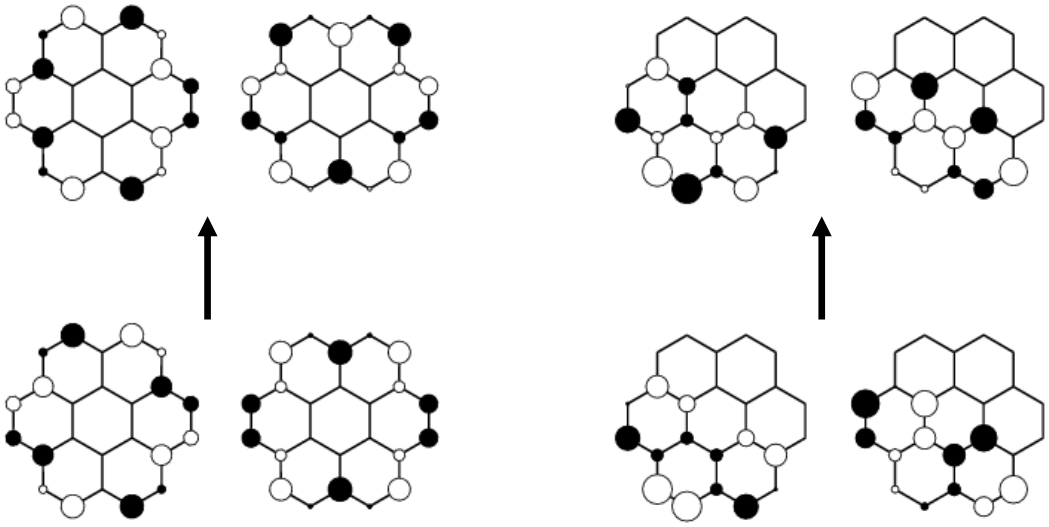

Figure 4.5. Nodal character of HOMO-LUMO virtual excitations in **1** (left) and **2** (right). Hückel molecular orbitals for the C_{18} and C_{14} circuits give a schematic indication of the nodal properties of the pairs; in **1** the (degenerate) HOMO has angular momentum component $\Lambda = 4$ and the (degenerate) LUMO has $\Lambda = 5$; in **2** the number of nodes also increases by one on going from the (near-degenerate) HOMO pair to the (near-degenerate) LUMO pair.

The localised parts of the current maps are retrieved by an analysis in terms of localised molecular orbitals. Pipek-Mezey analysis preserves σ/π separation[43] and hence is suitable for dissection of these partially localised π systems.[61] As Figure 4.6 shows, the global carbocyclic currents and lone-pair circulations in **1** and **2** are recoverable by consideration of sums of contributions of localised molecular π-orbitals.

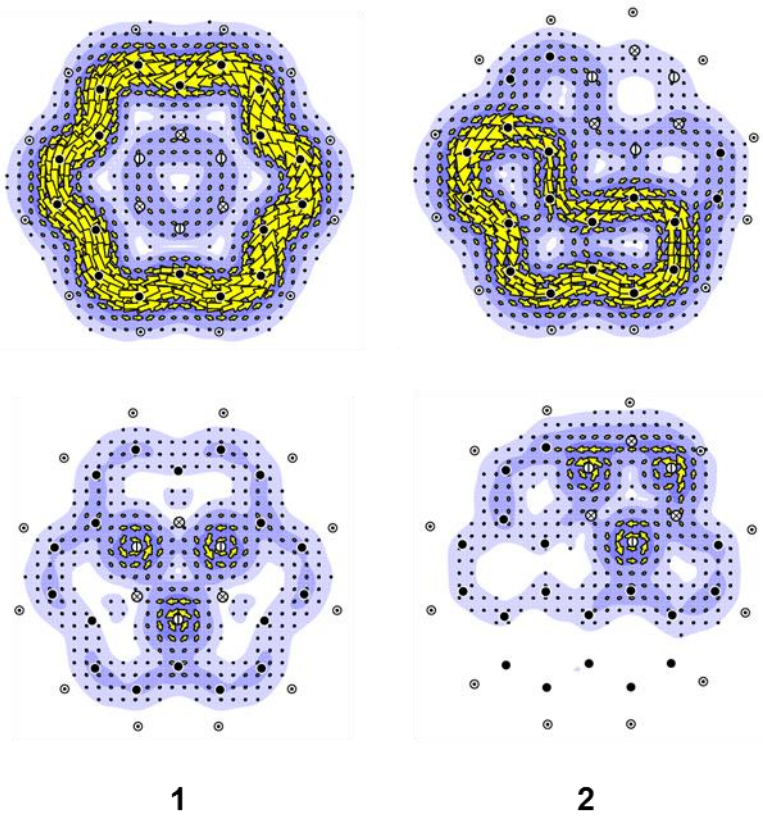

Figure 4.6. π current-density maps for localised MO (LMO) breakdown of species **1** and **2**, showing the contributions arising from the carbocyclic regions (top) and nitrogen lone-pairs (bottom). Plotting conventions are described in the text.

Although the choice of molecular orbitals is ultimately arbitrary, in the sense that any unitary transformation amongst occupied orbitals leads to the same electron density (and the same total current density), the breakdown into orbital contributions can give an insight into intrinsic localisation or otherwise of magnetic response.[61] The facts that (i) delocalised canonical MOs (CMOs) give the most economical description of the carbon-based currents in **1**, **2** and coronene itself (two CMOs each, rather than the full nine, seven and twelve occupied LMOs), and (ii) the nitrogen localised currents in **1**, **2** and **3** require one LMO each, give clear pointers to the different types of bonding in the two subsystems, and are in full accord with chemical intuition about the different natures of CC and BN π-bonding.

As an aside, it is worthwhile to note that in the manner of the products of central ($C_{24}H_{42}/C_{18}H_{18}$) or perimeter ($C_{24}H_{42}/C_6H_6$) hydrogenation of coronene (see Figure 3.3), the oligocyclic current survives when fully embedded in a borazinoid flake. Figure 4.7 shows the benzenoid/borazinoid hybrid corresponding to coronene with the perimeter 18 carbon cycles replaced by alternating BN units (calculated at the CHF/6-31G**//B3LYP/6-31G** level). The resultant D_{3h} $C_6B_9N_9H_{12}$ minimum-energy structure maintains the signature ring current of the benzene moiety, with the heteroatom framework again displaying a fully localised magnetic response.

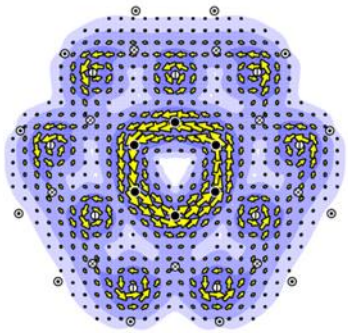

Figure 4.7. Total 12π current density maps of D_{3h} $C_6B_9N_9H_{12}$. Plotting conventions are described in the text.

It is interesting to compare the direct evidence from current density-maps with the deductions from the point-wise NICS[11] measure of aromaticity. Our calculations of the NICS(0) quantity, which is the negative of the absolute nuclear shielding at the geometric ring centre, performed at the B3LYP/6-31G**/GIAO level[40] for **1** and **2**, give the patterns shown in Figure 4.8. This is not a particularly high level of theory but should give indicative results for NICS patterns.

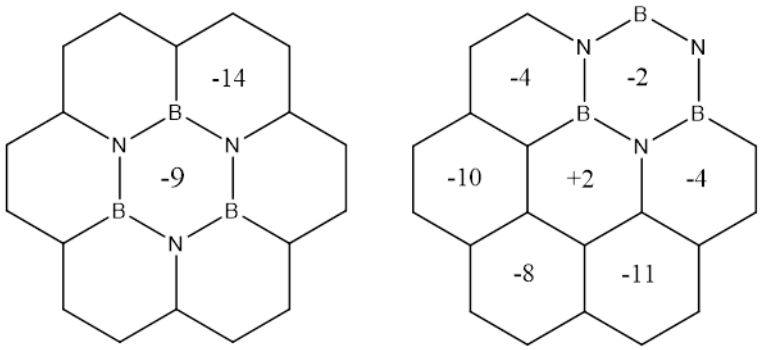

1 **2**

Figure 4.8. NICS(0) values (in ppm) obtained for **1** and **2** calculated at the B3LYP/6-31G**/GIAO level of theory. Note that in this basis the corresponding values for benzene and borazine are -10 ppm and -3 ppm, respectively.

If interpreted strictly locally, these would indicate aromaticity of all six outer rings and the central B_3N_3 ring aromaticity of **1**, but for **2**, aromaticity for only the three rings belonging to the phenanthrene region. **3** shows values close to zero for all rings. The results for **1** are compatible with those obtained with the *PZ*2 approach in reference,[162] but both molecules show some unexplained differences from those reported in reference,[163] particularly in the case of molecule **2**. In fact, the maps show that all such conclusions about local aromaticity would be risky: in each case, the presence of a strong current around the perimeter of a ring gives the impression of diatropic flow, even though there is no circulation localised on that ring.[35] Pointwise measures can be interpreted in many ways, whereas global maps give a single unambiguous message.

Understanding of magnetic response in these 'chemical' terms also has wider applicability. Borazine itself has purely localised induced π-currents[27,61] (see Chapter 2, Figures 2.13 and 2.15) and similar currents are predicted for larger $(BN)_x$ rings, as shown in Chapter 5.[88] Localisation also appears to hold for a range of BN-substituted analogues, as we now show.

Sample calculations of the all-BN equivalents of benzene, naphthalene, phenanthrene and phenalene (both anionic and cationic forms) are shown in Figure 4.9. All five systems have planar structures at the RHF/6-31G** level and their π current-density maps are simple superpositions of nitrogen-centred lone pair circulations. These are in sharp contrast to the current maps for the corresponding PAH molecules;[27,61,165] in particular, the anion and cation both show diatropic ring currents on the molecular perimeter, whereas their isoelectronic partners show the patterns of islands of lone-pair current, differing only in the number of N centres needed to achieve the electron count of the PAH ion. Partial replacement of carbon in PAH's, bond-by-bond or ring-by-ring, offers a rich set of possibilities for current patterns intermediate between the two extremes.

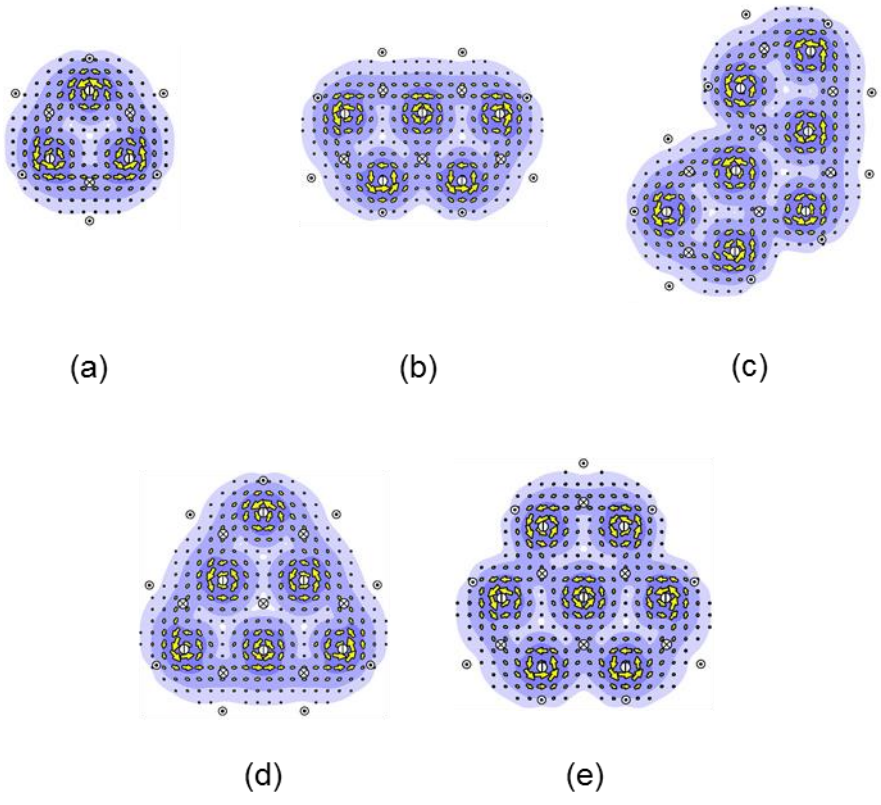

Figure 4.9. Total π current-density maps for the all-BN equivalents of (a) benzene, (b) naphthalene, (c) phenanthrene, and (d) the anionic and (e) cationic forms of phenalene. Plotting conventions are described in the text.

The overall conclusion from this work is clear: as benzenoid carbocycles are replaced by B_3N_3 units, the magnetic response becomes localised into atomic (nitrogen-centred) and oligocyclic (carbon) circulations. Magnetic response within each of these hybrid systems can be predicted by superposition of maps for the free carbocyclic fragment and the set of lone-pair islands. In this sense, it appears that hybrid systems can be designed to exhibit currents of desired sense, strength, and extent by mimicking PAH subsystems. The practical challenge, of course, is to synthesise such hybrid benzenoid-borazinoid systems.

This chapter has shown how replacement of complete B_3N_3 cycles affects the aromaticity of finite PAH flakes. The next chapter focuses specifically on $B_nN_nH_{2n}$ heterocycles, and introduces strategies for inducing ring current in these 'inorganic annulenes'.

Chapter 5: Aromatisation of Azabora-$B_nN_nH_{2n}$ Annulenes

Introduction

Borazine has formerly, and often controversially, been considered an 'inorganic benzene'.[1-13] Despite having an 'aromatic' 4*N*+2 electron count and frontier-orbital symmetries permissive of the presence of a global ring current, the magnetic properties of borazine are in fact consistent with non-aromaticity. *Ab initio* calculated π-current density maps for borazine show only localised diatropic nitrogen lone-pair circulations, rather than the global diatropic current that is diagnostic of aromaticity in isoelectronic benzene.[61] This type of magnetic response persists in the general case, where complete replacement in an even annulene of all C_2 pairs by isoelectronic BN-units destroys global circulation and yields a heterocycle that is non-aromatic, with localised lone-pair circulations about the nitrogen centres.[88] Previous calculated current-density maps also suggests that replacement of complete C_6 cycles or wholesale replacement of C_2 pairs by BN-units leads to localisation of magnetic response of polycyclic aromatic hydrocarbons (PAHs, or nanographenes[139,140,149]).

Other strategies for control of delocalisation in ring systems have been explored theoretically. Partial hydrogenation or fluorination of PAHs gives finite model systems that retain diagnostic aromatic features of the bare annulenes and polycycles that they mimic.[166] Through partial replacement of sp^2 with sp^3 centres it is predicted to be possible to 'write' both diatropic and paratropic ring currents within a PAH. Partial replacement of C_2 units in a PAH with isoelectronic BN units could lead to an extension of this model, with further regio-functionalisation providing a method of 'writing' currents on a mixed carbon/boron-nitride sheet.[123,161]

The differences in ring-current response between isoelectronic CC and BN analogues can be rationalised using rather simple considerations of the difference in electronegativity between neighbouring atoms. Soncini and co-workers[88] used a frontier-orbital model of induced currents to explain the transition from delocalised to localised magnetic response for simple cycles. Bonding orbitals tend to concentrate on electronegative centres, and anti-bonding orbitals on electropositive centres, and as a consequence, the field-perturbed orbitals, and hence the currents become more localised, rendering the all-BN heterocycles non-aromatic by the magnetic criterion. Within the ipsocentric approach,[27,33] this trend is explained in terms of changes in strength of virtual transitions between occupied and unoccupied π frontier orbitals, with widening of the gap, and decrease of the overlap, between HOMO and LUMO.[33]

A natural question arises from consideration of this argument and of the orbital energy level diagrams of BN-heterocycles. Can they be made aromatic or anti-aromatic through alteration of electron count in such a way as to yield an electronic configuration in which there are energetically accessible, symmetry-allowed HOMO-LUMO transitions?

Clearly, the example of borazine itself shows that ring-current aromaticity is not just a consequence of a 4*N*+2 electron count. The previously mentioned study[88] of planar equilateral X_nY_n heterocycles with D_{nh} symmetry, where X and Y represent atoms or groups isolobal with the C_2 unit, characterised the consequences of electronegativity alternation within the ipsocentric formulation.[88] It was found that the differential electronegativity parameter, η, played a crucial role in the balance between delocalisation and localisation in heterocycles. Until the threshold for a significant paratropic contribution, of ($|\eta| \geq 0.5\ |\beta|$) is reached, global diatropic currents are preserved.

In contrast, *charged* systems with $\eta \neq 0$ are expected to behave differently: π-excessive and π-deficient heterocycles occupy regions of the energy-level diagram far from the frontier for π-sufficient systems, and the relevant energy gaps and transition symmetry products differ from those in the neutral system.

The illustrative energy-level diagrams shown in Figure 5.1 explain why aromaticity is not expected for π-systems with high values of η, and suggest a way to make these systems aromatic in the ring-current sense. The diagrams suggest that adjustment of frontier-orbital populations by two and four electrons for 4*N* and 4*N*+2 systems, respectively, would lead to

narrowing of the HOMO-LUMO gap at fixed electronegativity, increasing the strength of the virtual excitations associated with induced ring-current. These simple-Hückel considerations neglect possible changes in electronic structure with charge (e.g., as induced by electron repulsion) and need to be checked against calculations at a higher theoretical level, as done in the present work.

The outline of this Chapter is as follows. Firstly, the π-current responses of D_{nh} planar-constrained $(BN)_nH_{2n}^{q}$ ring systems, with n = 2 to 7 and q = 0, ±2 (for *even n*), and ±4 (for *odd n*), are presented and analysed in terms of orbital contributions. The insights into the aromatisation of these cycles are then applied in the light of recent advances made in the preparation of benzenoid-borazinoid hybrids[167] to explore the potential of achieving 'designer' aromatic response via modifications of these systems. It will be shown that the design principles at play in controlling aromatic response in graphene/graphane hybrids[166] could also be successful here.

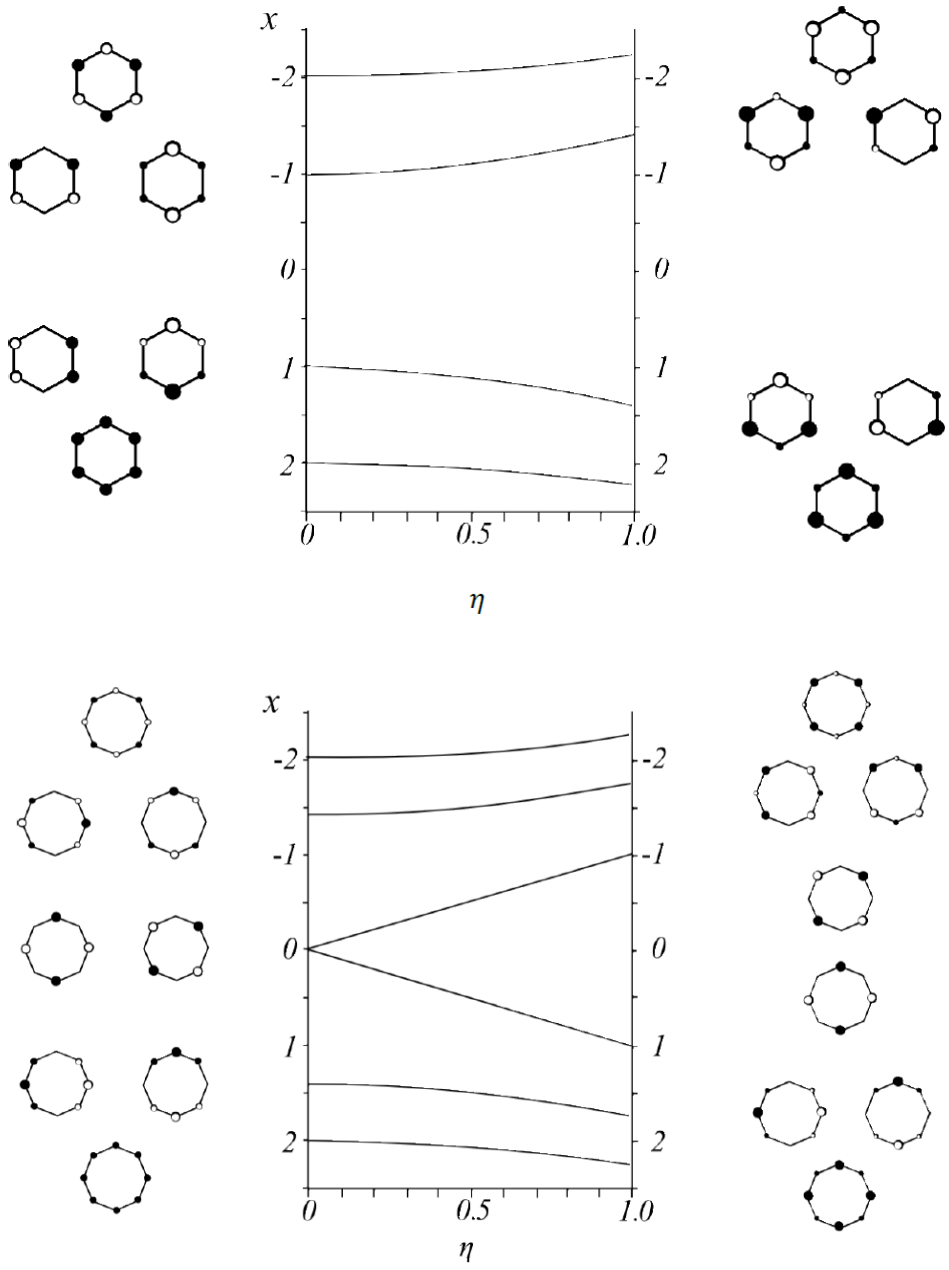

Figure 5.1. Hückel model correlation diagram of energy (as $x = (\varepsilon - \alpha)/\beta$) and orbital composition of: (top) benzene (left) and borazine (right); (bottom) planar cyclooctatetraene (left) and borazocine (right). Variation between annulene and BN-heteroannulene systems are modelled by the electronegativity parameter η, where $\alpha_B = \alpha - \eta\beta$, and $\alpha_N = \alpha - \eta\beta$. Figure adapted from reference[88].

Methods

Structures were obtained by optimisation of geometry at the B3LYP/6-31G** level using Gaussian09,[40] and current-density maps were computed at the CHF/6-31G** level using the ipsocentric approach,[27,33] as implemented in the SYSMO and GAMESS-UK packages.[39,62] This combination of the levels of theory has been shown to produce well-converged, consistent results, avoiding the broken-symmetry geometries that sometimes occur in Hartree-Fock optimisations[63] and the exaggerated magnetic responses that can occur in DFT calculations of response properties.[168] Structures were initially constrained to maximal symmetry, and the status of each stationary point was confirmed by diagonalisation of the Hessian.

The ipsocentric method,[27,33,144] provides physically realistic, readily interpretable currents at modest computational cost, and uniquely allows the calculated current density to be partitioned into non-redundant molecular-orbital contributions, in either a canonical[35] (CMO) or localised[61] (LMO) basis set. Both choices will be of use here. Under the ipsocentric formulation, the π-current in a ring with fully delocalised π electrons will be dominated by frontier-orbital contributions,[27,61] as for example in planar/planarised annulenes, where the diatropic current of the aromatic systems arises from the HOMO pair,[27,88,169,170] and the paratropic current of the antiaromatic system arises from the HOMO orbital itself. More generally, diatropic contributions to current arise from excitations of translational symmetry, i.e. a change in nodal count of +1 between the occupied and unoccupied orbitals involved, and paratropic contributions arise from excitations of rotational symmetry, i.e., a change in nodal count of 0 between the occupied and unoccupied orbitals involved.[33] In such cases, CMOs give the most economical description. In contrast, when the π-electrons are localised, the magnetic response is most effectively constructed from individual 'island' circulations described by virtual excitations from individual LMOs,[61] which are usually obtained by the Pipek-Mezey localisation procedure, as it yields LMOs with preserved σ/π separation.[43]

The maps in the figures below are plotted to show first-order current density in the plotting plane 1 a_0 above the plane of the nuclei. Arrows and contours show the vector current density resolved into the plotting plane and the modulus of the current-density, respectively. Nuclei, at positions projected into the plotting plane, are represented by Dalton's element symbols (see Figure 2.1). j_{max}, the maximum magnitude of current density in the plotting plane,

provides a quantitative measure of the strength of the current in a given system. This value is usually referred to the benzene standard (0.078 a.u. at the present level of theory).

$(BN)_n$ Heterocycles

The total π-current density maps for the optimised planar (D_{nh}) constrained ring systems, $(BN)_nH_{2n}^{q}$, with n = 3 to 7 and q = 0, ±2 (for *even n*), and ±4 (for *odd n*) are shown in Figure 5.2. The neutral heterocycles all show localised magnetic response patterns under the D_{nh} constraint. Only D_{3h} borazine, $(BN)_3H_6$ (n = 3), and D_{4h} borazocine, $(BN)_4H_8$ (n = 4), occupy local minima on the potential energy surface for neutral systems. Other neutral and all charged systems investigated exhibit two or more vibrations of imaginary frequency in the maximum symmetry configurations of nuclei.

Adjustment of electron count to realise an "aromatic" number of π electrons in a charged monocycle requires the removal or addition of 2π electrons to the frontier π orbitals (for even n), and the removal or addition of 4π electrons (for odd n). With the exception of D_{3h} borazine tetracation and tetraanion ($(BN)_3H_6^{\pm4}$), all charged D_{nh} $(BN)_nH_{2n}^{q}$ heterocyclic systems with the specified aromatic π electron counts show unambiguous aromaticity, with clear delocalised diatropic currents of a strength immediately comparable to that of benzene. Of these systems, D_{4h} borazocine dianion ($(BN)_4H_8^{2-}$) is the only species that occupies a local minimum on the potential energy surface; the rest occupy stationary points of higher order. The charged D_{3h} borazines are exceptional in that calculations do not converge to ground states with the required numbers of π electrons. Changes in the electronic structure lead to highly contorted structures when relaxation from D_{nh} is allowed.

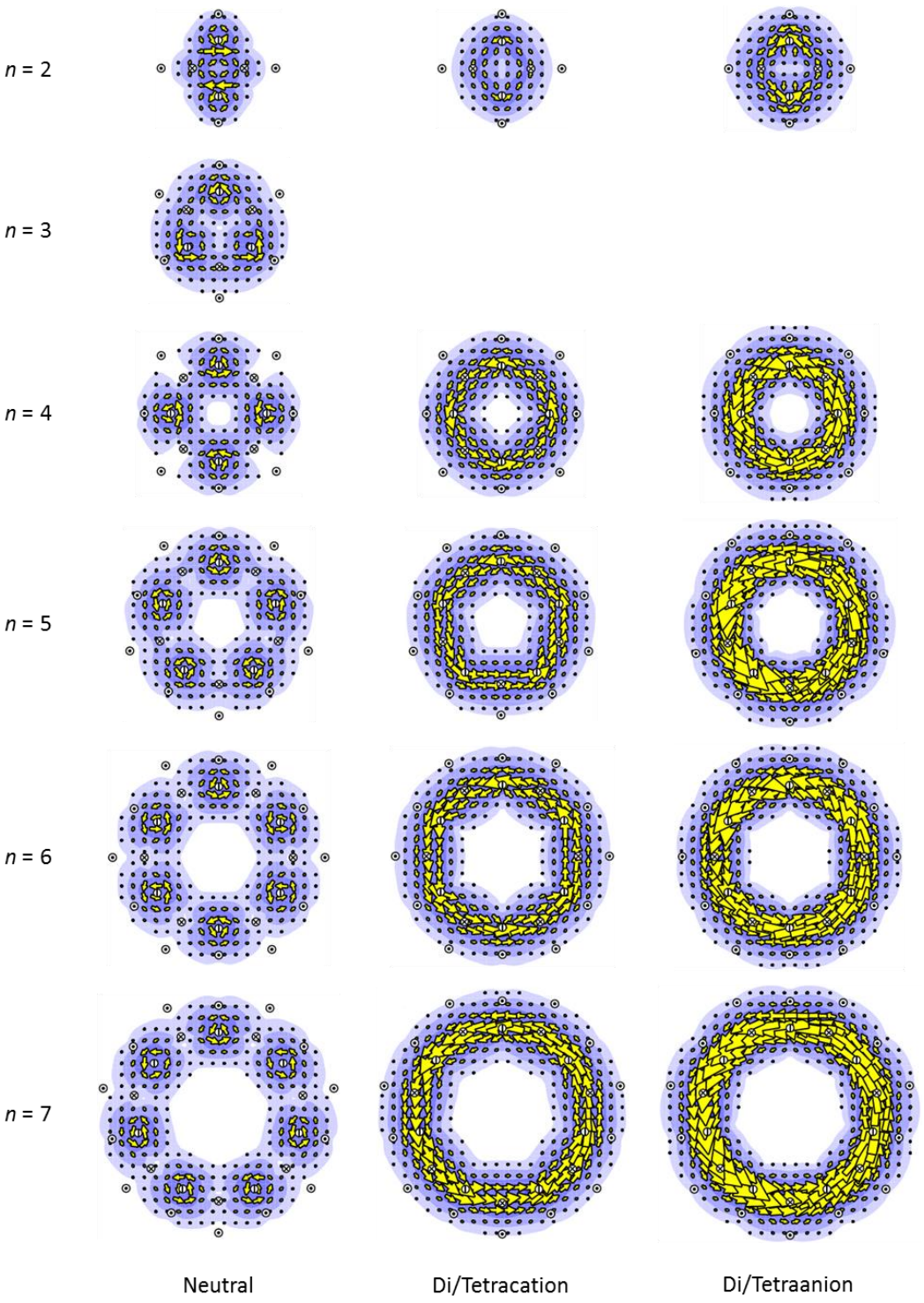

Figure 5.2. Total π current-density maps for D_{nh} planar-constrained $(BN)_nH_{2n}^{\ q}$ ring systems, with n = 2 to 7 and q = 0, ±2 (for *even* n), or ±4 (for *odd* n). Species with n = 3 and $q \neq 0$ do not converge as $(2n\text{-}q)\pi$ systems, as noted in the text. Plotting conventions are described in the text.

The general picture bears out the expectation from Hückel theory that it should be possible to aromatise BN-heterocycles by manipulating total charge and π occupancy. As an example of the success of this approach, addition of two electrons to neutral D_{4h} borazocine to produce D_{4h} borazocine dianion, both of which are predicted to be planar energetic minima at this level of theory, is now examined in more detail. This adjustment of charge causes no significant change to the topology or nodal character of the frontier π orbitals of borazocine (see Figure 5.3(a)) compared to those of neutral D_{4h} borazocine (Figure 5.4(a)), or even when compared to those of the neutral [8]annulene, D_{4h} cyclooctatetraene (Figure 5.4(b)). All retain the ordering by nodal count, with, crucially the π HOMO-π LUMO gap corresponding to π/4 rotation of nodal line between HOMO and LUMO.

The dominant contribution to π current in the dianion comes from diatropic transitions originating in the b_{1u}/b_{2u} $\Lambda = 2$ HOMO pair. This is consistent with the behaviour of 10π annulenes in general,[88,170] and can be roughly quantified by reference to the j_{max} values of different partitions of current. The total π current of D_{4h} borazocine (Figure 5.3(b)) has j_{max} = 0.103 a.u., 1.32 times the benzene standard calculated at the same level of theory. This matches well with the current originating from the HOMO pair, which has j_{max} = 0.110 a.u., 1.07 times the total π value. Spectral analysis,[41] which further breaks down CMO contributions to identify the effect of *individual* occupied-to-virtual transitions, shows that the dominant current arising from the HOMO pair can in turn be accounted for by the sum of four individual-node increasing (translational, see Figure 5.3(a)) excitations between the $\Lambda = 2$ HOMO/HOMO-1 and the $\Lambda = 3$ e_g LUMO pairs (Figure 5.3(c)). With j_{max} = 0.101 a.u., these frontier excitations qualitatively account for 98% of the total π response. Thus, D_{4h} borazocine dianion is a textbook example of the ipsocentric account of aromaticity of a monocycle. As the π currents can be understood in terms of ipsocentric node counting arguments, and as the system occupies a local minimum on the potential energy surface, D_{4h} borazocine dianion is the most plausible candidate for an inorganic aromat, in this case an "inorganic cyclooctatetraenide anion" rather than an "inorganic benzene".

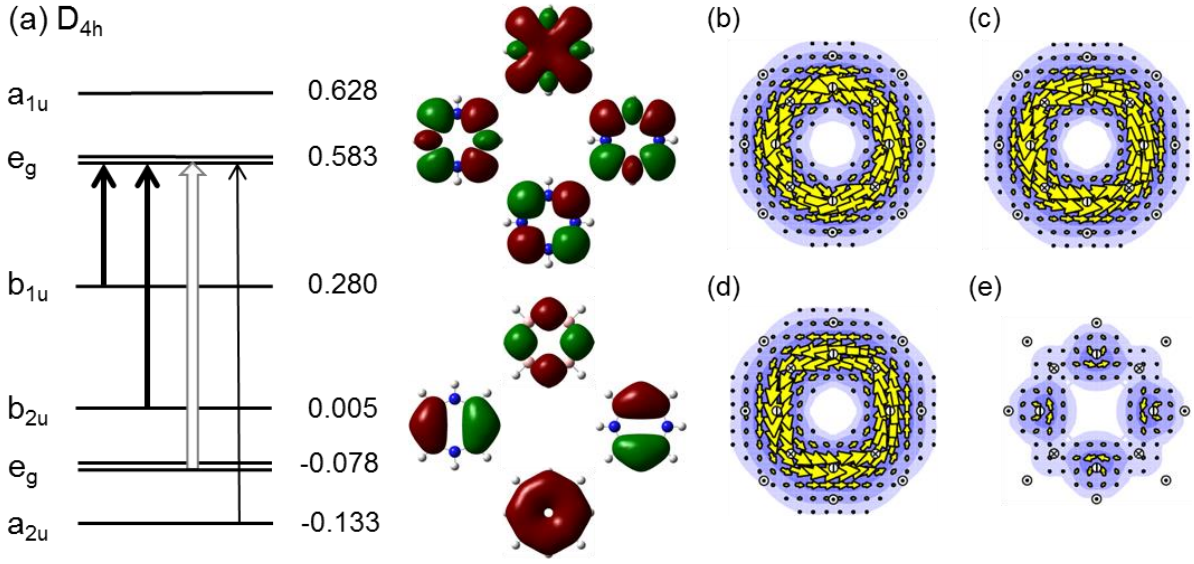

Figure 5.3. Energy level diagram and π-current analysis of D_{4h} borazocine dianion ($(BN)_4H_8^{2-}$) showing: (a) Schematic orbital-energy level diagram for D_{4h} borazocine dianion, highlighting the allowed frontier π-π* orbital excitations. Full and hollow arrows indicate respectively translationally and rotationally allowed excitations in this symmetry group. Dominant contributions to current, determined by examination of maps of individual occupied to virtual orbital transitions,[88] are shown in bold. CMO energies are given in E_h, orbital nodal patterns are shown on the right of the diagram, assignments to irreducible representations on the left. (b) The total 10π current. (c) The contributions to total π current arising from all possible transitions originating in the b_{1u}/b_{2u} Λ = 2 HOMO pair. (d) The combined contributions to total π current arising from the four possible transitions between the b_{1u}/b_{2u} Λ = 2 HOMO pair and the e_g Λ = 3 LUMO pair. (e) The current contributions of the π orbital complement of the HOMO pair, i.e., map (b) *minus* map (c). Plotting conventions are described in the text.

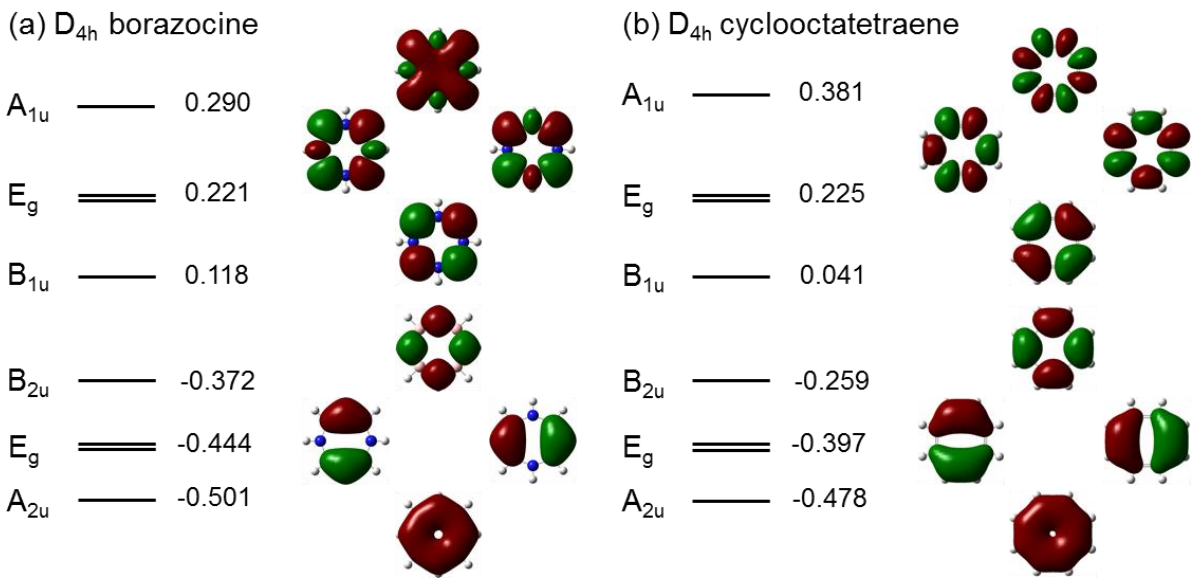

Figure 5.4. Energy-level diagrams of (a) D_{4h} borazocine ($(BN)_4H_8$) and (b) D_{4h} cyclooctatetraene (C_8H_8). Orbital energies are given in E_h, orbital nodal patterns are shown on the right of the diagram, and assignments to irreducible representations of the D_{4h} group on the left.

The schematic orbital-energy diagrams for BN-heterocycles (Figure 5.1) if taken at face value suggest an apparent symmetry between manipulation of frontier-orbital occupancy to facilitate diatropic and paratropic currents. However, *ab initio* CHF/6-31G**//B3LYP/6-31G** ipsocentric calculations of $4N$ π systems constructed as above do not produce delocalised magnetic response, and in particular do not show antiaromatic (paratropic) ring current. Ring-current calculations for these $4N$ π, nominally antiaromatic, systems are alarmingly dependent on method. For 12π C_{2v} $(BN)_5H_{10}^{2-}$, for example, the ipsocentric calculation for the B3LYP/6-31G** optimised geometry structure at the CHF/6-31G** level of theory results in a strong paratropic current (see Figure 5.5(a), j_{max} = 0.823 a.u.), as might have been expected from Figure 5.1. However, B3LYP/6-31G** treatment of the same optimised structure predicts a similarly strong (see Figure 5.5(b), j_{max} = 0.689 a.u.) but *diatropic* current.

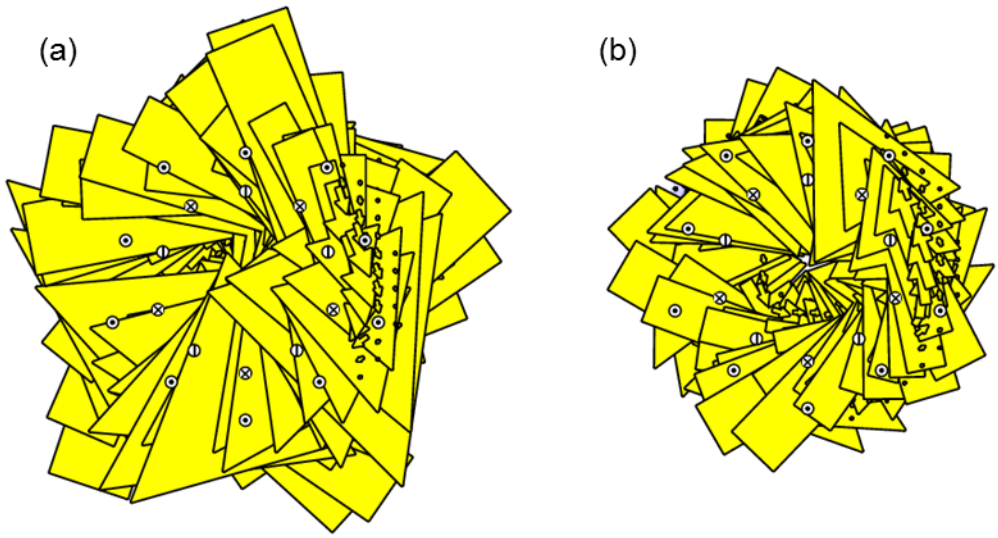

Figure 5.5. Total π current-density maps of BN-heterocycle C_{2v} $B_5N_5H_{10}^{2-}$ calculated at (a) the CHF/6-31G**//B3LYP/6-31G** and (b) B3LYP/6-31G**//B3LYP/6-31G** levels of theory. Plotting conventions are described in the text.

Comparison of nodal topologies and densities of the π orbitals employed in the CHF and B3LYP calculations show them to be essentially identical. Both the CHF and B3LYP frontier orbitals, the source of the overwhelmingly dominant contribution to current in this system, have the same symmetries of HOMO (b_1) and LUMO (a_2), and a nodal count of $\Lambda = 3$. Figure 5.6 shows the frontier orbitals of BN-heterocycle C_{2v} $B_5N_5H_{10}^{2-}$ calculated at the two levels of theory.

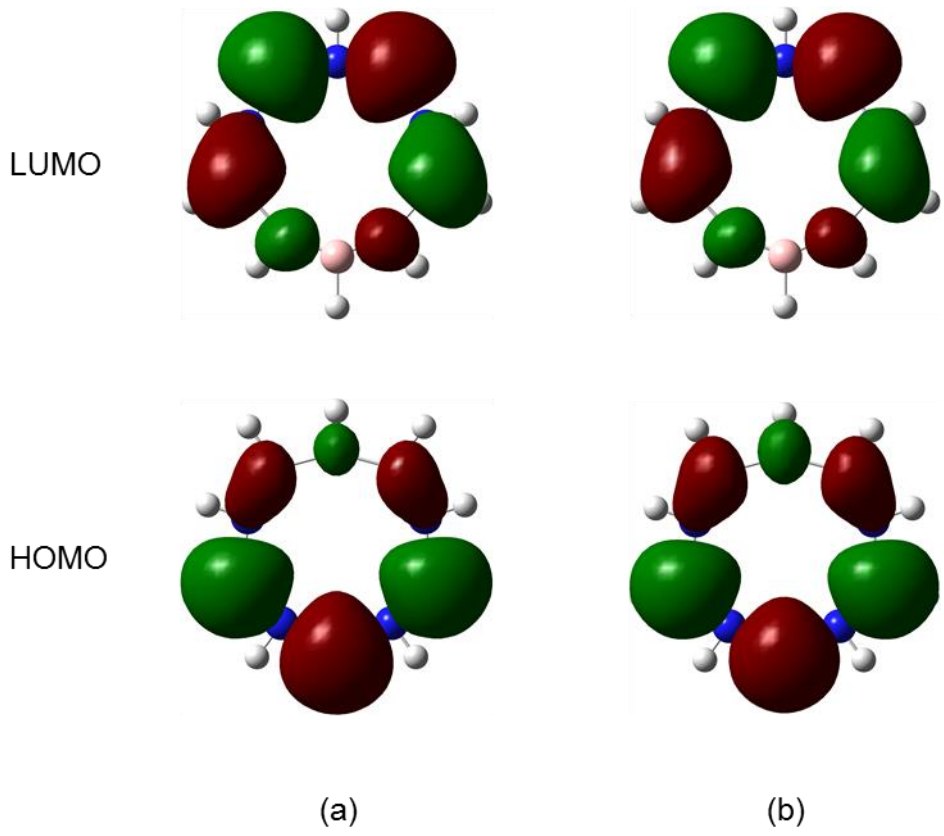

Figure 5.6. Frontier orbital topologies of BN-heterocycle C_{2v} $B_5N_5H_{10}^{2-}$ calculated at (a) the CHF/6-31G**//B3LYP/6-31G** and (b) B3LYP/6-31G**//B3LYP/6-31G** levels of theory.

Spectral decomposition of the current[41] provides a further layer of detail on the nature of the magnetic response of this system. As discussed in Chapter 1, ipsocentric calculation of ring current allows the diamagnetic and paramagnetic components to be calculated separately (see Equation 1.23). Figure 5.7 shows paratropic/diatropic split of the HOMO to LUMO transition for calculation at both levels of theory. In both cases the paratropic contribution is the source of ring current. Whilst the CHF/6-31G** displays the expected tropicity, the apparently diatropic B3LYP/6-31G** calculated current flows counter to the nature of the excitation. The reason for this anomaly is as yet unknown, and to date no other case of a rotational, and hence nominally paratropic, excitation that results in a diatropic current has ever been found.

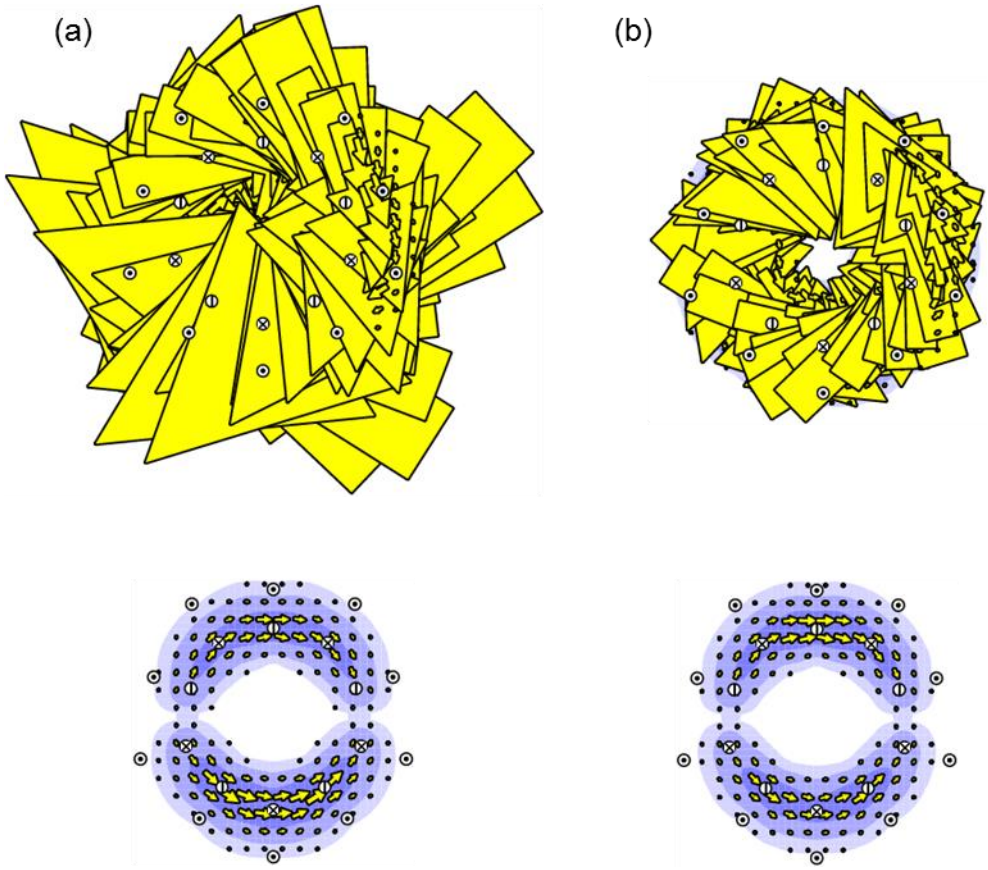

Figure 5.7. Paratropic (top) and diatropic (bottom) spectroscopic decomposition of ring current of the b_1 HOMO to a_2 LUMO transition of BN-heterocycle C_{2v} $B_5N_5H_{10}^{2-}$ calculated at (a) the CHF/6-31G**//B3LYP/6-31G** and (b) B3LYP/6-31G**//B3LYP/6-31G** levels of theory. Plotting conventions are described in the text.

This analysis is supported by NICS(0)[11] GIAO/B3LYP/6-31G** calculation at both the HF and B3LYP levels of theory, again with the same B3LYP/6-31G** optimised structure. Negative NICS(0) values are generally interpreted, for monocycles at least, as evidence of aromaticity, positive value as antiaromaticity and values close to zero as non-aromaticity. The NICS(0) at the B3LYP/6-31G** level of theory for D_{6h} benzene and D_{3h} borazine are -10 ppm and -3 ppm, and -12 ppm and -2 ppm at the HF/6-31G** level, respectively. The GIAO/HF/6-31G** level NICS(0) value calculated on the B3LYP/6-31G** optimised structure yielded a value of +115 ppm, consistent with the extremely large paratropic current found at this level. The

B3LYP calculation provided a NICS(0) value of -72 ppm, again correlating with the calculated diatropic ring current found at this level of theory. As a test of functional dependence of the result, further NICS(0) calculations were performed using the B3PW91 and MPW1PW91 functionals were undertaken, with results of -74 ppm and -78 ppm, respectively. As a final check of this unusual result, single-point UHF/6-31G** and UB3LYP/6-31G** calculations were also performed on the frozen B3LYP/6-31G** geometry. Both results possessed the same total energy as the restricted counterparts, and spin contamination was ruled out as possible source of the discrepancy, both levels reporting an expectation value of the total spin as $S^2 = 0$. It remains an open question as to whether it is possible to produce a true antiaromatic global current in an azabora-heterocycle.

Manipulation of Induced Aromaticity by Chemical Clamping

Previous models for 'writing' ring currents[166] through functionalisation (with H or F) of PAHs predicted systems that occupied local minima on the potential energy surface and, by implication, be stable when embedded in an infinite sheet. Viewing this idea in combination with recent experimental advances towards and theoretical considerations of benzenoid/borazinoid hybrids, and the principle of aromatising $(BN)_nH_{2n}$ hetero-annulenes discussed above, offers a possible strategy for designing inorganic aromatic systems.

Many attempts have been made to fix aromatic rings in chemical 'clamps' in order to manipulate their aromaticity. Of particular interest is the attempt of Siegel *et al.* who utilised bicyclic clamping groups to induce bond alternation the benzene moiety of tris(bicycle[2.1.1]hexeno)benzene in the hope of localising the π bonds into the 1,3,5-cyclohexatriene form,[45,171,172] which, if one were to view aromaticity as a geometric property, presumably would have the effect of switching off the ring current. Ipsocentric calculations later showed that the induced bond alternation did not to remove aromatic ring current in benzene, and merely diminished it by ~16%.[117] The preservation of the diatropic ring current was further confirmed by NICS values,[173] and the delocalised nature of the frontier orbitals was later confirmed by calculations using spin-coupled valence bond theory.[174]

The use of such bicyclic clamps offers a way to overcome the difficulties associated with the attempts of aromatising borazine, outlined above. Clamping the heterocycle and introducing a steric barrier to ring-buckling may allow borazine to support four fewer or four additional π electrons. As has been noted in a previous study of the effect of clamps on the magnetic response of benzene,[175] it is the *source* of bond alternation, and not the effect itself, that has the potential of altering ring current. Differentiating between *benign* clamps, i.e., those with an extended saturated σ-framework that induces strain in the unsaturated portion of a molecule, and *malign* clamps, i.e., those that induce geometric change by extension of the π framework, is key. The former will not significantly interfere with the basic frontier "π" orbital structure, and hence ring current effects, even though deviations from planarity may be introduced (previous studies have shown that current is remarkably resistant to geometric change[44,175,176]). The latter type of clamp will alter the nature of the electronic structure of the π space, and therefore change the nature of the current. The result of B3LYP/6-31G** optimisation of neutral, tetraanion and tetracation C_{3h}-clamped (see Figure 5.8(a)) tris(bicycle[2.1.1]hexeno)borazine is at most a limited success, in that the central ring remains planar in the tetracation.

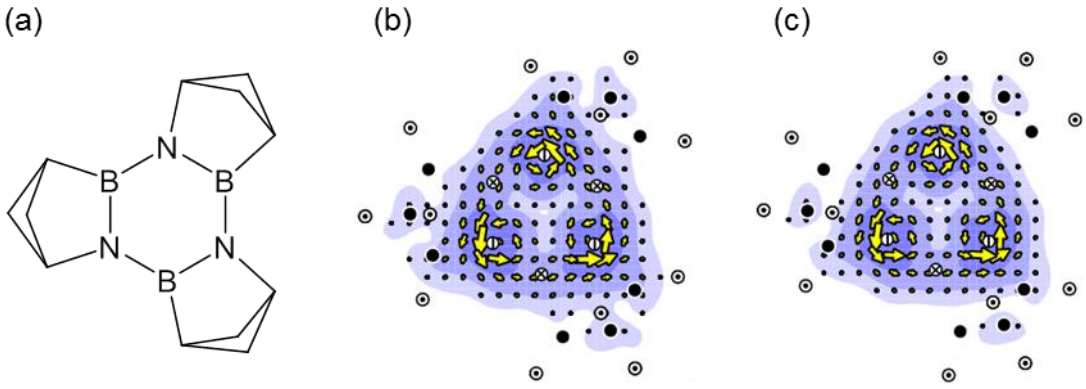

Figure 5.8. Schematic structure and π current-density maps of neutral and tetracationic C_{3h} clamped tris(bicycle[2.1.1]hexeno)borazine. Showing: (a) the schematic structure, (b) the π-current map of the neutral system, and (c) the π-current map of the tetracationic system. Plotting conventions are described in the text.

Neutral and tetracationic tris(bicycle[2.1.1]hexeno)borazine both occupy geometric, 'planar' minima on the potential energy surface, bond length alternation is present in both species, with neighbouring B and N atoms that share a clamp having a longer bond (1.47 Å for the neutral system and 1.48 Å for the tetracation) than those that do not (1.40 Å for the neutral system and 1.41 Å for the tetracation). The tetraanion on the other hand still does not support the addition of four electrons to its π system. The CHF/6-31G** π current-density maps for the neutral and tetracationic species are shown in Figure 5.8(b) and (c), respectively. In both cases the maps show a localised magnetic response, with three lone-pair 'islands' of current above each of the electronegative nitrogen centres, in the manner of D_{3h} borazine (see Figure 2.13). This behaviour in the positively charged species is due to the four electrons in the minimum energy system having been removed from the high energy σ-orbitals associated with the saturated clamps, not the π system. Given that the π electronic structure of the tetracation is unchanged from that of the neutral system, this result is to be expected.

A final recourse to hopefully delocalise the π response of the borazine moiety is exemplified by mimicking the finite graphene/graphane[166] and benzenoid/borazinoid[167] hybrids. In this approach, the σ framework is extended all the way around the central ring, leaving a ring of bare sp^2 centres in an otherwise fully saturated frame. The system we shall consider here is derived from D_{3h} 12b,12d,12f-triaza-12c,12e,12g-tribora-coronene ($C_{18}B_3N_3H_{12}$),[162,163,167] and is fully saturated by alternant antiperiplanar hydrogens along the 18-carbon perimeter see (Figure 5.9(a)).

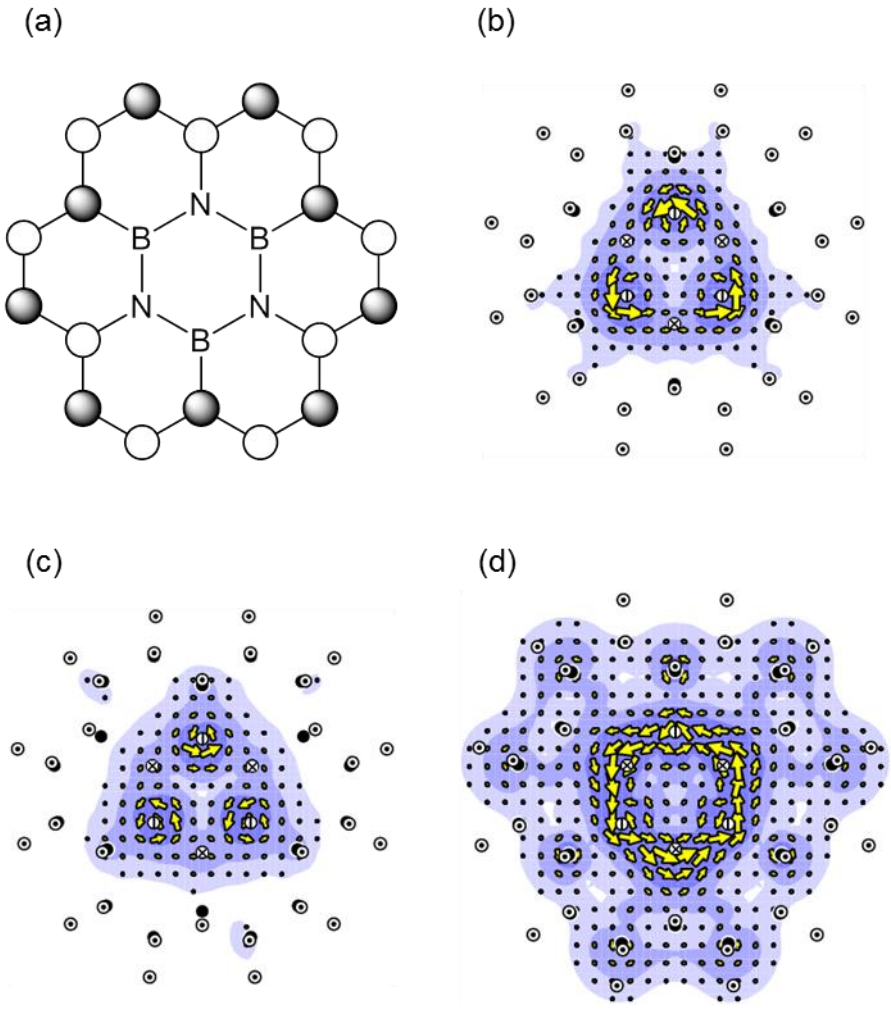

Figure 5.9. Schematic structure and π current-density maps, defined here by superposition of appropriate LMO contributions (see text), of neutral and tetracationic D_{3h} $C_{18}B_3N_3H_{30}$. Showing: (a) the schematic structure, where white spheres denote carbon centres with axial hydrogen atoms above the plane of the molecule, shaded spheres those with hydrogen atoms below; (b) the π-current map of the neutral system; (c) the π-current map of the tetraanionic system; (d) the π-current map of the tetracationic system. Plotting conventions are described in the text.

Optimisation of the neutral, tetracationic and tetraanionic perimeter saturated systems were carried out at the B3LYP/6-31G** level. In this instance, both the neutral system and the tetraanionic system were minimum energy structures. The tetracation possesses two imaginary frequencies (a pair at 280*i* cm^{-1}) corresponding to a ring-bending motion that may well be stabilised when the borazine fragment is embedded in a larger supporting framework

with a greater resistance to geometric change. All three structures displayed a near-planar borazine core, with a maximum deviation from planarity of 0.04 Å, 0.03 Å and 0.07 Å for the neutral, tetraanion and tetracation systems, respectively. Maps of CHF/6-31G** π current density, defined here by inspection of 'π-like' LMO contributions, rather than by symmetry, for the neutral, tetraanionic and tetracationic species are shown in Figure 5.9(b), (c), and (d), respectively.

If we are seeking aromatisation, the calculated current density maps are encouraging. In the neutral and tetraanion systems, the localised, three nitrogen lone-pair, signature of free borazine is observed, despite the reduced symmetry and a non-planar ring structure enforced by the saturated perimeter. This response, which is to be expected in the case of the neutral system, can be explained in the tetraanion by the additional electrons filling low-lying σ* orbitals belonging to the saturated framework. The current map plotted for the tetracation (Figure 5.9(d)) is more complex. The map shows a distinct, strong (j_{max} = 0.051 a.u., or 65% of the benzene standard), diatropic circulation around the borazine ring. However, this map results from the summed contributions of four LMO contributions: three consistent with π-like nitrogen lone pairs, and one that is of σ character. Summed together these maps show a clear delocalised aromatic current. Neither CMO nor LMO representations provide economical descriptions of the aromatic response of this system. There may perhaps be some molecular orbital basis that will simplify this picture, but this is not clear at present. All told, this system appears to be a good candidate for a true "inorganic benzene".

The first three results chapters in this thesis have focussed on how functionalisation, substitution, and now charge, can affect ring current aromaticity in a variety of carbon- or borazinoid-based ring systems. In the next chapter, pyrene will be used as a model system for establishing a unified view of these disparate changes, and to explore further the varied effects and causes of such modifications.

Chapter 6: Tuneable Aromaticity in Pyrene – a Case Study*

Introduction

As explored extensively in previous chapters, synthetic modifications of polycyclic aromatic hydrocarbons (PAHs) present chemists with the attractive prospect of creating aromatic systems by design. An extreme précis of the thesis so far could say that there exist three broad approaches that can be exploited to achieve bespoke aromatic response.

The first, explored extensively in Chapter 3, is chemical functionalisation of the system itself; treating PAHs as analogues of graphene (e.g., as nanographenes, or finite graphene flakes[140]) allows one to consider some of the advances made in the study of graphene in a new light. Work on chemically functionalised graphene[132,136] has led us to examine the possibilities offered by controlled regio-functionalisation as a method of 'writing' aromatic cycles onto a variety of PAHs.[166]

A second approach, encountered in Chapter 4, is to replace sp^2 carbons in the molecular framework with heteroatoms; swapping conducting (C_2) units for isoelectronic (BN) results in a 'benzenoid-borazinoid'[167] hybrid system, with mixed localised and aromatic magnetic response. In both approaches the induced π-currents in the oligocyclic carbon pathways were found to retain essentially the same strength, sense, and even orbital origin as those in the free hydrocarbons that they mimic.

The third approach, explored in Chapter 5, is to vary the number of electrons in the π system. Changing the occupation of the frontier orbitals alters the set of allowed virtual transitions between occupied and empty π orbitals.[33] In this way, charged species can display ring current responses different from, or even opposite to, those of their neutral

*Joseph Clarke is gratefully thanked for providing the results of Hückel-London calculations used in this chapter.

forms. An excellent example of this is D_{4h} planar-constrained transition state of cyclooctatetraene (COT, see Chapter 2, specifically Figures 2.10 to 2.12); in its neutral form, D_{4h} COT displays a strong antiaromatic current,[33] its dianion, on the other hand, has been found by calculation of NICS values to be aromatic.[177] This striking difference in current response arises from the origin of the dominant contribution to current in each system: D_{4h} COT has a Jahn-Teller split $\Lambda = 2$ HOMO-LUMO pair,[27] related by a node-preserving, paratropic transition, whilst the dianion possesses a $\Delta\Lambda = +1$ ($\Lambda = 2$ to $\Lambda = 3$) node increasing, diatropic transition.

In this chapter, pyrene, the smallest closed shell, neutral, peri-fused PAH, is used as a model system to explore some of the possibilities afforded by the three classes of modification outlined above. Specifically, the effect on ring current of modifying the central C_2 unit of pyrene by hydrogenation and/or substitution with BN, and the effects of charge on these systems and their closed-shell anionic forms will be probed in detail. In total, seven systems will be studied (see Figure 6.1): D_{2h} pyrene ($C_{16}H_{10}$), **1**; C_{2h} 'H_2-pyrene' ($C_{16}H_{12}$), **2**; C_{2v} 'BN-pyrene', 10a-aza-10b-borapyrene ($C_{14}BNH_{10}$), **3**; C_{2h} 'BNH_2-pyrene' ($C_{14}BNH_{12}$), **4**; D_{2h} pyrene dianion ($C_{16}H_{10}^{2-}$), **5**; C_{2h} 'H_2-pyrene' dianion ($C_{16}H_{12}^{2-}$), **6**; and C_{2h} 'BN-pyrene' dianion ($C_{14}BNH_{10}^{2-}$), **7**. Note that the systems presented here are not necessarily global optima on their respective potential energy surfaces; the aim of the present work is to explore the design principles themselves and use them to rationalise effects on π-current. These systems are offered as models for more complex cases, with the hope that the conclusions will serve as a scaffold for future work on 'designer ring-currents'.

The nature of magnetic response in pyrene is itself is of particular interest, separate from the general aim of exploring 'designer' aromaticity. Pyrene has long suffered under an apparent paradox: the mismatch between a 16 π (and hence, nominally *antiaromatic*) electron count, and extensive experimental[178] and theoretical[179–182] evidence in favour of an assignment to *aromaticity*. This disagreement arises from its assignment of aromaticity by the Platt perimeter model (and early simplified truncated-Hückel-type model),[183] which treats each centre that neighbours a perimeter atom as part of a separate cycle, with additional layers building in the same way for larger systems. The implications of this idea will be addressed in more detail when discussing the all sp^2 carbon species D_{2h} pyrene **1**, D_{2h} pyrene dianion **5**, and C_{2v} pyrene tetraanion **5a**.

The structure of the chapter is as follows. First, the total π current-density maps for systems **1** to **7** are displayed and their key features discussed. Each system is then be analysed in detail and the currents are rationalised using ipsocentric arguments. It will then be shown that it is possible to combine the results of the different modifications with an overarching model based on simple Hückel theory.

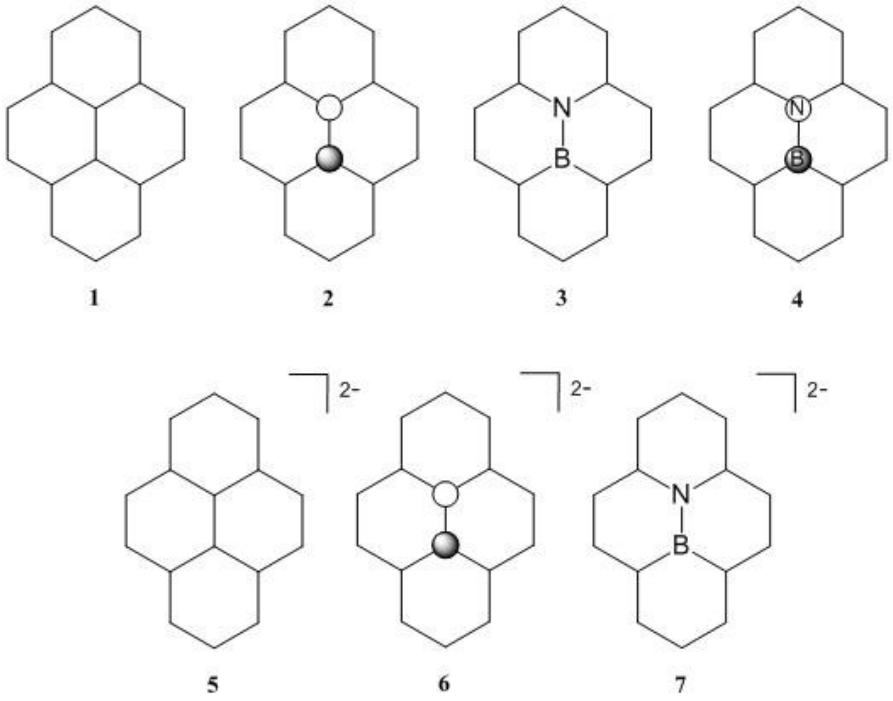

Figure 6.1. Schematic structures of the core systems discussed in this chapter: D_{2h} pyrene ($C_{16}H_{10}$), **1**; C_{2h} 'H_2-pyrene' ($C_{16}H_{12}$), **2**; C_{2v} 'BN-pyrene', 10a-aza-10b-borapyrene ($C_{14}BNH_{10}$), **3**; C_{2h} 'BNH_2-pyrene' ($C_{14}BNH_{12}$), **4**; D_{2h} pyrene dianion ($C_{16}H_{10}^{2-}$), **5**; C_{2h} 'H_2-pyrene' dianion ($C_{16}H_{12}^{2-}$), **6**; and C_{2h} 'BN-pyrene' dianion ($C_{14}BNH_{10}^{2-}$), **7**. Shaded spheres represent hydrogen centres in axial CH bonds above the median plane, white spheres those below.

Methods

The geometries of all structures were optimised at the B3LYP/6-31G** level using Gaussian09.[40] Hessian calculations were used to identify all structures in this chapter as local minima. Subsequently, current-density maps were calculated at the CHF/6-31G** level of theory using the ipsocentric[27,33] approach as implemented in the SYSMO[39] and GAMESS-UK[62] suites of programs. As noted in previous chapters, a unique feature of the ipsocentric approach is the possibility of analysing the induced current in terms of either *canonical* or *localised* molecular orbitals (CMOs and LMOs), obtained here by the localisation procedure of Pipek and Mezey,[43] which preserves σ/π separation. Once again, the application of both of these formulations proves to be essential in the understanding of the current maps.

The maps themselves are presented with the following plotting conventions: arrows show the current density resolved into the plotting plane, which as standard is $1a_0$ above the mean molecular plane; contours show the modulus of the full current-density vector Nuclear positions, resolved into the plotting plane, are represented by the elemental symbols shown in Figure 2.1.

Results and Discussion

Figure 6.2 shows the total π current-density map for **1** – **7**. Immediately, some patterns are evident; the neutral species **1** – **4** all possess coherent diatropic 14π perimeter circulations in the manner of the analogous C_{2h}-constrained [14]annulene, but with different internal structures depending on the identity of the two central pairs of atoms determining the nature of the perturbation arising from the core.

D_{2h} pyrene, **1**, has an inner C_2 'hub', and has been described as having, in addition to its outer current, Clar-like circulations (i.e., a local, C_6 aromatic circulation) in the two apical hexagons belonging to the biphenyl-like subunit.[179] Functionalisation of the two internal carbon centres with antiperiplanar hydrogens yields C_{2h} 'H_2-pyrene', **2**. Here, a 2π core has

been removed from 16π pyrene, resulting in a clean, coherent 14π aromatic current. Exchanging the central C_2 for BN gives a different response in C_{2v} 'BN-pyrene', **3**. The circulation above the electropositive boron atom in the apical rings is diminished, whilst that above the electronegative nitrogen centre appears stronger. C_{2h} 'BNH_2-pyrene', **4**, has a magnetic response almost identical to that of **2**, with a strong aromatic perimeter current avoiding the functionalised BN unit, as would be expected for a system with a geometrically and electronically similar 14π sp^2 hybridised circuit.

The charged systems **5** – **7** display different behaviour. All three are antiaromatic and have to a greater or lesser extent a paratropic perimeter, but the relationships between their ring current patterns are at first sight less clear. The most striking feature of D_{2h} pyrene dianion, **5**, is the strong 'anti-Clar' circulations on the apical rings, which accompany the weaker perimeter current. The current strengths are inverted (i.e., strong, local circulations on the outer hexagons and a weak perimeter vs. weak local circulations and a strong perimeter), and flows in the opposite direction to that of pyrene, **1**. C_{2h} 'H_2'-pyrene dianion, **6**, has a simpler pattern. As expected, the addition of 2π electrons has reversed the direction of current, the only subtlety being two small portions of paratropic flow on the opposite faces to the out-of-plane CH groups (one visible above the molecular plane and the other below). The cleanest picture comes from C_{2h} 'BN-pyrene' dianion, **7**. Here, as with **6**, a strong antiaromatic exterior current is in evidence, but as with **3**, the local effects on the interior BN unit are unbalanced. In this case the 'anti-Clar' circulation is localised entirely on the nitrogen containing outer ring, and is correspondingly stronger than those in **5**. The current response of each of the individual systems will now be examined in detail in terms of their orbital contributions.

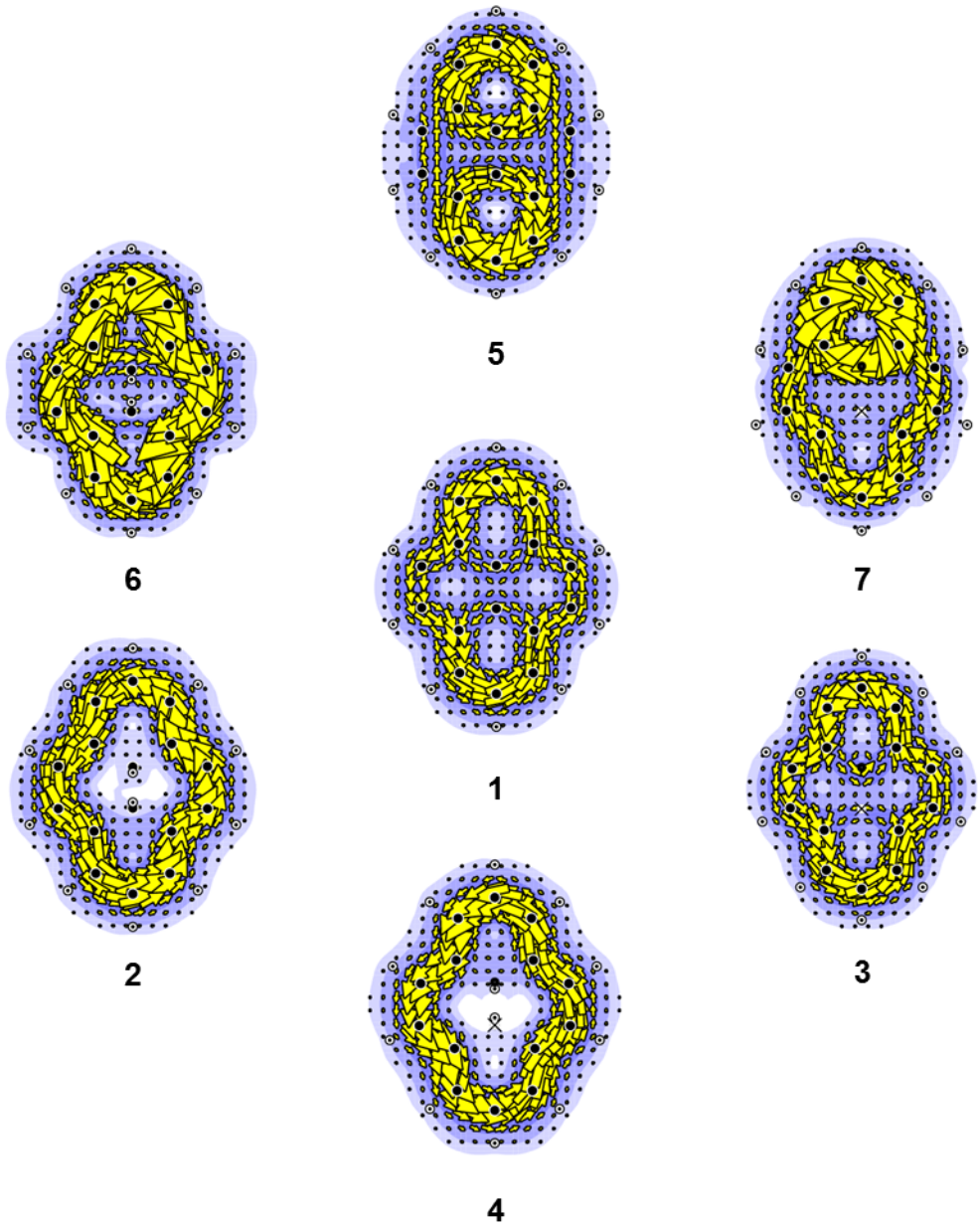

Figure 6.2. Total π current-density maps for the core systems discussed in this chapter: D_{2h} pyrene ($C_{16}H_{10}$), **1**; C_{2h} 'H_2-pyrene' ($C_{16}H_{12}$), **2**; C_{2v} 'BN-pyrene', 10a-aza-10b-borapyrene ($C_{14}BNH_{10}$), **3**; C_{2h} 'BNH_2-pyrene' ($C_{14}BNH_{12}$), **4**; D_{2h} pyrene dianion ($C_{16}H_{10}^{2-}$), **5**; C_{2h} 'H_2-pyrene' dianion ($C_{16}H_{12}^{2-}$), **6**; and C_{2h} 'BN-pyrene' dianion ($C_{14}BNH_{10}^{2-}$), **7**. Maps are plotted at a height of 1 a_0 above the mean molecular plane. Plotting conventions are described in the text.

1. D_{2h} Pyrene ($C_{16}H_{10}$)

The strong diatropic current around the 14π perimeter of pyrene is diminished on the external C_2 units of the naphthalene-like core and correspondingly stronger on the outer. j_{max}, the maximum value of the modulus of current density over the plotting plane, is used to give a quantitative measure of ring current strength. Pyrene has j_{max} = 0.106 a.u., 1.4 times the benzene standard. Spectral analysis,[41] which further breaks down CMO contributions to identify the effect of *individual* occupied-to-virtual transitions, shows that the dominant outer current can be accounted for by analogy with C_{2h}-constrained [14]annulene: node increasing (translational) excitations between the Λ = 3 HOMO/HOMO-1 and the Λ = 4 LUMO/LUMO+1 pairs (see Figure 6.3(a) and (b)). Contributions from the HOMO-pair to LUMO-pair reproduce the majority of the induced current, with the additional excitations adding the missing bifurcation of current across the hub of the molecule. A schematic breakdown of CMO contributions to π-current is given in Figure 6.3(c).

Two rationales are available to explain the imbalance of current in the perimeters of the apical and central rings. The first is the presence of Clar-like circulations on the outer hexagons of the system, as offered by Steiner and co-workers.[179] This viewpoint is the more intuitive, and is consistent with the simple Randić model,[145,182] in which the contributions of all possible conjugated circuits within a molecule are combined to yield bond currents. This method reports a stronger diatropic current in the two apical rings as they are active in a greater number of diatropic conjugated circuits of length 4n + 2 (see Figure 6.3(d)).

The second appears from a spectral decomposition of the CMO contributions;[41] the two rotationally allowed transitions, as documented in Figure 6.3(c), contribute *paratropic* components to the total π current. Localised on the central rings (see Figure 6.3(e)), they have the effect of partial cancellation of the diatropic perimeter current. As the choice of CMOs is, in a sense, arbitrary, as any transformation applied to all occupied π orbitals must result in the same total π current, these two justifications or accounts are not physically distinguishable, and must be judged by their applicability or otherwise as explanatory models.

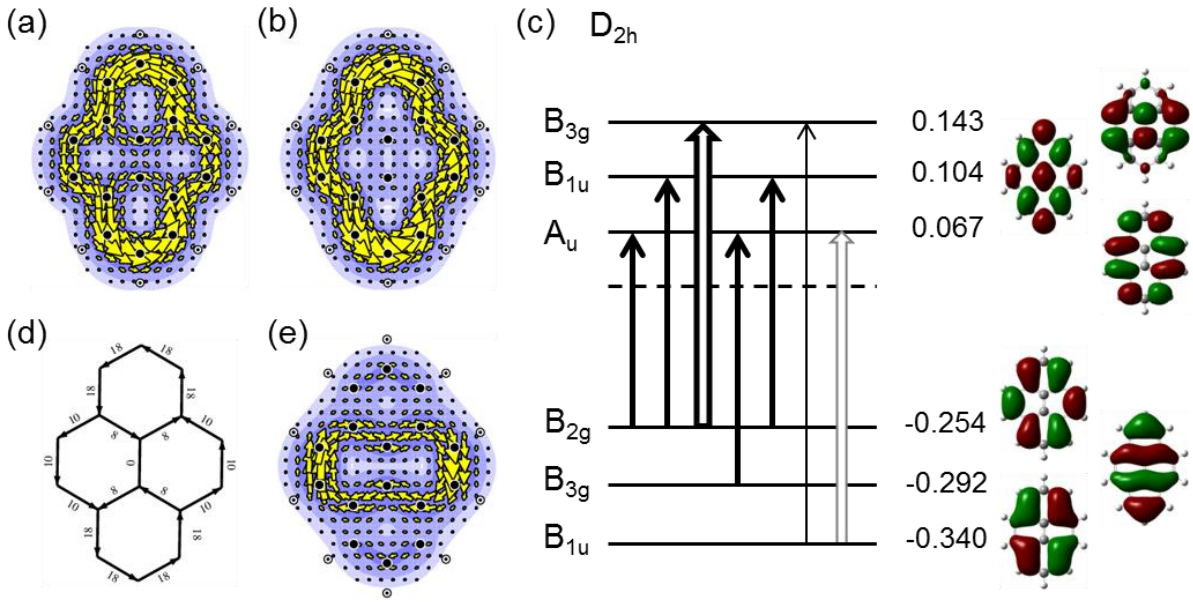

Figure 6.3. π-current analysis and energy level diagram of D_{2h} pyrene **1**, showing: (a) The total 16π current. (b) The combined contributions to total π current arising from the four possible transitions between the b_{2g}/b_{3g} Λ = 3 HOMO pair and the a_u/b_{1u} Λ = 4 LUMO pair. (c) Schematic orbital-energy level diagram for D_{2h} pyrene, **1**, showing the allowed frontier π-π* orbital excitations. Full and hollow arrows indicate respectively translationally and rotationally allowed excitations at this symmetry. Dominant contributions to current, determined by examination of maps of individual occupied to virtual orbital transitions, are shown in bold. CMO energies in E_h and orbital nodal patterns are shown on the right of the diagram, assignments to irreducible representations on the left. (d) The Randić model current map, as described in the text. (e) The combined contributions to π current arising from the two rotationally allowed excitations. Plotting conventions are described in the text.

This overall picture is broadly corroborated by earlier studies employing an alternative theoretical probe of aromaticity, the computed nucleus independent chemical shift[11] (NICS) at the geometric centre of a given ring. Large negative NICS values are taken to indicate diatropicity in possible aromatic systems. IGLO calculations on pyrene at the RHF/6-31G* geometry with the IGLO-III basis give NICS values of -12.6 ppm for the outer, exposed rings, and -3.5 ppm for the more embedded central two.[180] As NICS values are heavily influenced by neighbouring currents in their local environment, it is possible to interpret these values in the light of the calculated current map as indicating that there is a global perimeter circulation and two localised currents on the apical rings, and indeed, without the maps this assignment of current becomes a great deal more difficult. The true strength of the

global current, as indicated by the small NICS values of the central rings, is probably masked by the surrounding apical cycles.

2. C_{2h} 'H_2'-pyrene ($C_{16}H_{12}$)

Although this system would readily split into pyrene and H_2, the benign functional groups here are known to have the same effect on ring current as other groups such as fluorine (as shown extensively in Chapter 3).[166] This fact allows us to use this hydrogenated system as a proxy for synthetically achievable analogues such as the inner C_2Me_2 variant.[184] C_{2h} **2** has a near-planar carbon perimeter (maximum deviation from the molecular plane ±0.06 Å) with almost equal carbon-carbon bond lengths (maximum deviation 0.01 Å). The delocalised sp^2 carbon monocycle supports a strong diatropic current (with j_{max} = 0.136 a.u., 1.7 times the benzene standard, see Figure 6.4(a)) that is best understood again with direct analogy to C_{2h}-constrained [14]annulene, with the total π current arising almost entirely from transitions of translational symmetry from the Λ = 3 HOMO pair (see Figure 6.4(b) and (c)).

As with pyrene, **1**, **2** has two rotationally allowed virtual excitations on the frontier (π HOMO to π LUMO+2 and π HOMO-2 to π LUMO in both systems, see Figure 6.4(c)). However, in **2**, the functionalisation has altered the topology of the CMOs, reducing their overlap in the centre of the molecule to a point where, although the average energy difference between these occupied and unoccupied orbitals is similar ($\Delta E_{occ\text{-}unocc}$ = 0.402 E_h in **1**, c.f. 0.412 E_h in **2**), the transitions have a negligible contribution to current.

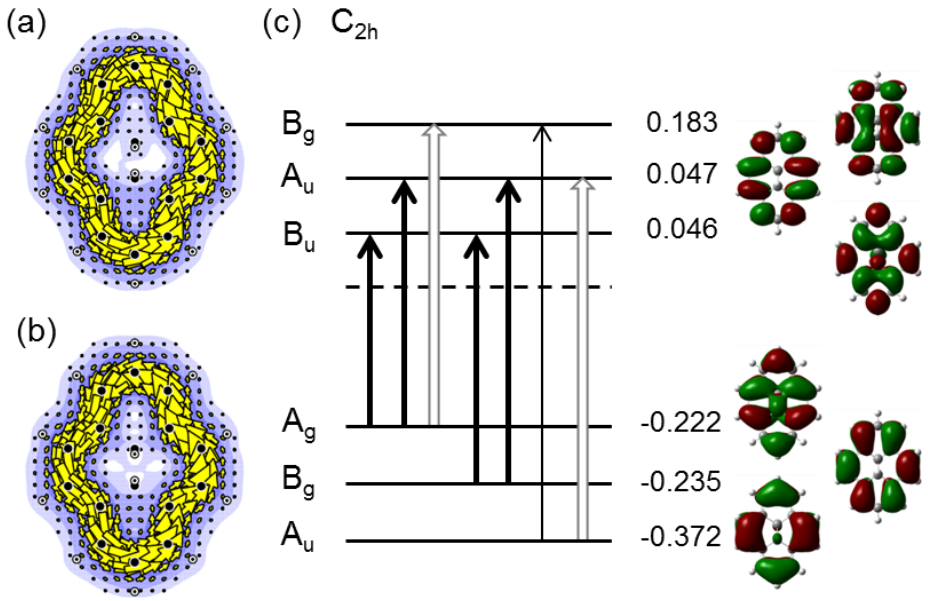

Figure 6.4. π-current analysis and energy level diagram of C_{2h} **2**, showing: (a) The total 14π perimeter current constructed by summation of the contributions from the seven π-like LMOs of the perimeter. (b) The contribution to total π current arising from the b_g/a_g $\Lambda = 3$ HOMO pair. (c) Schematic frontier orbital-energy level diagram showing selected allowed CMO contributions to current in **2**. Full and hollow arrows indicate respectively translationally and rotationally allowed excitations at this symmetry. Dominant contributions to current, determined by examination of maps of individual occupied to virtual orbital transitions, are shown in bold. Orbital energies are given in E_h. Plotting conventions are described in the text.

3. C_{2v} 'BN'-pyrene, 10a-aza-10b-borapyrene ($C_{14}BNH_{10}$)

Apart from the early work of Dewar, BN-doped PAHs were largely ignored until recent developments in the tuning of photophysical and electronic properties of PAHs caused them once again to become key synthetic targets.[139] This focus has been driven by, amongst other things, their potential to act as organic semiconductors[135,185] and components in hydrogen storage devices.[130,186] 10a-aza-10b-borapyrene, **3**, is of particular importance[46] as it serves as an isoelectronic analogue apt for comparison with pyrene.

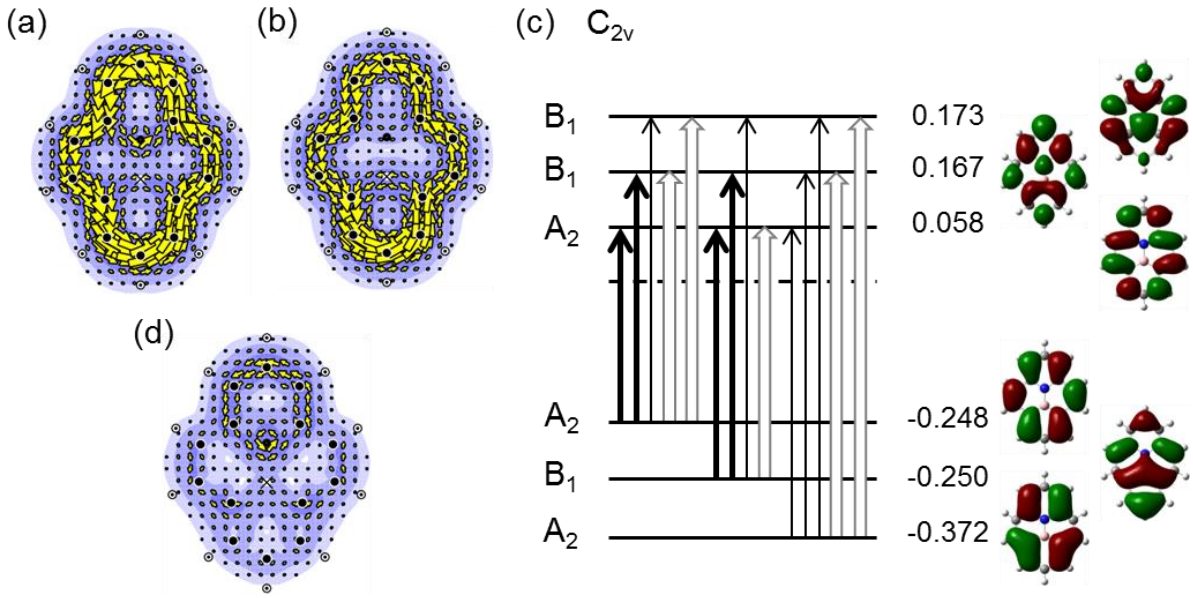

Figure 6.5. π-current analysis and energy level diagram of C_{2v} **3**, showing: (a) The total 16π perimeter current. (b) The contribution to total π current arising from the a_2/b_1 Λ = 3 HOMO pair. (c) Schematic frontier orbital-energy level diagram showing selected allowed CMO contributions to current in **3**. Full and hollow arrows indicate respectively translationally and rotationally allowed excitations at this symmetry. Dominant contributions to current, determined by examination of maps of individual occupied to virtual orbital transitions, are shown in bold. Orbital energies are given in E_h. (d) The contribution to total π current from the complement of the HOMO pair. Plotting conventions are described in the text.

On initial inspection, the total π ring-current response of planar C_{2v} **3** looks similar to that of **1**, presenting a strong perimeter diatropic current with weak bifurcation through the molecular interior, shown in Figure 6.5(a). The aromatic nature of the perimeter has the same orbital explanation as for the previous systems: a node-increasing transition from the a_2/b_1 Λ = 3 HOMO pair (see Figure 6.5(b) and (c)). Owing to the difference in the electronegativities of boron and nitrogen, the pattern of current in the centre of the molecule is different; here, instead of a uniformly stronger current in both halves of the apical rings of **1**, the response is localised on the outer C_5N ring. A breakdown of the LMO contributions shows that the two electrons donated to the π-system by the BN group are localised on the N atom, the flow lines suggest that they are in fact taking part in a Clar-like circulation on this outer ring. This behaviour is confirmed by inspection of the π-current

arising from the complement to the CMO π-HOMO pair (i.e., contributions from all π orbitals but the HOMO pair, Figure 6.5(d)).

To explore further the effect of substitution of C_2 for BN in pyrene, as a model for varying electronegativity in general, it is instructive to treat the two extreme systems, **1** and **3** as endpoints on a continuum where fractional nuclear charges are moved from one central carbon to the other. Here this has the effect of transforming pyrene into its isoelectronic analogue, 10a-aza-10b-borapyrene. This point charge model, previously used to investigate the aromatic/nonaromatic threshold between benzene and borazine,[119] and to understand substituent effect on ring currents in xanthine derivatives,[111] shows that as nuclear charge *Z* is transferred in increments of 0.1 of a proton from one interior carbon centre to its neighbour, a smooth change in ring current response occurs. Figure 6.6 displays the total π-current maps of pyrene, the midpoint of the transformation (where the two interior atoms have *Z* = 6.5 and 5.5) and the endpoint, 10a-aza-10b-borapyrene. Inspection of the maps shows that as the difference in electronegativities between the two central atoms becomes more pronounced, current flowing over the more electronegative centre becomes stronger, whilst that over the more electropositive centre is diminished. This observation is fully consistent with that of the original threshold of aromaticity study, where it was found that the transformation from aromatic benzene to nonaromatic borazine by stepwise variation of nuclear charge was essentially linear. Here, the Clar-like circulation on the electropositive C_5X ring is weakened as the charge is redistributed, but not fully quenched.

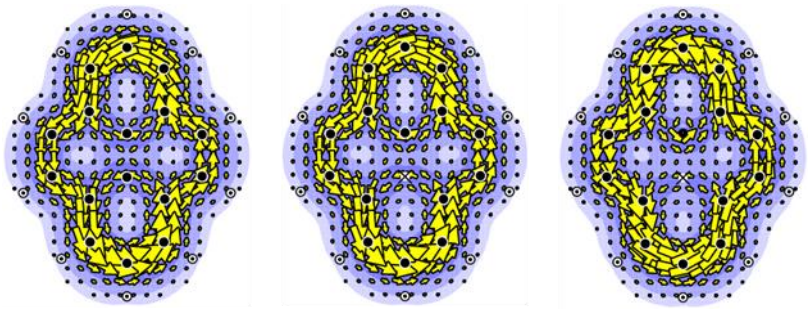

Figure 6.6. Total π-current maps of D_{2h} pyrene **1** (left), the intermediate C_{2v} isoelectronic system with fractional nuclear charge (*Z* = 6.5 and 5.5) on the central atoms (middle) and C_{2v} 10a-aza-10b-borapyrene **3** (middle). Plotting conventions are described in the text.

4. C_{2h} 'BNH_2'-pyrene ($C_{14}BNH_{12}$)

The total π current in C_{2h} **4** (Figure 6.7) appears almost indistinguishable from that of **2**. This should be expected as their delocalised sp^2 carbon cycles are structurally very similar; the perimeter of **4** has near-uniform carbon-carbon bond lengths (maximum deviation 0.01 Å) and is almost planar (deviation ±0.07 Å). Owing to these geometric similarities, and the similarity of π HOMO-LUMO gap (ΔE_{HL} = 0.272 E_h in **4**, c.f. 0.268 E_h in **2**), the diatropic current is almost identical in strength to that of **2**, j_{max} = 0.141 a.u. (c.f. 0.136 a.u.). Again, spectral decomposition shows that the total π current is dominated by node-increasing virtual excitations from the Λ = 3 HOMO to the Λ = 4 LUMO pairs.

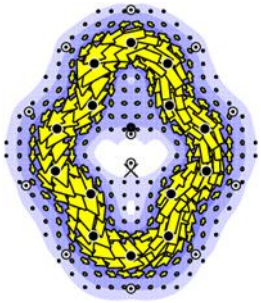

Figure 6.7. The total 14π perimeter current constructed by summation of the contributions from the seven π-like LMOs of the perimeter of **4**. Plotting conventions are described in the text.

5. D_{2h} pyrene dianion ($C_{16}H_{10}^{2-}$)

The addition of two π electrons to pyrene, **1**, by, for example, reduction with alkali metals,[178,187] results in D_{2h} pyrene dianion, **5**, with a total π electron count is 18, and hence nominally a $4n + 2$ Hückel count. This molecule has been described as antiaromatic. The ^{1}H NMR spectrum shows high-field resonances,[188] whilst calculations[189] and the temperature dependence of the chemical shifts[190] point to a small HOMO-LUMO gap. All these facts are consistent with the presence of a paratropic ring current.

Figure 6.8(a) shows the total 18π current of **5**, j_{max} = 0.252 a.u. The most significant contribution to current is the excitation from the a_u HOMO, with angular perimeter nodal count Λ = 4, to the B_{1u} Λ = 4 LUMO+1, which accounts not only for the perimeter current, but also the stronger 'anti-Clar' circulations on the two apical C_6 cycles, which locally possess an angular nodal count of Λ = 4 in both orbitals (see Figure 6.8(c)). A secondary, diatropic perimeter current arising from the HOMO complement is also of note as it weakens the paratropic perimeter, resulting in the overall dominance of the antiaromatic outer rings (as shown in Figure 6.8(b)).

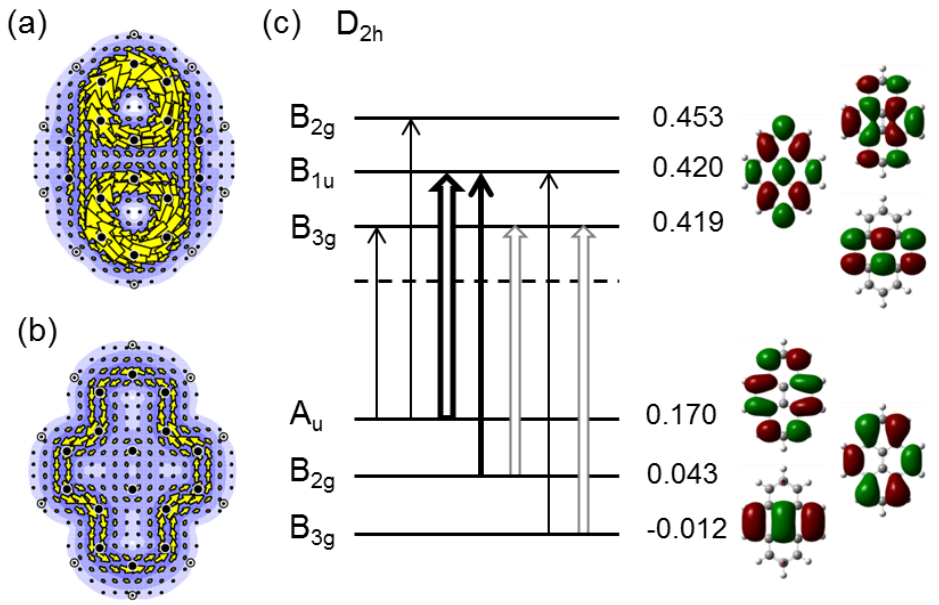

Figure 6.8. π-current analysis and energy level diagram of D_{2h} **5**, showing: (a) The total 18π current. (b) The contribution to total π current from the complement of the HOMO. (c) Schematic frontier orbital-energy level diagram showing selected allowed CMO contributions to current in **5**. Full and hollow arrows indicate respectively translationally and rotationally allowed excitations at this symmetry. Dominant contributions to current, determined by examination of maps of individual occupied to virtual orbital transitions, are shown in bold. Orbital energies are given in E_h. Plotting conventions are described in the text.

Addition of two π electrons to D_{2h} pyrene dianion, **5**, results in C_{2v} pyrene tetraanion, **5a**. The breaking of the maximum D_{2h} symmetry is associated with minor deviations from planarity, largely involving the hydrogen atoms. The total π electron count is 20, a 4*n* Hückel count. The experimental preparation of **5a**, again by reduction of pyrene with alkali metals, has yielded evidence for reduced symmetry[187] and also for aromaticity, the latter in the form of diatropic shifts in the ^{1}H NMR spectrum.[187] This evidence, by consideration of the arguments encountered so far, should not be surprising. The node-counting arguments invoked throughout this work so far show that, for simple systems at least, adding a pair of electrons to a π LUMO causes the excitation across the frontier to alternate between translational and rotational character. By this rationale, with **5** possessing a paratropic ring current, the tetraanion **5a** should indeed have a diatropic, aromatic, magnetic response. Figure 6.9(a) shows the total π current response of **5a** (again defined by summation of π-like LMOs).

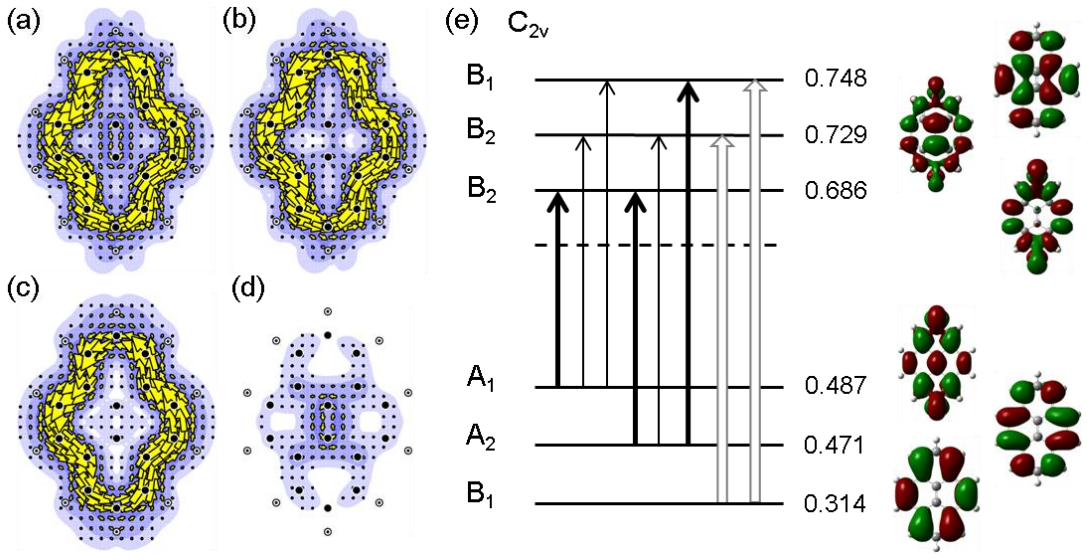

Figure 6.9. π current analysis and energy level diagram of C_{2v} **5a**, showing: (a) The total 20π current. (b) The current arising from the transition between the a_1 HOMO and a_2 HOMO–1 and the b_2 LUMO and b_1 LUMO+2 pairs. (c) The 19 LMO perimeter current. (d) The single LMO corresponding to the central CC circulation. (e) Schematic frontier orbital-energy level diagram showing selected allowed CMO contributions to current in **5a**. Full and hollow arrows indicate respectively translationally and rotationally allowed excitations at this symmetry. Dominant contributions to current, determined by examination of maps of individual occupied to virtual orbital transitions, are shown in bold. Orbital energies are given in E_h. Plotting conventions are described in the text.

The analysis of the π current of **5a** shown in Figure 6.9 is enlightening. The total π current (Figure 6.9(a), j_{max} = 0.148 a.u.) shows, as expected, a strong diatropic perimeter circulation. As is typical in these cases, the entire dominant response comes from the contributions of the transitions between the HOMO and HOMO–1, and LUMO and LUMO+2 pairs (Figure 6.9(b), j_{max} = 0.122 a.u.). LMO analysis adds to this picture, and solves the minor concern of the apparent conflict between a 4*n* π electron count and a global diatropic current. The current-density maps reported in Figures 6.9(c) and (d) display the contributions leading to the 19 LMO perimeter current (j_{max} = 0.155 a.u.) and the single LMO that accounts for the interior CC double bond circulation (j_{max} = 0.030 a.u.), respectively. As the central two electron circulation is a fully localised response, its origin is not clearly attributable from the orbitals present in the frontier (see Figure 6.9(e)). Instead, as with the localised response encountered with borazine (Chapter 2, Figure 2.14), the canonical basis is inefficient in describing this type of current response.

6. C_{2h} 'H_2'-pyrene dianion ($C_{16}H_{12}^{2-}$)

Again, considering the C_{2h} the delocalised sp^2 carbon monocycle with respect to its annulene analogue allows us to understand the total 16π current response of **6** (Figure 6.10(a)). The total π current, constructed by summation of the contributions from the eight π-like LMOs localised mainly on the perimeter has j_{max} = 0.232 a.u., 3.0 times the benzene standard, and 2.2 times the total 14π current in pyrene. The dianion, when compared with **2**, has an extra occupied π orbital, which results in a split Λ = 5 HOMO/LUMO pair across the frontier, as shown in Figure 6.10(b). The node-preserving excitation between these orbitals gives rise to strong, paratropic perimeter current (see Figure 6.10(c)).

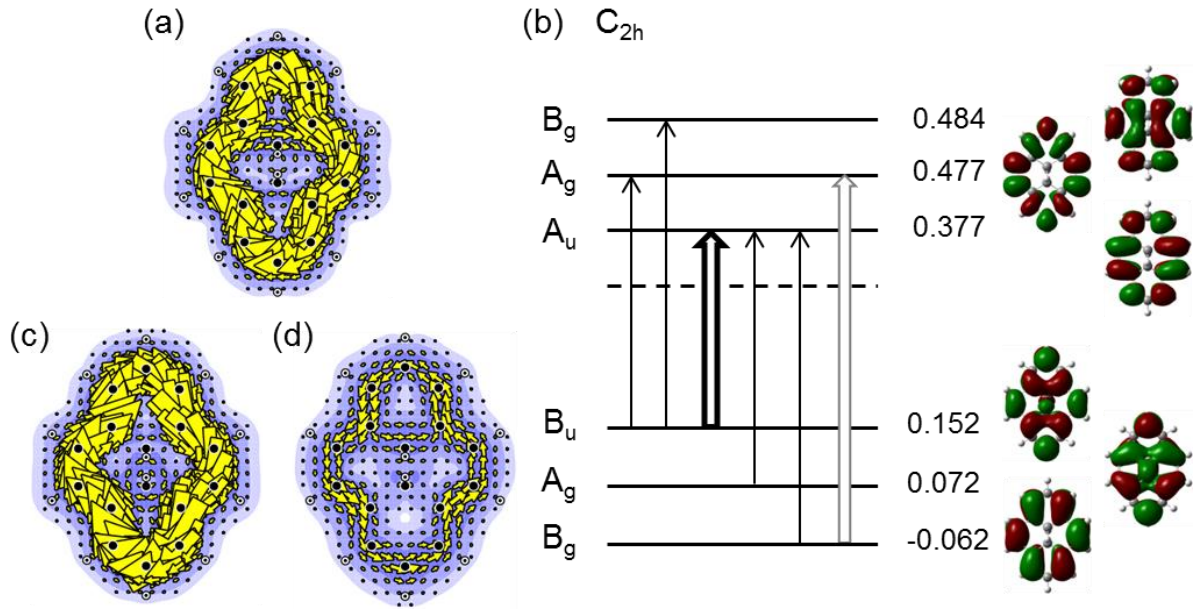

Figure 6.10. π-current analysis of C_{2h} **6**, showing: (a) The total 16π perimeter current constructed by summation of the contributions from the eight π-like LMOs of the perimeter. (b) Schematic frontier orbital-energy level diagram showing selected allowed CMO contributions to current in **6**. Full and hollow arrows indicate respectively translationally and rotationally allowed excitations at this symmetry. Dominant contributions to current, determined by examination of maps of individual occupied to virtual orbital transitions, are shown in bold. Orbital energies are given in E_h. (c) The contribution to total π current arising from the b_u/a_g Λ = 3 HOMO pair. (d) The contribution to π current arising from the complement of the b_u/a_g HOMO pair. All plotting conventions are described in the text.

Whereas in **2** the functionalisation simply alters the topology of the CMOs and reduces the density of the π-like orbitals in the centre of the molecule to a point where the entire π response is concentrated around the sp^2 perimeter, in **6** the effect is more subtle. Here, two small portions of paratropic current, one associated with each of the apical C_6 rings, flow on the face opposite to each of the two out-of-plane CH groups. The origin of this response is found to come from the π-current arising from the complement to the CMO π-HOMO pair (Figure 6.10(d)): a global, weak, diatropic perimeter and localised Clar-like benzene circulations on the opposite face to each of the two axial hydrogens.

7. C_{2v} 'BN-pyrene' 10a-aza-10b-borapyrene dianion ($C_{14}BNH_{10}^{2-}$)

The imbalance in current response caused by the internal BN unit in **3** is found to persist in the 10a-aza-10b-borapyrene dianion, **7**. As with pyrene and its dianion, the total π current of **7**, see Figure 6.11(a), is 'inverted' compared to that of its neutral analogue, **3.** The Clar-like circulation (localised above the C_5N ring in both **3** and **7**) is strengthened and reversed in direction, whilst the perimeter current is weakened and reversed, both becoming paratropic. Inspection of the frontier CMO contributions reveals the origin of the effect (see Figure 6.11(b)).

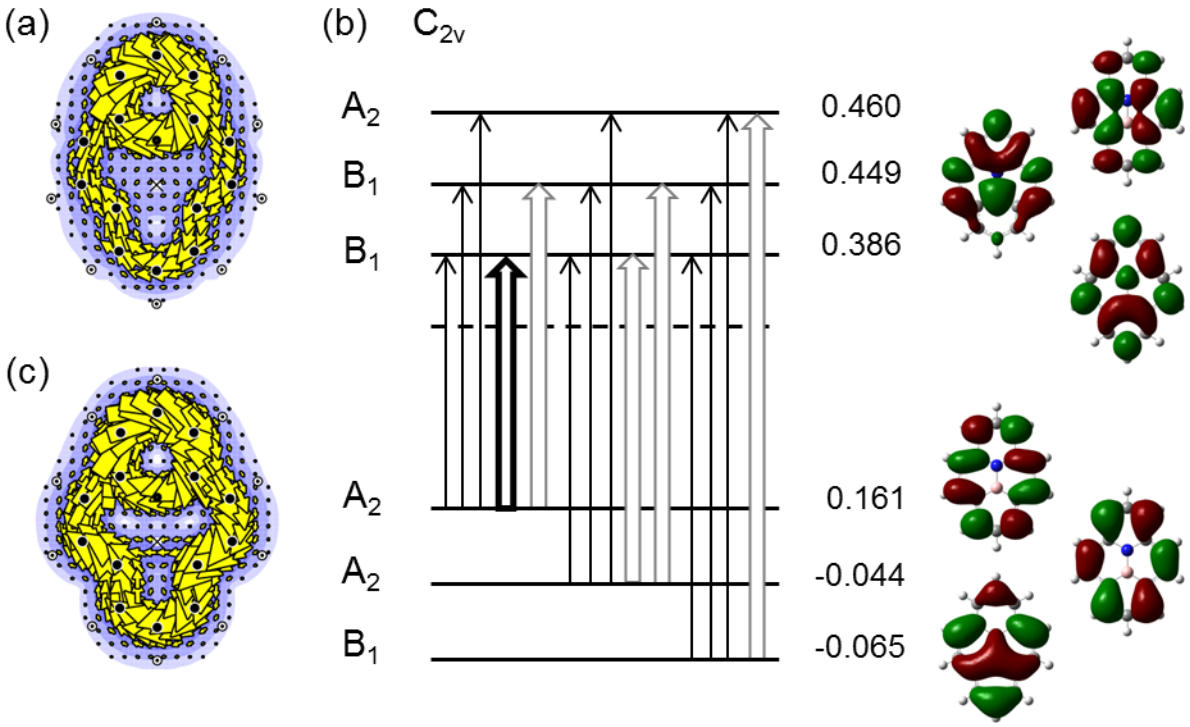

Figure 6.11. π-current analysis of C_{2v} **7**, showing: (a) The total 18π current. (b) Schematic frontier orbital-energy level diagram showing selected allowed CMO contributions to current in **3**. Full and hollow arrows indicate respectively translationally and rotationally allowed excitations at this symmetry. Dominant contributions to current, determined by examination of maps of individual occupied to virtual orbital transitions, are shown in bold. Orbital energies are given in e_h. (c) The contribution to total π current arising from the a_2 to b_1 $\Lambda = 4$ HOMO-LUMO excitation. Plotting conventions are described in the text.

The dominant contribution to current arises from the rotationally-allowed excitation from the $\Lambda = 4$ a_2 HOMO to b_1 LUMO, as shown in Figure 6.11(c). In addition to accounting for the paratropic perimeter current, focusing on the local topology of the C_5N and C_5B rings of the orbitals involved in this transition explains the difference in response of the two moieties. The HOMO and LUMO both have a local $\Lambda = 2$ nodal count situated on C_5N cycle. This rotational match results in the strong, antiaromatic 'anti-Clar' ring current seen. The C_5B cycle, which does not support a complete circulation, itself has a frontier with node-decreasing local topologies, the HOMO with a nodal count of $\Lambda = 2$, and the LUMO with a nodal count of $\Lambda = 1$.

As with the neutral systems pyrene, **1**, and 10a-aza-10b-borapyrene, **3**, it is interesting in this case to frame the aromaticity of the dianionic systems as extreme points on a continuum ranging from the all-carbon pyrene dianion, **5**, to the centrally BN-substituted dianion, **7**. Figure 6.12 displays the total π-current maps of pyrene dianion, the midpoint of the transformation (where the two interior atoms have $Z = 6.5$ and 5.5) and the endpoint, 10a-aza-10b-borapyrene dianion. For these charged systems, inspection of the maps shows that as the atomic charges are tuned between the two extremes, the effect on ring current is pronounced: current flowing over the more electronegative centre becomes stronger, whilst that over the more electropositive centre is, in this case, switched off. Additionally, the perimeter circulation is greatly strengthened. However, the gradual transformation of the internal pair from C_2 to BN again results in a smooth transition in current between the two end points.

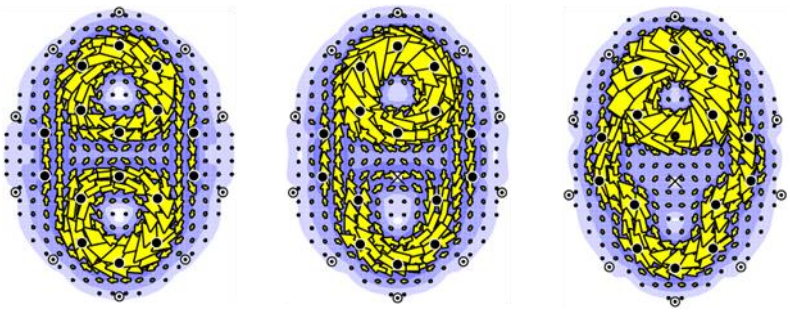

Figure 6.12. Total π-current maps of D_{2h} pyrene dianion, **5** (left), the intermediate C_{2v} isoelectronic dianionic system with fractional nuclear charge ($Z = 6.5$ and 5.5) on the central atoms (middle) and C_{2v} 10a-aza-10b-borapyrene dianion, **7** (right). Plotting conventions are described in the text.

Generalisations

The magnetic response of systems **1** to **7** can all be readily understood in terms of the ipsocentric model, with, in each case, π or π-like frontier CMOs providing the dominant contribution to ring current. The different design principles explored here, whether structural or electronic, all amount to a perturbation of these CMOs, either of their topology in the case of functionalisation and substitution, or of their occupation in the case of varying charge. Hückel theory provides a simple, unifying description of the effect of these different classes of modification. Functionalisation of the interior removes the central unit from the delocalised system, i.e., the β resonance integral, here denoted *k*, of the 'spoke' interior to exterior π bonds is cut, whilst leaving the perimeter of the system unaffected. Substitution of the central C_2 unit by a pair of heteroatoms can be modelled by including an electronegativity parameter, η to give $\alpha_X = \alpha + \eta\beta$ and $\beta_{XC} = k\beta$; this modification, validated by the fractional nuclear charge model used in sections 3 and 7 above, uses parameters for B and N (assuming them to be zero- and two-electron donors respectively) of $\alpha_B = \alpha - \beta$ and $\alpha_N = \alpha + \beta$. A schematic of the representation of this model system is shown in Figure 6.13.

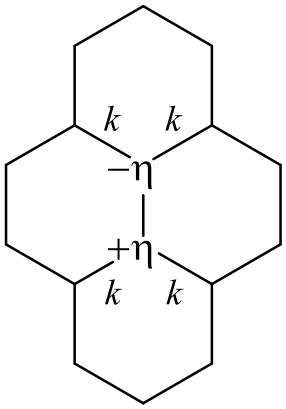

Figure 6.13. Schematic representation of the model pyrene system with modified electronegativity, η, and bond integral parameters, *k*.

Including these variable parameters in the Hückel matrix of pyrene furnishes us with a determinant of degree 16 in λ. As the graph is bipartite, this determinant contains only even powers of λ, and so may be simplified, by taking $\lambda^2 = \mu$, to the octic:

$$\mu^8 - \mu^7(4k^2 + \eta^2 + 15) + \mu^6(4k^4 + 48k^2 + 14\eta^2 + 91) - \mu^5(40k^4 + 228k^2 + 77\eta^2 + 287) + \mu^4(156k^4 + 548k^2 + 210\eta^2 + 504) - \mu^3(300k^4 + 708k^2 + 294\eta^2 + 490) + \mu^2(292k^4 + 480k^2 + 196\eta^2 + 245) - \mu(128k^4 + 152k^2 + 49\eta^2 + 53) + 16k^4 + 16k^2 + 4\eta^2 + 4 = 0$$

which can be solved numerically to yield the 16 real roots of λ corresponding to orbital energies, ε. Pictorially, these energies can be plotted as line graphs (see Figures 6.14 and 6.15), or, more usefully, in a Frost-like diagram (see Figure 6.16), but even alone the formula itself is immediately informative. The full degree 16 determinant is bipartite and has only even powers of both η and k, and so its spectrum will be symmetric under any of the possible perturbations owing to the symmetry of the graph. For varying η, this is due to the "mirror" relationship between η and $-\eta$ which we have chosen for B and N. In the case of varying k, occurrence of only even powers of k implies that as k is changed to $-k$, the spectrum is invariant. Such a change corresponds to a flipping of p orbitals on the central unit, which is a simple redefinition of the phase of the basis set, and hence cannot change the spectrum.

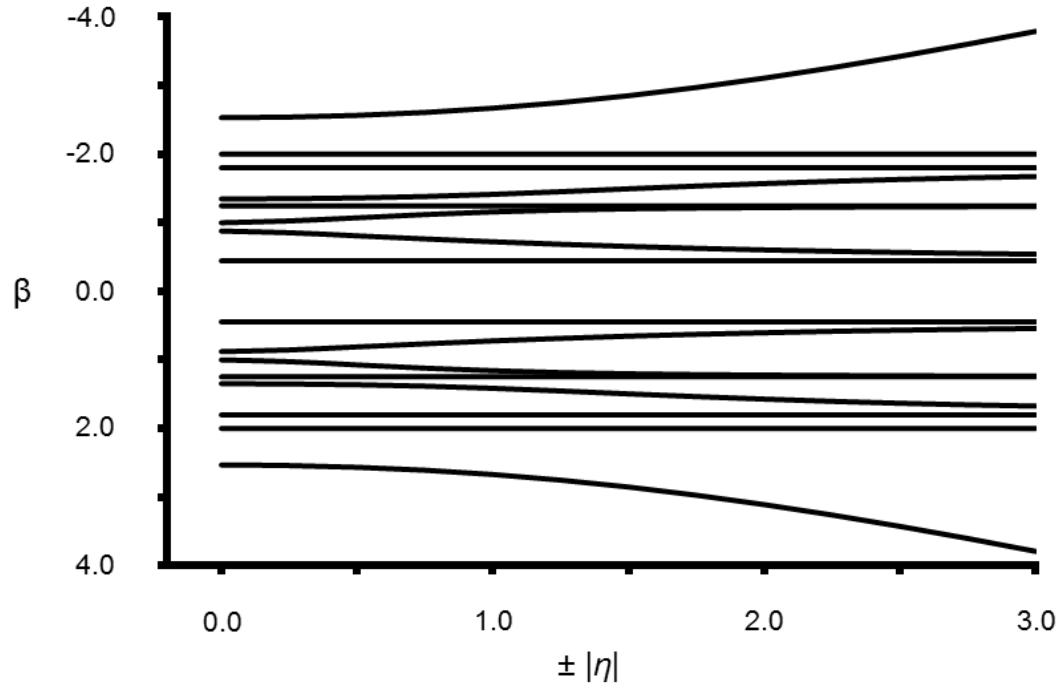

Figure 6.14. Hückel orbital energy plot showing the variation of orbital energy with the electronegativity parameter η within the range $0 \leq \eta \leq 3$.

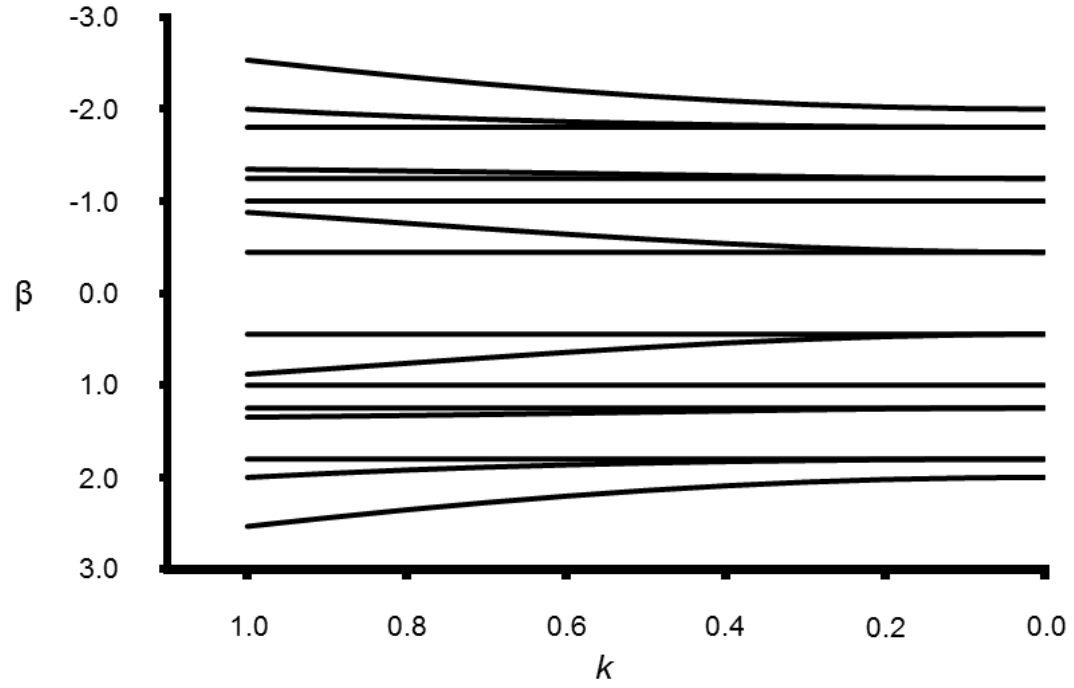

Figure 6.15. Hückel orbital energy plot showing the variation of orbital energy with the β resonance integral (k) within the range $1 \leq k \leq 0$.

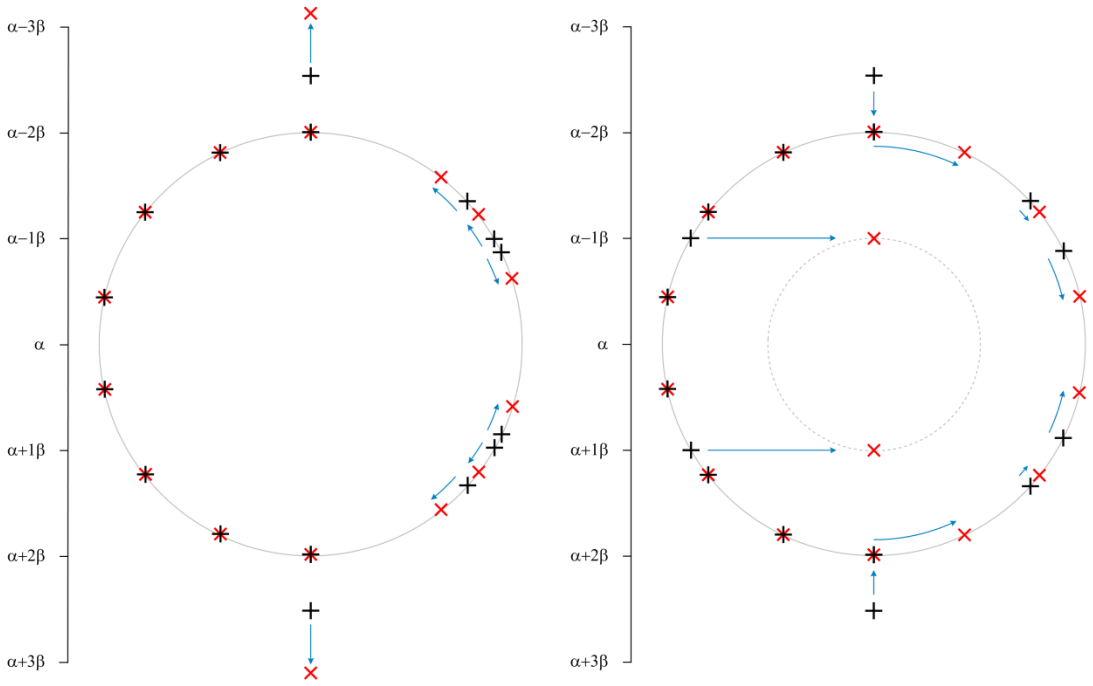

Figure 6.16. Hückel orbital energy plots showing (left) variation of |η| from 0 (black crosses) to 3 (red crosses) and the direction of change (blue arrows), and (right) variation of *k* from 1 (black crosses) to 0 (red crosses) and the direction of change (blue arrows).

Figure 6.16, left, shows the effect of varying the η parameter from 0 (black crosses) to, for ease of illustration, 3 (red crosses). When $\eta = 0$ (and indeed when $k = 0$ in Figure 6.14, right), the diagram represents the energy levels of standard pyrene. As η is changed from 0, the mirror plane across the two central rings is broken, and the symmetry of the graph is reduced from D_{2h} to C_{2v}; the eigenvalues on the right hand side of the graph begin to move, their direction determined by the final degeneracy of the system. As $\eta \rightarrow \infty$, the levels with the most positive and negative energy values go to infinity, their coefficients localise on $\pm\eta$, owing to the decreased C–$\pm\eta$ bond order, and, in accordance with Gershgorin's circle theorem,[191] the interior $\pm\eta$ pair decouples from the all carbon system, which, when the three Gershgorin discs separate, has a spectrum identical to that of [14]annulene.

The left and the right sides of the plot can be further rationalised with respect to the symmetry of their corresponding orbitals. The changing values on the right hand side span a_1 and a_2 symmetry, whilst the fixed values on the left span b_1 and b_2 which possess a mirror plane that places a node on the central four vertices of the system, disconnecting

these orbitals from any effect of varying η. The fixed values are therefore identical to that of the k_6 graph (i.e., a path of length 6).

Looking now at the Figure 6.14, right, varying k has a comparably large effect on the system. As k goes from $1 \rightarrow 0$ the inner C_2 pair smoothly decouples from the rest of the system into separate [14]annulene and k_2 contributions. This is shown in the right hand diagram as the invariant $\alpha \pm \beta$ values move into their own Frost-like domain, distinct from the original.

This general model has obvious descriptive power, but can be tested further. If, as it appears, the model accounts well for the variance of aromaticity of these pyrene derived systems, Hückel-London ring current calculations (as described in Chapter 1) on pyrene, 10a-aza-10b-borapyrene (with electronegativity parameters taken from reference[192]), and their appropriately charged antecedents, should show qualitatively similar ring current patterns to those found in the full *ab initio* calculations. Considering first the all carbon systems (Figure 6.15), the results are immediately encouraging. The strong perimeter diatropic current of pyrene is maintained, along with the weaker, Clar-like circulations in the two apical hexagons. Pyrene dianion shows similar success, the strong 'anti-Clar' circulations on the outer rings are preserved in this restricted calculation, as is the weaker antiaromatic perimeter current. The essential features of the tetraanion, the dominant aromatic perimeter current, also survives, but as the 'hub' central C_2 current seen in Figure 6.9(e) is a localised response, it cannot appear in this formulation.

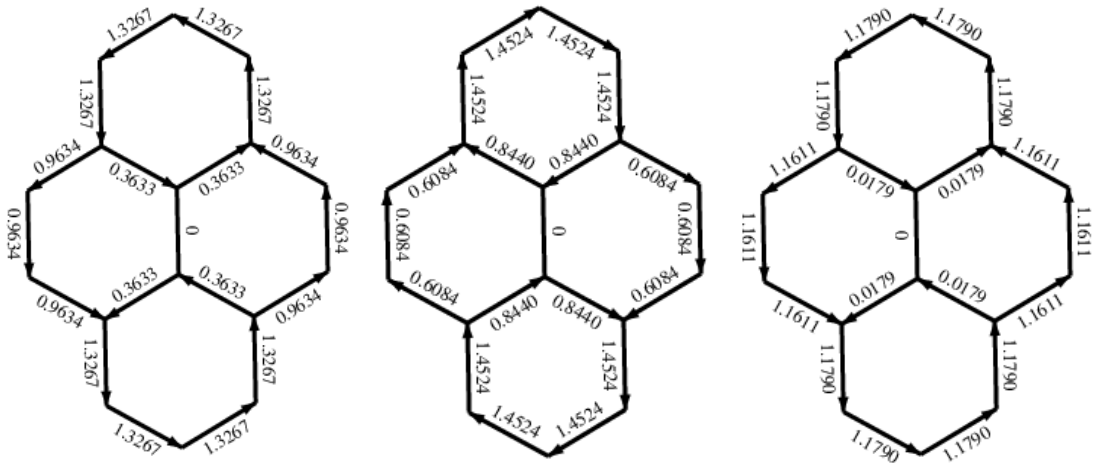

Figure 6.15. Hückel-London prediction of the current maps for (left) pyrene, **1**, (centre) pyrene dianion, **5**, and (right) pyrene tetraanion, **5a**. Currents are shown as multiples of the standard current for benzene. The molecular framework taken from the B3LYP/6-31G** optimised structures used to generate the ipsocentric current density maps.

Figure 6.16 shows the results of the BN containing species 10a-aza-10b-borapyrene and its dianion. Again, the success of these results in mimicking the full current density maps confirms the strength of the model. In the neutral system, the circulation above the electropositive boron atom in the apical ring is weaker than in pyrene, and that above the electronegative nitrogen centre is stronger. In the dianion, the strong antiaromatic exterior current clear, as are the unbalanced local 'anti-Clar' circulations localised entirely on the heteroatom containing outer rings.

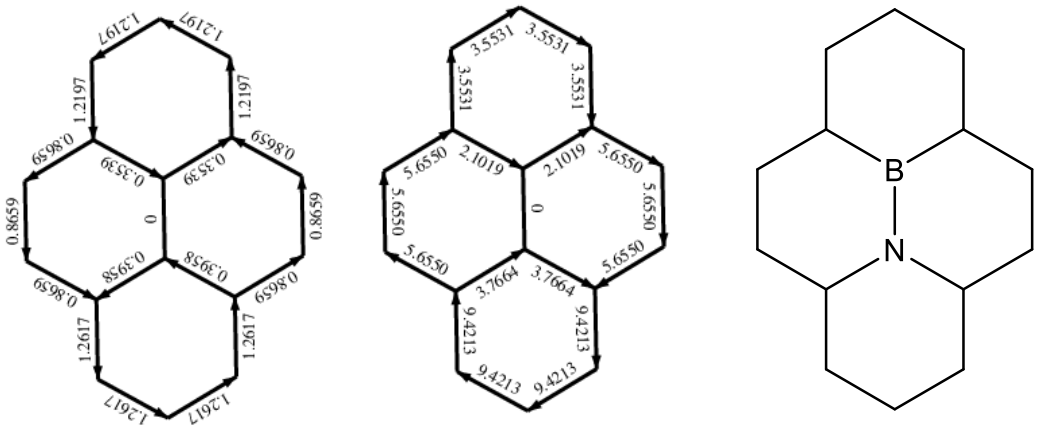

Figure 6.16. Hückel-London prediction of the current maps for (left) 10a-aza-10b-borapyrene, **3**, and (centre) 10a-aza-10b-borapyrene dianion, **7**. Currents are shown as multiples of the standard current for benzene. The molecular framework taken from the B3LYP/6-31G** optimised structures used to generate the ipsocentric current density maps. The orientation of the framework is shown on the right hand side of the figure.

This chapter has effectively acted as a collation and a summary of the previous three. Taking pyrene as a case study, the effect on ring current of substitution, functionalisation and charge were explored in depth, a common, simple orbital explanation was found, unifying these disparate approaches in a single model.

In the next chapter, the possibilities of controlling aromaticity offered by substitutions are further probed. More specifically, selected pairs of carbon atoms in a series of linear polyacenes are replaced by electronegative and electropositive heteroatoms, and the subsequent alteration of current is explored.

Chapter 7: Manipulation of Substitution Effects of Ring Current in Linear Polyacenes*

Introduction

The focus of this thesis so far has been on how functionalisation, charge, and substitution can affect the ring-current response of aromatic systems. The success of this approach has led to general design principles being identified for a range of families of molecules. Since simple, stepwise alterations of systems most easily allow the causes of changes in response of these systems to be identified, there are many further avenues to be pursued. Of the three hitherto explored, the last, substitution, has attracted the least attention, as we have focused exclusively on the replacement of C_2 with isoelectronic BN units (Chapters 4, 5 and 6). The aim of the present chapter is to broaden the narrow view of the potential offered by this approach in controlling ring current.

To achieve this widening of perspective, a special case of substitutions will be considered. Taking the well-studied family of linear polyacenes as starting systems, the effect of replacing specific pairs of 'peak' CH groups (i.e., opposite pairs of divalent vertices that neighbour trivalent sites where two rings connect) with three different functional groups is explored. These 'peak' positions are illustrated by the general structure shown in Figure 7.1. The substitute groups chosen are N, NH and BH, which are: isoelectronic with CH in the case of N, which donates one electron into the π system, electron rich in the case of NH, which donates two electrons into the π system, and electron deficient in the case of BH, which supplies no π electrons.

*Prof. Amnon Stanger is gratefully thanked for providing the NICS(xy) scan data and analysis used in this chapter. This chapter is intended as the basis for a joint publication of the Sheffield and Haifa groups.

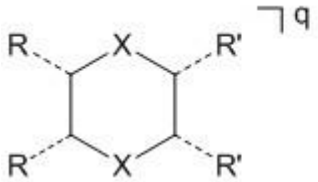

X = CH, N, NH, BH
R = benzene moiety, naphthalene moiety
R' = H, benzene moiety
q = 0 and 2+, 2- (for X = CH only)

Figure 7.1. Schematic structure of the disubstituted linear polyacene under investigation.

The inspiration for this study, and the choice of N and NH as two of the three substitutions examined here, originates in work undertaken by Gershoni-Poranne and Stanger on a new method for identifying the nature of ring-current response in multi-ring systems, the NICS(xy) scan.[193] The essence of this new method for probing the current response in polycycles is that a series of NICS calculations performed at intervals along a chosen molecular axis will avoid some of the location-specific drawbacks associated with relying on single-point NICS values as a probe for current. Sample calculations in the original paper on systems derived from tetracene, but with N and NH replacing the terminal 'peak' CHs, detected an apparent reversal in current on the NH-containing ring. This intriguing result will be discussed in detail below. In the view of the Sheffield group, previous work on correlating current density and NICS-based aromaticity indices[112] makes it clear that comparison of NICS results with ipsocentric current-density maps offers the only safe method of determining the validity of conclusions drawn from these NICS scans. As a test of this proposal, Prof. Amnon Stanger of the Technion, Haifa, Israel, has, in private correspondence, provided his results for a large number of NICS(xy) scans performed on the substituted polyacenes introduced above. the Sheffield and Haifa groups made a double-blind comparison, with neither group knowing the results of the other before preparing an interpretation of their respective results. The provided analysis of the NICS(xy) scans is quoted extensively throughout the chapter.

The structure of this chapter is as follows: first, the results of the ipsocentric current-density calculations of neutral naphthalene, anthracene and tetracene are presented alongside their isoelectronic N-substituted analogues. Next, the NH-substituted and BH-substituted species are compared to the all-carbon dianions and dications respectively, and an overall account of the π-response of the systems in general will be made. The focus then shifts to systems derived from anthracene, with each case analysed

in detail and maps compared to the NICS(xy) scans. This anthracene framework is chosen for particular attention as it is small enough to be analysed in full, whilst still having the complexities offered by a choice of two heteroatom substitution sites.

Methods

The geometries of all structures were optimised in maximum symmetry at the B3LYP/6-31G** level using Gaussian09.[40] Hessian calculations were used to identify all structures treated here as local energetic minima, except those containing pairs of NH functional groups, which are discussed below. Subsequently, current-density maps were calculated at the CHF/6-31G** level of theory using the ipsocentric[27,33] approach as implemented in the SYSMO[39] and GAMESS-UK[62] suites of programs.

The calculated current-density maps display first-order π-current density in the plotting plane 1 a_0 above the median plane of the molecule. Nuclear positions are represented by Dalton's symbols for the elements (see Figure 2.1). The induced magnetic field is positioned perpendicular to the plotting plane, contours and shading indicate the modulus of the induced current density per unit external magnetic field, and arrows indicate the vector current density resolved into the plotting plane. A quantitative measure of the strength of an induced current is given by the j_{max} value, the maximum current density per unit inducing field taken over the plotting plane. As always, these values are quoted for reference with that of related molecules or the benzene standard: 0.078 a.u. at this level of theory.

NICS data and interpretations were supplied by Prof. Amnon Stanger of Technion University, Israel. The NICS(xy) scan values were calculated using the Aroma package[194] for same optimised B3LYP/6-31G** structures at the GIAO/B3LYP/6-311G** level using Gaussian09.[40] NICS probes (bq centres) were positioned 1.7 Å above the molecular plane, along the mirror plane running the length of the molecule. The results were then plotted and analysed with the OriginLab software[195] using the NCS[196] and σ-only[197] methods, both of which report $NICS_{\pi zz}$ values, i.e., the π component of shielding separated from the effect of the molecular framework. NCS is a natural bond orbital (NBO) based method that allows chemical shielding values of NMR resonance shielding tensors to calculated in terms of

separate delocalised features in the electronic structure, whilst the σ-only method takes the difference between two NICS values, one of the molecule of interest, and one on the same molecule but with the face opposite the probe hydrogenated to remove the effect of the π electrons.

At this point a brief note is required to state the claims made by its originators about NICS(xy) scans and their suitability for identifying and analysing ring current.[193] The primary purpose of the method is to give a qualitative identification of global and well defined local ring currents, and to distinguish between cases where a system may possess multiple currents, for example pyrene (as discussed at length in Chapter 6), or a single global current only, as in naphthalene. Additionally, the approach also aims to decide between alternate descriptions of current, such as the possibility that the total current in anthracene arises from combined contributions of three local benzene-like circulations (discussed below).

Results and Discussion

Current-density maps for tetracene, anthracene, naphthalene and their isoelectronic N-pair substituted analogues are shown in Figure 7.2.

Initial inspection of the maps shows a very similar aromatic response in the substituted system to that of the neutral polyacene parent systems. Focusing on the heteroatoms, however, allows a slight strengthening of current to be discerned above these centres. This should be expected, as nitrogen is more electronegative than carbon, although it must be emphasised that this effect is subtle, and that the isoelectronic substituted systems and neutral benzenoids possess essentially the same total π current pattern, with even the characteristic strengthening of current in the centre of anthracene and tetracene maintained.[25,27] Consideration of j_{max} values quantifies this observation. The total π current in neutral anthracene, for example, is j_{max} = 0.101 a.u., whereas the total π current in centrally N-substituted anthracene is j_{max} = 0.104 a.u. (i.e., 1.03 times that in anthracene), and the total π current in the outer N-substituted anthracene is j_{max} = 0.100 a.u. (i.e., 0.99 times the anthracene value).

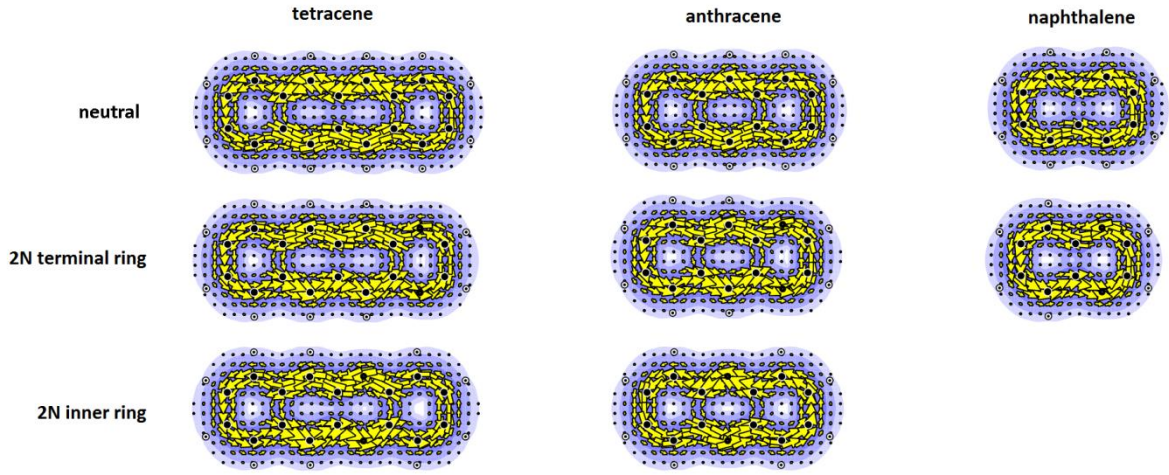

Figure 7.2. Total π current-density maps of tetracene, anthracene and naphthalene, and their appropriate N-substituted analogues. Plotting conventions are described in the text.

Substitution of two NH groups in the same positions shows strikingly different results, as predicted by Gershoni-Poranne and Stanger.[193] As each NH unit contributes 2π electrons to the π system, the NH-substituted systems possess one doubly occupied π-molecular orbital more than in the neutral polyacene. These systems are therefore isoelectronic with the dianions of the parent benzenoids. Figure 7.3 shows the current-density maps of the neutral benzenoids, their dianions, and the corresponding NH-substituted species.

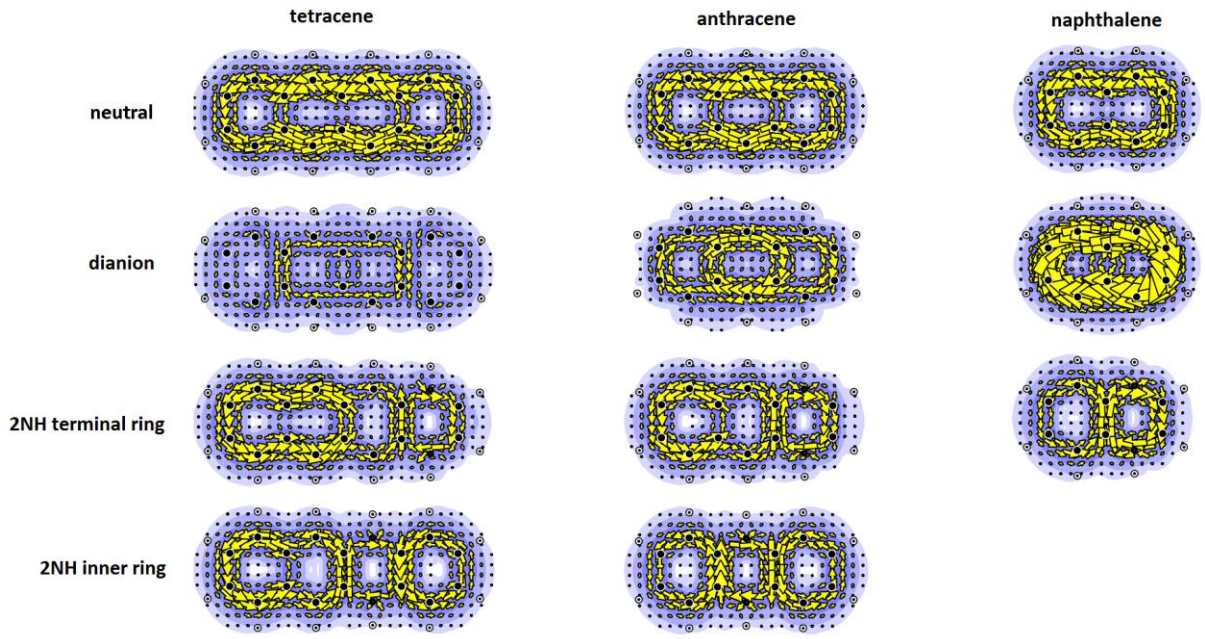

Figure 7.3. Total π current-density maps of tetracene, anthracene and naphthalene, their dianions and their appropriate NH-substituted analogues. Plotting conventions are described in the text.

This differences between the total π current-density maps of the different modifications of the neutral benzenoids, reported in Figure 7.3, are striking. At first sight it is clear that the NH-substituted systems, although isoelectronic with the dianions of the polyacenes, do not possess a ring current response comparable in sense, strength or direction. The dianions are globally antiaromatic in the smaller systems. Their frontier orbitals, as is seen later for the specific case of anthracene and anthracene dianion, correlate with the LUMO and LUMO+1 of the neutral systems, from which, by application of ipsocentric arguments, the origin of their paratropicity is clear: as they possess the same perimeter nodal count the frontier orbitals are related by a rotation. As the chain of rings is extended, the frontier current contribution is damped by its diatropic complement.

In stark contrast to the dianions, the NH-substituted systems display localised paratropicity on the electron-rich heteroatom containing rings, with the remaining oligocyclic all-carbon framework behaving in the manner of the corresponding smaller benzenoid(s). To give an example, when the central 'peak' CHs of anthracene are replaced by NHs, the two terminal C_6 carbocycles display individual benzene-like circulations. CMO breakdown of current density in Figure 7.4 confirm that the paratropic circulation is the result of excitations from the HOMO, with the diatropic regions attributable to the HOMO complement.

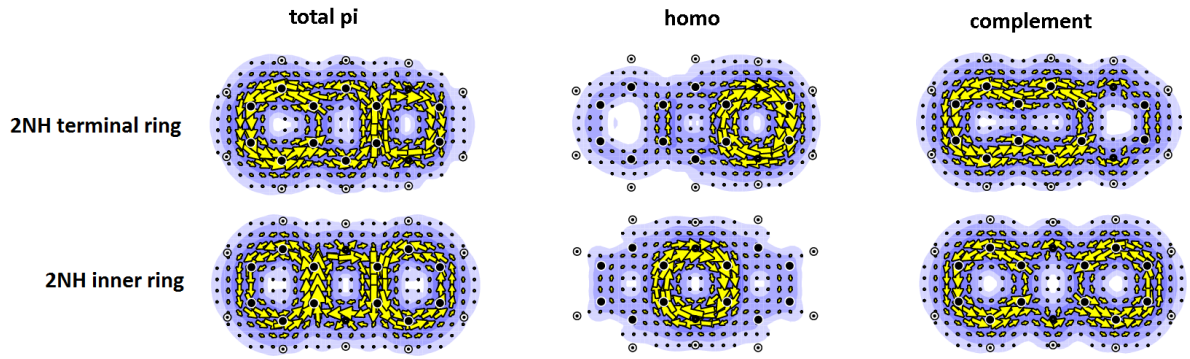

Figure 7.4. π current-density maps of terminal and central substitutes of NH for CH in anthracene, showing: total π, HOMO and HOMO complement (i.e., the total π map *minus* the HOMO map) contributions. Plotting conventions are described in the text.

The results of the third and final substitution, where electropositive and electron-deficient BH groups take the place of the selected 'peak' CHs, once again has a dramatic effect on the aromaticity of these polycycles, but different to that encountered so far (see Figure 7.5). Whereas the addition of two electrons to the π system introduces local paratropic circulation into the functionalised polyacene, removing two does not give a similar result, which may have been expected from simple electron counting arguments. Instead the electropositive boron atoms effectively block the global flow current on the perimeter, leaving the oligocyclic or carbon-carbon double bond patches that display the ring current response of their free all-carbon analogues. As will be seen later, electropositive boron has the effect of raising the energy of the LUMO, and hence reducing the contributions of the frontier transitions accordingly.

As we saw earlier, NH-substituted systems and the isoelectronic all-carbon dianions show different π-current response. A similar divergence between the BH-substituted systems and the all-carbon dication analogues is seen in Figure 7.5. The systems in general display varying degrees of antiaromaticity, with the nature of the dominant contributions nuanced by the length of the polyacene itself. With the shortest species, derived from the naphthalene framework, the removal of two π electrons from the occupied space opens a node preserving HOMO to LUMO transition, resulting in a classic paratropic current. As the length of the system increases, the HOMO and HOMO-1 pair of the neutral system do not necessarily possess the same number of angular nodes around the entire perimeter, thanks to the higher 'energy tariff' of introducing a node along the length of the molecule, complicating the balance of paratropicity/diatropicity in the system. This effect has already been seen in the dianionic systems, where, as the number of rings in the chain increases, the initially dominant paratropic contribution is damped by diatropic currents.

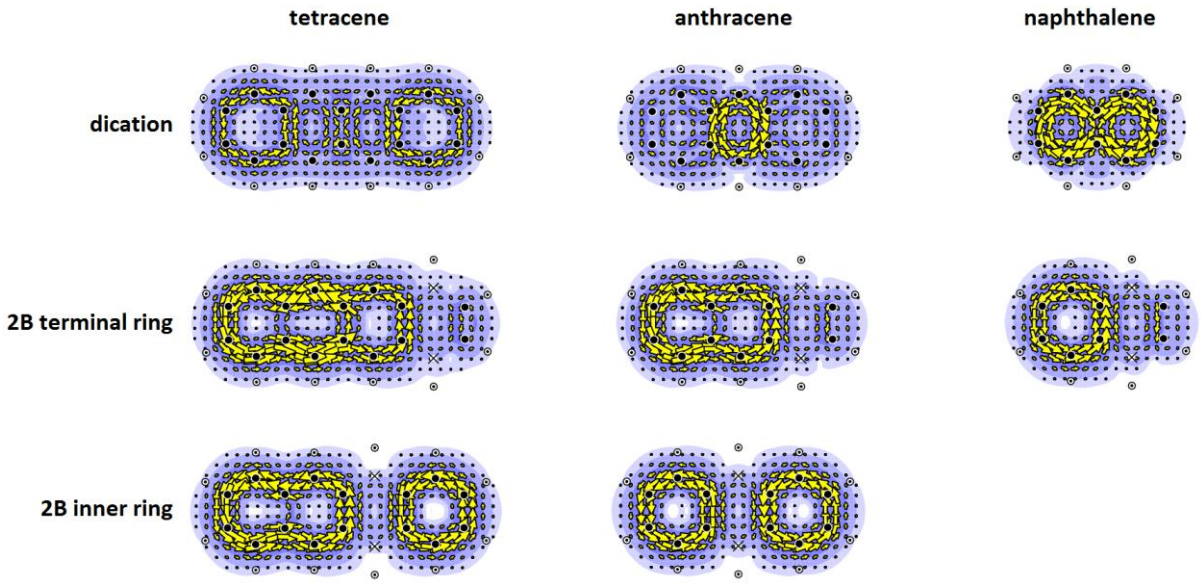

Figure 7.5. Total π current-density maps of tetracene dication, anthracene dication and naphthalene dication and their appropriate BH substituted analogues. Plotting conventions are described in the text.

The powerful possibilities that specific substitutions offer for controlling current in linear benzenoids are clear from the above calculations. Depending on whether selected CH groups are replaced by electron rich and electronegative NH, or by electron deficient and electropositive BH groups, currents can be reversed in specific rings, or even blocked altogether.

In the rest of this chapter, a detailed analysis of the systems derived from anthracene will be presented in order to tease out the origins of these intriguing ring currents. The NICS(xy) scan results will also be discussed in each case, providing a key test for this new method in a novel context for the possibilities of tuning aromaticity. This analysis of anthracene derived systems (**1** to **9**, as shown in Figure 7.6) begins with anthracene itself, before moving on to the isoelectronic central and outer N-substituted systems, anthracene dianion and the central and outer NH-substituted systems, and finally anthracene dication and the central and outer BH-substituted systems.

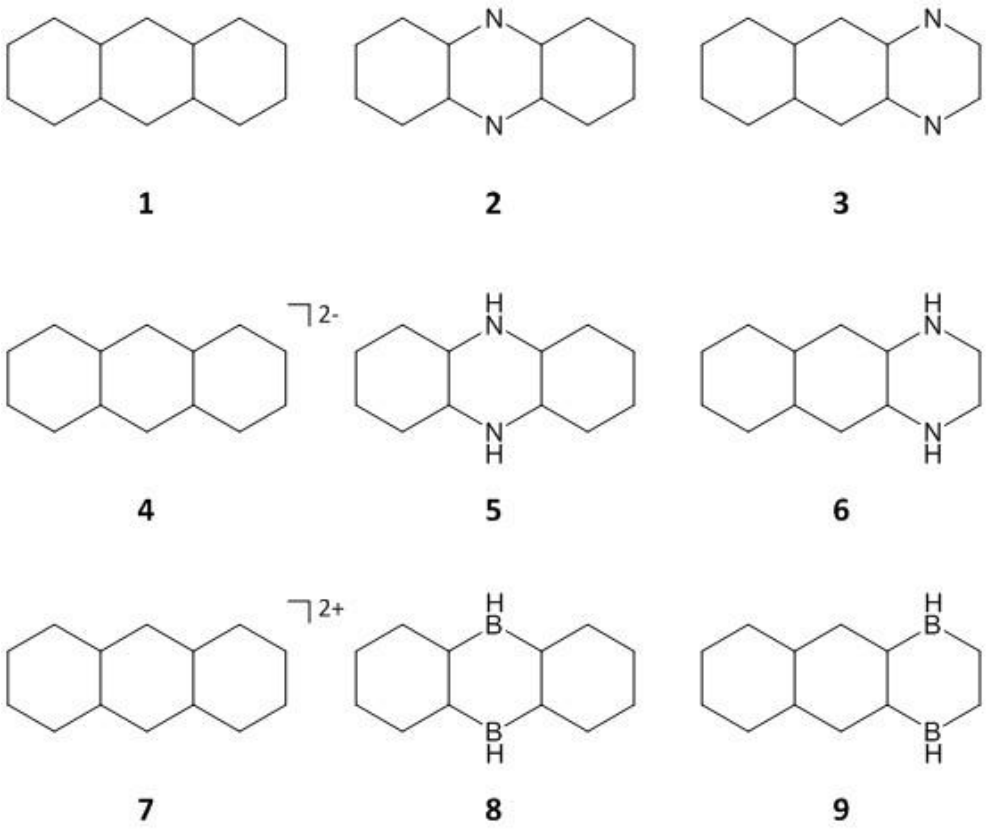

Figure 7.6. Schematic representation of the structures derived from anthracene (**1** to **9**).

1. Anthracene

Figure 7.7 shows the π-current breakdown for D_{2h} anthracene. The total π current (Figure 7.7(a), j_{max} = 0.101 a.u.) shows a clear, global, aromatic perimeter current that is slightly stronger on the central ring. This tendency to stronger ring current on central rings in linear polyacenes has been discussed by Fowler and Myrold in reference 25,[25] and is also a feature of all qualitative models of ring current. Contributions from the HOMO pair (Figure 7.7(b), j_{max} = 0.101 a.u.) show that, as is to be expected from the vast majority of aromatic molecules encountered so far, the current can be qualitatively accounted for in its entirety by excitations from the frontier orbitals.

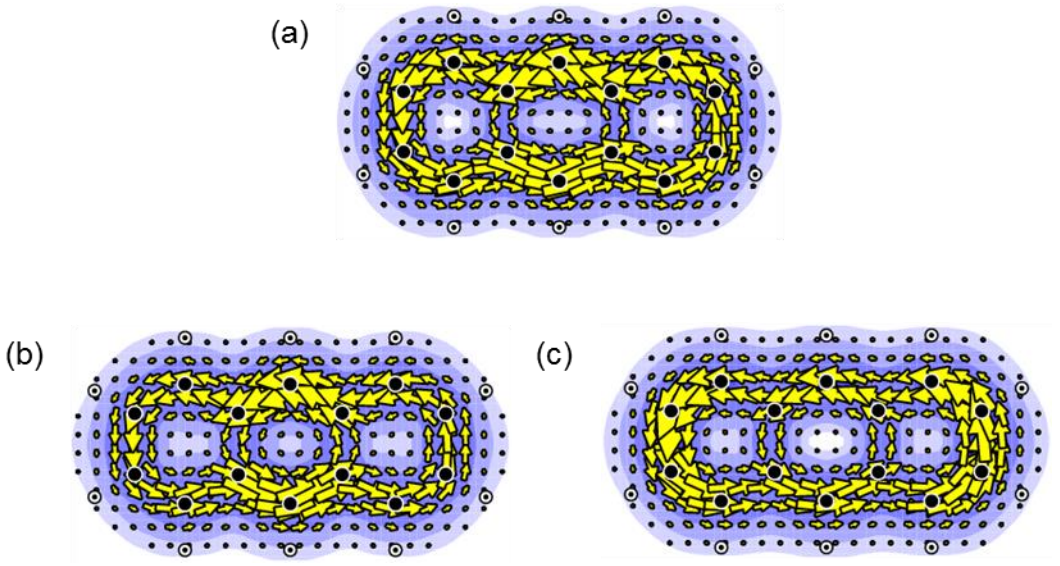

Figure 7.7. π-current analysis of D_{2h} anthracene **1**, showing: (a) The total 14π current. (b) The contribution to total π current arising from the b_{3g} and b_{2g} HOMO pair (Λ = 3). (c) The contribution to total π current arising from the four possible transitions between the b_{3g} and b_{2g} HOMO pair (Λ = 3) and the b_{1u} and a_u LUMO pair (Λ = 4). Plotting conventions are described in the text.

Spectral decomposition of the current, as detailed in the schematic energy level diagram of anthracene (Figure 7.8), once again confirms the suitability of simple angular momentum node-counting, or more accurately in the language of Monaco and Zanasi, half azimuthal node count (HANC),[198] arguments for predicting current. The summed contributions to total π current arising from the four possible transitions between b_{3g} and b_{2g} Λ = 3 HOMO and the b_{1u} and a_u Λ = 4 LUMO pairs (indicated by the bold arrows in Figure 7.8) account well for the complete ring current response, as can be seen from Figure 7.7(c) (j_{max} = 0.105 a.u.), which efficiently captures the dominant effect present in the total π map. The success of this argument for rationalising the magnetic response of all the systems discussed below will be seen again and again as each case is discussed in turn.

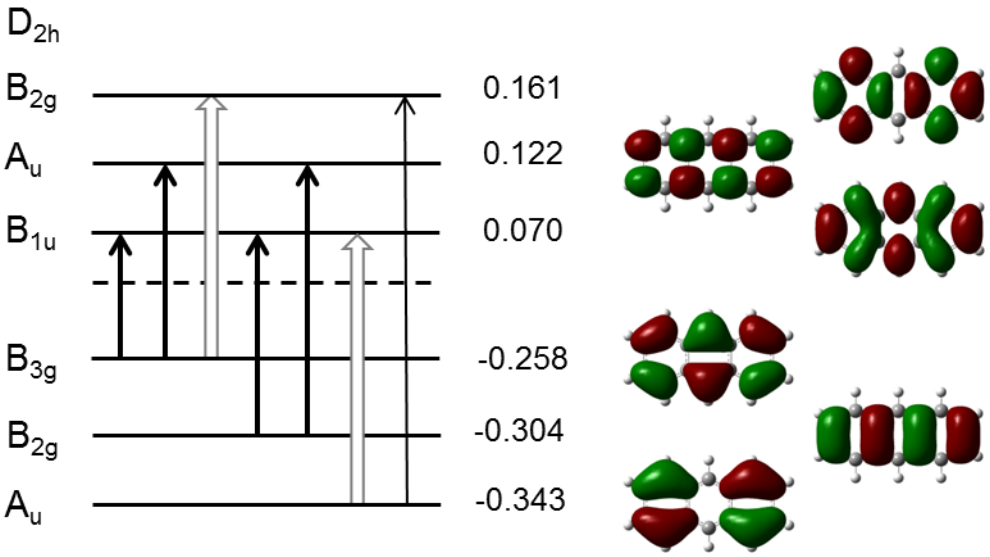

Figure 7.8. Schematic energy level diagram of D_{2h} anthracene **1**. Full and hollow arrows indicate respectively translationally and rotationally allowed excitations at this symmetry. Dominant contributions to current, determined by examination of maps of individual occupied to virtual orbital transitions, are shown in bold. CMO energies in E_h and orbital nodal patterns are shown on the right of the diagram, assignments to irreducible representations on the left.

Having taken a detailed look at the current-density maps of anthracene, the results and interpretation of the NICS(xy) scan can be evaluated. The first piece of information that can be read from the scan is that the molecule is "aromatic", owing to the strong negative $NICS_{\pi zz}$ values obtained. The presence of a single global circulation, as would be indicated by a smooth parabola line shape, is ruled out by the inflection points in the plots at positions b and c. The extreme alternate view, that the π current in anthracene comprises three local benzene-like circulations, as would be inferred from three sharp negative peaks focused on positions A, B, and C, can likewise be discounted. It is therefore concluded that the current in anthracene is neither purely local nor global in character. Although the exact nature of the current cannot be extracted from the scan, the scan is entirely consistent with the current-density map shown in Figure 7.7(a).

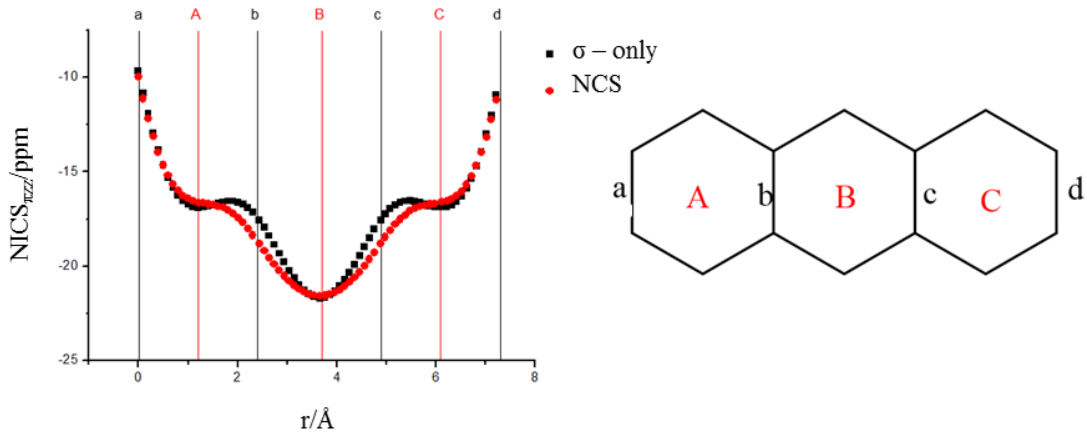

Figure 7.9. NICS(x) scan of D_{2h} anthracene **1**. The NICS probe travels the length of the molecule from left to right along the mirror plane, r. r = 0 Å, the starting point of the scan, corresponds to bond a on the schematic structure. The bonds it passes through are denoted with lower case letters, ring centres with capitals. All scans are performed at a height of 1.7 Å.

2. Central N-Substituted Anthracene

As discussed above, the substitution of two N centres for the central two CH groups of D_{2h} anthracene **1** has no strong effect on global ring current. Figure 7.10(a) shows the total π ring current of D_{2h} **2**. Qualitatively, the current displays the same diatropic flow patterns as **1**. The stronger current on the central ring is maintained, and, as mentioned previously, slightly strengthened. j_{max} values quantify this effect: the total π j_{max} of **1** is 0.101 a.u., cf. 0.104 a.u. for **2**. CMO analysis of the current shows that, as should be expected, the orbital origins of current in **2** are exactly the same as those in **1**. The contributions to current arising from the b_{3g} and b_{2g} HOMO pair (see Figure 7.10(b)) again account for the dominant diatropic circulation found, with j_{max} = 0.102 a.u., 98% of the total π current.

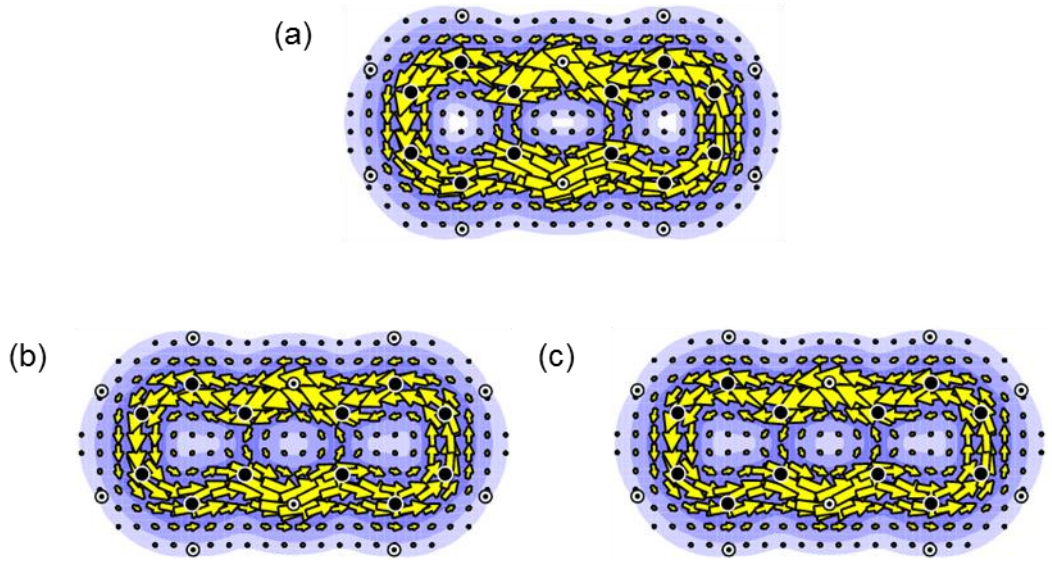

Figure 7.10. π-current analysis of the result of the substitution of the two central 'peak' CH for N, D_{2h} **2**. Showing: (a) The total 14π current. (b) The contribution to total π current arising from the b_{3g} and b_{2g} HOMO pair (Λ = 3). (c) The contribution to total π current arising from the combined four possible transitions between the b_{3g} and b_{2g} HOMO pair (Λ = 3) and the b_{1u} and a_u LUMO pair (Λ = 4). Plotting conventions are described in the text.

Spectral analysis provides the final confirmation of the equivalence of current in **1** and **2**. Figure 7.10(c) shows the summed contributions to total π current arising from the four possible transitions between the Λ = 3 b_{3g} and b_{2g} HOMO and the Λ = 4 b_{1u} and a_u LUMO pairs of **2** (j_{max} = 0.097 a.u.). Comparison of the frontier orbital topology of **1** and **2** (Figures 7.8 and 7.11), and the corresponding maps of these contributions (Figures 7.7(c) and 7.10(c)), demonstrates that this case is undeniable.

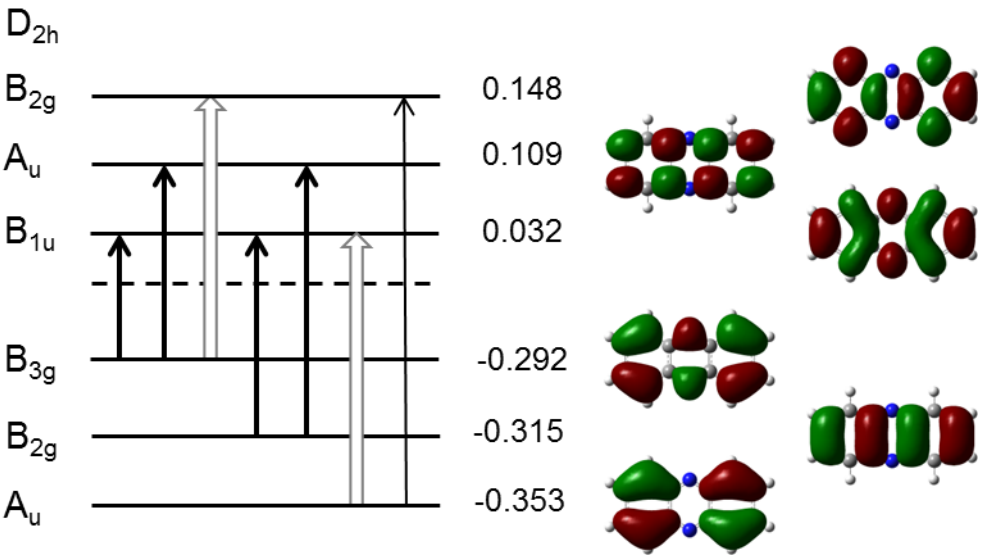

Figure 7.11. Schematic energy level diagram of the result of the substitution of the two central 'peak' CH for N, D_{2h} **2**. Full and hollow arrows indicate respectively translationally and rotationally allowed excitations at this symmetry. Dominant contributions to current, determined by examination of maps of individual occupied to virtual orbital transitions, are shown in bold. CMO energies in E_h and orbital nodal patterns are shown on the right of the diagram, assignments to irreducible representations on the left.

Broadly, the similarities observed between the maps of **1** and **2** survive into the NICS(xy) scan. The results show the same mixed local and global response in **2** as in **1**, as evidenced by the inflections present in the lines at points b and c. Closer inspection of the plots show that perhaps the central ring may be slightly less diatropic in the substituted system, an effect that is not evident in the current-density maps.

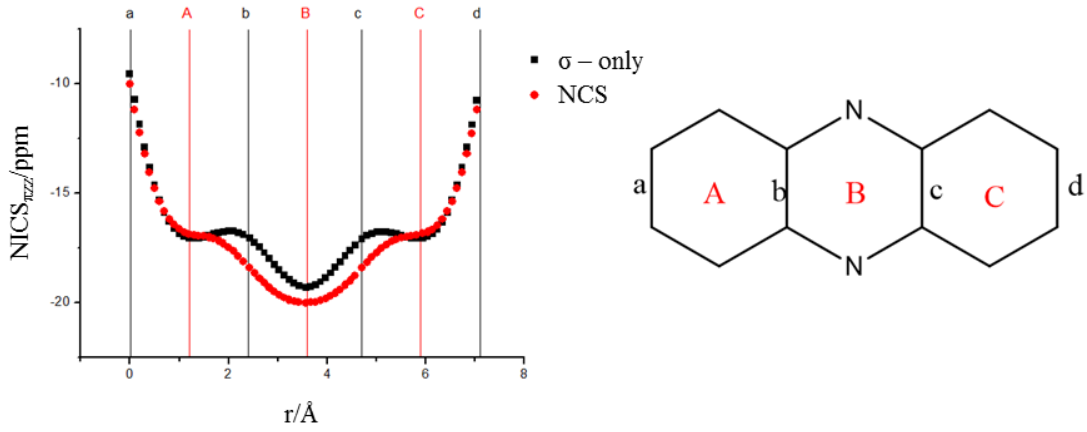

Figure 7.12. NICS(x) scan of the result of the substitution of the two central 'peak' CH for N, D_{2h} **2**. The NICS probe travels the length of the molecule from left to right along the mirror plane, r. r = 0 Å, the starting point of the scan, corresponds to bond a on the schematic structure. The bonds it passes through are denoted with lower case letters, ring centres with capitals. All scans are performed at a height of 1.7 Å.

3. Outer N-Substituted Anthracene

Moving the site of N-substitution from the central CH position to the outer ring again results in a similar ring-current pattern. The total π current of C_{2v} **3** once again displays the global diatropic circulation as well as the accompanying local circulation on the central ring (see Figure 7.13(a)). The strength of this current is similar to that of anthracene itself; with j_{max} = 0.100 a.u., **3** has a total π current 99% of the strength of that of **1**.

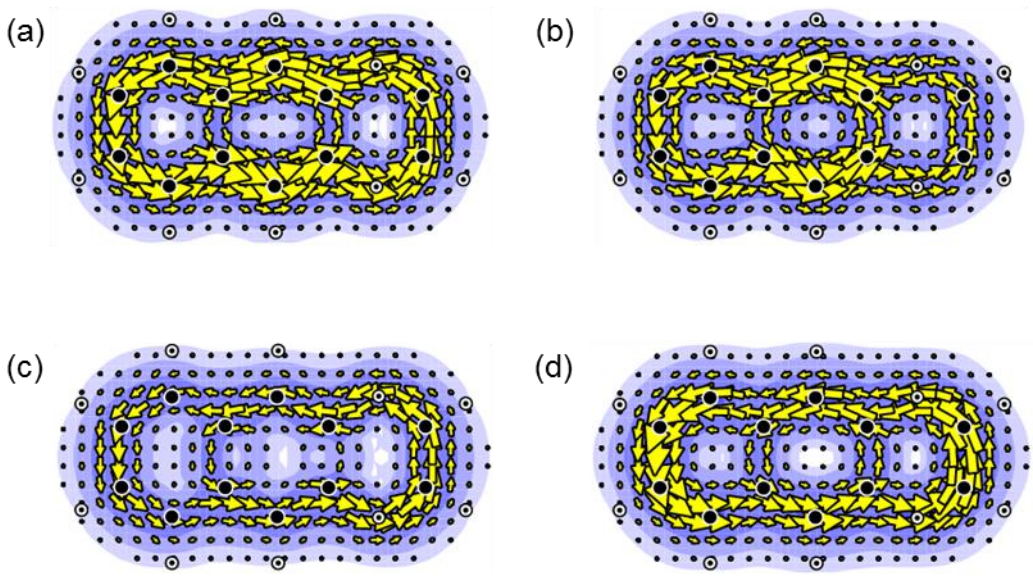

Figure 7.13. π-current analysis of the result of the substitution of an outer 'peak' pair of CH for N, C_{2v} **3**. Showing: (a) The total 14π current. (b) The contribution to total π current arising from the a_2 and b_1 HOMO pair (Λ = 3). (c) The contribution to total π current arising from the complement of the a_2 and b_1 HOMO pair. (d) The combined contributions to total π current arising from the transitions between the a_2 and b_1 HOMO pair (Λ = 3) and the b_1 and a_2 LUMO pair (Λ = 4). Plotting conventions are described in the text.

Examination of CMO contributions to current shows that in this case, although the π current arises from contributions from more than just the HOMO pair (cf. Figures 7.13(b) and (c)), the most significant effects still arise from transitions between the a_2 and b_1 (Λ = 3) HOMO and b_1 and a_2 (Λ = 4) LUMO pairs (Figure 7.13(d)), illustrated in the schematic orbital energy-level diagram Figure 7.14. This interpretation of the current-density maps is supported by examination of j_{max}: the summed four transition contribution has j_{max} = 0.096 a.u., 96% of the strength of the total π current.

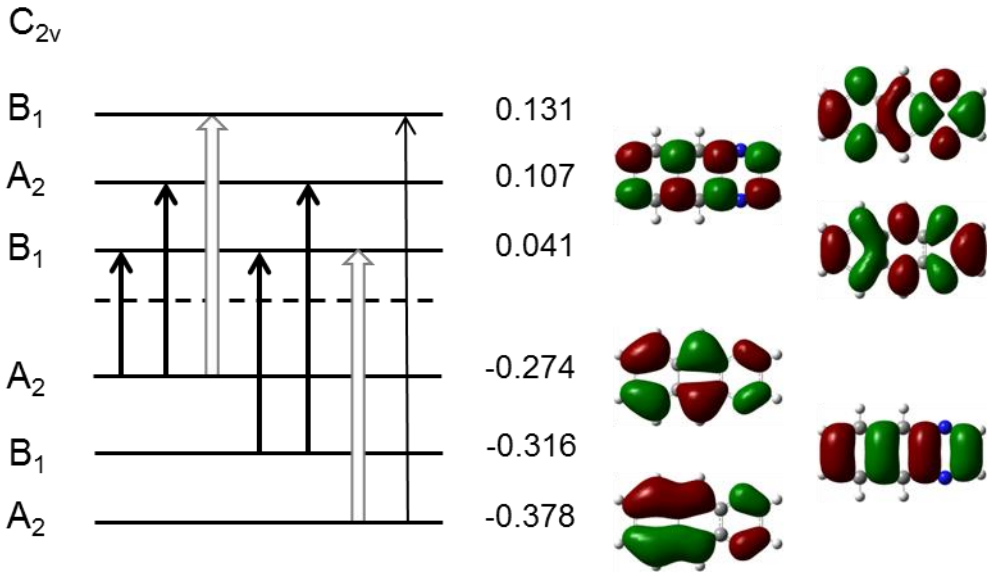

Figure 7.14. Schematic energy level diagram of the result of the substitution of an outer 'peak' pair of CH for N, C_{2v} **3**. Full and hollow arrows indicate respectively translationally and rotationally allowed excitations at this symmetry. Dominant contributions to current, determined by examination of maps of individual occupied to virtual orbital transitions, are shown in bold. CMO energies in E_h and orbital nodal patterns are shown on the right of the diagram, assignments to irreducible representations on the left.

Again, the overall picture of current in the maps can be inferred from the NICS(xy) scan Figure 7.15. The results still show the same mixed local and global response as in **1** and **2**. The inflection point at d in **3** is of lower value than in the other systems encountered so far. This indicates reduced diatropicity in the heteroatom containing ring. In this case the result, alluded to earlier in discussing the more complex interpretation of current in **3**, is supported by the current-density maps above.

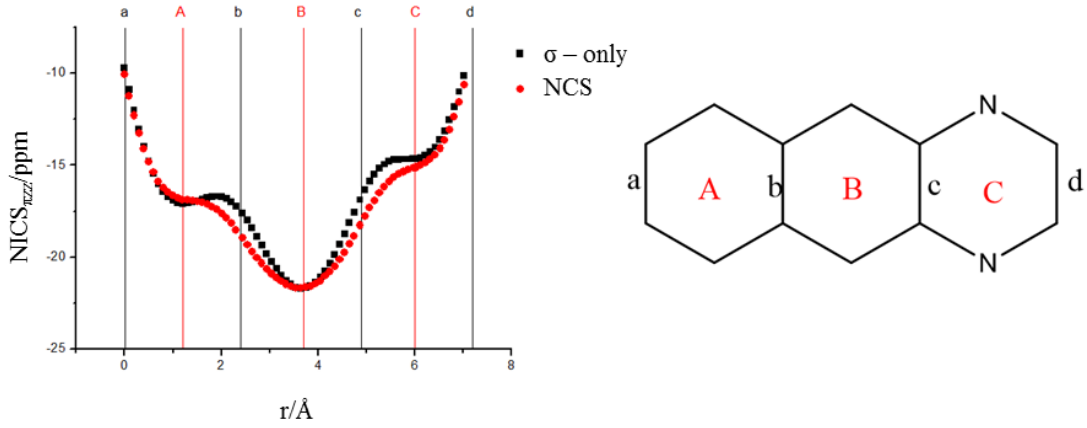

Figure 7.15. NICS(x) scan of the result of the substitution of an outer 'peak' pair of CH for N, C_{2v} **3**. The NICS probe travels the length of the molecule from left to right along the mirror plane, r. r = 0 Å, the starting point of the scan, corresponds to bond a on the schematic structure. The bonds it passes through are denoted with lower case letters, ring centres with capitals. All scans are performed at a height of 1.7 Å.

4. Anthracene Dianion

The addition of two electrons into the π system of D_{2h} anthracene, **1**, results in D_{2h} anthracene dianion, **4**. The total π-current response in **4** is a relatively weak (j_{max} = 0.089 a.u.) paratropic current flowing over the whole system (see Figure 7.16(a)). The anthracene dianion displays both a global perimeter current and what can be viewed as a localised circulation on the central ring. The contribution to current from the b_{1u} HOMO (Figure 7.16(b)) is, as is usual for antiaromatic systems, considerably stronger that the total π current, with a j_{max} of 0.138 a.u.. The strong paratropicity arising from the HOMO current is partially cancelled by node-increasing diatropic contributions originating in lower lying orbitals. Figure 7.16(c) shows the overall global diatropic current arising from the complement to the HOMO.

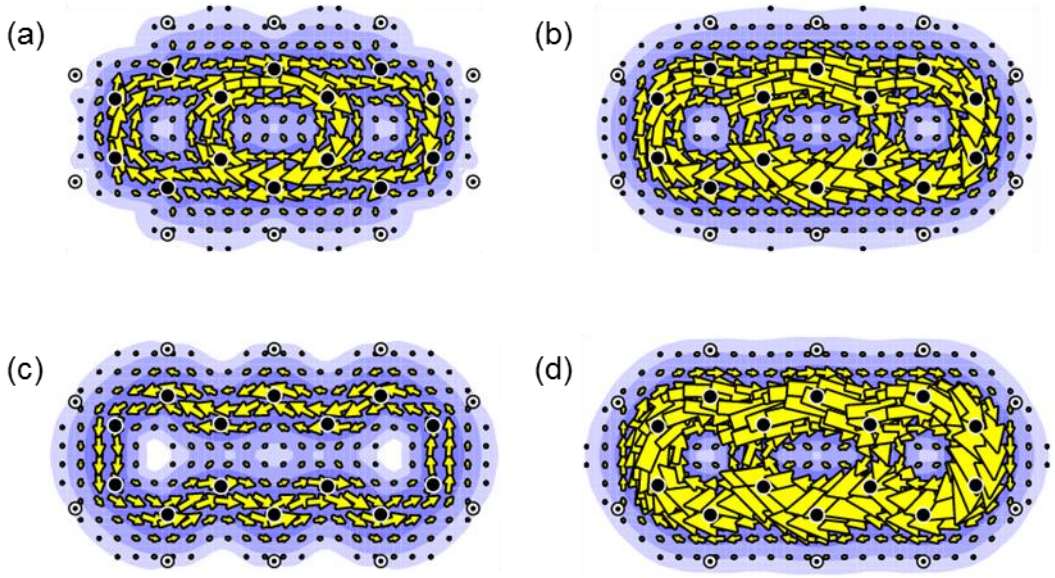

Figure 7.16. π-current analysis of D_{2h} anthracene dianion **4**. Showing: (a) The total 16π current. (b) The contribution to total π current arising from the b_{1u} HOMO (Λ = 4). (c) The contribution to total π current from the complement of the HOMO. (d) The contribution to total π current arising from the transition between the b_{1u} HOMO (Λ = 4) and the a_u LUMO+1 (Λ = 4). Plotting conventions are described in the text.

As the schematic orbital energy-level diagram (Figure 7.17) shows, the dominant effect is accounted for by the angular momentum node-preserving Λ = 4 to Λ = 4, ΔΛ = 0, transition between the b_{1u} HOMO and a_u LUMO+1 orbitals. The map corresponding to this individual transition is shown in Figure 7.16(d).

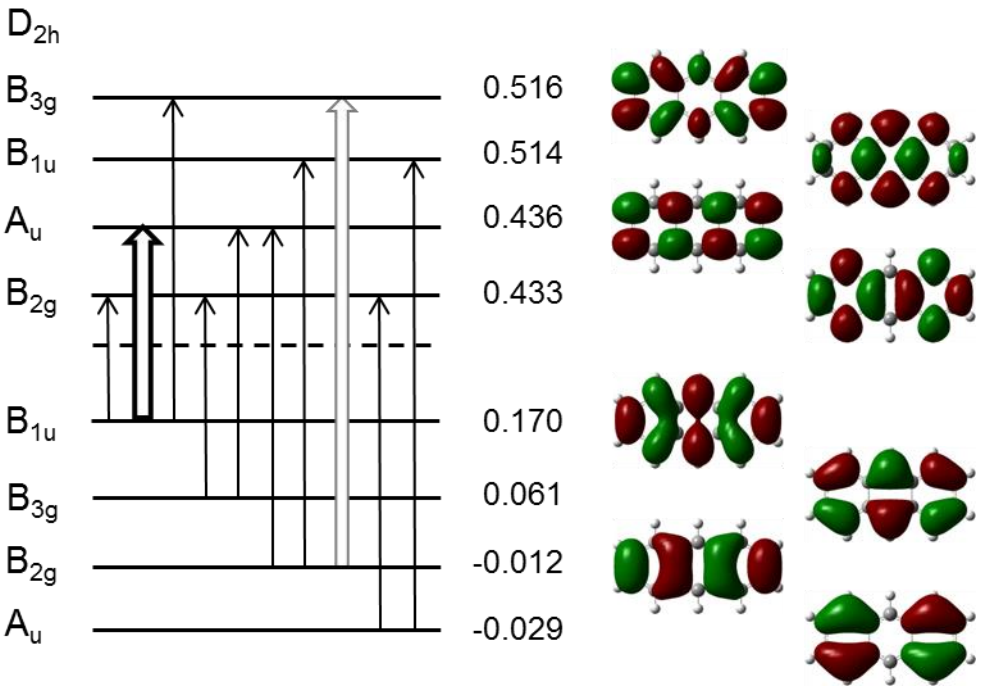

Figure 7.17. Schematic energy level diagram of D_{2h} anthracene dianion **4**. Full and hollow arrows indicate respectively translationally and rotationally allowed excitations at this symmetry. Dominant contributions to current, determined by examination of maps of individual occupied to virtual orbital transitions, are shown in bold. CMO energies in E_h and orbital nodal patterns are shown on the right of the diagram, assignments to irreducible representations on the left.

The form of plot of the NICS(xy) scan of anthracene dianion is strongly reminiscent of the mirror image of the plot for anthracene itself (Figure 7.9). All values $NICS_{\pi zz}$ are positive, which is consistent with the global antiaromaticity portrayed in the maps. In fine detail, the lower values from the NICS probes placed above the terminal rings match the weaker paratropicity seen in the maps. Some detail however is lost on the central ring, which, although accurately capturing the strong local paratropic circulation, predicts a slight fall-off of current above centre B that is not seen in the ipsocentric maps.

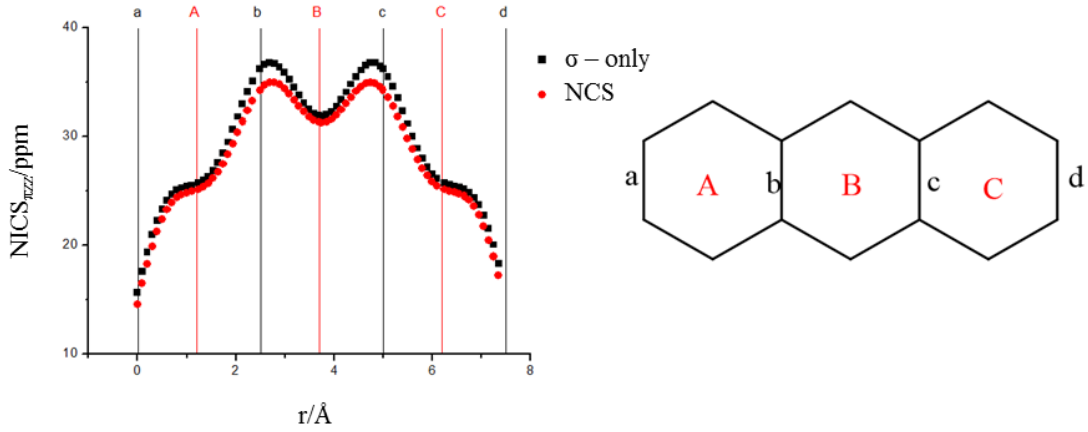

Figure 7.18. NICS(x) scan of D_{2h} anthracene dianion **4**. The NICS probe travels the length of the molecule from left to right along the mirror plane, r. r = 0 Å, the starting point of the scan, corresponds to bond a on the schematic structure. The bonds it passes through are denoted with lower case letters, ring centres with capitals. All scans are performed at a height of 1.7 Å.

5. Central NH-Substituted Anthracene

The product of central substitution of CH for NH in anthracene, D_{2h} **5**, is a transition state with an imaginary frequency ($48i$ cm^{-1}) corresponding to a bend hinged on the heteroatoms. The most notable feature of the total π current-density map (j_{max} = 0.105 a.u.) is the presence of a paratropic circulation around the central ring, as shown in Figure 7.19(a). This antiaromatic current sits in stark contrast to the rest of the molecule, for which the magnetic response can be viewed of as two separate benzene-like diatropic circulations around each of the terminal C_6 cycles. The CMO breakdown of π current shows the origin of this unusual ring current response. The contribution to current arising from the b_{1u} HOMO (Figure 7.19(b)) is a single, strong paratropic flow localised on the central ring (j_{max} = 0.090 a.u., 86% of the total π current). The diatropic circulations that dominate the remainder of the molecule arise from the lower-lying orbitals, as seen from the map of the HOMO complement, Figure 7.19(c). Reference to the schematic orbital energy level diagram, Figure 7.20, allows the origin of these effects to be understood.

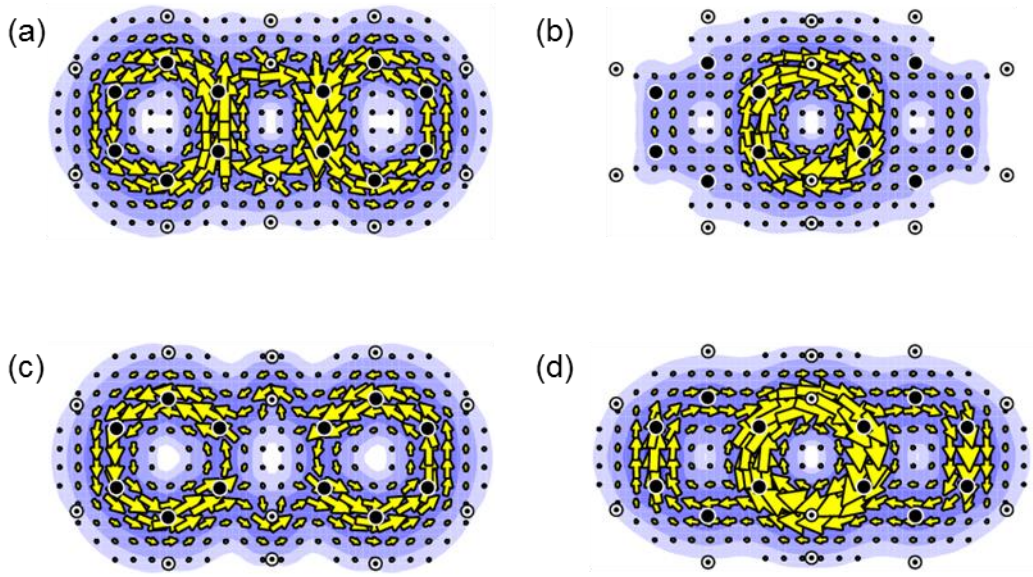

Figure 7.19. π-current analysis of the result of the substitution of the central 'peak' pair of CH for NH, D_{2h} **5**. Showing: (a) The total 16π current. (b) The contribution to total π current arising from the b_{1u} HOMO (Λ = 4). (c) The contribution to total π current arising from the complement of the b_{1u} HOMO. (d) The contribution to total π current arising from the transition between the b_{1u} HOMO (Λ = 4) and the a_u LUMO (Λ = 4). Plotting conventions are described in the text.

Once again, examination of the orbital topologies and the application of simple node-counting arguments immediately allow the nature of the current response in this molecule to be rationalised. Focusing on the nodal pattern of the HOMO on the central pyrazine moiety, a ring-localised nodal-line count, or HANC, of Λ = 2 is discernible. This count is matched, but rotated, in the LUMO. This is not, in itself, a significant observation as the selection rules state that under D_{2h} symmetry b_{1u} and a_u orbitals are related by rotational symmetry, and hence any contribution to current from such a transition would be paratropic. Figure 7.19(d) shows the result of this excitation. It is interesting to note, however, that the current shown in the map is still dominated by the flow in the central ring. Although the terminal rings show some paratropicity, the relatively poor overlap between the HOMO and LUMO on these sites renders the resulting vector current density in these parts of the molecule as insignificant, and the antiaromatic element in **5** is therefore localised entirely on the central, NH-substituted ring.

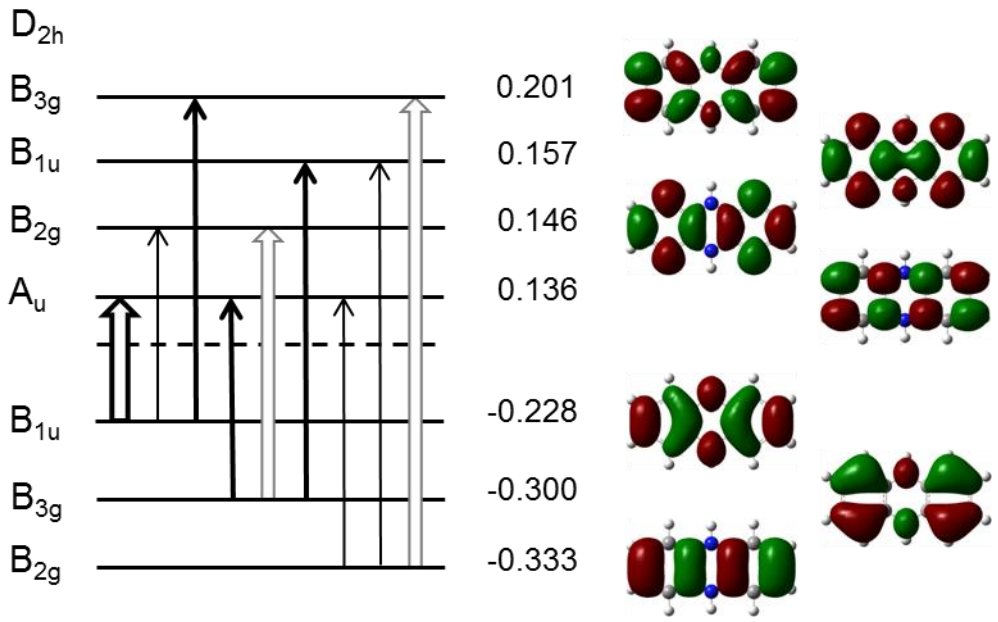

Figure 7.20. Schematic energy level diagram of the result of the substitution of the two central 'peak' CH for NH, D_{2h} **5**, showing selected allowed frontier π-π* orbital excitations. Full and hollow arrows indicate respectively translationally and rotationally allowed excitations at this symmetry. Dominant contributions to current, determined by examination of maps of individual occupied to virtual orbital transitions, are shown in bold. CMO energies in E_h and orbital nodal patterns are shown on the right of the diagram, assignments to irreducible representations on the left.

The simplest interpretation of the NICS(xy) scan for D_{2h} **5** (Figure 7.21) is a global paratropic current with two local diatropic currents on the terminal rings. If this is so, the global current is contributing 17-18 ppm, which means that the local diatropic currents would contribute approximately -25 to -26 ppm, which from the currents seen so far appears too large. Thus, a more complicated picture, essentially that of anthracene, but with a strong local paratropic current on the central ring (instead of the strong diatropic current in the central ring of anthracene) is favoured. This interpretation agrees well with what is seen in the current-density maps.

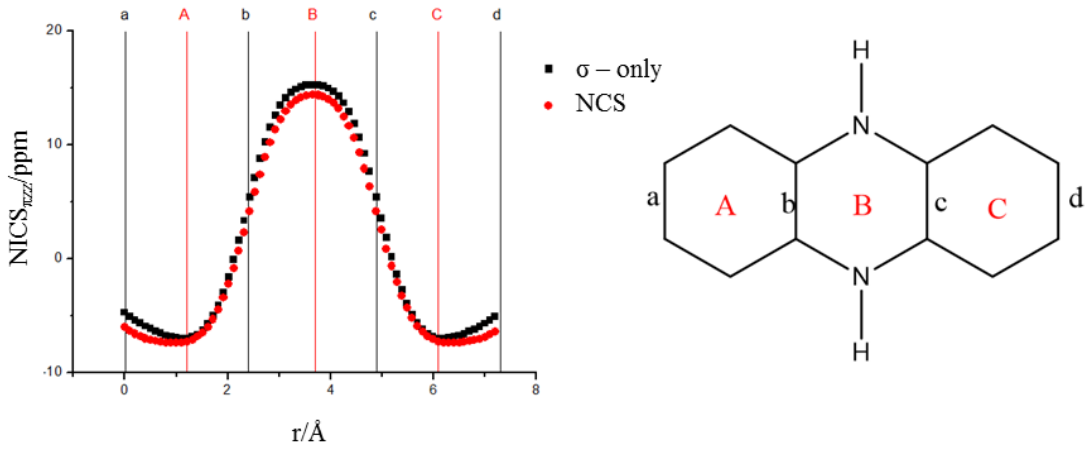

Figure 7.21. NICS(x) scan of the result of the substitution of the two central 'peak' CH for NH, D_{2h}, **5**. The NICS probe travels the length of the molecule from left to right along the mirror plane, r. r = 0 Å, the starting point of the scan, corresponds to bond a on the schematic structure. The bonds it passes through are denoted with lower case letters, ring centres with capitals. All scans are performed at a height of 1.7 Å.

6. Outer NH-Substituted Anthracene

C_{2v} **6**, in which the terminal ring is the subject of NH-substitution, is also a transition state with an imaginary frequency (146*i*) corresponding to a bend hinged on the heteroatoms. **6** displays the same substitution-site dependent local antiaromaticity as the central NH-substituted case D_{2h} **5**. The total π map Figure 7.22(a) shows an antiaromatic circulation above the pyrazine moiety and a naphthalene-like current around the remaining two cycles. Again, a CMO breakdown of the current shows that the paratropic contribution is caused by excitations from the b_1 HOMO (Figure 7.22(b)), with the oligocyclic C_{10} diatropic contribution arising from excitations from the remainder of the occupied orbitals (Figure 7.22(c)).

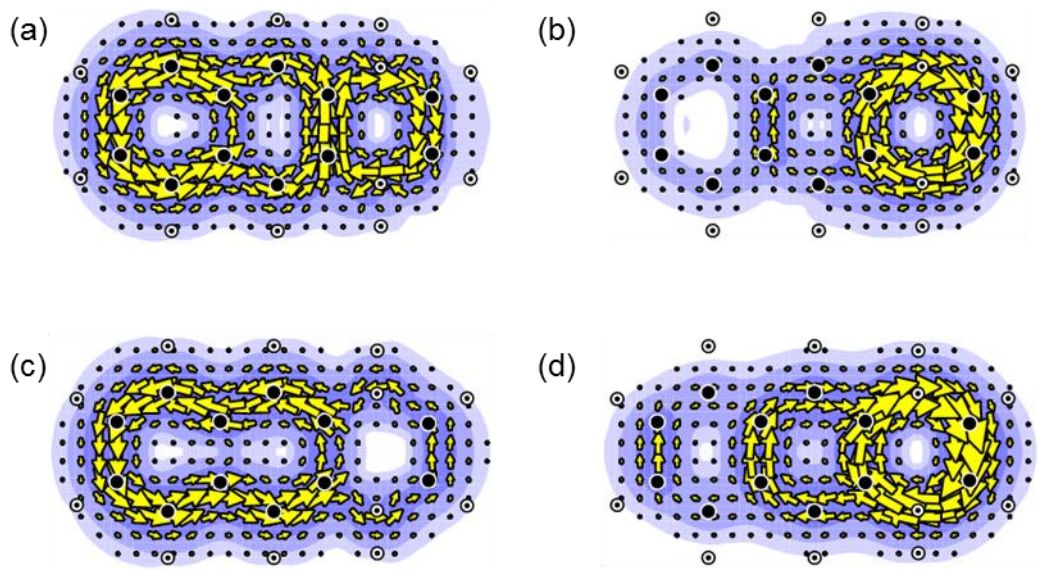

Figure 7.22. π-current analysis of the result of the substitution of an outer 'peak' pair of CH for NH, C_{2v} **6**. Showing: (a) The total 16π current. (b) The contribution to total π current arising from the b_1 HOMO (Λ = 4). (c) The contribution to total π current arising from the complement of the b_1 HOMO. (d) The contribution to total π current arising from the transition between the b_1 HOMO (Λ = 4) and the a_2 LUMO+1 (Λ = 4). Plotting conventions are described in the text.

As with D_{2h} **5**, the contrasting magnetic response in different parts of the molecule can be explained with reference to the schematic orbital energy diagram, Figure 7.23. Once again, the form of the orbital topologies, specifically the ring-localised nodal-line, or HANC, count of Λ = 2 on the terminal pyrazine moiety of the b_1 HOMO and the a_2 LUMO+1 immediately brings to light the cause of the paratropicity on the substituted ring. Figure 7.22(d) shows the contribution to ring current of this rotational transition. The map shows a strongly localised paratropic flow on the terminal ring. In the same manner as **5**, the oligocyclic regions display relatively poor overlap between the occupied and virtual orbitals, rendering the resulting paratropicity on these rings as relatively insignificant compared to that of the heterocycle. In spite of this statement, a small amount paratropic flow on the central ring in evidence. This contribution has the effect of weakening the diatropic current above this middle ring in the total π response map Figure 7.22(a).

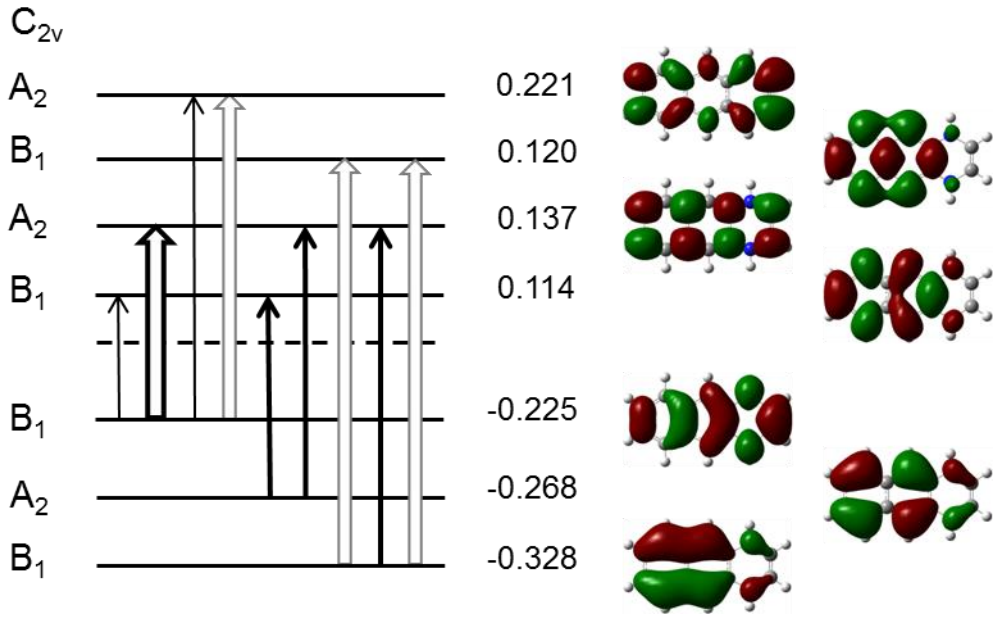

Figure 7.23. Schematic energy level diagram of the result of the substitution of an outer 'peak' pair of CH for NH, C_{2v} **6**, showing selected allowed frontier π-π* orbital excitations. Full and hollow arrows indicate respectively translationally and rotationally allowed excitations at this symmetry. Dominant contributions to current, determined by examination of maps of individual occupied to virtual orbital transitions, are shown in bold. CMO energies in E_h and orbital nodal patterns are shown on the right of the diagram, assignments to irreducible representations on the left.

The result of the NICS(xy) scan of **6**, displayed in Figure 7.24, are consistent with the patterns of current-density found in the total π map. The values displayed are negative in rings A and B, which correspond to the oligocyclic region, and positive in ring C, the pyrazine moiety. Overall, the diatropic component is predicted to be reasonably weak, with the outer ring slightly stronger than the inner, as is found in the ipsocentric calculation. The scan results can however be criticised for reporting the strength of paratropic current in excess of that of the diatropic currents, a result not found in the current density maps. Figure 7.22(a) clearly shows that the terminal C_6 ring possesses a flow of greater strength that any other ring in the molecule.

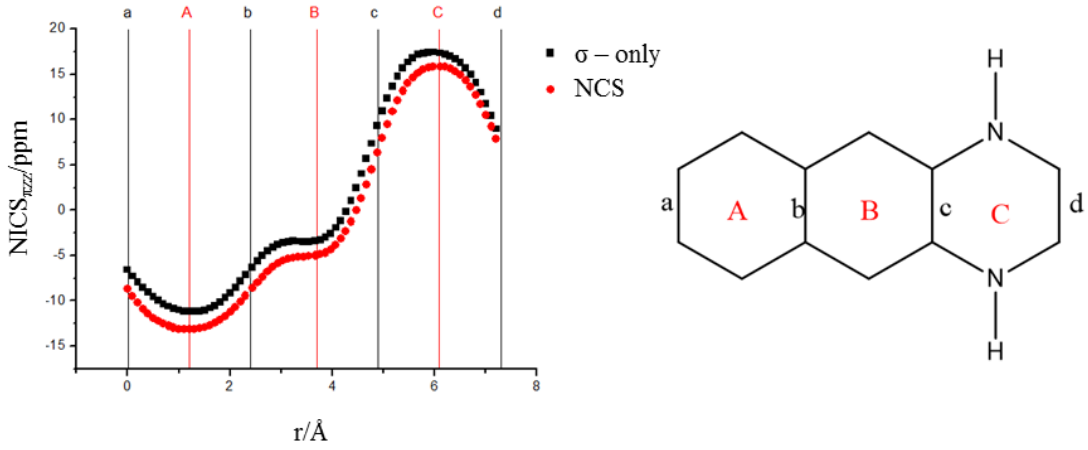

Figure 7.24. NICS(x) scan of the result of the substitution of an outer 'peak' pair of CH for NH, C_{2v} **6**. The NICS probe travels the length of the molecule from left to right along the mirror plane, r. r = 0 Å, the starting point of the scan, corresponds to bond a on the schematic structure. The bonds it passes through are denoted with lower case letters, ring centres with capitals. All scans are performed at a height of 1.7 Å.

7. Anthracene Dication

Figure 7.25 shows π-current analysis of D_{2h} anthracene dication **7**. The total π current (Figure 7.25(a), j_{max} = 0.068 a.u.) shows a very unusual pattern, an antiaromatic current of moderate strength localised on the central ring, but no coherent flow on either of the two terminal rings. CMO analysis of total current shows that the paratropic contribution from the HOMO-1 (Figure 7.25(b), j_{max} = 0.069 a.u.), which is of similar form to that of the total π response found in anthracene dianion **4** (see Figure 7.16(a)), is cancelled by the consistent, diatropic, current of the HOMO-1 complement (Figure 7.25(c)), leaving the single paratropic central flow found in the total π map.

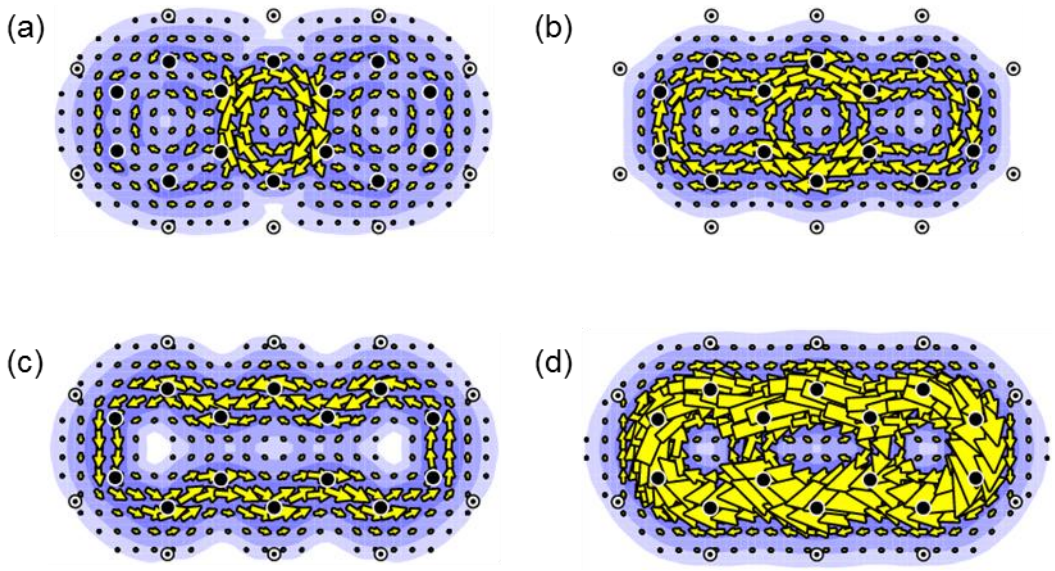

Figure 7.25. π-current analysis of D_{2h} anthracene dication **7**. Showing: (a) The total 12π current. (b) The contribution to total π current arising from the b_{2g} HOMO–1 (Λ = 3). (c) The contribution to total π current from the complement of the b_{2g} HOMO–1. (d) The contribution to total π current arising from the transition between the b_{2g} HOMO–1 (Λ = 3) and the b_{3g} LUMO (Λ = 3). Plotting conventions are described in the text.

Orbital reordering between **7** and **1** leads to the paratropicity observed in this molecule. Ordering by Λ is an approximation well suited to nearly circular molecules such as naphthalene, but becomes increasingly inappropriate in cases where splitting is significant. The difference in energy of orbitals with longitudinal and transverse nodes is consistent with a gradual shift from a particle in a circular box model to a particle in a rectangle model. In linear polyacenes this drift occurs with increasing number of hexagons. The origins of paratropicity in this molecule can be rationalised by reference to the schematic orbital energy-level diagram Figure 7.26. Orbital analysis shows that the most significant paratropic contribution to current is seen from the above CMO analysis to arise from the b_{2g} (Λ = 3) HOMO–1 (Figure 7.25(c)). This orbital is related by rotational symmetry to the b_{3g} (Λ = 3) LUMO. Spectral analysis shows the current associated with this excitation (see Figure 7.25(d)): a stronger, paratropic version of the total π current found in anthracene itself.

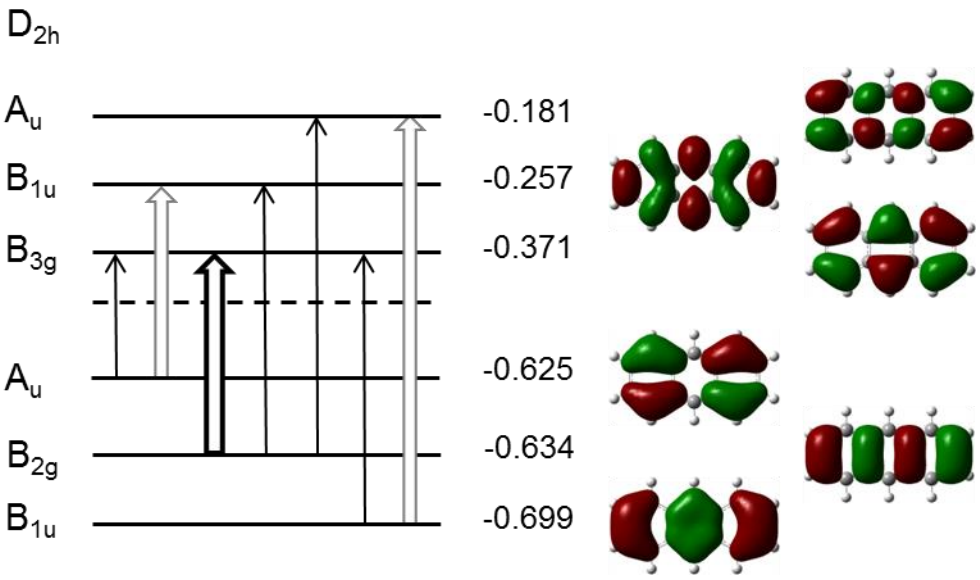

Figure 7.26. Schematic energy level diagram of D_{2h} anthracene dication **7**. Full and hollow arrows indicate respectively translationally and rotationally allowed excitations at this symmetry. Dominant contributions to current, determined by examination of maps of individual occupied to virtual orbital transitions, are shown in bold. CMO energies in E_h and orbital nodal patterns are shown on the right of the diagram, assignments to irreducible representations on the left.

Even more so than for the dianion (Figure 7.18), the plots of the NICS(xy) scan of anthracene dication strongly resemble an inversion of the plots of anthracene itself (Figure 7.9). As the magnitude of the $NICS_{\pi zz}$ values are all lower in **7** than **1**, the scan accurately captures the strong central circulation and damped outer cycles of the maps.

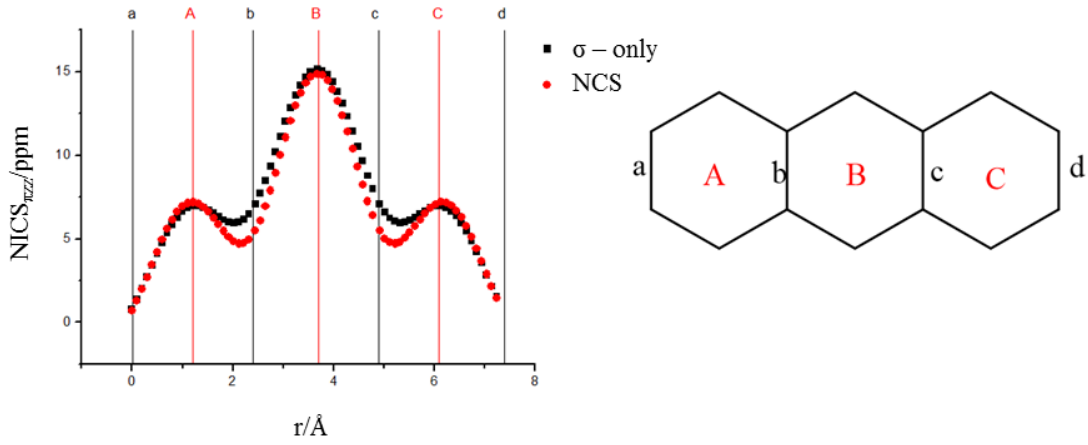

Figure 7.27. NICS(x) scan of D_{2h} anthracene dication **7**. The NICS probe travels the length of the molecule from left to right along the mirror plane, r. r = 0 Å, the starting point of the scan, corresponds to bond a on the schematic structure. The bonds it passes through are denoted with lower case letters, ring centres with capitals. All scans are performed at a height of 1.7 Å.

8. Central BH-Substituted Anthracene

BH replacement of the CH peaks, the final class of substitution considered, has the effect of isolating the current in the oligocyclic regions either side of the functional groups. In central BH-substituted anthracene, D_{2h} **8**, this results in two individual C_6 benzene-like diatropic circulations, insulated from each other, as shown in Figure 7.28(a). The strength of these two localised flows are comparable to that of benzene itself; the j_{max} value of the total π current map of **8** is 0.079 a.u., 1.01 times the strength of the benzene standard.

The CMO breakdown of π current shows the origin of localised nature of the currents. The contribution to current arising from the b_{2g} HOMO is a weak (Figure 7.28(b), j_{max} = 0.038 a.u.) paratropic circulation above the central ring, stronger above the carbon centres, and weaker above the electropositive heteroatoms.

Examination of the schematic orbital energy level diagram, Figure 7.29, explains the unusually weak HOMO contribution to current in **8**: the large energy gap between the Λ = 3 HOMO and Λ = 3 LUMO. Further CMO analysis shows the dominant effect originates in the lower-lying Λ = 2 a_u HOMO–1, the Λ = 1 b_{3g} HOMO–2 and the Λ = 2 b_{1U} HOMO–3 (see Figure 7.28(c)).

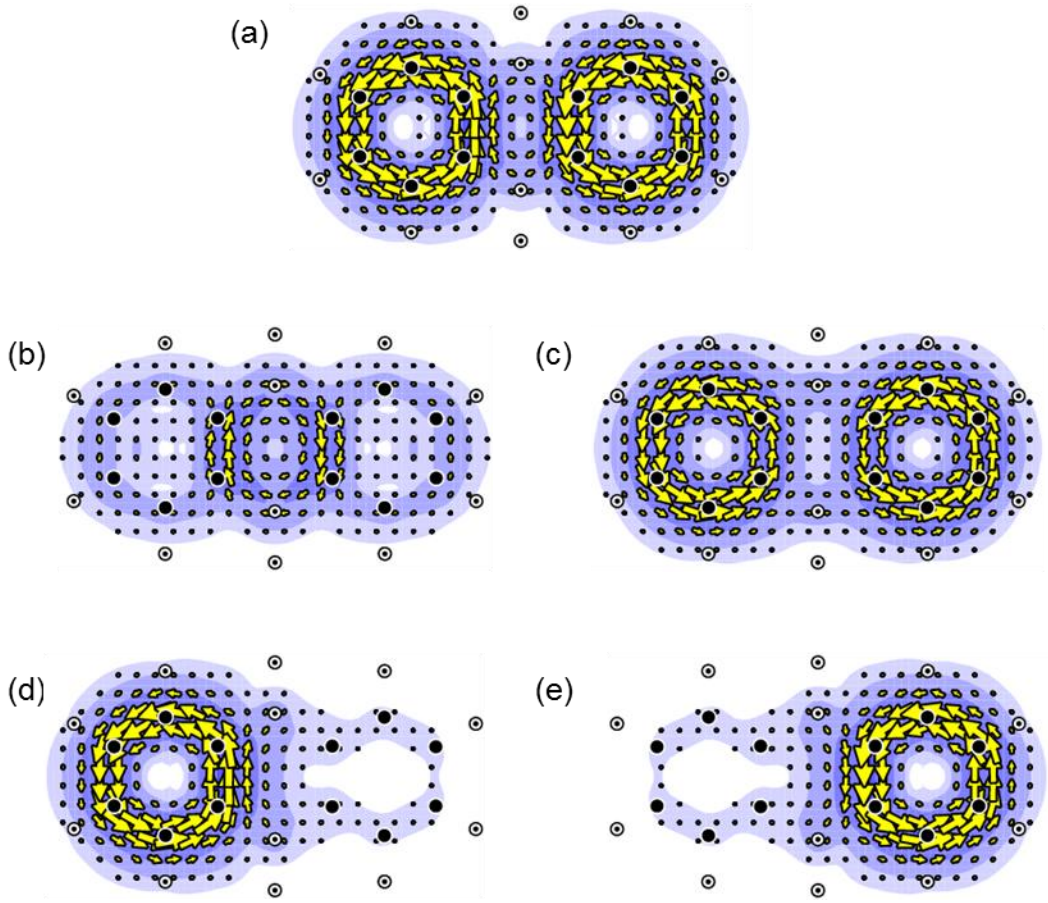

Figure 7.28. π-current analysis of the result of the substitution of the two central 'peak' CH for BH, D_{2h} **8**. Showing: (a) The total 12π current. (b) The contribution to total π current arising from the b_{2g} HOMO (Λ = 3). (c) The combined contribution to total π current arising from the a_u HOMO–1 (Λ = 2), the b_{3g} HOMO–2 (Λ = 1) and the b_{1U} HOMO–3 (Λ = 2). (d) The contribution to total π current arising from the three π LMOs localised on the left hand C_6 cycle. (e) The contribution to total π current arising from the three π LMOs localised on the right hand C_6 cycle. Plotting conventions are described in the text.

LMO breakdown of the current confirms the apparent independence of the two benzene-like circulations. Figures 7.28(d) and (e) show the contributions to current from the 3 LMOs that correspond to the left- and right-hand circulations, respectively. Summing the two maps, by definition, returns the total 12π map Figure 7.28(a). The fact that the LMO breakdown allows the construction of two 6π maps with closed circulations confirms the interpretation that the BH substitution acts as an insulating buffer to conduction in the system.

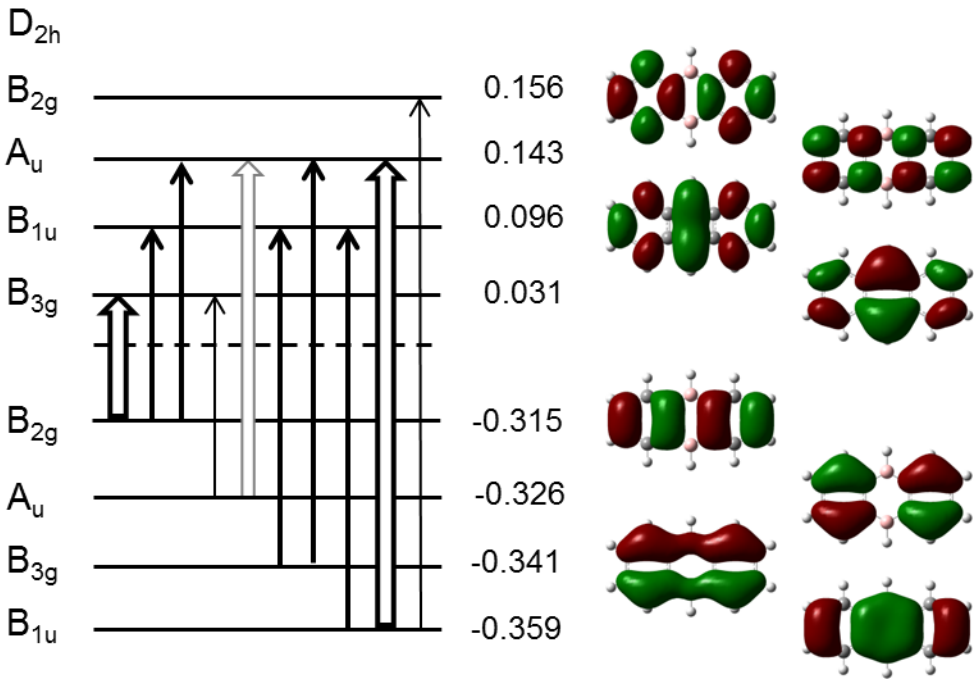

Figure 7.29. Schematic energy level diagram of the result of the substitution of the two central 'peak' CH for BH, D_{2h} **8**. Full and hollow arrows indicate respectively translationally and rotationally allowed excitations at this symmetry. Dominant contributions to current, determined by examination of maps of individual occupied to virtual orbital transitions, are shown in bold. CMO energies in E_h and orbital nodal patterns are shown on the right of the diagram, assignments to irreducible representations on the left.

The NICS(xy) scan plot of **8** (Figure 7.30) again, in a similar way to the central NH-substituted form of anthracene **5**, has a similar shape to the mirror image of the scan of anthracene **1**. The $NICS_{\pi zz}$ values indicate that the terminal rings A and B are diatropic, whilst the central ring displays some paratropicity, though again the problem with interpretation of low magnitude values persists.

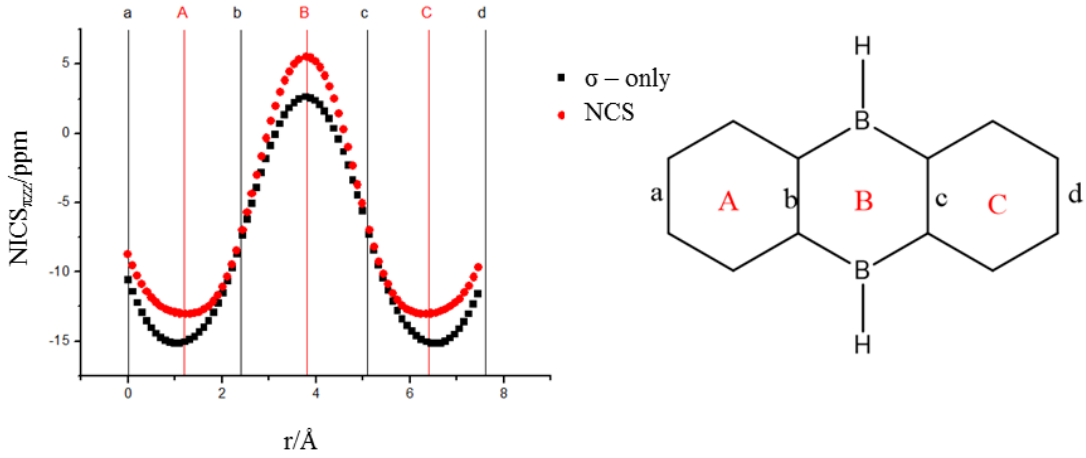

Figure 7.30. NICS(x) scan of the result of the substitution of the two central 'peak' CH for BH, D_{2h} **8**. The NICS probe travels the length of the molecule from left to right along the mirror plane, r. r = 0 Å, the starting point of the scan, corresponds to bond a on the schematic structure. The bonds it passes through are denoted with lower case letters, ring centres with capitals. All scans are performed at a height of 1.7 Å.

9. Outer BH-Substituted Anthracene

The final case, the outer BH-substituted anthracene, C_{2v} **9**, again shows the insulating effect of this functional group. The two boron atoms separate the molecule into an oligocyclic C_{10} naphthalene-like framework, and a C_2 fragment. The total π current map (Figure 7.31(a)) shows a coherent diatropic flow of current around the former, with a local, double-bond-like circulation around the latter.

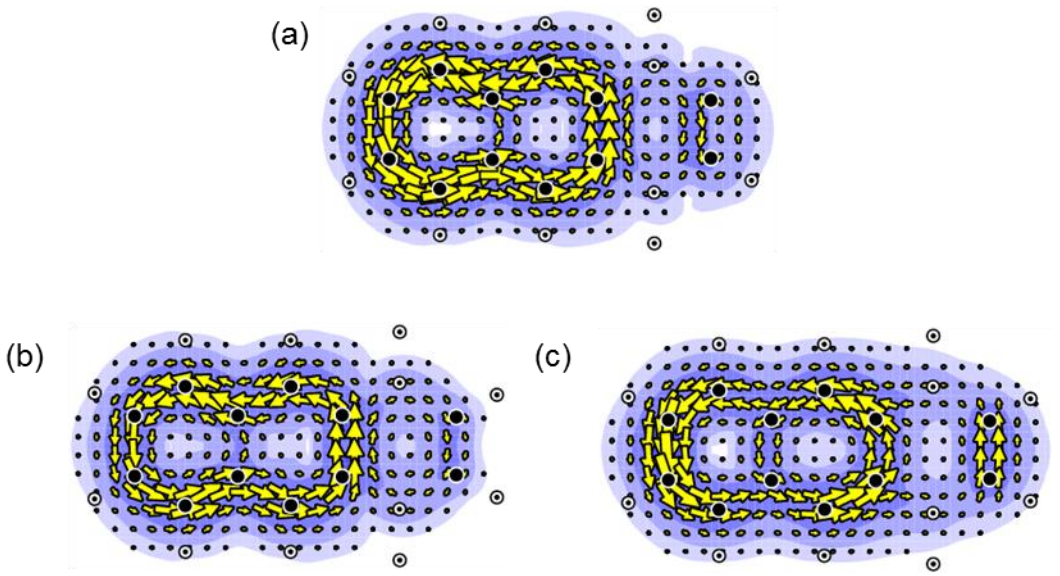

Figure 7.31. π-current analysis of the result of the substitution of an outer 'peak' pair of CH for B, C_{2v} **9**. Showing: (a) The total 12π current. (b) The contribution to total π current arising from the a_2 and b_1 HOMO pair. (c) The contribution to total π current arising from the combined four possible transitions between the a_2 and b_1 HOMO pair and the a_2 and b_1 LUMO pair. Plotting conventions are described in the text.

CMO analysis again confirms that the familiar ipsocentric arguments are once again able to rationalise the currents in this system. The a_2 and b_1 HOMO pair are predictably the origin of the dominant current effect. Spectral analysis[41] gives the precise form of the transition, node-increasing translational excitations between the a_2 and b_1 HOMO pair and the b_1 and a_2 LUMO pair. Low orbital density on the heteroatom ring in the occupied orbitals, and the relatively large energy gap across the frontier accounts for the lack of current on the functionalised terminal cycle.

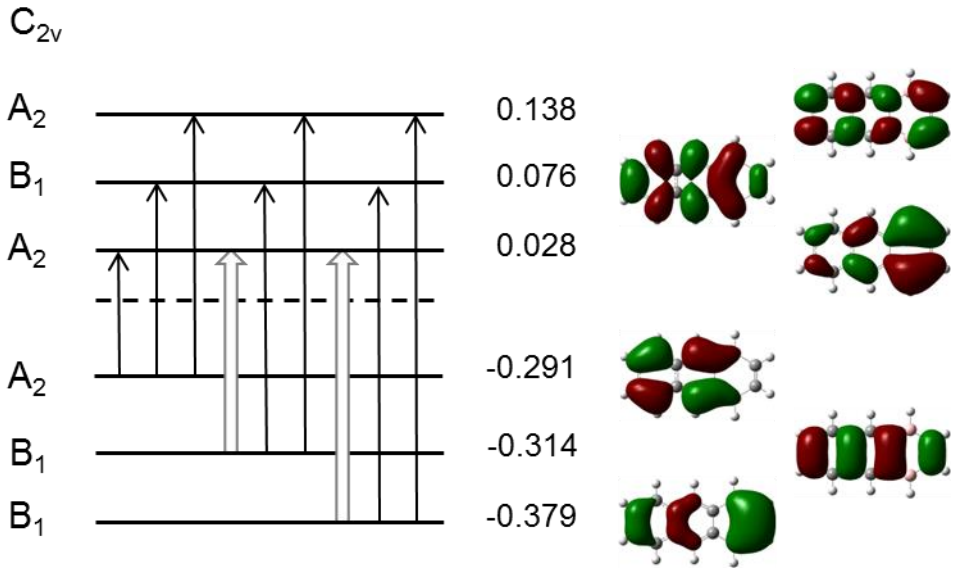

Figure 7.32. Schematic energy level diagram of the result of the substitution of an outer 'peak' pair of CH for B, C_{2v} **9**. Full and hollow arrows indicate respectively translationally and rotationally allowed excitations at this symmetry. Dominant contributions to current, determined by examination of maps of individual occupied to virtual orbital transitions, are shown in bold. CMO energies in E_h and orbital nodal patterns are shown on the right of the diagram, assignments to irreducible representations on the left.

The NICS(xy) scan of this final outer-substituted system (Figure 7.33) captures the essential features of the map of the BH-containing species as in centrally-substituted **8**. Once again low, positive, $NICS_{\pi zz}$ values in the electron-deficient heteroatom containing ring (in this case ring C) is on the cusp of non-aromaticity and antiaromaticity, whilst the remainder of the system displays the diatropicity of a naphthalene-like moiety, in accordance with the ipsocentric ring-current result in Figure 7.31(a).

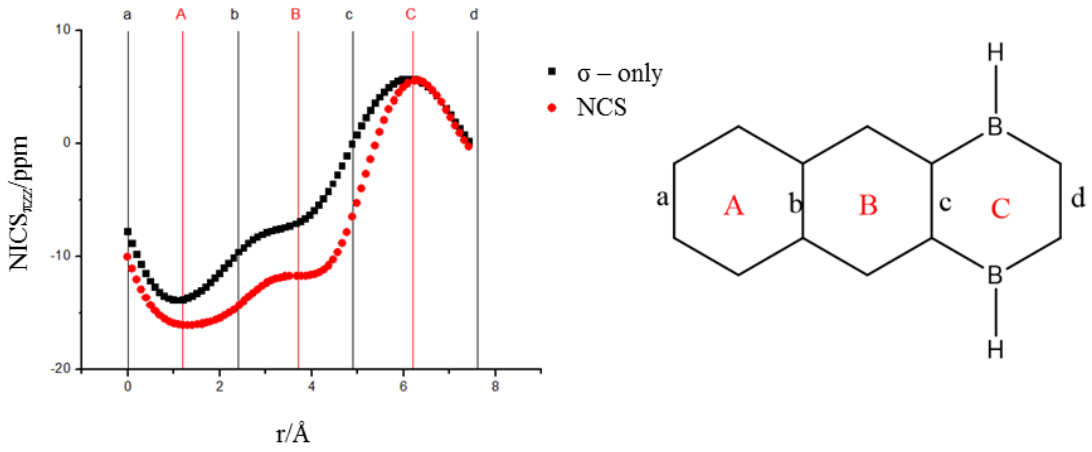

Figure 7.33. NICS(x) scan of the result of the substitution of an outer 'peak' pair of CH for B, C_{2v} **9**. The NICS probe travels the length of the molecule from left to right along the mirror plane, r. r = 0 Å, the starting point of the scan, corresponds to bond a on the schematic structure. The bonds it passes through are denoted with lower case letters, ring centres with capitals. All scans are performed at a height of 1.7 Å.

The substitutions considered in this chapter clearly offer an attractive new route to controlling ring current aromaticity in benzenoids. The analyses of the current-density maps provided in this chapter demonstrate the significance of the interplay between electronegativity and occupation in these systems. The behaviour of these new systems is once again found to be explicable by application of the powerful ipsocentric arguments.

Regarding the NICS(xy) scan methods which were applied to the nine systems examined in detail above, their utility is favourable. Although questions remain about the interpretability of the results in areas where low magnitude $NICS_{\pi zz}$ values are reported, and any form of detailed analysis of current is not possible, their ability to predict the results found in total π current density maps in linear multi-ring systems is clear.

This chapter marks the end of the main focus of the thesis. With this chapter we have now considered the effects of variations of electronic environment within a more or less fixed structure, by substitution, functionalisation and charge. The final results chapter, Chapter 8, will consider how structural change can itself provoke electronic change, with a case study of the homotropenylium cation and the *N*-homoannulenes.

Chapter 8: Structurally Tuneable Aromaticity – The Homotropenylium Cation*

Introduction

Aromaticity appears in many guises,[199,200] each with a signature ring current. In the case of the archetypal 6π-homoaromatic homotropenylium cation (**1**, $C_8H_9^+$, see Figure 8.1(a) and Figure 8.2),[201–205] proposed aromaticity of the system is corroborated by current-density maps which show a π ring current of a peculiar character.[206] At the equilibrium geometry of this molecule, a double horseshoe of conventional π current pinches down to a single σ current that flows through space under the conjugation-breaking CH_2 bridge. The experimental evidence for the horseshoe π current in **1** is based on the difference in ^{1}H chemical shifts δ_{exo} and δ_{endo} for the two types of bridge methylene site.[207] Measurement is complicated by experimental difficulties, but the estimated shift of $\Delta\delta = \delta_{endo} - \delta_{exo} = 5.8$ ppm is supported by *ab initio* calculation (IGLO/6-31G**//HF/6-31G*: $\Delta\delta = 5.1$ ppm[208]). Equivalent conformations of the homotropenylium cation, **1**, are formally linked by inversion of the methylene bridge, which swaps *exo* and *endo* ^{1}H nuclei, and can be envisaged as proceeding via an 8π C_{2v}-symmetric transition state (**2**), over a relatively high barrier of 93 kJ/mol.[209] An alternative 'circumambulant' process for this transition was raised, and then discounted, by Berson and Jenkins.[210]

* Some of the material in this chapter has been published in: Gibson, C. M.; Havenith, R. W. A.; Fowler, P. W. and Jenneskens, L. W. *J. Org. Chem.* 2015, **80**, 1395-1401. The chapter contains additional systems, figures, current-density maps, and discussion.

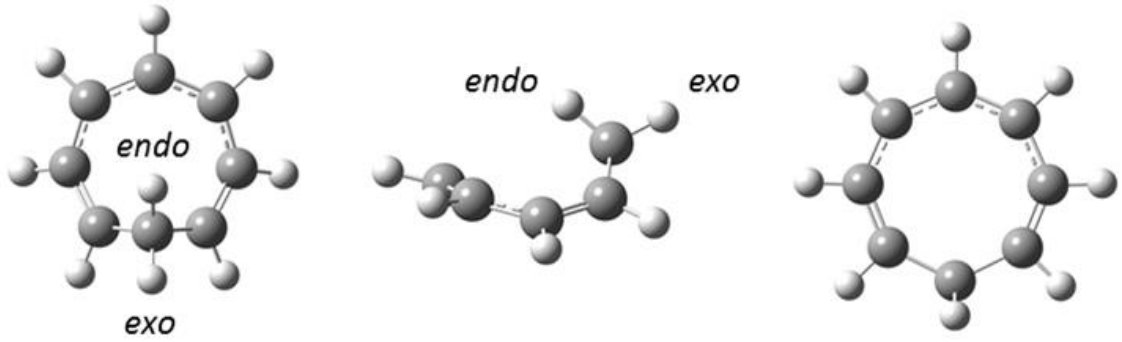

Figure 8.1. Optimised structures of two conformations of the homotropenylium cation $C_8H_9^+$: (a) C_s equilibrium structure, **1**, (orthogonal views, identifying bridge *exo* and *endo* positions), and (b) C_{2v} transition state, **2**.

More recently, in a computational study of benzylic and cyclic delocalised cations,[211] the C_{2v} transition state, **2** (see Figure 8.1(b) and Figure 8.2, noting the strong short/long bond alternation), was found to exhibit a positive NICS(0)[11] of +11.0 ppm at the GIAO-SCF/6-31+G*//B3LYP/6-311+G** level of theory, which would generally be taken as indicative of canonical π antiaromatic character. This value mirrors the negative NICS(0) of -11.1 ppm at the same level of theory for the equilibrium structure, C_s **1**.[211] Alternative explanations of this reversal of NICS values have been offered,[211] but we find here that explicit calculation of ring current confirms the obvious implication of magnetic antiaromaticity of **2**. Further evidence comes from calculations by Cremer *et al.,*[208] who found a significant difference in magnetisability, χ, between the equilibrium (IGLO/6-31G**//HF/6-31G*: **1** $R(C_1...C_7)$ = 2.285 Å, ($\chi/ 10^{-6}$ cm^3mol^{-1}) = 86.4 calc.,[208] 72 exp.[212]) and transition-state (IGLO/6-31G**//HF/6-31G*: **2**, $R(C_1...C_7)$ = 2.675 Å, $\chi/10^{-6}$ cm^3mol^{-1} = 52.9[208]) structures; in view of our results, this difference also points to ring-current antiaromaticity of the transition state.

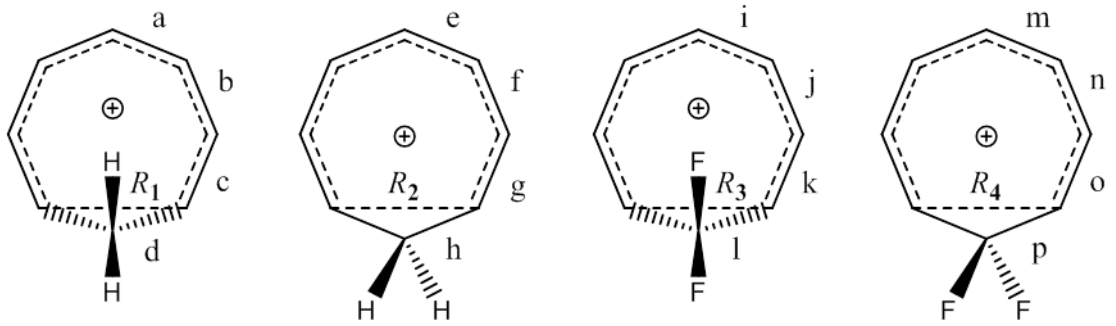

1 **2** **3** **4**

Figure 8.2. Schematic representations and salient structural features of systems **1** to **4**. Bond lengths are given in Å. R_x refers to the through-space distance between the carbon centres at either side of the 'bridge'. (a) 1.402;[206] (b) 1.405;[206] (c) 1.382;[206] (d) 1.490;[206] (e) 1.393; (f) 1.429; (g) 1.360; (h) 1.501; (i) 1.400; (j) 1.413; (k) 1.373; (l) 1.494; (m) 1.394; (n) 1.425; (o) 1.360; (p) 1.497; (R_1) 2.127;[206] (R_2) 2.689; (R_3) 2.254; (R_4) 2.701.

Thus, we have the interesting situation of *reversal of aromaticity* along a reaction coordinate, corresponding to inter-conversion of aromatic systems *via* an antiaromatic transition state. In this chapter, direct theoretical evidence for the paratropic (antiaromatic) character of the C_{2v} transition state is presented, and it is shown that this character is critically dependent on the energies of the CH bonds of the CH_2 bridge, which have a π-like combination that can interact with the π system of the ring. This energy match would not be found in the CF_2-bridged analogues of **1** and **2** (*i.e.,* **3** and **4**, Figure 8.2), and the transition state **4** is accordingly found to be weakly diatropic (aromatic). Here, calculations will be used to document the reversal of aromaticity between **1** and **2**, and to suggest a general model for rationalising the net tropicity of planar-constrained homoannulenes. The observation that a bridge can behave as a pseudo-π donor in these cases, with a CH_2 bridge donating two electrons,[213] will be useful here.

Methods

Geometries of all structures were optimised at the B3LYP/6-31G** DFT level using Gaussian09.[40] Minima and transition states were identified by Hessian calculations. In terms of the potential energy surface, if local minimum C_s **1** is taken as the zero of energy, C_{2v} **2** is a transition state (with a single imaginary frequency of 125*i* cm^{-1}) with a relative energy of 91 kJ mol^{-1} (corrected for zero-point vibration). The F_2-bridge structures C_s **3** and C_{2v} **4** are also a local minimum and a transition state (relative energy corrected for zero-point vibration 70 kJ mol^{-1}, with single imaginary frequency 51*i* cm^{-1}), respectively. All other structures will be introduced later in the Chapter. Subsequently, current-density maps were calculated at the same level of theory using the ipsocentric approach (B3LYP/6-31G**//B3LYP/6-31G**)[144] implemented in the GAMESS-UK[62] and SYMSO[39] packages, as previously used for **1**.[206] The advantages of this method for calculation of currents, in terms of economy and interpretability are well documented,[27,36] and have already been discussed at length. As is a running theme of the thesis, a key feature in the application to **1** and **2** is the possibility of using either *canonical* or *localised* molecular orbitals (CMOs and LMOs) to partition total π current density. This again proves to be essential in the understanding of the maps.

The maps themselves are presented with the following plotting conventions: arrows show the current density resolved into the plotting plane, which as standard is $1a_0$ above the mean molecular plane; contours show the modulus of the full current-density vector. Nuclear positions, resolved into the plotting plane, are represented by the elemental symbols shown in Figure 2.1.

Results and Discussion

In the C_s-symmetric system, **1**, there is no formal separation of σ and π molecular orbitals, and the CMOs necessarily have mixed character. However, each carbon atom not involved in the methylene bridge has three co-planar single bonds,[206] allowing definition of an orthogonal π atomic orbital on each centre[214] and construction of π-like localised molecular orbitals (LMOs) by combination. Nearest-neighbour interactions are of p_π-p_π type around the formally conjugated portion of the ring but have p_σ-p_σ character in the C_1…C_7 bridge region. Pipek-Mezey localisation[43] was used to find these combinations and their contributions to current.[61] The Pipek-Mezey LMOs for **1** here include three ring-localised π-like occupied orbitals, contributing both the horseshoe of conventional π ring current and the single stream of current crossing from carbon C_1 to C_7 under the methylene bridge, as seen in Figure 8.3. Note that the two CH bonds in the bridge give rise to two LMOs which contribute neither to the π current around the ring nor to the current crossing the $R(C_1…C_7)$ gap in C_s **1**.[206] However, in the C_{2v} symmetry of **2**, these CH-bonding orbitals may make a contribution (see below).

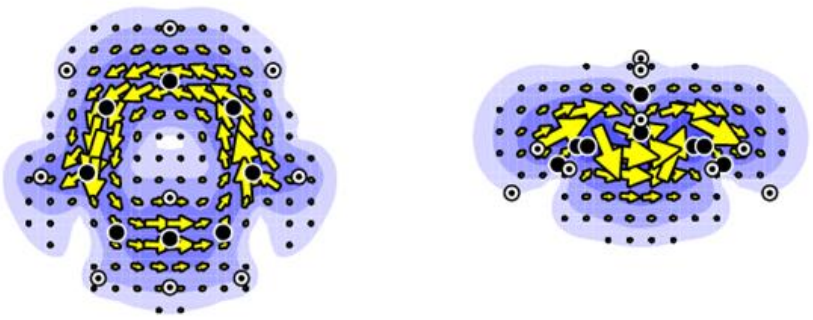

Figure 8.3. Diatropic ring current in the energetic minimum of the homotropenylium cation **1**, attributable to the combined contributions of the three occupied π-like localised molecular orbitals obtained from the Pipek-Mezey procedure. (a) The horseshoe current in the ring: current density at 1.75 a_0 below the $C_1…C_3…C_5…C_7$ reference plane[206] on the side away from the bridge (j_{max} = 0.092 a.u.). (b) The gap-crossing current under the bridge: current density in a plane perpendicular to the $C_1…C_3…C_5…C_7$ reference, 1 a_0 away from the $C_1…C_7$ centres, on the *endo* (ring) side of the bridge (j_{max} = 0.101 a.u.). Plotting conventions are described in the text.

The transition state **2** has C_{2v} symmetry, and hence a well defined σ/π separation. Figure 8.4 shows the calculated π current maps for this system. The gap-jumping diatropic ring current of **1** has disappeared, and has been replaced by a paratropic circulation that follows closely the line of carbon centres, with strength 0.096 a.u. (as measured by j_{max}, the maximum in the plane of current density per unit inducing external magnetic field), 1.2 times that of the diatropic standard benzene current (j_{max} = 0.079 a.u. at this level of theory).

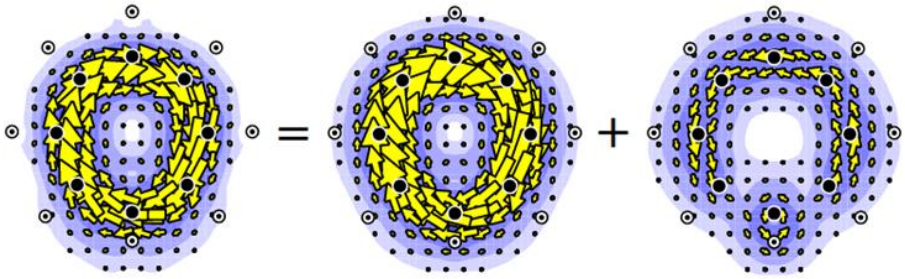

Figure 8.4. CMO contributions to current density of C_{2v} transition state **2**, from: (left) all four occupied π-orbitals, (centre) the paratropic π-HOMO and (right) the diatropic π complement of the HOMO (i.e., the left map *minus* the central map). Orbitals of π character are defined solely by their symmetry with respect to reflection in the plane of the ring. Plotting conventions are described in the text.

Under the ipsocentric approach, in which total current density is partitioned into orbital contributions governed by rotational and translational symmetry selection rules,[33,61] the paratropic current is seen to arise almost entirely from the π-π* HOMO-LUMO induced virtual excitation, which corresponds to a transition across a split pair with orbital angular momentum Λ = ±2, and is thus rotationally allowed as it preserves the number of angular nodes in the active π orbitals (Δ|Λ| = 0). There is a close analogy between this current and the characteristic antiaromatic current of the eight-membered cyclooctatetraene (COT) ring in planar geometries (Figure 2.9),[33] which again arises from a split pair with Λ = ±2 (see Figure 2.11). In exact analogy with planar-constrained COT, the main paratropic HOMO contribution to π current in **2** (Figure 8.4) is partially cancelled by a weaker diatropic circulation arising from translationally allowed Δ|Λ| = 1 virtual excitations into the LUMO from orbitals

lying immediately below the HOMO (Figure 8.4). The HOMO contribution itself is dominated by the HOMO-LUMO virtual excitation, as confirmed by spectral decomposition[41] (see Figure 8.5). Seen in this way, **2** offers a textbook example of how the two-electron paratropic current arises in an 8π system.

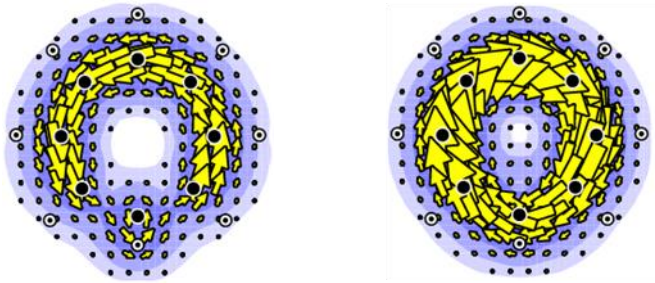

Figure 8.5. Spectral analysis of the canonical contributions to π currents of the C_{2v} planar transition state **2** ($C_8H_9^+$). (a) all occupied π-orbitals *minus* the contribution of the in-plane rotational HOMO to LUMO transition, and (b) the contribution of the in-plane rotational HOMO to LUMO transition. Their sum equals the total π-map in Figure 8.3. Plotting conventions are descrbed in the text.

The total current can also be described in a basis of LMOs. This LMO description is less economical but more revealing. The occupied molecular orbitals of π symmetry span $a_2 + 3b_1$ in C_{2v} **2**, and correlate with the three occupied π orbitals of a heptatriene moiety *plus* the antisymmetric combination of the CH bonds of the methylene bridge. As Figure 8.6 shows, these four orbitals taken together give rise to the closed paratropic ring current, with the heptatriene-like LMOs contributing the open horseshoe of π ring current as in **1**, and with continuity of the twin-loop circulation supplied by the π orbital of the CH_2 bridge.

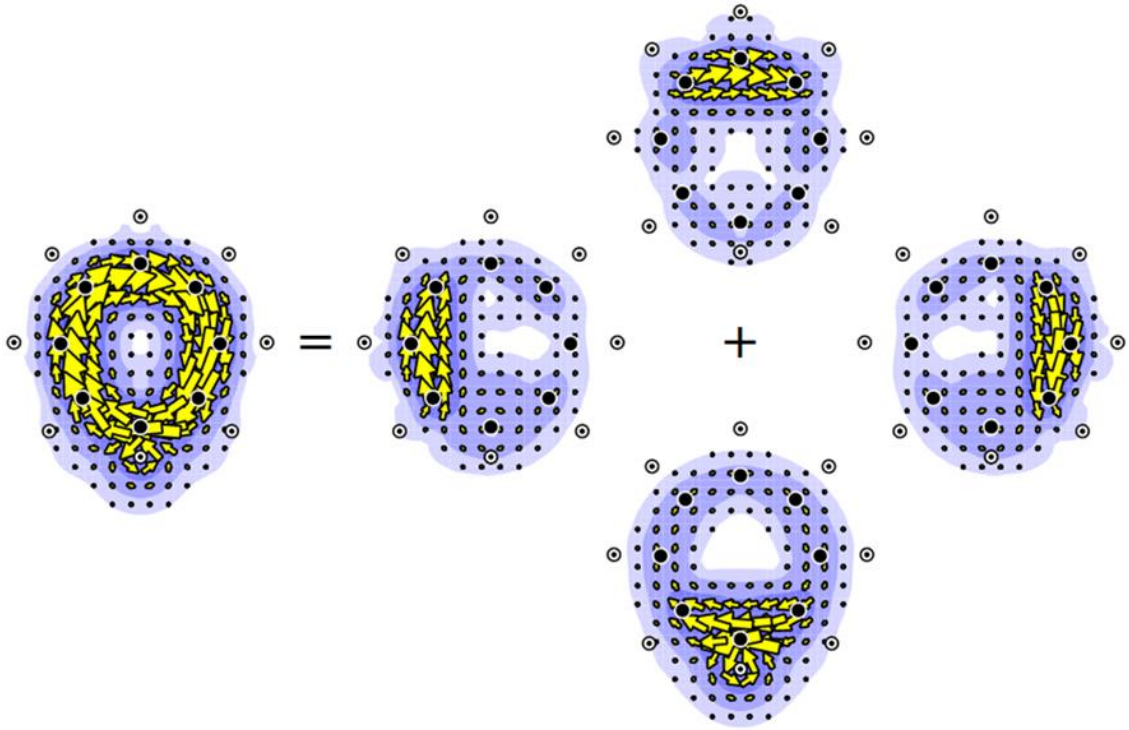

Figure 8.6. LMO breakdown of the π-current in the C_{2v} transition state **2**. (left) The total (five-LMO) π current map. (right) Maps corresponding to the three LMO contributions to the 'horseshoe' of π ring current, and the current from the CH-bridge bond LMO contributions that complete the circulation (bottom). Plotting conventions are described in the text.

Attention should be drawn to a small technical point alluded to earlier concerning the way that current arising from the CH-based π-like orbital is calculated. The localisation procedure produces *two* spatially separated CH bonds (rather than σ and π combinations). Inclusion of *both* LMOs is therefore necessary for the maps shown in Figure 8.6; these orbitals make equal contributions to the two loops of π ring current, but their in-phase combination also gives rise to a small diatropic σ current concentrated in the region *exo* to the bridge. This inevitable CH-based σ contamination accounts for the small differences between the canonical (four-orbital) and localised (five-orbital) π maps shown in Figures 8.4(left) and 8.6(left), respectively. However, both are describing what is effectively a pseudo [8]annulene containing 8 pseudo π-electrons. In contrast with homoaromatic **1**, the bridge in **2** is active in transmission of the current, leading to hyperaromaticity/antiaromaticity[215] (also known as hyperconjugative aromaticity/ antiaromaticity[213]). A pictorial model (Figure 8.7) can account

qualitatively for the variation of the main features of the currents along the C_s-to-C_{2v} reaction coordinate **1**-to-**2**: the carbon centres at the 'ends' of the bridge (*i.e.*, C_1 and C_7) have planar sp^2 bonding with p_σ-p_σ overlap across the gap,[206] and the π combination of CH bonds is not sterically available. As the system moves along the inversion coordinate, p_π functions at the ends of the bridge *dis-rotate* towards parallel alignment with each other, and concomitantly the CH_2 group descends into the widening gap between carbon centres C_1 and C_7. In the limit, the cyclic '6π' system, completed by a $\beta_{\sigma\sigma}$ C-C resonance integral across the gap, becomes an '8π' system with two $\beta_{\pi\pi}$ C-H integrals crossing the gap.

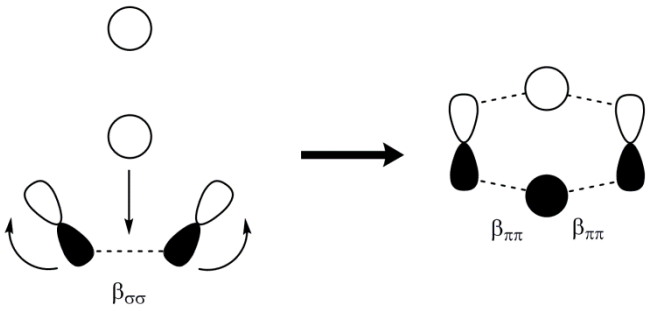

Figure 8.7. Pictorial model for the transformation between homoaromatic '6π' C_s **1** and hyperantiaromatic '8π' C_{2v} **2**. During the geometric change, the CH_2 bridge descends, breaking the $\beta_{\sigma\sigma}$ link of **1** and forming two $\beta_{\pi\pi}$ links, resulting in the complete 'π' conjugation of **2**.

An IRC-following calculation suggests that the switchover from diatropic to paratropic ring current takes place roughly halfway along the intrinsic reaction coordinate defined by the end geometries of **1** and **2**.[216]

The crucial rôle of the CH bonds in the providing continuity in the paratropic ring current of **2** is already evident from this localised analysis and is confirmed by comparison with an analogous system where there are CF bonds in the bridge. This fluorinated system **3** also has C_s symmetry at equilibrium ($R(C_1 \ldots C_7)$ = 2.254 Å) and supports a homoaromatic ring current with the pinched signature found in **1** (Figure 8.8).[206]

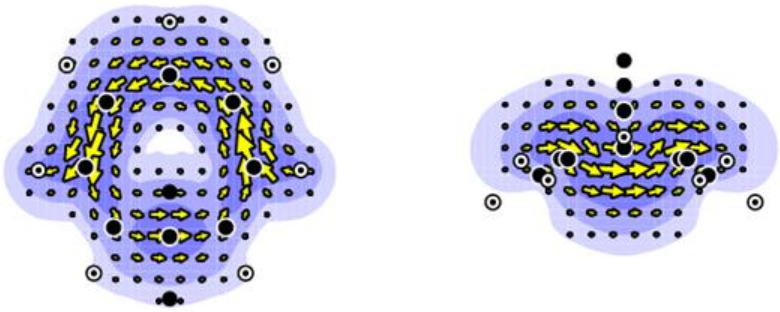

Figure 8.8. Diatropic ring current for the bridge-fluorinated analogue, **3**, of the homotropenylium cation. Current is attributed to the three occupied π-like orbitals obtained from the Pipek-Mezey procedure. (left) The horseshoe π current in the ring: current density 1.75 a_0 below the $C_1\cdots C_3\cdots C_5\cdots C_7$ reference plane[206] on the side away from the bridge (j_{max} = 0.058 a.u.). (right) The gap-crossing current under the bridge: current density in a plane perpendicular to the $C_1\cdots C_3\cdots C_5\cdots C_7$ reference, 1 a_0 from the $C_1\cdots C_7$ centres on the *endo* (ring) side of the bridge (j_{max} = 0.046 a.u.). Plotting conventions are described in the text.

The C_{2v}-symmetric transition state **4**, however, for interconversion of minima **3**, is strikingly different from **2** in that it displays a *weak diatropic* rather than a *strong paratropic* current. As Figure 8.9 shows, the total π current in **4** is dominated, not by the π-HOMO orbital contribution, which is still (albeit weakly) paratropic, but by the diatropic contribution from the HOMO-complement. As before, this analysis is confirmed by spectral analysis of the π current (Figure 8.10).

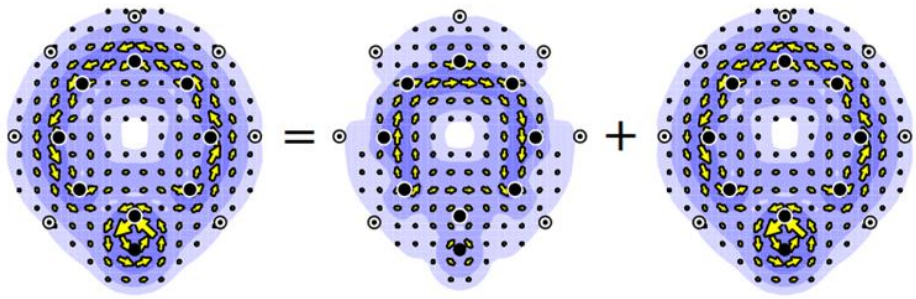

Figure 8.9. CMO contributions to current density of the bridge-fluorinated C_{2v} transition state, **4**, arising from (left) *all* occupied orbitals of π symmetry, (centre) the paratropic π-HOMO and (right) the diatropic HOMO complement (the difference of the left map *minus* the central map). Plotting conventions are described in the text.

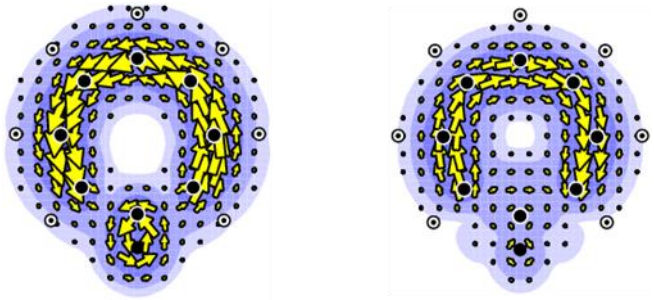

Figure 8.10. Spectral analysis of the contributions to canonical π currents of the C_{2v} planar transition state **4** ($C_8H_7F_2^+$). Showing (a) all occupied π-orbitals *minus* the contribution of the in-plane rotational HOMO to LUMO transition, and (b) the contribution of the in-plane rotational HOMO to LUMO transition. Their sum equals the total π-map in Figure 8.7. Plotting conventions are descrbed in the text.

Comparative analysis of the frontier orbitals for **2** and **4** reveals the source of this discrepancy. The HOMO-LUMO gap is *larger* in **4** (Δ_{HL} (**2**) = 2.62 eV, Δ_{HL} (**4**) = 3.34 eV), and there is an accompanying *change in topology* of the HOMO; in **2** the HOMO-LUMO excitation is almost purely rotational in character, as both orbitals have four lobes on each face of the ring, one localised on the CH_2 fragment, whereas in **4** reduced participation of the CF_2 fragment leads to a HOMO that has three lobes on each ring face and a poorer rotational match to the LUMO (see Figure 8.11). Both effects contribute to attenuation of the orbital paratropic current: if the energy difference is too large, continuity of the current will be disrupted; if the nodal character is unchanged, the sense of the current will not be reversed. In the CF_2 analogues of **1** and **2**, the π combination of CF bonds has a lower energy, resulting in poorer interaction with the ring π orbitals, even in the optimal alignment of the planar transition state (Figure 8.11).

An interesting alternative interpretation of the effect of substitution of F for H is proposed by Fernández *et al.*[213] who suggest that the CR_2 unit in charge-neutral planar bridged cyclopolyenes *always* provides a pseudo-π orbital, and adds two to the 'π' electron count for R = H, but zero for electronegative R = F. This binary choice concentrates on electron counting rather than the subtle continuous variation of orbital energetics and topology and is based on a choice of only three bridge groups.

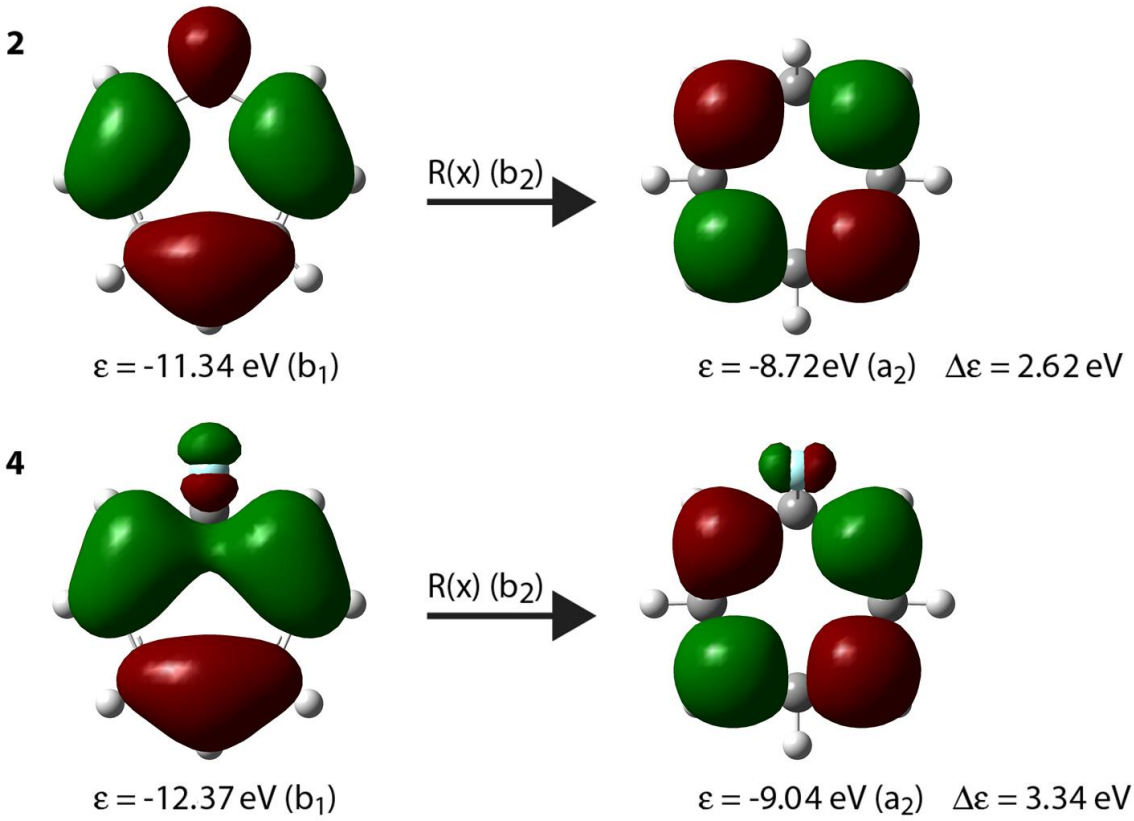

Figure 8.11. Contour plots of the HOMO and LUMO of the planar C_{2v} transition states **2** and **4**, illustrating the poorer rotational match in **4**.

Generalisations

Similar reasoning can be applied to give a model of currents in the planar-ring geometries of analogues of **2** and **4**, allowing for different ring sizes and electron counts. Consider a C_{2v} symmetric structure for the species $(CR_2)C_{N-1}H_{N-1}^{q}$, derived formally by insertion of a (CR_2) bridge in a C-C bond of a (possibly charged) [*N*-1]annulene. The precise form taken by the model for ring current in this species depends on the role assigned to the bridge. In the version implied by the interpretation of Fernández *et al.*,[213] the bridge is assumed to provide a pseudo-π orbital compatible in energy with the conventional sp^2 π system of the remainder of the ring. Differences between CR_2 bridges are attributed to differing numbers of electrons donated by the bridge, governed by changes in relative electronegativity of R. The

(CR_2)-bridged C_{2v} structure is then a pseudo-[*N*]annulene. Counting gives $n_\pi = N - 1 - q + \delta$ electrons in the π system, where δ is the number of electrons donated by the (CR_2) group. In the case of CH_2 or $C(SiMe_3)$, the bridge is taken to donate two electrons, but in the case of CF_2, none.[213] Ring currents in the species $(CR_2)C_{N-1}H_{N-1}^{\ q}$ can then be derived from the ipsocentric model for annulenes.[33]

When n_π is divisible by 4, i.e., $n_\pi \equiv 0 \bmod 4$, the π HOMO and LUMO for this planar geometry are members of a split angular momentum subshell and hence are connected by a rotationally allowed transition, giving rise to a paratropic HOMO current in the ipsocentric model.[33] Conversely, when $n_\pi \equiv 2 \bmod 4$, the HOMO-LUMO transition is translationally allowed and the HOMO current is diatropic. Thus, for fixed *N* and *q*, if the CH_2-bridged species is paratropic, the CF_2-bridged species is diatropic, and *vice versa*. Current strengths will differ, as the active virtual excitations span energy gaps of different sizes.

To test this electron counting scheme, calculations were carried out on an extended series of either neutral or charged systems $(CR_2)C_{N-1}H_{N-1}^{\ q}$, with R = H and F, *N* = 3 to 10 and *q* = -1, 0, +1, with $q = 0$ for odd *N*, and $q \neq 0$ for even *N*, making 24 closed-shell systems in all (see Figure 8.12, arranged according to Figure 8.13). Structures with the ring constrained to planarity were optimised at the B3LYP/6-31G** level and ipsocentric current-density maps were computed at the CTOCD-DZ/B3LYP/6-31G** level.

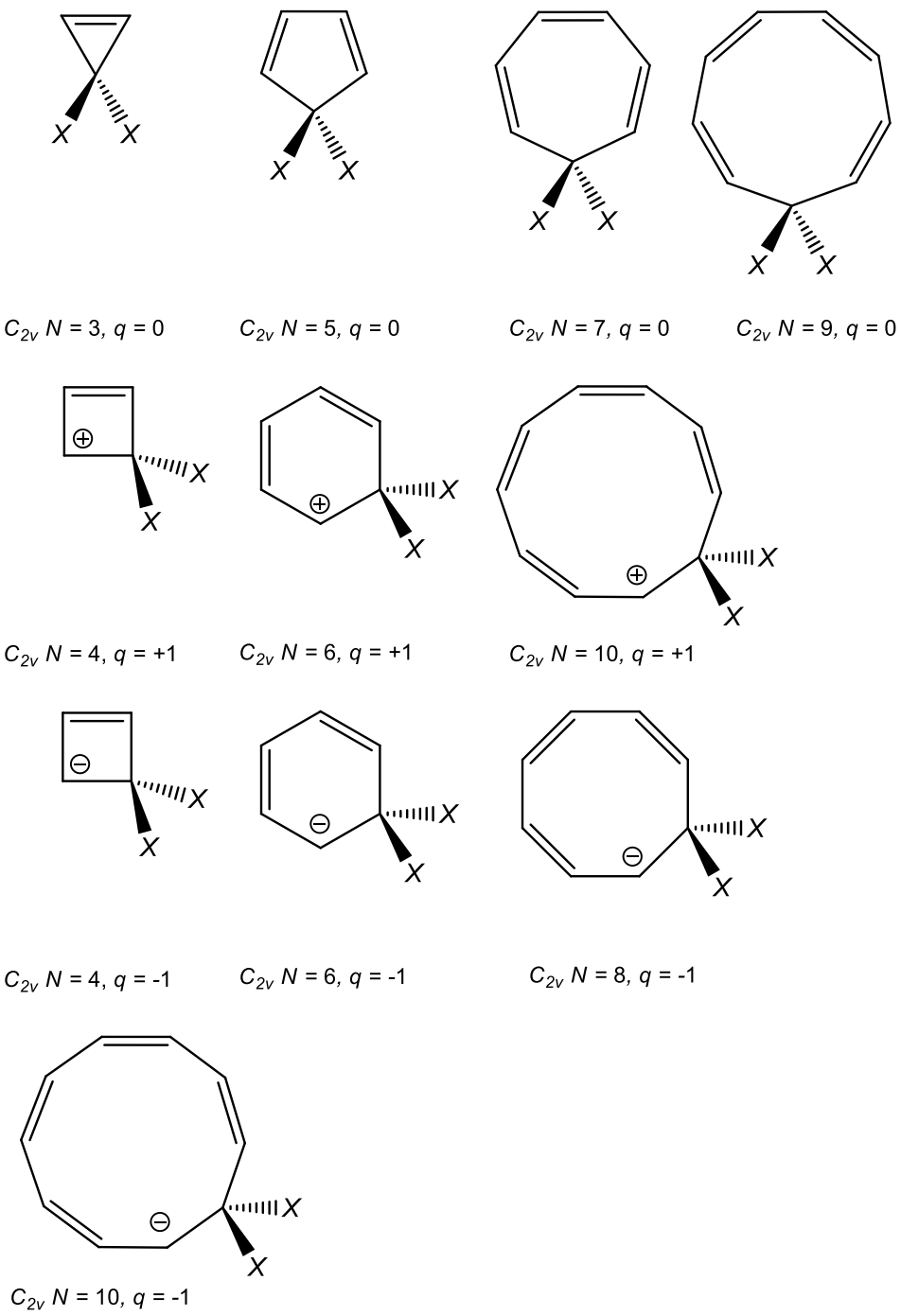

Figure 8.12. Schematic representations of the additional CX_2-bridged (X = H or F) systems in Figure 8.13, arranged by ring size, *N*, and charge, *q*, as in the text.

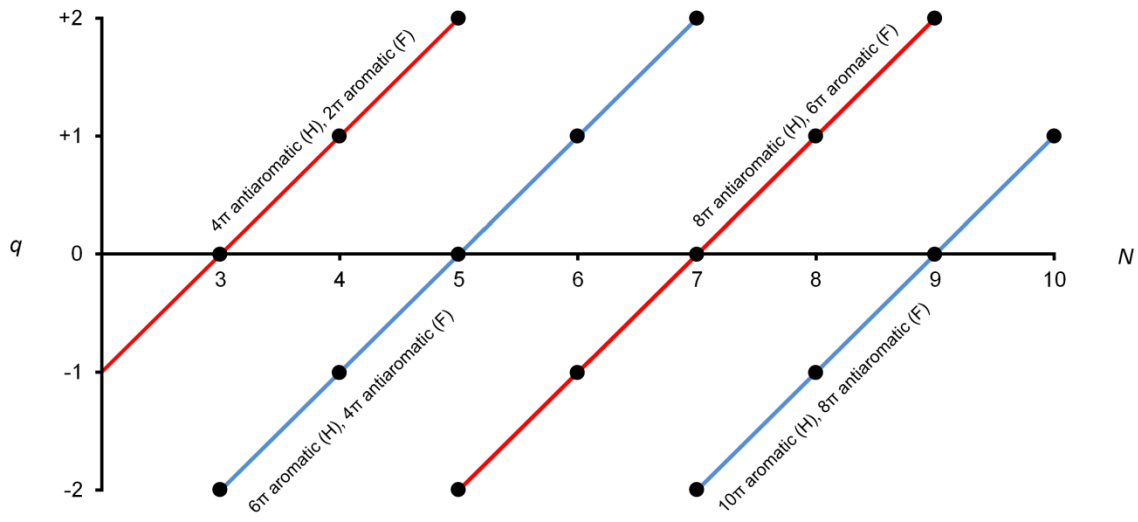

Figure 8.13. Classes of aromatic and antiaromatic C_{2v}-symmetric bridged annulene species $(CR_2)C_{N-1}H_{N-1}^{\ q}$ defined by the electron counting rule $n_\pi = N - 1 - q + \delta$, where δ pseudo-π electrons are donated by the bridge.

According to the case, minima, transition states or stationary points of higher order were found. Where the planar geometry corresponded to a transition state, the imaginary frequency represents the expected conjugation-breaking mode in which the bridge moves out of the molecular plane. Stationary points of higher order were typically found for the larger values of *N* (*e.g.*, *N* = 9 and 10), with extra imaginary frequencies for distortion of the ring. However, we note that ring currents have been shown to be surprisingly robust under such conformational distortions, *e.g.*, in the conversion of planar COT to the equilibrium tub shape,[29] where the σ/π distinction is formally lost as soon as the structure departs from planarity, but an identifiable π current persists for much of the pathway.

The current-density maps are collected in Figure 8.14. It can be seen that the n_π rule is successful in predicting the sense of π ring current for each planar or planar-constrained system, capturing the aromatic/antiaromatic alternation with changes of two in either electron count or ring size, and the inversion of behaviour between H and F species at the same electron count. The NICS calculations of Fernández *et al.*[213] on the *neutral* odd cyclic polyenes are consistent with the currents calculated here, fitting neatly into the overall pattern for neutral and charged systems with different ring sizes.

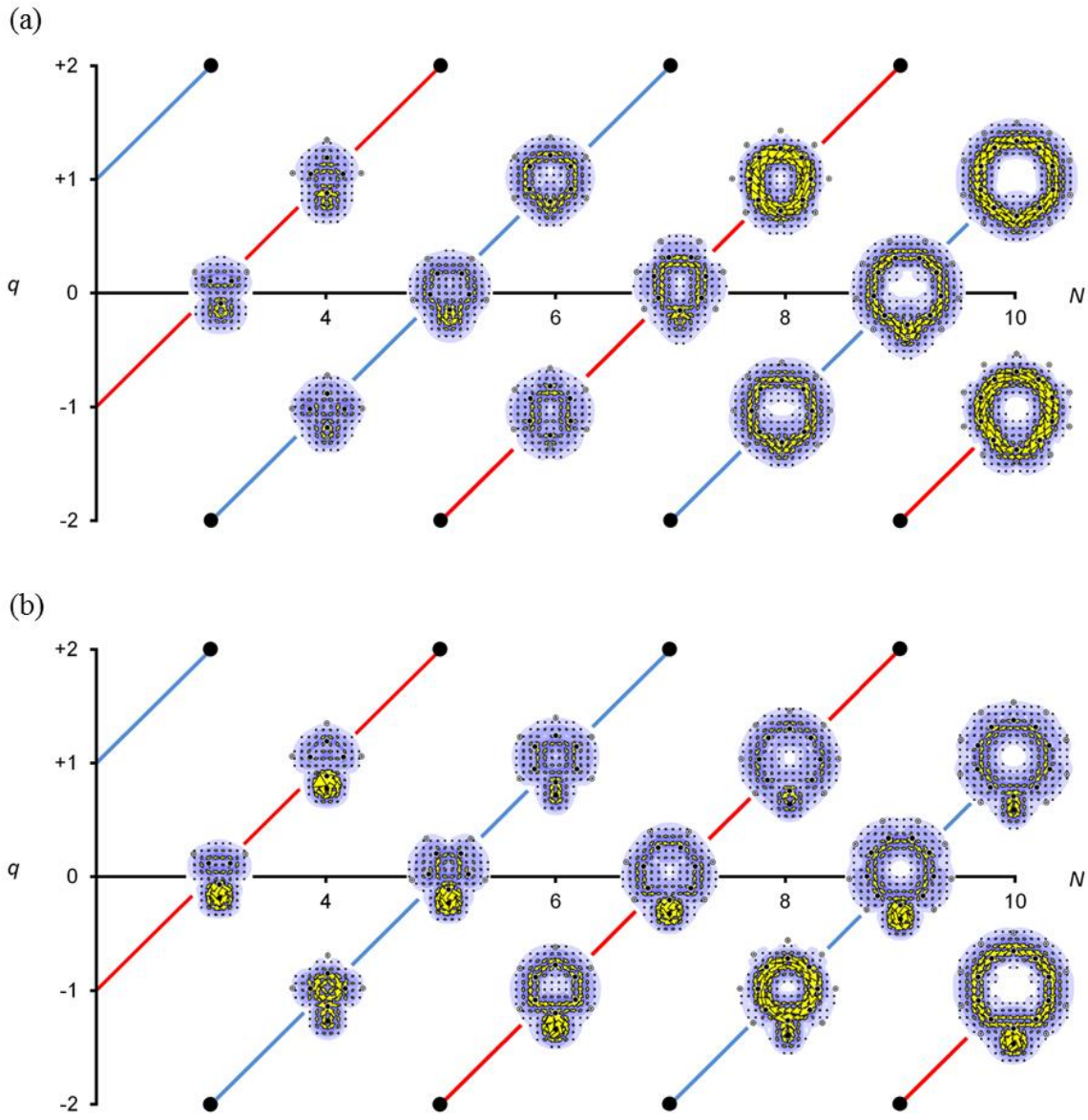

Figure 8.14. Current-density maps for C_{2v}-constrained bridged homoannulenes, $(CR_2)C_{N-1}H_{N-1}^{q}$, with (a) R = H, and (b) R = F. Species are arranged according to *N* and *q* as in Figure 8.13. Maps show total current arising from the full set of canonical π-like orbitals. Plotting conventions are described in the text.

In the pure 'annulene' form described above, the model is probably an oversimplification as it ignores differences in energy between C-C π bonds and the C-R σ bonds of the bridge. If the discrepancy in energy is too great, loss of conjugation and extinction of ring current can be expected. If desired, this feature could be accommodated by treating the CR_2 bridge as a pseudo heteroatom with full electron count of two, but with variable Hückel coulomb and resonance parameters α_x and β_x. The general tendency would then be for gaps to open up and for current to decrease as these parameters were allowed to diverge from the values appropriate to sp^2 carbon. As the set of maps in Figure 8.9 show, current *is* generally weakened when F is substituted for H in the bridge, which is consistent with a modification of the pure annulene model in this direction. The advantage of a variable parameter model of this kind is that it can accommodate 'mixed' situations. If the bridging group is CHF (Figure 8.15), for example, the parameters would be expected to be close to averages of CH_2 and CF_2 values, and indeed, when *ab initio* current maps are calculated for this mixed system, the π-like current is found to be very weak and paratropic (see Figure 8.16). It is not clear how a pure electron-counting model would deal with this case.

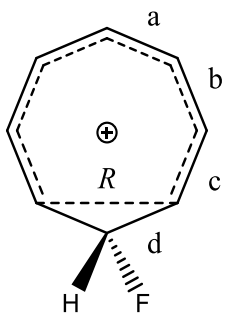

Figure 8.15. Bond lengths (in Å) for C_s $C_8H_8F^+$ CHF-bridged transition state structure, optimised at the B3LYP/6-31G** level of theory using Gaussian09.[40] *R* refers to the through-space distance between the carbon centres at either side of the 'bridge'. (a) 1.394; (b) 1.426; (c) 1.361; (d) 1.500; (*R*) 2.689.

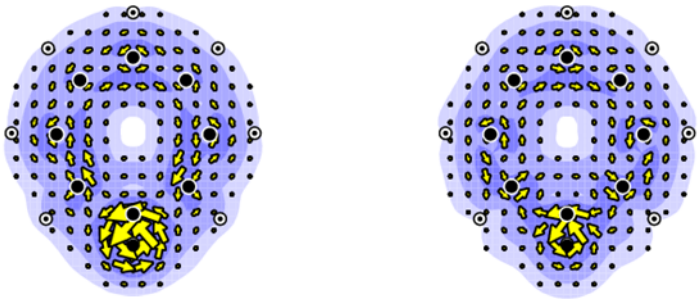

Figure 8.16. Current-density maps for the CHF-bridged species, constructed from LMO contributions corresponding to the π-like system (i.e., 3 LMOs from the carbon framework, 1 LMO from the bridging CH and 3 LMOs from the bridging CF). The lefthand map is 1 a_0 from the plane of the ring on the F side of the bridge. The righthand map is plotted 1 a_0 from the plane of the ring (defined by the carbon centres only) on the H side of the bridge. Plotting conventions are described in the text.

In this chapter a fourth strategy for controlling ring current, geometric alteration, has been introduced, joining the trifecta of functionalisation, substitution, and charge. By altering the structural framework, different substituents are able to interact with π system, completely changing the ring current response of the equilibrium structure. In the final chapter, a brief summary of the work contained in this thesis is presented, and the future outlook for the manipulation of ring current aromaticity is discussed.

Chapter 9: Outlook*

In Chapters 3 to 8 of this thesis four methods of controlling ring-current response in a variety of annulene- and polyene-type systems have been explored in detail. The three major approaches investigated, namely control of current by functionalisation, substitution, and charge, all alter the current in different ways. Despite this, a common explanation in terms of simple molecular orbital arguments is able to successfully rationalise the response of every system examined, as seen in the case study of pyrene and pyrene-derived systems in Chapter 6. The fourth method of controlling ring current, geometric alteration, demonstrated the versatility of these arguments, showing that even the unusual reversal of aromaticity along the inversion coordinate of the homotropenylium cation can be understood by their application.

The potential for designing current response is by no means limited to the approaches above. A brief introduction to a further strategy is the subject of this outlook: systems built out of non-standard ring architectures. This option offers such a wealth of possible directions that only a few selected cases are discussed here.

When compared to alternant hydrocarbons and benzenoids more specifically, non-alternant hydrocarbons have received relatively little attention. Some research on structural features such as the Stone-Wales defect have been made,[217–220] but in general the aromaticity of such systems has not been studied in detail.

The current response of some 'linear' (i.e., non catafused) and condensed 'pentaheptite' systems are displayed in Figure 9.1. Pentaheptite here refers to benzenoid-like structures comprised of equal numbers of five- and seven-membered unsaturated sp^2 carbon rings. The

* Some of the material in this chapter has been published in: Oziminski, W. P.; Palusiak, M.; Dominikowska, J.; Krygowski, T. M.; Havenith, R. W. A.; Gibson, C. M.; Fowler, P. W. *Phys. Chem. Chem. Phys.* **2013**, *15*, 3286–3293.

linear structures are analogous to linear polyacenes with the same number of rings, and the condensed structures are related to finite PAH flakes. Current-density maps are calculated at the pseudo-π[65] CHF/6-31G** level using the SYSMO package[39] on geometries obtained from optimisation of the full structures at the B3LYP/6-31G** level of theory with Gaussian09.[40]

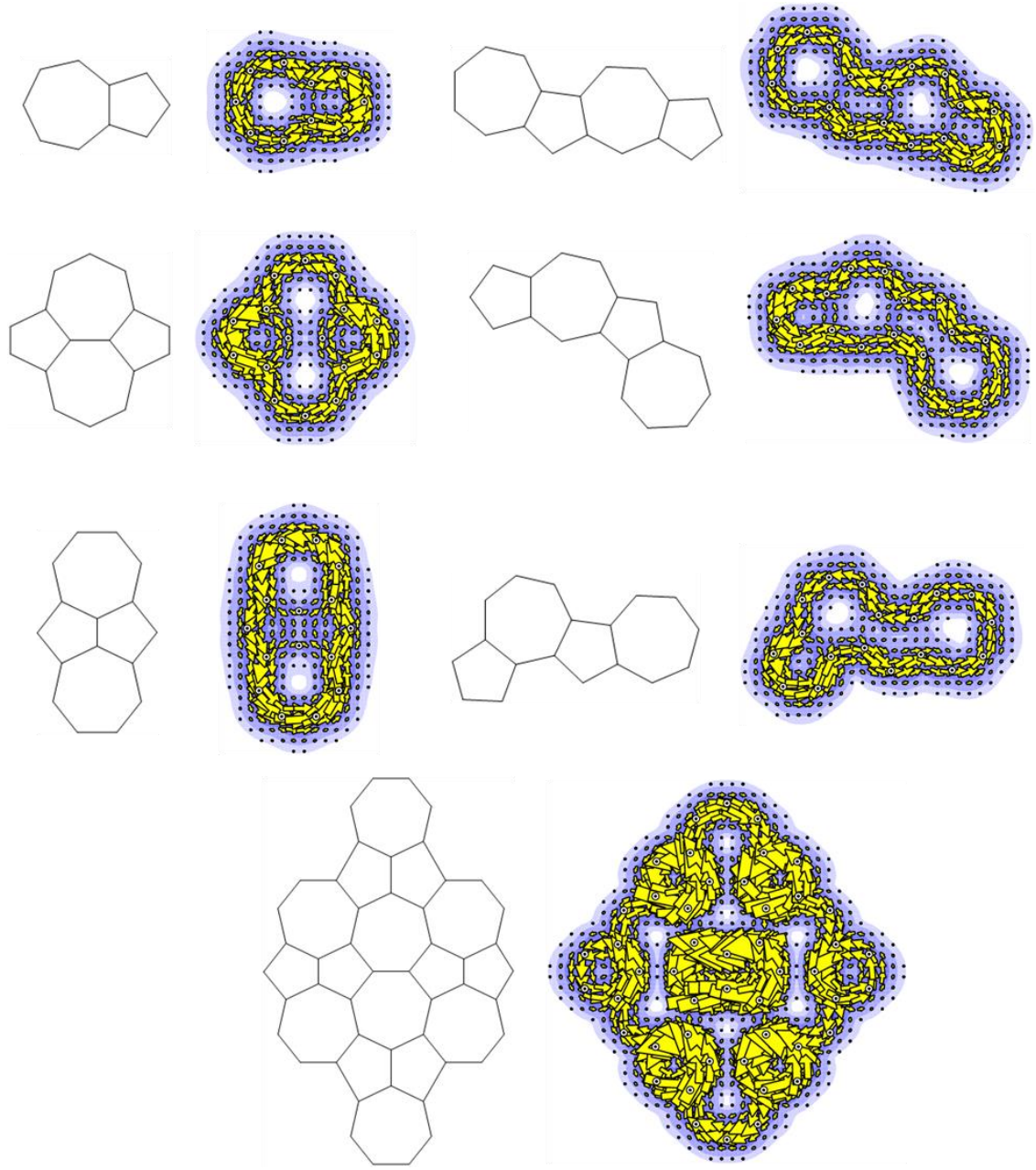

Figure 9.1. Schematic structures and pseudo-π total current-density maps for seven 'pentaheptite' systems. Maps are plotted in the molecular plane. Arrows and contours show the vector current density resolved into the plotting plane and the modulus of the current-density, respectively.

Previous work on the smallest system shown above, azulene,[221] has demonstrated that the ipsocentric method is able to rationalise the current-response in non-alternant systems. It has been shown that the aromaticity of non-alternant hydrocarbons such as bicalicene[222] (Figure 9.2(a)), cannot always be understood in simple terms.[223] Conjugated-circuit approaches miss-assign the 16π system as antiaromatic.[223]

As with many of the systems treated in this thesis, the ability of the ipsocentric approach to partition current into CMO and LMO bases is key to understanding the aromaticity of bicalicene. The total π current response of bicalicene is complex, the map (see Figure 9.2(b) is dominated by two aromatic circulations above the pentagons, with weaker circulations above the two triangle units. CMO analysis[27,35] reveals a cancellation of paratropic and diatropic frontier-orbital contributions (Figures 9.2(c) and (d)), which explains the difficulties that simpler models have in producing qualitatively correct current-density maps for this molecule. LMO analysis[43,61] (Figures 9.2(e) and (f)) shows that the molecule is not aromatic in a global sense; it has two aromatic cyclopentadienide-like subunits, and two, weaker, cyclopropenyl cation-like subunits, reflecting the 'tetraionic' nature of its aromaticity.

The complexity of the ring-current patterns shown by the pentaheptite systems mean that more detailed consideration of the ipsocentric treatment, and the selection rules that it generates, will be required to rationalise the behaviour of such systems, as was necessary with bicalicene. Systems with odd rings (and hence non-bipartite molecular graphs) also present problems for existing qualitative approaches,[145,182] and it is clear that study of such systems will form an important next step for ring-current studies.

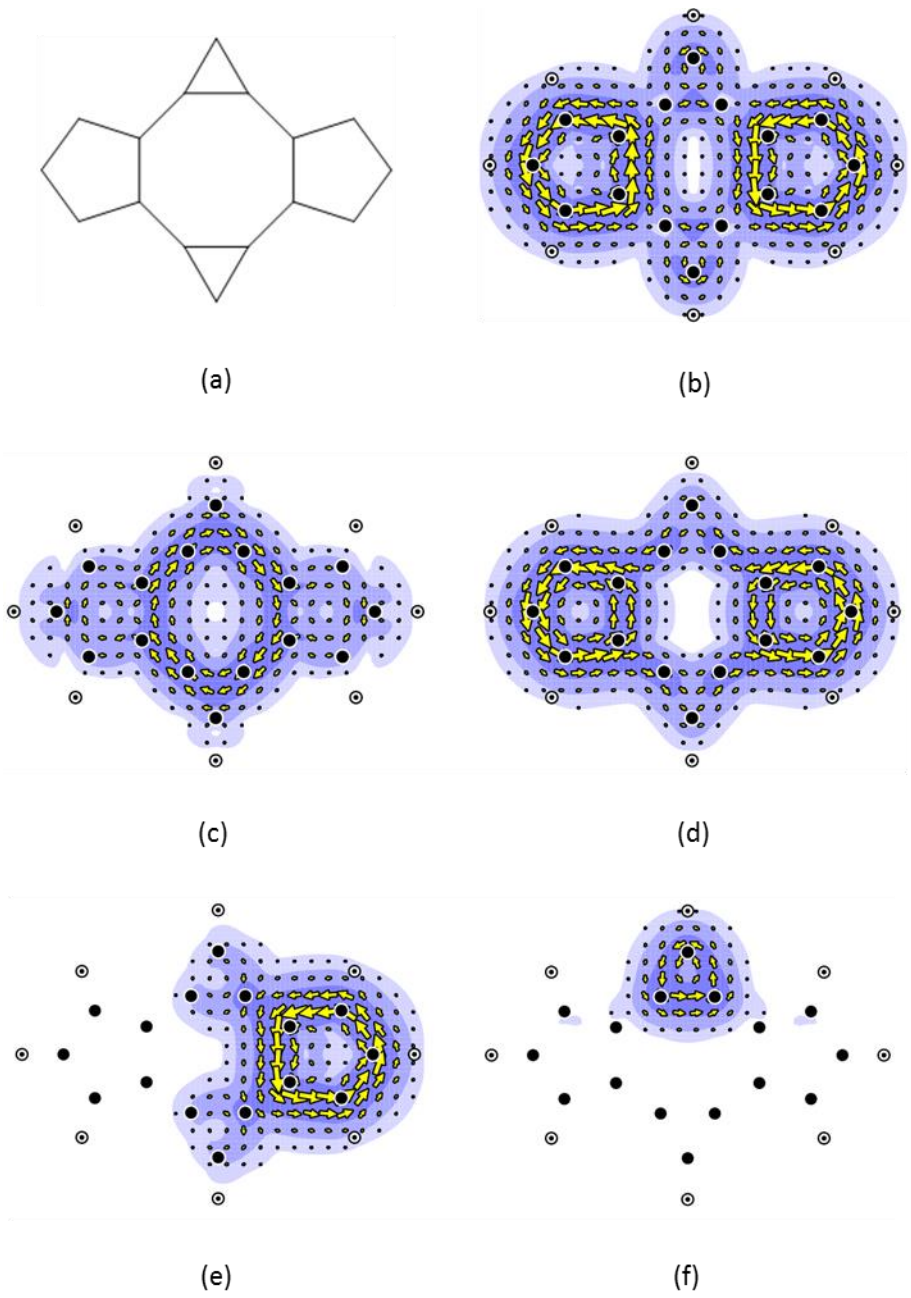

Figure 9.2. Schematic structure and current-density maps of D_{2h} bicalicene. Showing: (a) Schematic structure of bicalicene; (b) The total π current-densty map; (c) The weak, paratropic contribution from the HOMO; (d) The dominant, diatropic contribution from the HOMO-1/HOMO-2 pair; (e) The three LMO contribution corresponding to the local diatropic circulation on the right-hand cyclopentadieneide moiety; (f) The single LMO contribution corresponding to the local diatropic circulation on the top cyclopropenyl cation moiety. Calculations were performed at the CHF/6-31G** level using the B3LYP/6-31G** optimised structure. Plotting conventions are as in Chapter 2.

References

(1) Hofmann, A. W. *Proc. R. Soc.* **1856**, *8*, 1–3.

(2) Faraday, M. *Philos. Trans. R. Soc.* **1825**, *115*, 440–466.

(3) Kekulé, A. *Bull. Soc. Chim. Paris.* **1865**, *3*, 98–110.

(4) Kekulé, A. *Ann. Chem. Pharm.* **1866**, *137*, 129–196.

(5) Kekulé, A. *Liebigs Ann. Chem.* **1872**, *162*, 77–124.

(6) Kekulé, A. *Liebigs Ann. Chem.* **1872**, *162*, 309–320.

(7) Lloyd, D. *Chem. Inf. Comput. Sci.* **1996**, *36*, 442–447.

(8) Schleyer, P. v. R.; Jiao, H. *Pure Appl. Chem.* **1996**, *68*, 209–218, and references cited therein.

(9) Smith, M. B.; March, J. *March's Advanced Organic Chemistry*; Fifth.; John Wiley & Sons: New York, 2001.

(10) Pople, J. A. *J. Chem. Phys.* **1956**, *24*, 1111.

(11) Schleyer, P. v R.; Maerker, C.; Dransfeld, A.; Jiao, H.; Hommes, N. J. R. v. E. *J. Am. Chem. Soc.* **1996**, *118*, 6317–6318.

(12) Pauling, L. *J. Chem. Phys.* **1936**, *4*, 673–677.

(13) Gershoni-Poranne, R.; Stanger, A. *Chem. Soc. Rev.* **2015**, *44*, 6597–6615.

(14) Salem, L. *The Molecular Orbital Theory of Conjugated Systems*; Benjamin: New York, 1966; pp. 177–205.

(15) Saunderson, A. *Phys. Edu.* **1968**, *3*, 272–273.

(16) Musher, J. I. *J. Chem. Phys.* **1965**, *43*, 4081–4083.

(17) Pascal, P. *Ann. Chim. Phys.* **1910**, *19*, 5–70.

(18) Bain, G. A.; Berry, J. F. *J. Chem. Edu.* **2008**, *85*, 532–536.

(19) Dauben, J. H. J.; Wilson, J. D.; Laity, J. L. *J. Am. Chem. Soc.* **1968**, *90*, 811–813.

(20) Dauben, J. H. J.; Wilson, J. D.; Laity, J. L. *J. Am. Chem. Soc.* **1969**, *91*, 1991–1998.

(21) Atkins, P. W.; de Paula, J. *Atkins' Physical Chemistry*; 8th ed.; Oxford University Press: Oxford, **2006**.

(22) Hinchliffe, A.; Munn, R. W. *Molecular Electromagnetism*; First.; John Wiley & Sons: Chichester, **1985**.

(23) Gauss, J. *J. Chem. Phys.* **1993**, *99*, 3629–3643.

(24) London, F. J. *Radium* **1937**, *8*, 397–409.

(25) Fowler, P. W.; Myrvold, W. *J. Phys. Chem. A* **2011**, *115*, 13191–13200.

(26) Haddon, R. C. *Nature* **1995**, *378*, 249.

(27) Steiner, E.; Fowler, P. W. *J. Phys. Chem. A* **2001**, *105*, 9553–9562.

(28) Keith, T. A.; Bader, R. F. W. *J. Chem. Phys.* **1993**, *99*, 3669–3682.

(29) Lazzeretti, P. *Prog. Nucl. Magn. Reson. Spectrosc.* **2000**, *36*, 1–88.

(30) Kutzelnigg, W. *Isr. J. Chem.* **1980**, *19*, 193–200.

(31) Schindler, M.; Kutzelnigg, W. *J. Chem. Phys.* **1982**, *76*, 1919–1933.

(32) Zanasi, R.; Lazzeretti, P. *Mol. Phys.* **1996**, *89*, 157–170.

(33) Steiner, E.; Fowler, P. W. *Chem. Commun.* **2001**, 2220–2221.

(34) Coriani, S.; Lazzeretti, P.; Malagoli, M.; Zanasi, R. *Theor Chim Acta* **1994**, *89*, 181–192.

(35) Steiner, E.; Fowler, P. W. *Phys. Chem. Chem. Phys.* **2004**, *6*, 261–272.

(36) Fowler, P. W.; Steiner, E.; Zanasi, R.; Cadioli, B. *Mol. Phys.* **1999**, *96*, 1099–1108.

(37) Zanasi, R. *J. Chem. Phys.* **1996**, *105*, 1460–9.

(38) Soncini, A.; Fowler, P. W. *Chem. Phys. Lett.* **2004**, *396*, 174–181.

(39) Lazzeretti, P.; Zanasi, R. SYSMO package (University of Modena). Additional Routines by Fowler, P.W.; Steiner, E.; Havenith, R.W.A.; Soncini, A. **1980**.

(40) Frisch, M. J.; Trucks, G. W.; Schlegel, H. B.; Scuseria, G. E.; Robb, M. A.; Cheeseman, J. R.; Scalmani, G.; Barone, V.; Mennucci, B.; Petersson, G. A.; Nakatsuji, H.; Caricato, M.; Li, X.; Hratchian, H. P.; Izmaylov, A. F.; Bloino, J.; Zheng, G.; Sonnenberg, J. L.; Hada, M.; Ehara, M.; Toyota, K.; Fukuda, R.; Hasegawa, J.; Ishida, M.; Nakajima, T.; Honda, Y.; Kitao, O.; Nakai, H.; Vreven, T.; Montgomery, Jr., J. A.; Peralta, J. E.; Ogliaro, F.; Bearpark, M.; Heyd, J. J.; Brothers, E.; Kudin, K. N.; Staroverov, V. N.; Kobayashi, R.; Normand, J.; Raghavachari, K.; Rendell, A.; Burant, J. C.; Iyengar, S. S.; Tomasi, J.; Cossi, M.; Rega, N.; Millam, J. M.; Klene, M.; Knox, J. E.; Cross, J. B.; Bakken, V.; Adamo, C.; Jaramillo, J.; Gomperts, R.; Stratmann, R. E.; Yazyev, O.; Austin, A. J.; Cammi, R.; Pomelli, C.; Ochterski, J. W.; Martin, R. L.; Morokuma, K.; Zakrzewski, V. G.; Voth, G. A.; Salvador, P.; Dannenberg, J. J.; Dapprich, S.; Daniels, A. D.; Farkas, Ö.; Foresman, J. B.; Ortiz, J. V.; Cioslowski, J.; Fox, D. J. Gaussian 09, Revision D.01; Gaussian, Inc.: Wallingford, CT **2009**.

(41) Steiner, E.; Soncini, A.; Fowler, P. W. *J. Phys. Chem. A* **2006**, *110*, 12882–12886.

(42) Frost, A. A.; Musulin, B. *J. Chem. Phys.* **1953**, *21*, 572–573.

(43) Pipek, J.; Mezey, P. G. *J. Chem. Phys.* **1989**, *90*, 4916–4926.

(44) Havenith, R. W. A.; Fowler, P. W.; Jenneskens, L. W. *Org. Lett.* **2006**, *8*, 1255–1258.

(45) Frank, N. L.; Baldridge, K. K.; Siegel, J. S. *J. Am. Chem. Soc.* **1995**, *117*, 2102–2103.

(46) Bosdet, M. J. D.; Piers, W. E.; Sorensen, T. S.; Parvez, M. *Angew. Chemie Int. Ed.* **2007**, *46*, 4940–4943.

(47) Bruns, D.; Miura, H.; Vollhardt, K. P. C.; Stanger, A. *Org. Lett.* **2003**, *5*, 549–52.

(48) Wiberg, E.; Hertwig, K.; Bolz, A. Z. *Anorg. Chem.* **1948**, *256*, 177–256.

(49) Wiberg, E.; Hertwig, K. Z. *Anorg. Chem.* **1948**, *257*, 138–144.

(50) Kiran, B.; Phukan, A. K.; Jemmis, E. D. *Inorg. Chem.* **2001**, *40*, 3615–3618.

(51) Fowler, P. W.; Steiner, E. *J. Phys. Chem.* **1997**, *101*, 1409–1413.

(52) Schleyer, P. v. R.; Jiao, H.; Eikema Hommes, N. J. R. v.; Malkin, V. G.; Malkina, O. L. *J. Am. Chem. Soc.* **1997**, *119*, 12669–12670.

(53) Chiavarino, B.; Crestoni, M. E.; Di Marzio, A.; Fornarini, S.; Rosi, M. *J. Am. Chem. Soc.* **1999**, *121*, 11204–11210.

(54) Engelberts, J. J.; Havenith, R. W. A.; Lenthe, J. H. v.; Jenneskens, L. W.; Fowler, P. W. *Inorg. Chem.* **2005**, *44*, 5266–5272.

(55) Islas, R.; Chamorro, E.; Robles, J.; Heine, T.; Santos, J. C.; Merino, G. *Struct. Chem.* **2007**, *18*, 833–839.

(56) Chattaraj, P. K.; Roy, D. R. *J. Phys. Chem. A* **2007**, *111*, 4684–4696.

(57) Shen, W.; Li, M.; Li, Y.; Wang, S. *Inorganica Chim. Acta* **2007**, *360*, 619–624.

(58) Chowdhury, C. B.; Basu, R. *J. Indian Chem. Soc.* **1968**, *45*, 469–472.

(59) Bosdet, M. J. D.; Piers, W. E. *Can. J. Chem.* **2009**, *87*, 8–29.

(60) Boyd, R. J.; Choi, S. C.; Hale, C. C. *Chem. Phys. Lett.* **1984**, *112*, 136–141.

(61) Steiner, E.; Fowler, P. W.; Havenith, R. W. A. *J. Phys. Chem. A* **2002**, *106*, 7048–7056.

(62) Guest, M. F.; Bush, I. J.; Dam, H. J. J. v.; Sherwood, P.; Thomas, J. M. H.; Lenthe, J. H. v.; Havenith, R. W. A.; Kendrick, J. *Mol. Phys.* **2005**, *103*, 719–747.

(63) Havenith, R. W. A.; Meijer, A. J. H. M.; Irving, B. J.; Fowler, P. W. *Mol. Phys.* **2009**, *107*, 2591–2600.

(64) Stowasser, R.; Hoffmann, R. *J. Am. Chem. Soc.* **1999**, *121*, 3414–3420.

(65) Fowler, P. W.; Steiner, E. *Chem. Phys. Lett.* **2002**, *364*, 259–266.

(66) Weinberg, B. A.; Bealer, B. K. *The world of caffeine: the science and culture of the world's most popular drug*; 2nd ed.; Routledge: London, 2002; pp. xiii–xiv.

(67) Sella, A. *Chem. World* **2013**, *10*, 35.

(68) Morelli, M. *Exp. Neurol.* **2003**, *184*, 20–23.

(69) Fahn, S. *Mov. Disord.* **2010**, *25 Suppl 1*, S2–14.

(70) Ross, G. W.; Abbott, R. D.; Petrovitch, H.; Morens, D. M.; Grandinetti, A.; Tung, K. H.; Tanner, C. M.; Masaki, K. H.; Blanchette, P. L.; Curb, J. D.; Popper, J. S.; White, L. R. *J. Am. Med. Assoc.* **2000**, *283*, 2674–2679.

(71) Palacios, N.; Gao, X.; McCullough, M. L.; Schwarzschild, M. a; Shah, R.; Gapstur, S.; Ascherio, A. *Mov. Disord.* **2012**, *27*, 1276–1282.

(72) Popat, R. A.; Den Eeden, S. K. v.; Tanner, C. M.; Kamel, F.; Umbach, D. M.; Marder, K.; Mayeux, R.; Ritz, B.; Ross, G. W.; Petrovitch, H.; Topol, B.; McGuire, V.; Costello, S.; Manthripragada, A. D.; Southwick, A.; Myers, R. M.; Nelson, L. M. *Eur. J. Neurol.* **2011**, *18*, 756–765.

(73) Doré, A. S.; Robertson, N.; Errey, J. C.; Ng, I.; Hollenstein, K.; Tehan, B.; Hurrell, E.; Bennett, K.; Congreve, M.; Magnani, F.; Tate, C. G.; Weir, M.; Marshall, F. H. *Structure* **2011**, *19*, 1283–1293.

(74) Jörg, M.; Shonberg, J.; Mak, F. S.; Miller, N. D.; Yuriev, E.; Scammells, P. J.; Capuano, B. *Bioorg. Med. Chem. Lett.* **2013**, *23*, 3427–3433.

(75) Arnaud, M. J. *Handb. Exp. Pharmacol.* **2011**, *200*, 33–91.

(76) Ferré, S. *J. Neurochem.* **2008**, *105*, 1067–1079.

(77) Orrú, M.; Guitart, X.; Karcz-Kubicha, M.; Solinas, M.; Justinova, Z.; Barodia, S. K.; Zanoveli, J.; Cortes, A.; Lluis, C.; Casado, V.; Moeller, F. G.; Ferré, S. *Neuropharmacology* **2013**, *67*, 476–484.

(78) Osswald, H.; Schnermann, J. *Handb. Exp. Pharmacol.* **2011**, *200*, 391–412.

(79) Woziwodzka, A.; Gwizdek-Wiśniewska, A.; Piosik, J. *Bioorg. Chem.* **2011**, *39*, 10–17.

(80) Hernandez Santiago, A. A.; Gonzalez Flores, M.; Rosas Castilla, S. A.; Cervantes Tavera, A. M.; Gutierrez Perez, R.; Khomich, V. V.; Ovchinnikov, D. V.; Parkes, H. G.; Evstigneev, M. P. *J. Mol. Struct.* **2012**, *1010*, 139–145.

(81) Fritzsche, H.; Petri, I.; Schutz, H.; Weller, K.; Sedmera, P.; Lang, H. *Biophys. Chem.* **1980**, *11*, 109–119.

(82) Platonov, M. O.; Samijlenko, S. P.; Sudakov, O. O.; Kondratyuk, I. V; Hovorun, D. M. *Spectrochim. Acta, Part A* **2005**, *62*, 112–114.

(83) Sutor, D. J. *Acta Crystallogr.* **1958**, *11*, 453–458.

(84) Egawa, T.; Kamiya, A.; Takeuchi, H.; Konaka, S. *J. Mol. Struct.* **2006**, *825*, 151–157.

(85) Prager, M.; Pawlukojc, A.; Wischnewski, A.; Wuttke, J. *J. Chem. Phys.* **2007**, *127*, 214509: 1–10.

(86) Lehmann, C. W.; Stowasser, F. *Chem. Eur. J.* **2007**, *13*, 2908–2911.

(87) Nonella, M.; Hänggi, G.; Dubler, E. *J. Mol. Struct. Theochem* **1993**, *279*, 173–190.

(88) Soncini, A.; Domene, C.; Engelberts, J. J.; Fowler, P. W.; Rassat, A.; Lenthe, J. H. Van; Havenith, R. W. A.; Jenneskens, L. W. *Chem. Eur. J.* **2005**, *11*, 1257–1266.

(89) Ollis, W. D.; Stanforth, P. *Tetrahedron* **1985**, *41*, 2239–2329.

(90) Ollis, W. D.; Ramsden, C. A. *Adv. Heterocycl. Chem.* **1976**, *19*, 1–122.

(91) Baker, W.; Ollis, W. D. *Q. Rev.* **1957**, *11*, 15–29.

(92) Stewart, F. H. C. *Chem. Rev.* **1964**, *64*, 129–147.

(93) Browne, D. L.; Harrity, J. P. A. *Tetrahedron* **2010**, *66*, 553–568.

(94) Earl, J. C.; Mackney, A. W. *J. Chem. Soc.* **1935**, 899–900.

(95) Chandrasekhar, R.; Nanjan, M. J. *Mini-Reviews Med. Chem.* **2012**, *12*, 1359–1365.

(96) Browne, D. L.; Vivat, J. F.; Plant, A.; Gomez-Bengoa, E.; Harrity, J. P. A. *J. Am. Chem. Soc.* **2009**, *131*, 7762–7769.

(97) Browne, D. L.; Taylor, J. B.; Plant, A.; Harrity, J. P. A. *J. Org. Chem.* **2010**, *75*, 984–987.

(98) Foster, R. S.; Adams, H.; Jakobi, H.; Harrity, J. P. A. *J. Org. Chem.* **2013**, *78*, 4049–4064.

(99) Specklin, S.; Decuypere, E.; Plougastel, L.; Aliani, S.; Taran, F. *J. Org. Chem.* **2014**, *79*, 7772–7777.

(100) Hill, R. W. A.; Sutton, L. E. *J. Chem. Soc.* **1949**, 746–753.

(101) Orgel, L. E.; Cottrell, T. L.; Dick, W.; Sutton, L. E. *Trans. Faraday. Soc.* **1951**, *47*, 113–119.

(102) Mais, F.-J.; Dickopp, H.;Middelhauve, B.; Martin, H.-D.; Mootz, D.; Steigel, A. *Chem. Ber.* **1987**, *120*, 275–283.

(103) Gilchrist, T. L. *Heterocyclic Chemistry*; 3rd ed.; Longman: Harlow, 1997; pp. 342–343.

(104) Simas, A. M.; Miller, J.; de Athayade Filho, P. F. *Can. J. Chem.* **1998**, *76*, 869–872.

(105) Wiechmann, S.; Freese, T.; Drafz, M. H. H.; Hübner, E. G.; Namyslo, J. C.; Nieger, M.; Schmidt, A. *Chem. Commun.* **2014**, *50*, 11822–11824.

(106) De Athayade Filho, P. F.; Miller, J.; Simas, A. M. *Synthesis (Stuttg).* **2000**, 1565–1568.

(107) Fabian, J.; Hess Jr, B. A. *Int. J. Quantum Chem.* **2002**, *90*, 1055–1063.

(108) Jaźwiński, J.; Staszewska-Krajewska, O. *J. Mol. Struct.* **2002**, *602-603*, 269–274.

(109) Bärnighausen, H.; Jellinek, F.; Munnik, J.; Vos, A. *Acta Crystallogr.* **1963**, *16*, 471–475.

(110) Scott, A. P.; Radom, L. *J. Phys. Chem.* **1996**, *100*, 16502–16513.

(111) Gibson, C. M.; Fowler, P. W. *Tetrahedron Lett.* **2014**, *55*, 2078–2081.

(112) Gershoni-Poranne, R.; Gibson, C. M.; Fowler, P. W.; Stanger, A. *J. Org. Chem.* **2013**, *78*, 7544–7553.

(113) Baker, W.; Ollis, W. D. *Chem. Ind.* **1955**, 910–911.

(114) Bieber, T. I. *Chem. Ind.* **1955**, 1055–1056.

(115) Coulson, C. A. *Valence*; 2nd ed.; Oxford University Press: London, 1969.

(116) Barber, M.; Broadbent, S. J.; Connor, J. A.; Guest, M. F.; Hillier, I. H.; Puxley, H. J. *J. Chem. Soc. Perkin Trans. 2* **1972**, 1517–1521.

(117) Fowler, P. W.; Havenith, R. W. A.; Jenneskens, L. W.; Soncini, A.; Steiner, E. *Chem. Commun.* **2001**, *1*, 2386–2387.

(118) Fowler, P. W.; Havenith, R. W. A.; Jenneskens, L. W.; Soncini, A.; Steiner, E. *Angew. Chemie Int. Ed.* **2002**, *41*, 1558–1560.

(119) Fowler, P. W.; Bean, D. E.; Seed, M. *J. Phys. Chem. A* **2010**, *114*, 10742–10749.

(120) Geim, A. *Science* **2009**, *324*, 1530–1534.

(121) Nicholas, R. J.; Mainwood, A.; Eaves, L. *Philos. Trans. R. Soc. A Math. Phys. Eng. Sci.* **2008**, *366*, 187–193.

(122) Singh, V.; Joung, D.; Zhai, L.; Das, S.; Khondaker, S. I.; Seal, S. *Prog. Mater. Sci.* **2011**, *56*, 1178–1271.

(123) Yan, L.; Zheng, Y. B.; Zhao, F.; Li, S.; Gao, X.; Xu, B.; Weiss, P. S.; Zhao, Y. *Chem. Soc. Rev.* **2011**, 97–114.

(124) Boukhvalov, D. W.; Katsnelson, M. I. *J. Phys. Condens. Matter* **2009**, *21*, 344205: 1–12.

(125) Zhou, J.; Sun, Q. *Appl. Phys. Lett.* **2012**, *101*, 073114: 1–4.

(126) Tsetseris, L.; Pantelides, S. T. *J. Mater. Sci.* **2012**, *47*, 7571–7579.

(127) Poh, H. L.; Šaněk, F.; Sofer, Z.; Pumera, M. *Nanoscale* **2012**, *4*, 7006–11.

(128) Tang, Q.; Zhou, Z.; Chen, Z. *Nanoscale* **2013**, *5*, 4541–4583.

(129) Schäfer, R. a.; Englert, J. M.; Wehrfritz, P.; Bauer, W.; Hauke, F.; Seyller, T.; Hirsch, A. *Angew. Chemie Int. Ed.* **2013**, *52*, 754–757.

(130) Peng, Q.; Liang, C.; Ji, W.; De, S. *Phys. Chem. Chem. Phys.* **2013**, *15*, 2003–2011.

(131) Dreyer, D. R.; Park, S.; Bielawski, C. W.; Ruoff, R. S. *Chem. Soc. Rev.* **2010**, *39*, 228–40.

(132) Sofo, J. O.; Chaudhari, A. S.; Barber, G. D. *Phys. Rev. B* **2007**, *75*, 153401: 1–4.

(133) Samarakoon, D. K.; Wang, X.-Q. *ACS Nano* **2009**, *3*, 4017–4022.

(134) Elias, D.; Nair, R.; Mohiuddin, T.; Morozov, S.; Blake, P.; Halsall, M.; Ferrari, A.; Boukhvalov, D.; Katsnelson, M.; Geim, A.; Novoselov, K. *Science* **2009**, *323*, 610–613.

(135) Balog, R.; Jørgensen, B.; Nilsson, L.; Andersen, M.; Rienks, E.; Bianchi, M.; Fanetti, M.; Laegsgaard, E.; Baraldi, A.; Lizzit, S.; Sljivancanin, Z.; Besenbacher, F.; Hammer, B.; Pedersen, T. G.; Hofmann, P.; Hornekaer, L. *Nat. Mater.* **2010**, *9*, 315–319.

(136) Cheng, S.-H.; Zou, K.; Okino, F.; Gutierrez, H. R.; Gupta, A.; Shen, N.; Eklund, P. C.; Sofo, J. O.; Zhu, J. *Phys. Rev. B* **2010**, *81*, 205435:1–5.

(137) Martin-Gago, J. A. *Nat. Chem.* **2011**, *3*, 11–12.

(138) Liu, H.; Liu, Y.; Zhu, D. *J. Mater. Chem.* **2011**, *21*, 3335–3345.

(139) Rieger, R.; Müllen, K. *J. Phys. Org. Chem.* **2010**, *23*, 315–325.

(140) Narita, A.; Wang, X.-Y.; Feng, X.; Müllen, K. *Chem. Soc. Rev.* **2015**, *44*, 6616–6643.

(141) Fias, S.; Fowler, P. W.; Delgado, J. L.; Hahn, U.; Bultinck, P. *Chem. Eur. J.* **2008**, *14*, 3093–3099.

(142) Ernzerhof, M.; Bahmann, H.; Goyer, F.; Zhuang, M.; Rocheleau, P. *J. Chem. Theory Comput.* **2006**, *2*, 1291–1297.

(143) Domene, C.; Fowler, P. W.; Jenneskens, L. W.; Steiner, E. *Chem. Eur. J.* **2007**, *13*, 269–276.

(144) Havenith, R. W. A.; Fowler, P. W. *Chem. Phys. Lett.* **2007**, *449*, 347–353.

(145) Randić, M. *Chem. Phys. Lett.* **2010**, *500*, 123–127.

(146) Dral, P. O.; Kivala, M.; Clark, T. *J. Org. Chem.* **2013**, *78*, 1894–1902.

(147) Allamandola, L. J.; Tielens, A. G. G. M.; Barker, J. R. *Astrophys. J. Supp. Ser.* **1989**, *71*, 733.

(148) Gutman, I.; Furtula, B. *Resonance* **2008**, *13*, 730–737.

(149) Zhi, L.; Müllen, K. *J. Mater. Chem.* **2008**, *18*, 1472–1484.

(150) Itami, K. *Pure Appl. Chem.* **2012**, *84*, 907–916.

(151) Milledge, H. J.; Nave, E.; Weller, F. H. *Nature* **1959**, *184*, 715.

(152) Kawaguchi, M.; Kuroda, S.; Muramatsu, Y. *J. Phys. Chem. Solids* **2008**, *69*, 1171–1178.

(153) Marwitz, A. J. V; Matus, M. H.; Zakharov, L. N.; Dixon, D. A.; Liu, S. *Angew. Chemie Int. Ed.* **2009**, *48*, 973–977.

(154) Hatakeyama, T.; Hashimoto, S.; Seki, S.; Nakamura, M. *J. Am. Chem. Soc.* **2011**, *133*, 18614–18617.

(155) Abbey, E. R.; Zakharov, L. N.; Liu, S. *J. Am. Chem. Soc.* **2011**, *133*, 11508–11511.

(156) Neue, B.; Fröhlich, R.; Wibbeling, B.; Fukazawa, A.; Wakamiya, A.; Yamaguchi, S.; Wu, E. *J. Org. Chem.* **2012**, *77*, 2176–2184.

(157) Campbell, P. G.; Marwitz, A. J. V; Liu, S. *Angew. Chemie Int. Ed.* **2012**, *51*, 6074–6092.

(158) Ashe, A. J.; Fang, X.; Fang, X.; Kampf, J. W. *Organometallics* **2001**, *20*, 5413–5418.

(159) Fang, X.; Yang, H.; Kampf, J. W.; Holl, M. M. B.; Ashe, A. J. *Organometallics* **2006**, *25*, 513–518.

(160) Tönshoff, C.; Müller, M.; Kar, T.; Latteyer, F.; Chassé, T.; Eichele, K.; Bettinger, H. F. *ChemPhysChem* **2012**, *13*, 1173–1181.

(161) Xu, J.; Jang, S. K.; Lee, J.; Song, Y. J.; Lee, S. *J. Phys. Chem. C* **2014**, *118*, 22268–22273.

(162) Steiner, E.; Fowler, P. W.; Viglione, R. G.; Zanasi, R. *Chem. Phys. Lett.* **2002**, *355*, 471–477.

(163) Turker, L. *Polycycl. Aromat. Compd.* **2012**, *32*, 61–74.

(164) Steiner, E.; Fowler, P. W.; Jenneskens, L. W. *Angew. Chemie Int. Ed.* **2001**, *40*, 362–366.

(165) Cyrański, M. K.; Havenith, R. W. A.; Dobrowolski, M. A.; Gray, B. R.; Krygowski, T. M.; Fowler, P. W.; Jenneskens, L. W. *Chem. Eur. J.* **2007**, *13*, 2201–2207.

(166) Fowler, P. W.; Gibson, C. M.; Bean, D. E. *Proc. R. Soc. A* **2014**, *470*, 20130617:1–18.

(167) Fowler, P. W.; Gibson, C. M.; Nightingale, E. L. *Polycycl. Aromat. Compd.* **2013**, *33*, 72–81.

(168) Domene, C.; Fowler, P. W.; Jemmer, P.; Madden, P. *Chem. Phys. Lett.* **1999**, *299*, 51–56.

(169) Soncini, A.; Fowler, P. W.; Jenneskens, L. W. *Phys. Chem. Chem. Phys.* **2004**, *6*, 277–284.

(170) Fowler, P. W.; Soncini, A. *Polycycl. Aromat. Compd.* **2004**, *24*, 353–366.

(171) Burgi, H.-B.; Baldridge, K. K.; Frank, N. L.; Gantzel, P.; Siegel, J. S.; Ziller, J. *Angew. Chemie Int. Ed.* **1995**, *34*, 1454–1456.

(172) Frank, N. L.; Baldridge, K. K.; Gantzel, P.; Siegel, J. S. *Tetrahedron Lett.* **1995**, *36*, 4389–4392.

(173) Matsurra, A.; Komatsu, K. *J. Am. Chem. Soc.* **2001**, *123*, 1768–1769.

(174) Hill, J. G.; Karadakov, P. B.; Cooper, D. L. *Mol. Phys.* **2006**, *104*, 677–680.

(175) Soncini, A.; Havenith, R. W. A.; Fowler, P. W.; Jenneskens, L. W.; Steiner, E. *J. Org. Chem.* **2002**, *67*, 4753–4758.

(176) Bean, D. E.; Fowler, P. W. *J. Phys. Chem. A* **2011**, *115*, 13649–13656.

(177) Sokolov, A. Y.; Magers, D. B.; Wu, J. I.; Allen, W. D.; Schleyer, P. v. R.; Schaefer III, H. F. *J. Chem. Theory Comput.* **2013**, *9*, 4436–4443.

(178) Aprahamian, I.; Bodwell, G. J.; Fleming, J. J.; Manning, G. P.; Mannion, M. R.; Sheradsky, T.; Vermeij, R. J.; Rabinovitz, M. *Angew. Chemie Int. Ed.* **2003**, *42*, 2547–2550.

(179) Steiner, E.; Fowler, P. W.; Jenneskens, L. W.; Havenith, R. W. A. *European J. Org. Chem.* **2002**, 163–167.

(180) Havenith, R. W. A.; Lenthe, J. H. v.; Jenneskens, L. W. *J. Org. Chem.* **2005**, *70*, 4484–4489.

(181) Gomes, J. A. N. F.; Mallion, R. B. *Chem. Rev.* **2001**, *101*, 1349–1383.

(182) Randić, M. *Chem. Rev.* **2003**, *103*, 3449–605.

(183) Platt, J. R. *J. Chem. Phys.* **1954**, *22*, 1448.

(184) Boekelheide, V.; Phillips, J. B. *Proc. Natl. Acad. Sci.* **1964**, *51*, 550–552.

(185) Avouris, P.; Chen, Z.; Perebeinos, V. *Nat. Nanotechnol.* **2007**, *2*, 605–615.

(186) Ströbel, R.; Wolf, G.; Institut, F. *J. Power Sources* **2006**, *157*, 781–801.

(187) Eliasson, B.; Lejon, T.; Edlund, U. *J. Chem. Soc. Chem. Commun.* **1984**, 591–593.

(188) Acta, H. C.; Laboratorium, K. M.; Chemie, O. *Helv. Chim. Acta* **1978**, *61*, 2307–2317.

(189) Zhou, Z.; Parr, R. G. *J. Am. Chem. Soc.* **1989**, *111*, 7371–7379.

(190) Minsky, A.; Meyer, A. Y.; Rabinovitz, M. *Tetrahedron Lett.* **1982**, *23*, 5351–5354.

(191) Gershgorin, S. *B. Acad. Sci. USSR.* **1931**, *6*, 749–754.

(192) Catledge, F. A. v. *J. Org. Chem.* **1980**, *45*, 4801–4802.

(193) Gershoni-Poranne, R.; Stanger, A. *Chem. Eur. J.* **2014**, *20*, 5673–5688.

(194) Rahalkar, A.; Stanger, A. Aroma. This software may be downloaded free of charge from http://schulich.technion.ac.il/Amnon_Stanger.htm.

(195) OriginLab Pro 8.6.0, Origin Lab Corporation, Northampton MA, 01060, USA

(196) Bohmann, J. A.; Weinhold, F.; Farrar, T. C. *J. Chem. Phys.* **1997**, *107*, 1173–1184.

(197) Stanger, A. *J. Org. Chem.* **2010**, *75*, 2281–2288.

(198) Monaco, G.; Zanasi, R. *Phys. Chem. Chem. Phys.* **2013**, *15*, 17654–17657.

(199) Minkin, V. L.; Glukhovstev, M. N.; Simkin, Y. B. *Aromaticity and Antiaromaticity. Electronic and Structural Aspects*; First Edition; Wiley: New York, **1994**.

(200) Williams, R. V. *Chem. Rev.* **2001**, *101*, 1185–1204, and references cited therein.

(201) Rosenberg, Jr., J. L. v.; Mahler, J. E.; Pettit, R. *J. Am. Chem. Soc.* **1962**, *84*, 2842–2843.

(202) Keller, C. E.; Pettit, R. *J. Am. Chem. Soc.* **1966**, *88*, 604–606.

(203) Keller, C. E.; Pettit, R. *J. Am. Chem. Soc.* **1966**, *88*, 606–607.

(204) Childs, R. F.; Varadarajan, A.; Lock, C. J. L.; Faggiani, R.; Fyfe, C. A.; Wasylishen, R. E. *J. Am. Chem. Soc.* **1982**, *104*, 2452–2456.

(205) Childs, R. F.; Faggiani, R.; Lock, C. J. L.; Mahendran, M. *J. Am. Chem. Soc.* **1986**, *108*, 3613–3617.

(206) Lillington, M.; Havenith, R. W. A.; Fowler, P. W.; Baker, J.; Jenneskens, L. W. *Phys. Chem. Chem. Phys.* **2014**, *16*, 11566–11572.

(207) Winstein, S.; Kaesz, H. D.; Kreiter, C. G.; Friedrich, E. C. *J. Am. Chem. Soc.* **1965**, *87*, 3267–3269.

(208) Cremer, D.; Reichel, F.; Kraka, E. *J. Am. Chem. Soc.* **1991**, *113*, 9459–9466.

(209) Winstein, S.; Kreiter, C. G.; Brauman, J. I. *J. Am. Chem. Soc.* **1966**, *88*, 2047–2048.

(210) Berson, J. A.; Jenkins, J. A. *J. Am. Chem. Soc.* **1972**, *94*, 8907–8908.

(211) Reindl, B.; Clark, T.; Schleyer, P. v. R. *J. Phys. Chem. A* **1998**, *102*, 8953–8963.

(212) Dauben, J. H. J.; Wilson, J. D.; Laity, J. L. *Nonbenzenoid Aromatics*; Snyder, J. P., Ed.; Volume 2.; Academic Press: New York, 1967; pp. 167–206.

(213) Fernández, I.; Wu, J. I.; Schleyer, P. v R. *Org. Lett.* **2013**, *15*, 2990–2993.

(214) Haddon, R. C. *J. Am. Chem. Soc.* **1988**, *110*, 1108–1112.

(215) Lawlor, D. A.; Bean, D. E.; Fowler, P. W.; Keeffe, J. R.; Kudavalli, J. S.; O'Ferrall, R. A. M.; Rao, S. N. *J. Am. Chem. Soc.* **2011**, *133*, 19729–19742.

(216) Gibson, C. M.; Havenith, R. W. A.; Fowler, P. W.; Jenneskens, L. W. *J. Org. Chem.* **2015**, *80*, 1395–1401.

(217) Stone, A. J.; Wales, D. J. *Chem. Phys. Lett.* **1986**, *128*, 501–503.

(218) Fowler, P. W.; Baker, J. *J. Chem. Soc. Perkin Trans. 2* **1992**, 1665–1666.

(219) Deza, M.; Fowler, P. W.; Shtogrin, M.; Vietze, K. *J. Chem. Inf. Comput. Sci.* **2000**, *40*, 1325–1332.

(220) Brayfindley, E.; Irace, E. E.; Castro, C.; Karney, W. L. *J. Org. Chem.* **2015**, *80*, 3825–3831.

(221) Havenith, R. W. A.; Lugli, F.; Fowler, P. W.; Steiner, E. *J. Phys. Chem. A* **2002**, *106*, 5703–5708.

(222) Yoneda, S.; Shibata, M.; Kida, S.; Yoshida, Z.; Kai, M.; Kasai, N. *Angew. Chemie Int. Ed. Engl.* **1984**, *23*, 63–64.

(223) Oziminski, W. P.; Palusiak, M.; Dominikowska, J.; Krygowski, T. M.; Havenith, R. W. A.; Gibson, C. M.; Fowler, P. W. *Phys. Chem. Chem. Phys.* **2013**, *15*, 3286–3293.